Archaeomagnetism as a Geochronological Tool: Dating a Levantine Iron Age Conflagration

A Dissertation
Submitted to the Faculty of the
UNIVERSITY OF MINNESOTA
by

Michele D. Stillinger

In Partial Fulfillment of the Requirements
For the Degree of
Doctor of Philosophy

Joshua M. Feinberg, Adviser

June 2018

Acknowledgements

This dissertation would not have been possible without the support and encouragement of family, friends, and colleagues, especially during my battle with cancer, which briefly detoured this journey. I am particularly grateful to my adviser Joshua Feinberg, Mike Jackson, Peter Solheid, Dario Bilardello, and Bruce Moskowitz at the Institute for Rock Magnetism for their expertise, guidance, and invaluable assistance. I'd also like to thank Ron Shaar at the The Hebrew University of Jerusalem for his input and assistance with data analysis. A heartfelt thank you to Jeffery Blakely and James Hardin of the Tel El Hesi Regional Project for providing me with the materials and research questions for my PhD, introducing me to the intricacies of Biblical archaeology, reminding me that fieldwork, even in the desert, can really be a blast, and enthusiastically encouraging me throughout the process. I'd also like to thank my friends Jason Massey, Ellery Frahm, and Becky Strauss for patiently and empathetically putting up with my occasional outbursts and episodes of "imposter syndrome" quintessential of the graduate school pilgrimage, and the rest of my friends and family for sympathetically listening to the same tirades.

Dedication

This dissertation is dedicated to my mother and father
who unwaveringly accept, support, and extol my multifarious endeavors.

Abstract

Meaningful interpretation of past human culture requires an accurate chronology that can be correlated with our modern calendar. The timing of seminal events during the Levantine Iron Age (~ 1200 to 600 BCE) is hotly debated because conventional dating methods are fraught with subjective interpretations and analytical inaccuracies. This research uses archaeomagnetism, a subfield of paleomagnetism, as an alternative geochronological dating technique. Utilizing traditional archaeomagnetic materials (e.g. pottery) and testing new geologically based materials (ancient bread ovens called tabuns), a new Near East Archaeomagnetic Dating Curve (NEAC) was constructed to date four occupational deposits and a large conflagration at the Iron Age village of Khirbet Summeily, Israel. The results indicate that the destruction was likely associated with the 925 BCE Egyptian military campaign of Sheshonq I (22nd Dynasty). In addition, a new high in geomagnetic field intensity was measured that confirms the recently identified 8th Century BCE intensity spike for the region. This research provides new data that will enable geophysical researchers to improve models of geomagnetic field variability and core processes for the first three millennia BCE.

Table of Contents

List of Figures

List of Tables

1 Introduction

1.1 The Dating Quandary

One of the primary goals for Levantine historians and archaeologists is matching archaeological sites with important places and events documented in the Bible, Egyptian inscriptions, or Greek literature especially if they incorporate physical evidence of places and events represented in these narratives. To do this, extremely narrow chronologies (down to the decadal scale) are necessary, especially for sites dated to the first three millennia BCE (before common era), a period represented by an often ephemeral political and cultural history, epitomized by major Egyptian conquests and repeated geographic redistribution of lands governed by the kingdoms of Philistia, Judea and Israel.

Prior to the mid-20th century CE (common era), Levantine/Biblical archaeologists relied heavily on Egyptian and Assyrian inscriptions, Hebrew Scriptures, or relative dating techniques (like the change in diagnostic pottery development through time) to construct site chronologies. Unfortunately, incorrect translation and transcription associated with textual evidence, and the inherent uncertainties and broad resolution of relative dating led to conflicting interpretations and competing theories (which continue today) surrounding paramount regional histories.

The introduction of radiocarbon dating by W. F. Libby and colleagues in 1949, provided archaeologists with a new 'absolute' dating technique based on the known decay rate of radioactive carbon in organic materials younger than 50 thousand years (ka) before present (BP), a method ideally suited for providing absolute calendar dates to Holocene archaeological sites [*Libby et al.*, 1949]. The widespread acceptance of radiocarbon dating in the 1960s resulted in the aptly termed "Radiocarbon Revolution," which highlighted the power of absolute dating techniques to identify bias and discrepancies in traditionally constructed chronologies. The consequence was a complete reassessment of the timing, development, and transmission (or lack thereof) of human technology, art, and culture previously defined by archaeologists of the 19th century, particularly theories of cultural diffusion [*Renfrew*, 1979; *Taylor et al.*, 1999].

Despite the advantages of radiocarbon dating, many Levantine archaeologists continue to view radiocarbon dating as a secondary dating technique, preferring to rely on textual evidence and pottery seriation to construct site chronology for the Iron Age. This reluctance is mainly due to discrepancies resulting from natural fluctuations of carbon-14 (^{14}C) produced in the upper atmosphere that cause bimodal or indeterminate calendar ages during this period. The lack of precision in radiocarbon dating, along with the long standing bias towards relative dating techniques, has resulted in three competing chronological paradigms for the Iron Age II period (~1000 to 700 BCE), which differ by as much as 100 years, a significant span of time in a period characterized by rapid changes in political geography. The impact of these differing paradigms has led to major debates in the archaeological community surrounding the

interpretation of three key historic events: 1) the physical evidence for a major Egyptian military campaign by 22nd Dynasty pharaoh Sheshonq (Shishak) I into the region circa 925 BCE, 2) the sociodemographics of the region during the Iron Age, in particular the timing of Egyptian, Philistine, and Israelite control over the Land of Canaan (modern day Israel), and 3) whether or not the United Monarchy (Kingdoms of Israel and Judah) actually existed [*Finkelstein*, 2010; *Mazar*, 2010]. Details of the Levantine chronology paradigms can be found in [*Finkelstein*, 1996, 2002, *Mazar*, 1997, 2005, 2011; *Blakely*, 2002; *Mazar and Bronk Ramsey*, 2010; *Finkelstein and Piasetzky*, 2010b, 2011, *Fantalkin et al.*, 2011, 2015; *Lee et al.*, 2013; *Gilboa et al.*, 2013; *Blakely et al.*, 2014; *Toffolo et al.*, 2014; *Ussishkin*, 2015; *Garfinkel et al.*, 2015].

1.2 Thesis Objectives

An appeal to address these paradigms led to this research, which applies paleomagnetic analysis techniques developed in the Earth Science community to fired anthropogenic materials from the Bronze and Iron Ages in order to provide a complementary dating method to archaeologists. Paleomagnetism is the study of the Earth's pre-historic magnetic field variability, on the millennial-scale, as recorded by and stored in geological materials containing magnetic minerals. Archaeomagnetism, a subfield of paleomagnetism, uses the same techniques to measure the ancient field record (magnetic remanence) stored in anthropogenic materials, primarily those that are heated to high temperatures, like pottery. A series of measurements of the Earth's ancient field strength stored in pottery of known age, for example can be plotted to

create a reference curve of the Earth's field variability through time (secular variation). These reference curves can subsequently be used for dating artifacts and sites of unknown age.

Previous research on Bronze Age (~3300 to 1200 BCE) archaeological materials from the site of Tell Mozan in Syria [*Stillinger et al.*, 2015] was conducted to test the applicability of archaeomagnetic dating on high-fired ceramics. The methodology from that study (see Chapter 5) is used here to analyze materials from five Levantine archaeological sites located in the Negev Desert of present day Israel. Four of these sites contain previously well-dated materials spanning the period between 1400 and 600 BCE. These sites are used as sources of calibration data. The final site, Khirbet Summeily, is used to test the application of archaeomagnetic dating to the period when radiocarbon dating is inconclusive.

Located in the Shephelah, the low hill country between the Judaean mountains and the coastal plain, Khirbet Summeily (Figure 2-1) is a small but significant Iron Age administrative center situated on the ancient border between the Kingdoms of Philistia and Judah and along the major trade route between Gaza City and Hebron [*Blakely*, 2002; *Blakely and Hardin*, 2002; *Hardin et al.*, 2012; *Blakely et al.*, 2014]. The site has multiple occupational layers containing traditional Philistine and Judaic ceramic wares, Egyptian artifacts, and other diagnostic materials, which have provided a relatively dated chronology between 1200 and 800 BCE. Around 950 BCE, the site displays evidence of a major conflagration as indicated by a thick (30+ cm) layer of ash. Oddly,

the destruction layer has no carbon-rich materials suitable for radiocarbon dating, making it ideally suited for testing of the archaeomagnetic dating reference curve produced in this research. Summeily also contained two *in situ* household bread ovens called tabuns, and a number of scattered tabun fragments. These fired features, made with local clay sediments, have the ability to record ancient magnetic field direction (declination and inclination) and strength (intensity), at the time of their last use. If the structures were reheated to a high temperature during the conflagration, they could also provide archaeomagnetic dates for the specific event.

The destruction layer at Summeily is believed to be associated with the 925 B.C.E. Egyptian campaign of Sheshonq I. This campaign, which conquered over 150 cities in the region, is inscribed on the famed Bubastite Portal of Karnak in Egypt, a key reference to the understanding of geopolitical history in the region. Levantine archaeologists have long assumed that certain massive Iron Age II destruction deposits correspond with this campaign. However, destruction layers are a frequent occurrence at many sites in the region, and, depending on their favored chronology paradigm, researchers disagree on the timing and importance of their particular conflagration [e.g. *Blakely and Hardin*, 2002; *Finkelstein and Na'aman*, 2004].

Many of the samples chosen for this research came from conflagration events in order to provide dates for these historical markers and make archaeomagnetic comparisons between sites. However, conflagrations could conceivably exhibit variable temperatures and/or physical extents (i.e. room by room variability), affecting the

recording of magnetic remanence. Therefore, this research was designed to answer two primary questions:

1) **Can tabuns and destruction event materials adequately record magnetic remanence?**
2) **Can we date the destruction at Khirbet Summeily using archaeomagnetic dating?**

Accordingly, I framed my dissertation research around the following three goals: 1) to measure the ancient field recording in materials from key archaeological sites in Israel that are already well dated to immediately before and after the Iron Age period where radiocarbon provides disputable dates, 2) to use the results from those samples as principal chronology markers in order to construct a more robust archaeomagnetic dating curve for the region, and 3) to demonstrate the application of this curve to date the destruction layer at Khirbet Summeily.

1.3 Interdisciplinary Merit

This research, by its very design, is interdisciplinary, and thus, has a number of ramifications to both the social and Earth sciences. First, by providing new data for constructing a Levantine/Near East archaeomagnetic dating reference curve and a more precise chronology for the site of Khirbet Summeily, archaeologists (and historians) can reassess the current chronology paradigms and correctly interpret the geo-political history of ancient Judah and Philistia during the 10th Century BCE.

Second, data derived from this archaeomagnetic research will provide new transient magnetic information to the paleomagnetic community. The recent discovery of high frequency, high-amplitude fluctuations in the Earth's geomagnetic field strength during the Holocene has stimulated the need for more sub-century to decadal-scale field data to understand fine-scale geodynamo processes. Very high intensity anomalies centered around the 1st millennium BCE in the Levant have now been identified at several locations in the Near East, North America, and China [Ben-Yosef et al., 2009; Shaar et al., 2011; Cai et al., 2014; Bourne et al., 2016]. These "spikes" or "jerks" in field strenth are three to five times the average global field strength estimated for the Holocene. This research provides new data for this critical period, which can be used to augment geophysical models designed to infer core flow processes. Archaeomagnetic data may also provide the information necessary to address the radiocarbon dating problem for the Iron Age, given the relationship between the Earth's magnetic field and ^{14}C production.

The following chapter provides a brief introduction to archaeomagnetism, the dating issues for the Levantine Iron Age and the potential for archaeomagnetic dating as a complementary dating technique. It also presents preliminary results as of 2014 from this research. Chapter 3 reviews the other current dating techniques available to archaeologists for the Iron Age period, with an emphasis on radiocarbon dating, the primary and yet currently disputed method of dating. This is followed by an outline of the magnetic theory relevant to the field of archaeomagnetism in Chapter 4. Chapter 5 will present materials and methods used in this research by outlining the

archaeointensity methods used for Tell Mozan, Syria and the updates to that methodology as applied in this study. Results and interpretations from this research are covered in Chapter 6, which will include a new archaeomagnetic dating curve. Discussion, as it pertains to the initial research questions, will be covered Chapter 7.

2 Archaeomagnetism as a Complementary Dating Technique to Address the Iron Age Chronology Debate in the Levant

The contents of this chapter were originally published in the *Journal of Near Eastern Archaeology,* Vol 79:2*,* and are included here with permission of all authors [*Stillinger et al.*, 2016]. Note: several non-essential images from the original article are omitted, a new image added (Fig. 2-6), and site phase plans updated to present the most recent illustrations.

Synopsis:

Meaningful interpretation of past human culture and political geography requires an accurate chronology that can be correlated with our modern calendar. The timing of seminal events during the Levant Iron Age is hotly debated because conventional dating methods are limited by subjective interpretations and analytical ambiguities. Archaeomagnetism, the study of the Earth's ancient geomagnetic field recorded by heat-treated anthropogenic objects, can provide a complementary dating tool to build a stronger, more robust chronology for the Iron Age. Here we present a description of the field of archaeomagnetic dating, and a brief overview of the chronological issues and radiocarbon dating problems for the Iron Age Levant. We also present a new Near East Archaeomagnetic Curve (NEAC) model for the region along with preliminary data from Khirbet Summeily, Israel.

2.1 Introduction

A fundamental goal of archaeological research in the Near East is the determination of accurate chronology, particularly in situations where one is attempting to correlate specific events and places in written history with archaeological features and sites. In the past, Near East archaeologists have relied heavily on 'relative' dating techniques, such as pottery seriation and comparison with ancient text and/or inscriptional evidence to ascribe ages to their materials and sites, all of which are necessary for site interpretation and a basic understanding of chronology. However, while the relative ordering of many seriation chronologies is often correct, interpretive problems and even heated chronological debates can arise when attempting to fix seriation-derived dates within an absolute time scale such as our modern calendar dating system.

To address the subjective nature of relative dating, a number of geochronological dating techniques developed within the Earth Sciences and Physics communities have been applied to archaeological materials. These 'absolute' dating techniques utilize well-constrained radioactive decay processes, quantifiable levels of thermoluminescence (TL), or other natural variations in biological and planetary processes that have a known rate of occurrence. The most widely accepted absolute dating technique is radiocarbon (^{14}C) analysis, used to date carbonaceous archaeological materials younger than ~50,000 years old (<50 ka). As archaeologists strive to refine site chronologies to ever finer temporal resolutions with radiocarbon dating, we have

begun to approach the analytical limit of the technique for some time periods and new controversies have arisen that are presently not possible to resolve. For example, the natural fluctuation in the production rate of atmospheric ^{14}C through time can create de Vries effects (often termed 'wiggles') in the radiocarbon reference curve, which can cause an artifact's measured radiocarbon concentration to coincide with multiple ages. Additionally, there are certain periods on the reference curve that plateau, resulting in indeterminate ages (Fig. 2-2). Unfortunately, both of these situations arise between the 10th and 9th centuries BCE, a critical period for understanding the formation of Iron Age kingdoms and/or states in the southern Levant. Another issue is that many sites lack suitable or sufficient quantities of material for radiocarbon analysis. Finally, recent attempts to address the chronology issues in the Levant have brought into question the use of Bayesian dating models based on radiocarbon measurements across multiple unrelated sites (e.g. Lee, Bronk Ramsey, and Mazar (2013) and references therein). Given these ongoing issues, it is necessary for archaeologists to consider incorporating other complementary dating methods in order to constrain their chronologies.

Here, we introduce the potential of archaeomagnetic dating for addressing the Iron IIA chronology debate in the Levant in the context of its application to the Hesi Regional Project's excavations at Khirbet Summeily (Fig. 2-1), a site occupied during the 11th through 8th Centuries BCE (see Hardin, Rollston, and Blakely (2012 and 2014) for details of the Hesi Regional Project). Depending on one's chronological views and the relative ambiguity of radiocarbon and seriation dating for this time period, different reconstructions of the history and archaeology of the Iron IIA transitions in the Levant

are followed (discussed below). Therefore, we chose to institute a comprehensive program of archaeomagnetic dating from the onset of the Khirbet Summeily project.

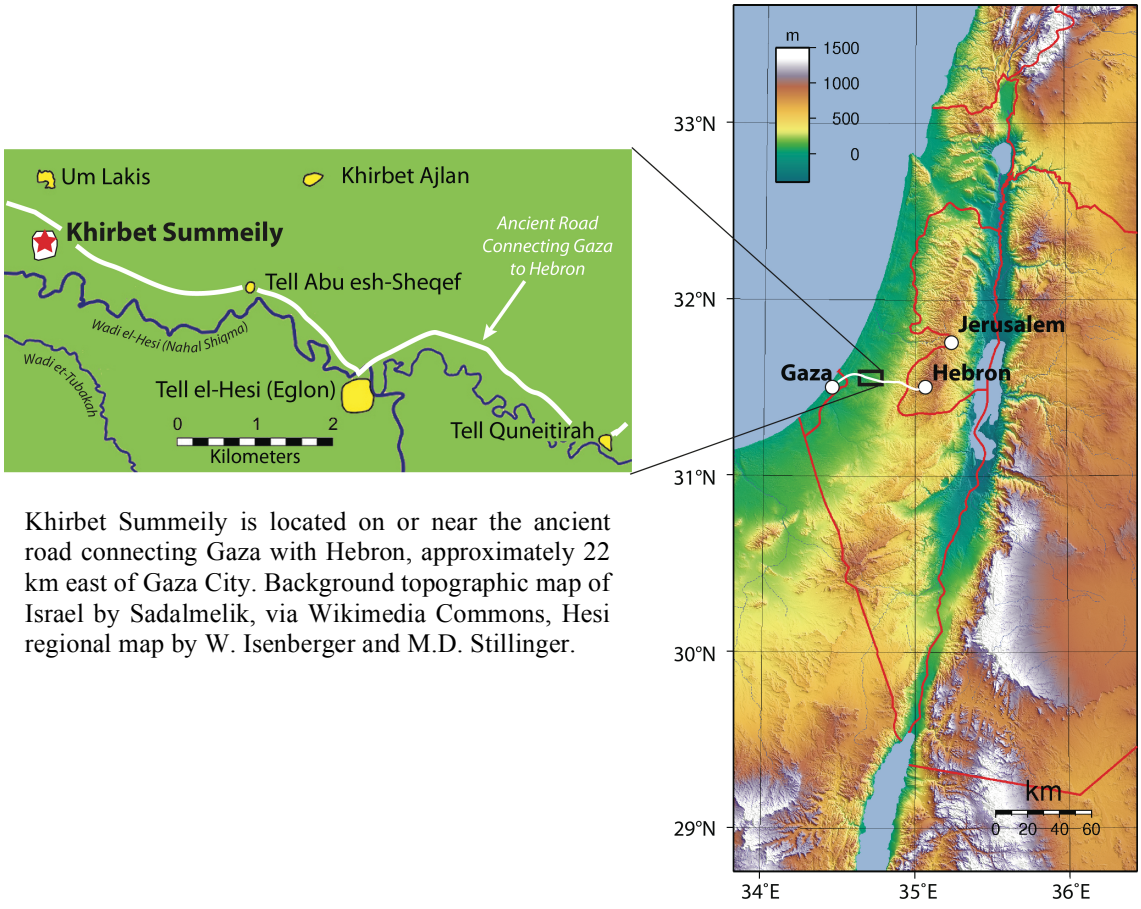

Khirbet Summeily is located on or near the ancient road connecting Gaza with Hebron, approximately 22 km east of Gaza City. Background topographic map of Israel by Sadalmelik, via Wikimedia Commons, Hesi regional map by W. Isenberger and M.D. Stillinger.

Figure 2-1 Location of Khirbet Summeily and the Hesi Region

2.2 What is Archaeomagnetic Dating?

Archaeomagnetism is a subfield of paleomagnetism, the study of the Earth's ancient magnetic field as recorded by volcanic rocks, soils, and sediments. The Earth's magnetic field, which acts like a giant dipole magnet, is generated in the planet's core and propagates through the mantle and crust, surrounding the Earth and protecting our

atmosphere from solar and cosmic radiation (see Fig. 4-1). The field is dynamic, both temporally and spatially and can be directly measured using specialized land or satellite based equipment. Under the right circumstances, geological materials that contain magnetic minerals, like magnetite and hematite, can record these field variations during thermal or depositional processes. In the case of archaeomagnetism, human-made archaeological materials, such as fired ceramics, mudbrick, *in situ* clay ovens, slag, and heat-treated rock can also record the field because they contain these same magnetic grains. When these objects are heated to high temperature, conditions commonly found in a kiln or oven, and then cooled, the magnetic minerals record the Earth's field strength (intensity) and direction at that moment in time. This recording can be preserved for millions of years and can be measured in the laboratory using super-conducting cryogenic rock magnetometers. Compilations of ancient field measurements from materials that have been previously well-dated using other methods can be used to construct a regionally specific reference curve of field behavior through time. These reference curves can then be used to date artifacts of unknown age.

The accuracy and precision of archaeomagnetic dating is dependent on the quality of its reference curves. For recent history (the last 3000 years) archaeomagnetic reference curves are calibrated using several different sources of chronologic information: direct measurements of the field (land and satellite), dendrochronology, lake sediment data, radiocarbon, and definitive archaeological evidence, usually in the form of textual evidence. Thus, in the best of circumstances, archaeomagnetic dating can achieve uncertainties as low as one or two decades, which is comparable to

radiocarbon dating. For pre-historic periods or regions where dendrochronological or lake varve data are not present, important calibration points are often set using radiocarbon, pottery seriation, or other archaeological dating techniques. Radiocarbon analysis of materials associated with continuous and successive archaeological layers often provides the most accurate calibration. Calibration using seriation dating is less desirable; but in many cases, definitive and undisputed seriation dates, along with the use of additional complementary dating methods, can still provide suitable calibration points on the curve. Archaeomagnetic specialists must take great care to ensure that the calibration of regional reference curves avoids circular logic that may arise from using relative dating techniques or ambiguous radioisotopic calibration points. This is particularly important for the Iron Age Levant, which is discussed further below.

One of the primary advantages of archaeomagnetic dating is that it uses materials that are often abundant or of low cultural value at many archaeological sites, such as pottery sherds and fired brick, making it ideally suited for dating sites that lack carbonaceous materials for radiocarbon analysis. Archaeomagnetic dating is also relatively inexpensive. The ability to analyze multiple specimens at the same time equates to half the cost (approx. $200) per sample as radiocarbon analysis, which can run over $600 for a single test. In some instances, archaeomagnetic research may actually have the potential to improve the resolution of the radiocarbon method. For example, a high quality archaeomagnetic reference curve from a quickly deposited sedimentary sequence (e.g., laminated lake sediments or a rapidly deposited cave speleothem) could provide a clear record of the earth's magnetic field behavior across

an interval where the production rate of ^{14}C was perturbed. The geochronology of this record could be constrained by layer counting of lake laminae or growth layer counting in the speleothem, as well as by ^{238}Th dating. This archaeomagnetic reference curve could be used to accurately date materials at archaeological sites that were created during these perturbed radiocarbon intervals. If there were existing radiocarbon ages associated with these intervals, then the archaeomagnetic reference curve would provide a mechanism for correcting (and hence "refining") the radiocarbon curve. The final concentration of ^{14}C in a material is a product of many independent natural processes, including the Earth's overall field strength (discussed below). Therefore, isotopic geochemists seeking to model the production rate of ^{14}C in the upper atmosphere can also use high-resolution reference curves of geomagnetic field behavior to isolate the attenuating effects of magnetic shielding on ^{14}C production, thus improving the radiocarbon dating curve.

As the paleomagnetic community continues to uncover additional information about the Earth's magnetic field over the last 10 ka, archaeomagnetic reference curves will continue to improve in accuracy and precision. This steady improvement will make archaeomagnetic dating progressively more invaluable to the archaeological community, which can play a vital role in refining these reference curves by providing more *in situ* archaeological materials that represent successive occupations at a particular site. One of the goals of the extensive archaeomagnetic research currently underway at Khirbet Summeily and neighboring sites is to provide new intensity data to improve the reference curve for the Levant and to demonstrate the potential of

archaeomagnetic dating as a complementary technique for addressing the Iron IIA chronological debate.

2.3 Development of Archaeomagnetic Methods

The phenomenon of magnetism was first documented in the 6th century BCE and the study of the directional variability of the Earth's field followed not long after, with the invention of the compass and identification of the magnetic north pole in the first millennium C.E. In the 1600s, William Gilbert wrote the first modern treatise on magnetism, "De Magnete", which summarized all previous magnetic discoveries, confirmed the properties of permanent magnetism, and presented the idea that the Earth itself generated the observed field similar to a dipole magnet. He also confirmed the acquisition of magnetism in iron by successive heating and cooling, paving the way for the field of paleomagnetism. By the 1700s detailed maps of global declination and inclination were being produced and instruments were being invented to measure the field's strength. By the 1800s the scientific field of geomagnetism blossomed, resulting in worldwide expeditions and the construction of geomagnetic observatories from Canada to the Antarctic, all with the goal of measuring the geographic and temporal variability of Earth's field. By the late 1800s, rock magnetism and paleomagnetism had set the stage for the methodological foundations of archaeomagnetic dating, long before the development of radiocarbon dating (see Courtillot and Le Mouël (2007) for an overview of the development of the different fields of magnetism).

In 1899, Giuseppe Folgheraiter identified the stability of magnetization held by

archaeological objects, particularly fired clay bricks from Roman walls and ancient Greek and Etruscan pottery [*Folgheraiter*, 1899]. In the 1940s, the husband and wife team of Emile and Odette Thellier developed the fundamental techniques for recovering the strength of the Earth's magnetic field at the time an object was originally heated or formed. They used their results to publish some of the first reference curves of field variation through time for Western Europe [*Thellier and Thellier*, 1959]. The 1970s and 80s saw a surge in regionally specific archaeomagnetic data generation from the American southwest, Great Britain, Eastern Europe, Russia, and the Far East. At the time, this line of archaeomagnetic research was primarily driven by geoscientists interested in describing the short-term behavior of the Earth's magnetic field and understanding the processes that modulated its behavior. As a potential dating tool; however, the method remained under-utilized by archaeological researchers and was viewed solely as a novel dating technique.

Since the 1990s, technological advances in instrumentation and new paleomagnetic methodologies have resulted in improved characterization and measurement of magnetic materials, increasing the accuracy of our ability to estimate the strength of the Earth's ancient magnetic field. For example, the original Thellier and Thellier method has been expanded to include stepped heating procedures to identify problematic mineralogical alteration that may occur during laboratory heating experiments and/or effects of non-ideal magnetic behavior. Analysis of magnetic fabric enables researchers to identify and correct for issues of anisotropy, such as the preferential alignment of clay platelets in pottery resulting from various manufacturing

processes. And cooling rate corrections are now applied to address the difference between laboratory and natural cooling situations.

Today, several research groups and laboratories, such as the Institute for Rock Magnetism (IRM) at the University of Minnesota, engage in archaeomagnetic research with the goal of improving the density of high quality measurements and applying more robust modeling techniques to construct new reference curves for different regions of the world. Reference curves spanning the last 5000 years now exist for sites throughout much of Western Europe and the Near East and nearly 8000 years at archaeological sites in Eastern Europe (Genevey and Gallet 2003; Hervé, Chauvin, and Lanos 2013; Kovacheva et al. 2014; Pavón-Carrasco et al. 2014; Stillinger, Feinberg, and Frahm 2015 and references therein).

2.4 Iron Age IIA Chronological Issues in the Levant

2.4.1 The Chronology Quandary

The accuracy of the traditional Levantine Late Bronze through Iron Age chronology was brought into question in the mid 1990s after Israel Finkelstein questioned the accepted chronology of the Iron I/Iron II transition [*Finkelstein*, 1996]. At the time, there were relatively few radiocarbon dates for the Iron Age and arguments for two different chronologies (the High or Traditional Chronology and the alternative Low Chronology) centered on textual biases, questionable stratigraphy, and the dating of Philistine or imported pottery styles. Over the past several decades this issue has

become the most debated topic within the archaeology of the region, impacting the absolute dating of material remains and their relevance for understanding the historical monarchies of Israel and Judah. The details of the original debate have been covered extensively in previous publications and will not be repeated here (Fantalkin, Finkelstein, and Piasetzky 2011; Finkelstein and Piasetzky 2011; Lee et al. 2013; Mazar 2011; and references therein).

The issues in the debate are at once archaeological (typological/stratigraphic), anthropological (processes of secondary state formation), and historical/biblical (Egyptian & Levantine material culture synchronism as well as contrasting textual relevance for understanding the Iron Age II). The addition of more reliable radiocarbon dates and complicated statistical analyses (e.g. Fantalkin, Finkelstein, and Piasetzky 2015; Garfinkel et al. 2015; Lee et al. 2013; Toffolo et al. 2014) have narrowed the range of disagreement between the chronologies to approximately 50 years but the interpretive impact still remains large (e.g. compare Fantalkin et al. 2011; Mazar 2011; van der Plicht, Bruins, and Nijboer 2009). Given that the centuries involved are viewed as historic periods and that historic documents and monuments can be brought to bear along with the archaeological data, it is surprising that the gap has not narrowed more significantly. The continued chronology contention arises mainly from limitations in the relative and absolute dating methods currently in use, primarily artifact typologies/seriations for the former and radiocarbon dating for the latter. While both of these dating techniques are integral and important tools for accurate chronology construction and site interpretation, it is clear that an additional dating technique is

necessary to address the problem. Here, we will focus on the problem with radiocarbon dating during the Iron Age period as this method is most often used to address the limitations of seriation dating.

2.4.2 Radiocarbon Dating Issues

Since the 1970's radiocarbon has become one of the most highly regarded methods for dating archaeological sites. Radiocarbon dating is based on the known decay rate of the radioactive isotope of ^{14}C found in organic materials like wood, ash, and carbonized seeds. In most cases, its accuracy is excellent and sufficient for answering broader questions of human time at scales of several decades or less, especially if obtained from sites with strong stratigraphic controls and collection standards (see Boaretto 2008 for a detailed overview). Unfortunately, during the Iron Age, the radiocarbon calibration curve contains a number of plateaus spanning several decades and two robust de Vries effects (de Vries 1958), which result in indeterminate or bimodal radiocarbon ages (Fig. 2-2). Consequently, radiocarbon analyses near and during these intervals can produce a range of potential ages with subsequent error rates up to 100 years. The underlying causes of these plateaus and de Vries effects are complex, but at their heart, these changes are due to fluctuations in the intensity of solar radiation and cosmic rays interacting with nitrogen in the Earth's upper atmosphere, the source of ^{14}C production. The two primary moderating influences are (1) the production rate and energy spectrum of cosmic radiation generated by the Sun, and (2) the Earth's magnetosphere (a function of field strength), which acts as a shield against this cosmic

radiation.

When the Earth's magnetic field strength increases, fewer cosmic rays are capable of penetrating into our upper atmosphere and less ^{14}C is produced. Between the 11th through 9th centuries BCE, the Earth's magnetic field displayed an exceptionally high and prolonged period of field strength, the highest in the last 50 ka. In fact, the Near East regional field strength during this interval was three times the global average strength over the last 300 million years [*Selkin and Tauxe*, 2000] and significantly higher than the average strength for the Northern Hemisphere. The effect of this prolonged period of high field intensity is reduced ^{14}C production, resulting in the numerous plateaus in the radiocarbon curve, which are the source of some of the dating difficulties associated with radiocarbon analysis. The de Vries effects, on the other hand, appear to be associated with a number of rapid and intense field fluctuations that punctuate this same time period (discussed below) and are possibly linked to the overall increase in the field. Despite the use of numerous calibration techniques to fix the radiocarbon reference curve to specific calendar dates, such as dendrochronology and lake varves, these underlying features remain, causing dating discrepancies.

In an attempt to narrow the range of possible radiocarbon dates further, Bayesian analytical techniques [*Buck et al.*, 1991; *Bronk Ramsey*, 1995; *Lanos and Philippe*, 2015] are often applied to chronology dates derived from radiocarbon and seriation. However, the use of different assumptions to drive the models (particularly cross cultural pottery use and inter-site stratigraphic sequences) by different research

groups (e.g. Boaretto et al. 2005; Bruins et al. 2005; Finkelstein and Piasetzky 2010; Mazar and Bronk Ramsey 2008; Sharon et al. 2007) often leads to variable outcomes for absolute dates (see Lee et al. 2013 and references therein for a recent overview of the different Bayesian methodologies and how they are applied). In this light, it appears to us that concerted efforts to rely solely on radiocarbon for a period when radiocarbon dates cannot be definitively obtained will not, in itself, further refine the absolute dating of Iron Age IIA. Consequently, this debate has stagnated over the last decade with opposing sides becoming ever more entrenched. It is clear that an alternative and/or complementary absolute dating method is required.

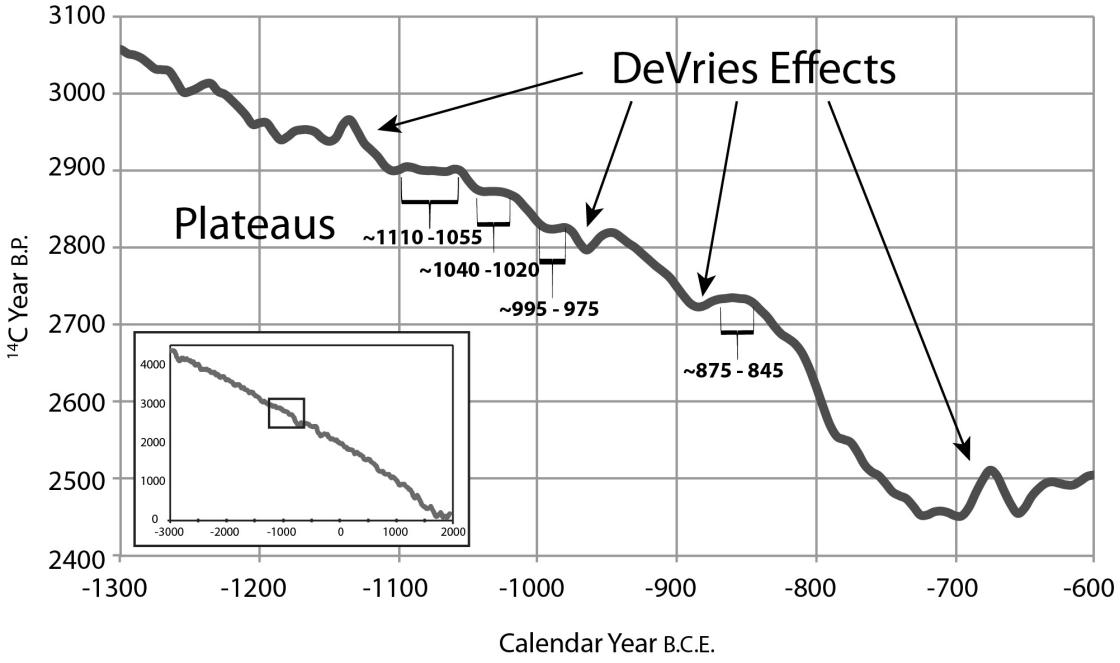

Figure 2-2 IntCal13 Radiocarbon Calibration Curve for the Iron Age
IntCal13 radiocarbon calibration curve for the northern hemisphere for the 13th through 7th Centuries BCE highlighting plateaus and de Vries effects, which cause indeterminate age distributions. Inset is curve for the last 5000 years (curve data from Reimer et al. (2013)).

2.5 Archaeomagnetic Dating in the Levant

Over the last decade, several research groups have begun to use new techniques in archaeomagnetic dating to address this very issue. The Bronze Age, for example, is well represented by archaeomagnetic data from many locations, particularly from Syrian pottery analyzed by the research group at the Institut de Physique du Globe de Paris, but many periods of the Iron Age are still lacking in reliable data. Recent studies, several conducted by the research group at Scripps Institute of Oceanography, have incorporated more ^{14}C calibration and utilized unique materials such as copper slag deposits, clay furnace fragments, and tuyère (clay bellow pipe nozzles). In particular, these types of materials at the sites of Khirbet en-Nahas and Timna-30 have been integrated with highly detailed stratigraphic analysis to investigate an unusual geomagnetic "spike" around 980 BCE, a rapid and very high increase in field strength and an ideal chronological marker for dating curves [*Ben-Yosef et al.*, 2009; *Shaar et al.*, 2011]. At first, this spike appeared geographically constrained to the region around the Levant, but has since been identified in Anatolia and North America [*Ertepinar et al.*, 2012; *Bourne et al.*, 2016]. The overall regional increase in field intensity during the 10th Century BCE has also been confirmed from materials at several sites in Syria (Gallet et al. 2014 and references therein).

Despite this growing archaeomagnetic database of field behavior, there is still very little magnetic data for the Iron I/Iron II transition through the end of the Iron IIB period (between 1000 and 701 BCE). Additionally, archaeomagnetic reference curves

for the region continue to rely heavily on seriation and radiocarbon dates for calibration because these are the preferred archaeological dating methods. Because the chronology paradigms are relatively undisputed bounding the Iron IB and IIA periods, these dating methods, especially in conjunction with strong stratigraphic controls, can, therefore, be considered acceptable in terms of archaeomagnetic calibration for the Iron IA and IIB periods. An integral part of our research at Khirbet Summeily includes archaeomagnetic sampling of several nearby sites with well-dated materials, strong stratigraphic constraints, and destruction layers of undisputed age that are dated to immediately before, during, and after the Iron Age period in question. Results from these sites will be incorporated with other high quality archaeomagnetic research in the region to refine the regional reference curve (below), which will subsequently be used to date the materials from Summeily.

2.6 The Near East Archaeomagnetic Curve (NEAC)

As mentioned previously, a robust reference curve is necessary to date material of unknown age. Figure 2-3a displays our new archaeomagnetic reference curve model of the Earth's field intensity for the first three millennia BCE for the Near East and Levant regions, which we call the "Near East Archaeomagnetic Curve" (NEAC). This model was generated using only high quality archaeomagnetic data from Israel, Jordan, Syria, Egypt, Turkey, and Cyprus following similar methodology and suitability criteria as outlined in Stillinger, et al. (2015) and including recent dates from Gallet et al. (2014), Shaar et al. (2015), and Stillinger et al. (2015 and sites referenced therein).

In paleomagnetism, the Earth's field intensity or strength is commonly described in units of Virtual Axial Dipole Moment (VADM), or the total field generated by the Earth's core that would give rise to measurable field strength in microtesla (μT) for a specific location. In the Levant the VADM has been slowly decreasing since the 1st millennium BCE and is currently about 76 ZAm^2 (bold dashed line on graph). Over the last decade the geomagnetic research community has begun to produce time-varying global models of Earth's magnetic field behavior using spherical harmonic mathematics. These models tend to smooth out high-frequency field perturbations and cannot yet be used for archaeomagnetic dating, but they are useful for comparing with regional archaeomagnetic reference curves to see if broad trends are in agreement. Here we show a number of spherical harmonic models for comparison with our archaeomagnetic model. The ARCH3k.1e (purple) field model [*Korte et al.*, 2009] is based on only archaeomagnetic data for the last 3000 years and published up until 2009. This model is strongly biased to the Northern Hemisphere and contains data from some studies that are outdated in terms of methodology. The CALS10k.1 model (blue) [*Korte et al.*, 2011] covers the last 10,000 years and includes all archaeological, sediment, and lava data up until 2011. The PFM9k.1a (green) field model [*Nilsson et al.*, 2014] is similar to the CALS10k model but incorporates new data treatments and sedimentary data. It is notable that while all of these models show the same broad trends in geomagnetic field strength as the NEAC model, none of them appear to capture the dramatic increase in field strength that is recorded by Near East archaeological materials during the 10th Century BCE.

Creating a robust regional archaeomagnetic reference curve requires that we only use data whose ages are well constrained, and not affected by problematic ambiguities associated with the radiocarbon technique. Unfortunately, the current Iron Age data are derived primarily from relative and radiocarbon dating techniques. In an attempt to demonstrate the importance of unequivocal radiocarbon dates on the ultimate shape of the NEAC model, we removed all ^{14}C calibrated intensity data between 1250 and 625 BCE and remodeled the curve (Fig. 2-3b). As mentioned previously, this period is when a number of de Vries effects and plateaus could result in unclear ^{14}C dates (red shaded regions). First, the removal of these data shows the marked lack of archaeointensity data for this period. Second, the removal of these data reduces the strength of the field during this interval to be in closer agreement with the spherical harmonic models. Both the modified NEAC and PFM9k models still indicate a regional field intensity that is higher than average during the 1st millennium BCE; but the unusually high regional spike in the early 10th century is not captured unless the ^{14}C data are taken into account. This highlights an urgent need to acquire additional archaeomagnetic data for this period from sites with well defined successive occupational strata that are definitively dated using chronologic techniques other than radiocarbon in order to firmly calibrate the archaeomagnetic dating curve.

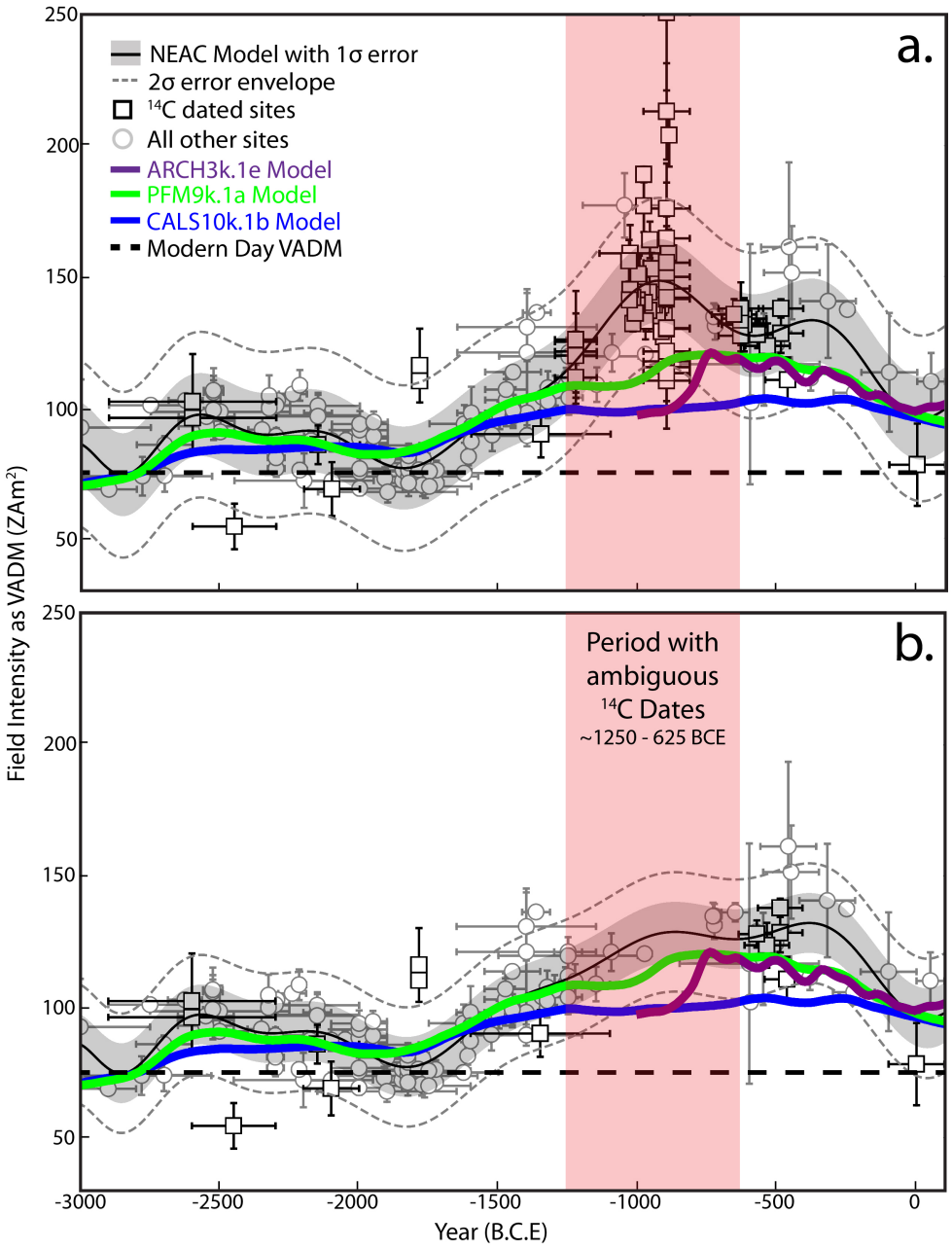

Figure 2-3 Near East Archaeomagnetic Dating Curve (NEAC)

Virtual Axial Dipole Moment (VADM) represents the Earth's total generated field strength that gives rise to a locally measured intensity. (a) New NEAC model includes all data as cited in the text and modeled using procedures outlined in Stillinger et al., (2015). (b) NEAC model with all ^{14}C-calibrated data removed for period shaded in red. Both models are based only on high quality archaeomagnetic data from Israel, Syria, Jordan, Egypt, Cyprus, and Turkey. See text for description of the ARCH3k, CALS10k, and PFM9k models derived from the Geomagia50 online database [*Brown et al.*, 2015a].

2.7 Khirbet Summeily: An Iron Age Administrative Center

2.7.1 Excavations and Phasing

Khirbet Summeily is a small archaeological site located about 4 km from Tell el-Hesi, which was first described as being pre-Roman by Petrie in 1890. Like Tell el-Hesi, the largest and most extensively excavated Bronze and Iron Age tell site in the surrounding region, Summeily is situated on the coastal plain along the northern edge of the Negev Desert, where agriculture was marginal for most archaeological periods. It was on, or at least near, the road connecting Gaza with Tell el-Hesi and Hebron. Unlike Hesi, which has multiple strata spanning 2000 years of occupation (EB III to Persian), Summeily appears to be a one period site, with four structural phases of occupation, tentatively dating from the late 11th through mid-8th centuries BCE (Table 2-1). Because of its proximity to Tell el-Hesi and the retrieved material culture, we believe Summeily was most likely a Judahite site as opposed to Philistine [*Blakely et al.*, 2014].

Excavation at Summeily began in 2011 with the belief the site was an Iron Age rural village. The 2011 and 2012 field school seasons initially identified two primary phases of occupation with material culture and features atypical of domestic structures. In 2014, two additional phases were revealed for a total of 4 occupational strata (Phases 2 through 5) and one disturbed surface layer with more modern artifacts (Phase 1). Phase 5 is the earliest Iron Age phase currently identified and has only been reached in a couple of excavation areas. Phase 5 is tentatively dated to the transition between the

11th and 10th centuries BCE based on Iron IB type pottery and artifacts. Phase 4 was better identified in our last season of excavation and includes a large non-domestic building, which has guided us to a different understanding of both the site's and the region's function during the Iron Age. A number of anepigraphic fired clay bullae were found associated with this phase, confirming their Iron Age IIA association (see Hardin, Rollston, and Blakely (2014) for details of this discovery). Further excavation of Phase 4 will clarify its precise date between Phases 5 and 3, but both pottery and stratigraphic location suggest the mid-10th century BCE *(see Figure 2-4 for current occupational phase plans updated after this publication in 2017 and drawn under the direction of the original authors by W. Isenberger).*

Phase 3 was excavated at the start of the 2011 season in two excavation units and quickly became the pivotal Phase at Summeily leading to its cultural reassessment. As the Phase was exposed, a thick destruction deposit from a large conflagration presented itself. One room was quickly identified as a cult room based on the presence of an altar, a zoomorphic ceramic head, and a unique ceramic "chalice-like" object that seemed to have been resting on the altar before the destruction. In addition, a broken but complete bowl (sample KS107) was found nearby (Figs. 2-5 and 2-6). Both of these artifacts are stylistically dated to the Iron IIA. The integration of stratigraphic controls and ceramic observations suggests that Phase 3 dates to the mid to late 10th century BCE using the modified standard chronology as outlined by Lee et al. (2013). This phase was followed by a brief occupational gap before Phase 2 deposits, which are tentatively dated to the late 9th century to the mid 8th century BCE using the same

chronology.

Table 2-1 Phase Dates and Preliminary Archaeomagnetic Results

Summeily Phase	Estimated Phase Dates BCE[a]	Pottery Style	Archaeomagnetic Sample[b]	VADM Intensity (ZAm^2)[c]
2	~830–732	Iron IIB	KS1419	123.7±13.5
			KS2357A	158.6±8.7
			KS2357B	132.3±3.9
			weighted average	***137.7±7.0***
Occupational Hiatus				
3	~980–900	Iron IIA	KS1606	126.4±13.1
			KS107	110.4±7.8
			KS2348B	107.6±3.7
			KS2362	138.6±8.7
			weighted average	***116.7±6.8***
4	*Currently Under Review*			
5	~1100–980	Iron IB	KS2368	140.6±19.7
			KS2369	127.8±4.9
			KS2371	177.8±15.0
			weighted average	***140.2±9.3***

[a] *Based on Modified Chronology after Lee et al. (2013) and site stratigraphy.*

[b] *Each sample result based on a weighted average of 3 specimens (2 for KS2362), corrected for anisotropy, and meeting the following archaeointensity statistics: MAD<10° and DANG<15°.*

[c] *VADM is the total field moment generated by the Earth given the strength recorded at a specific location. Archaeomagnetic dating curves are typically represented in either VADM or field strength in microtesla (μT).*

Archaeomagnetic dating at Summeily, and neighboring contemporary sites, is situated perfectly in time to contribute towards a resolution of the debates of the past two decades regarding the absolute chronology of the Iron Age. This line of research was aided by the discovery of the major destruction and conflagration ending Phase 3 and less pronounced burn layers ending Phases 2 and 4. In particular, *in situ* fired hearths and tabuns (small bread ovens) were found associated with Phases 2 and 3,

materials suitable for providing both directional and field strength archaeomagnetic data. These materials, along with samples from both the chalice and bowl, other burned and broken pottery, and burnt mudbrick were collected for archaeomagnetic analysis at the IRM using the procedures outlined in Stillinger et al. (2015). To date, archaeomagnetic analysis has been completed on 51 specimens representing 17 different samples. Preliminary results from 10 archaeomagnetic samples passing strict selection criteria are listed in Table 2-1.

2.7.2 Preliminary Archaeomagnetic Results

Preliminary archaeomagnetic results for Khirbet Summeily are plotted in Figure 2-7, which focuses on the Iron Age period in question. In the absence of independent absolute ages on these materials, we can use the current NEAC model to refine the ages of the various occupational phases at Summeily. Each data point's age errors are based on a combination of the modified chronology and our current evaluation of site stratigraphy. For example, the average VADM intensity of Phase 5 samples is 140.2 ZAm^2 (solid orange diamond), placing it at approximately 1050 BCE on the curve; however, the actual date of the Phase, as currently derived from seriation, could range between 1100 and 980 BCE. Individual samples, each representing 3 measured specimens, are also plotted for each phase (open diamonds) to show the range of intensity obtained by sample. As more samples are measured, especially for Phase 4 materials, these average occupational ages can be further refined.

These preliminary results indicate that samples from Phase 5 show similar

archaeointensities to archaeomagnetic results from other sites in the region associated with the 980 BCE geomagnetic spike. The unusually high intensity for one of the Phase 2 samples may indicate an additional regional spike not captured by the spherical harmonic models. This new spike has recently been identified in ceramics from Megiddo and Hazor [*Shaar et al.*, 2016]. At first glance, Phase 3 results appear unusually low; however, a closer look at the other regional data for the Iron IIA Period indicates a decreasing trend in field intensity leading up to 900 BCE. This trend may indicate that the Phase 3 occupation dates to just prior to 900 BCE. From the model, it can also be noted that the archaeointensity results previously recorded for 900 BCE range from ~100 ZAM^2 to an unusually high peak of nearly 250 ZAm^2. This peak tends to pull the model up and mask the preceding downward trend in the individual data points. This unusual range of values for ~900 BCE and their associated dating errors suggest that the Earth's field experienced a number of rapid fluctuations within a 100 year timespan. Combined with the known decreasing intensity trend in the late 9^{th} century, it is unclear if the other low intensity values reported in previous studies for 900 BCE are for the decades directly preceding or following the spike. The ~900 BCE spike is currently being re-evaluated [*Shaar et al.*, 2016], but it is clear that additional independent ages on archaeomagnetic samples from Summeily and its neighboring sites may help clarify all three geomagnetic spikes and improve our understanding of the field behavior during the 10^{th} through 8^{th} centuries.

2.8 The Way Forward

Archaeomagnetic dating holds the potential for addressing the Iron Age II chronology by providing an additional complementary dating technique that can easily be incorporated into any excavation's research design. Archaeomagnetic dating uses fired materials such as broken pottery, tabuns, and mudbrick, which are often abundant and of little cultural value at archaeological sites in the Levant and is relatively inexpensive compared to other radioisotope methods. An intensive archaeomagnetic dating project is currently underway at the site of Khirbet Summeily, an Iron Age site located in the Northern Negev near Tel el-Hesi, along with materials from several contemporary sites in the region, in order to provide additional data to the regional record of the Earth's magnetic field behavior, construct a more robust archaeomagnetic reference curve, and refine the absolute dates at Summeily. Preliminary results for three Phases at Summeily are consistent with archaeomagnetic dates previously reported for the region. We also introduce an updated Near East Archaeomagnetic Curve (NEAC) that can be used as a basic reference curve for archaeomagnetic dating in the region.

This research underscores the importance of integrating a variety of dating methods in order to refine the absolute chronology of the Iron Age. As more archaeomagnetic research is conducted on materials from nearly continuous archaeological sequences or *in situ* materials that can provide magnetic directional data, the NEAC curve can be further refined. Decadal-scale resolution is ultimately achievable, but will require the incorporation of additional absolute dating methods to

firmly calibrate the curve, including uranium-series dating (e.g., ^{230}Th, ^{238}U) of carbonate nodules or speleothems, regional freshwater lake sediments, TL, and optical stimulated luminescence dating, in order to comprehensively address the ambiguities inherent in radiocarbon and seriation dating and resolve the Iron Age chronology debate.

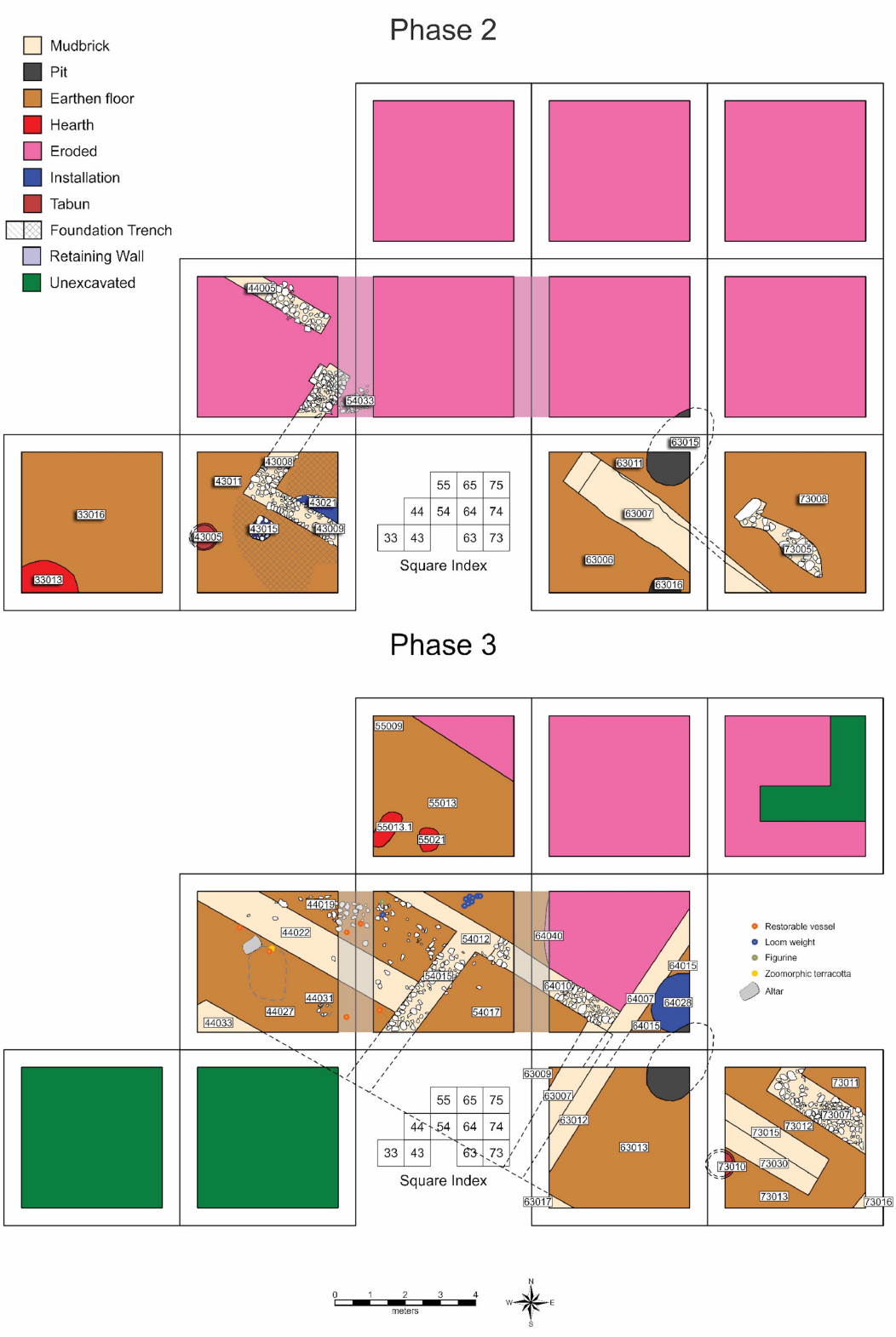
Phase 2
Mudbrick
Pit
Earthen floor
Hearth
Eroded
Installation
Tabun
Foundation Trench
Retaining Wall
Unexcavated
44005
54033
43008
43011
43021
43015
43009
43005
38016
38013
55 65 75
44 54 64 74
33 43 63 73
Square Index
63015
63011
63007
63006
63016
73008
73005
Phase 3
55009
55013
55013.1
55021
44019
44022
54012
54015
64040
64015
64010
64007
64028
44031
44027
44033
54017
Restorable vessel
Loom weight
Figurine
Zoomorphic terracotta
Altar
63009
63007
63012
63013
63017
73011
73007
73012
73015
73010
73030
73013
73016
0 1 2 3 4
meters
N
W
E
S

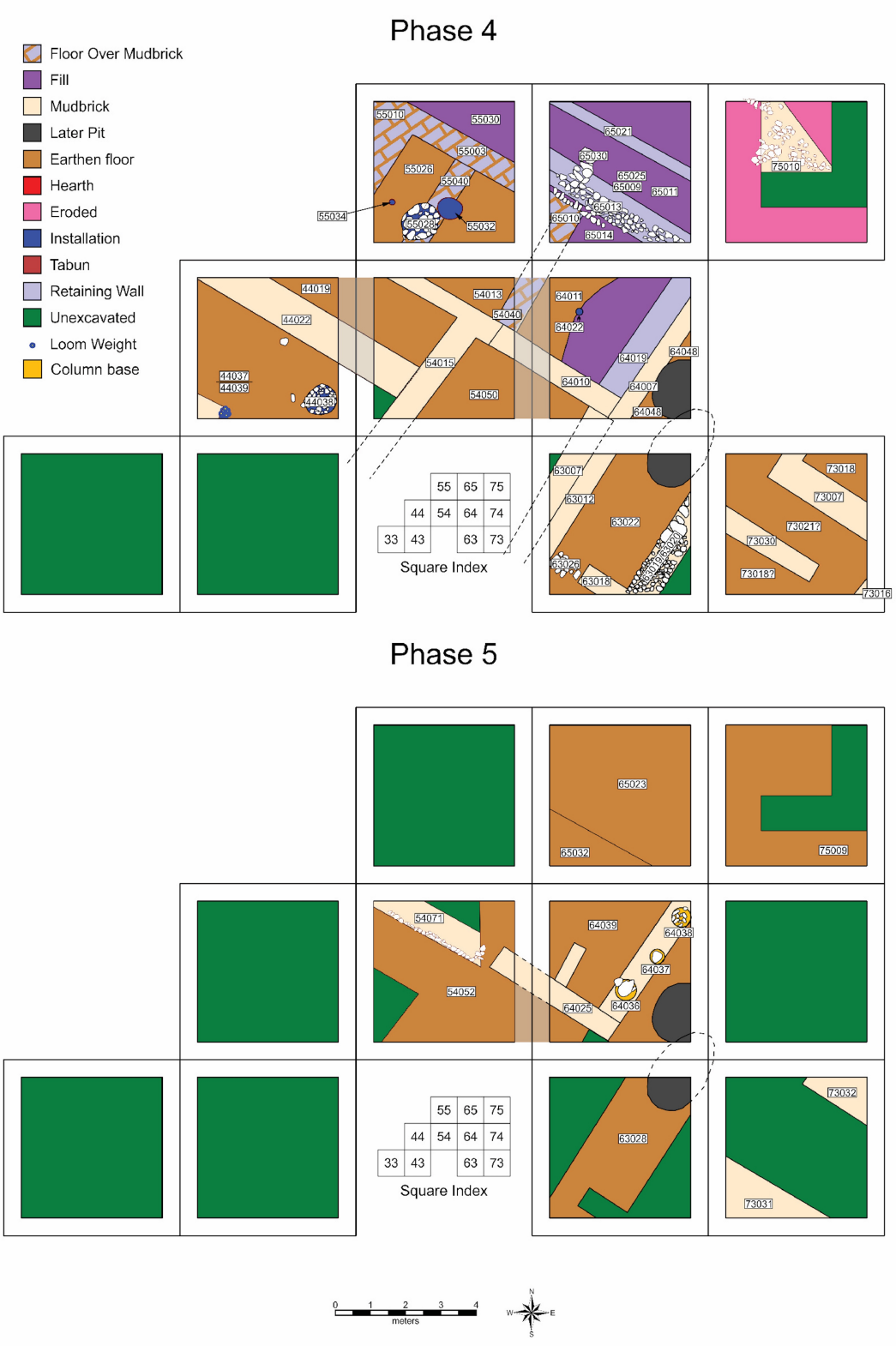

Figure 2-4 Khirbet Summeily Phase Plans as of 2017

Occupational phases from most recent (Phase 2) to oldest (Phase 5). See table 2.1 for estimated dates.

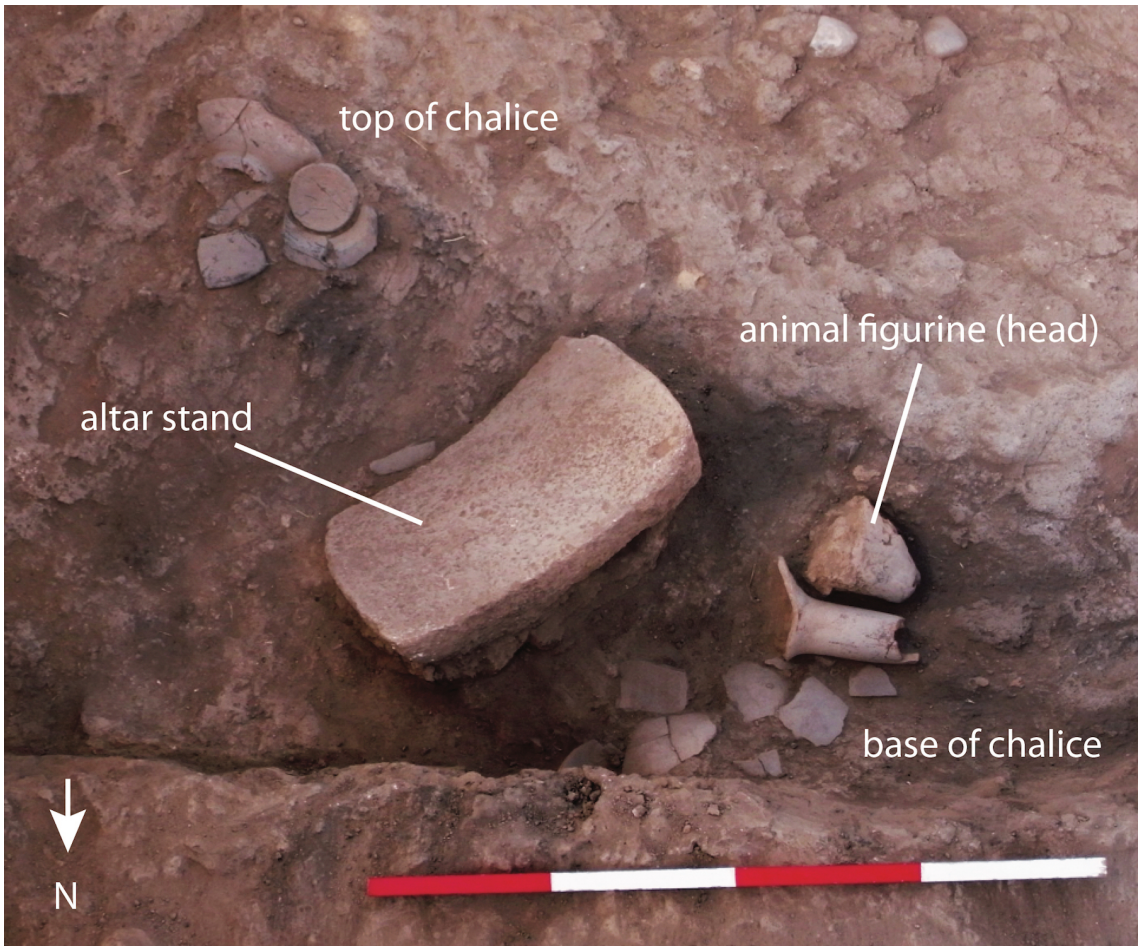

Figure 2-5 Unit 44 Altar Installation

Collapsed altar installation found in religious/cult room destruction deposit. A unique and complete chalice or offering dish along with part of a large animal figurine was found near limestone cult stand. Photograph by W. Isenberger courtesy of the Hesi Regional Project.

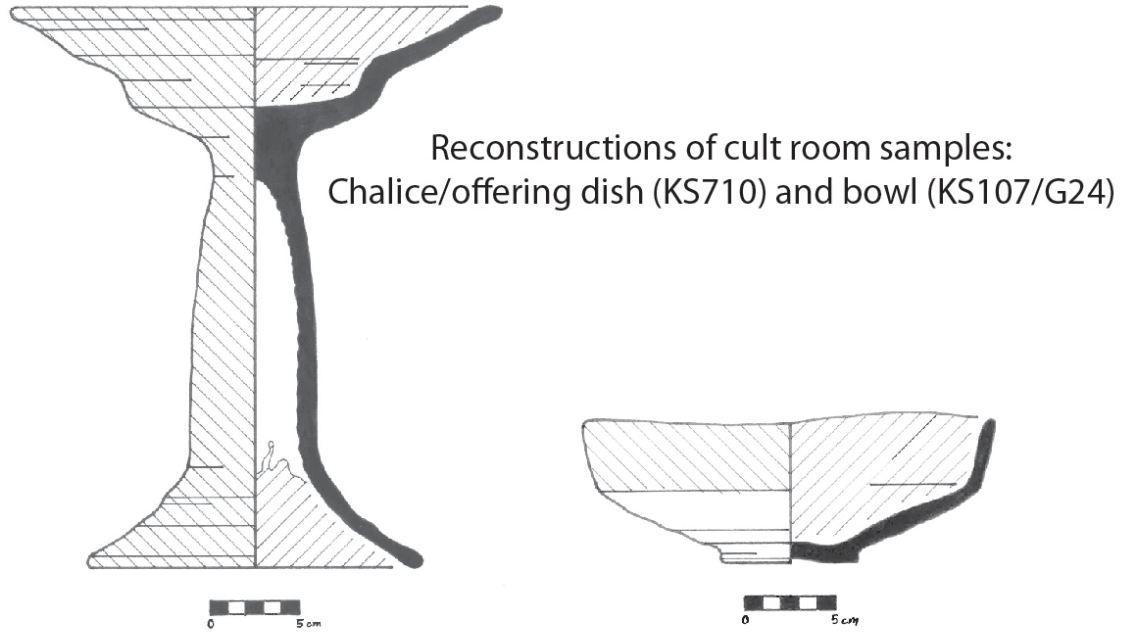

Figure 2-6 Cult Room Chalice and Bowl

Iron IIA cult room chalice (upper left and bottom) and bowl (upper right) from Unit 44, Phase 3. (Samples numbers for bowl KS107 later renamed to KSG24 to avoid confusion with chalice). Drawings by Dylan Karges. Photo courtesy of the Hesi Regional Project.

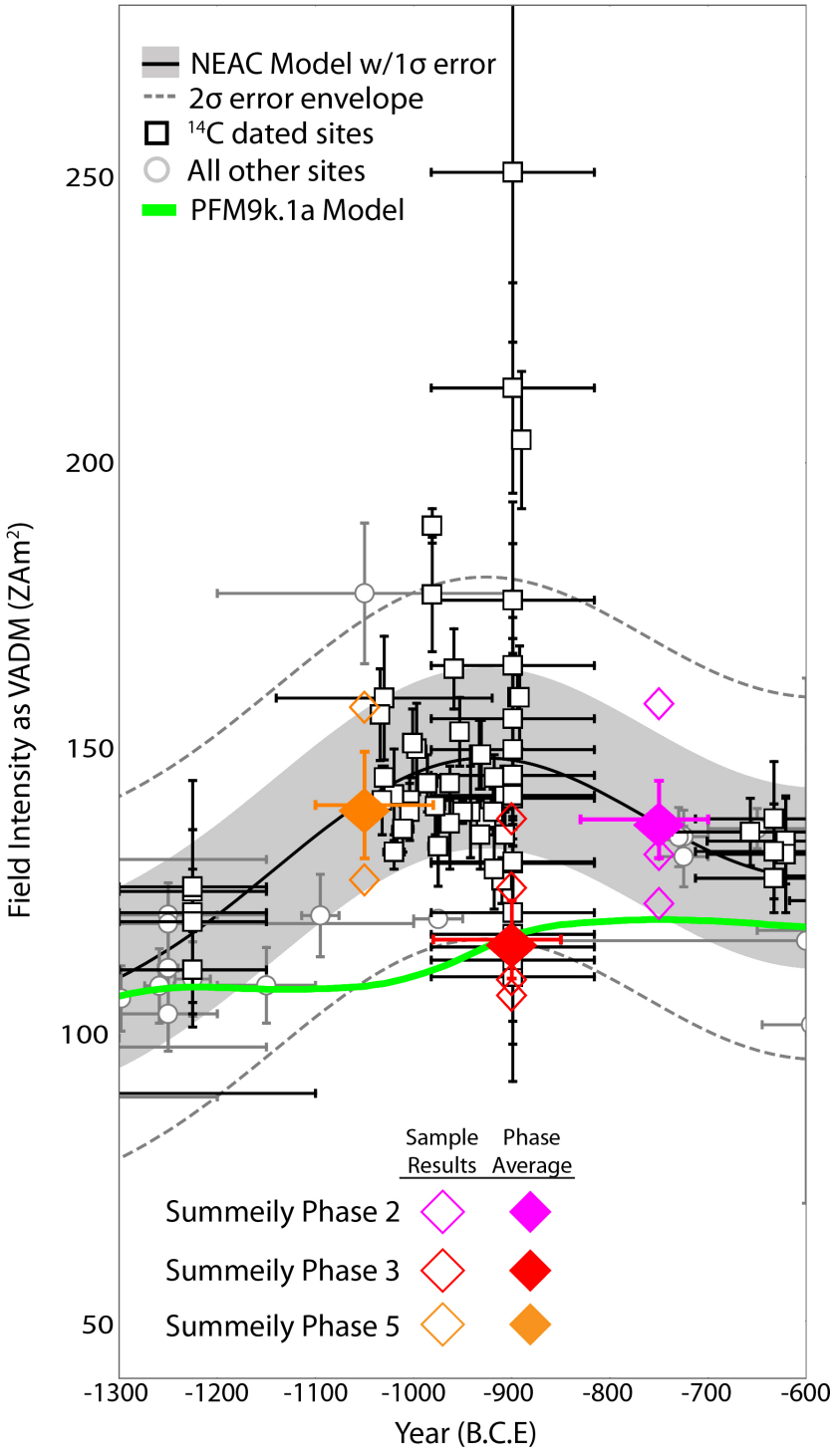

Figure 2-7 Preliminary Results for Khirbet Summeily

NEAC curve for the 11th through 8th Centuries BCE highlighting preliminary results for Khirbet Summeily. See Figure 2-3 and text for description of models and regional data. Filled/Open diamonds are the preliminary average/individual sample results for each Phase at Summeily.

3 Dating Methods

A comprehensive and accurate chronology requires the incorporation of a number of absolute and relative dating methods to ascribe ages to characteristic anthropogenic materials and deposits associated with archaeological sites. For the Holocene Epoch (~12 ka to present), there are three primary types of dating methods: 1) inscribed or textual evidence dating, 2) relative dating (sequential age assignment based on perceived age from older to younger), and 3) absolute dating (ascribing ages based on the known rate of occurrence of an associated component).

3.1 Textual Evidence Dating

When we think of Levantine or Biblical archaeology, it is easy to conjure images of Victorian era archaeologists excavating famous Egyptian tombs or Roman ruins in Jerusalem, Masada, or Caesarea. In fact, scholarly investigation of the region began in the 4th century CE as pilgrims traveled to the Holy Land to find the locations of the cities mentioned in the Bible [*Hardin et al.*, 2012]. Modern Levantine archaeologists frequently utilize Egyptian documents and inscriptions, Biblical texts, and other regional historical accounts for constructing chronologies. While ancient texts and inscriptions can be the most reliable dating sources, they can still be subject to error. For instance, incorrect or biased translation and interpretation on the part of past or modern scholars, error in transcription by ancient scribes, or inaccurate conversion to

the modern calendar can occur. Additionally, many writings may have embellishments or adaptions to historical events to meet the demands or prevailing ideologies of the target audience, not to mention the assumption that all ancient texts are non-fictional histories.

3.2 Relative Dating

Along with textual evidence, or in its absence, many established chronologies for Levantine archaeological sites are based on relative dating methods, primarily seriation dating of pottery or other ancient technologies like stone tools. These methods are considered 'relative' dating in that they are based on the principles of stratigraphic superposition or their relative position within a cultural deposit and their association with diagnostic artifacts.

Seriation dating involves the relative ordering of the changing complexity or style of a culture's technology or artistic achievements through time. For example, the early hominid shift from making large, simple, stone chopping tools to producing shapely bifaces or arrow points, is a type of seriation based primarily on changes in manufacturing complexity. This uniformitarian or gradualist approach assumes that change in technology must progress from simple to complex through time.

The progressive development of pottery, metal production, and monumental constructions are the most often used dating techniques for the Levant and the foundation for most chronologies. Major transformations in these technologies are even

the basis for the commonly used archaeological/cultural subdivisions of the Holocene (e.g. Neolithic (pre-pottery), Chalcolithic (Copper Age), Bronze Age, Iron Age, and Classical Periods). It is important to note that these periods vary by region and stage of technological development and are not congruent between broader landscapes. For example, the Mesolithic, or pre-agricultural period, began around 20 ka before present (BP) in the Levant and Near East but not until 10 ka BP in Europe.

While often correct, seriation dating may be influenced by the interpretation of changing cultural style or assumed technological dispersion as defined by the individual archaeologist or theoretical paradigm. The Clovis-First stone tool controversy [*Waters and Stafford*, 2013] in American archaeology is a prime example. Additionally, cross-cultural exchange and interaction, external pressures like climate change or diminished resources, or even shifts in ideology can be the impetus for rapid diversification, sudden innovations, and even the reversion back to simpler technologies. In addition, relative dating often relies on inter and intra-site comparison of materials and temporal relationships, such as the presence of Cypriot ceramic wares at sites in Israel.

In terms of precision, relative dating can determine which materials are oldest and which are youngest, and provide a general age range. It cannot always assign actual ages/dates to materials correlated to our modern calendar dating system. Thus, the limitations to relative dating methods can result in broadly defined chronologies with uncertainties of several hundreds of years or more, lacking the definitive ages required by scholars attempting to associate materials with specific decadal scale

events. For example, the Levantine Iron Age II period (~1000 BCE to 800 BCE) currently has three competing chronology paradigms that vary by as much as 100 years, a significant period of time when attempting to correlate archaeological sites with Biblical texts.

3.3 Absolute Dating

To address the issues of relative dating, a number of geochronological techniques developed within the Earth Sciences community are often utilized with anthropogenic materials to 'absolutely' date artifacts, features, and sites (Figure 3-1). These dating methods utilize radioactive decay processes of various isotopes, quantifiable levels of luminescence in geological substrates, or other natural variations in biological and planetary mechanisms that have a known, temporally specific rate of change. The primary absolute dating methods applicable to Holocene archaeology include several radiometric dating techniques such as radiocarbon (^{14}C) and Uranium-series (i.e. $^{230}Th/^{234}U$), annual depositional data such as dendrochronology (tree-ring dating), and trapped charge dating (i.e. thermoluminescence, electron spin resonance, and optically-stimulated luminescence), which utilize a variety of natural and human modified archaeological materials (Table 3-1).

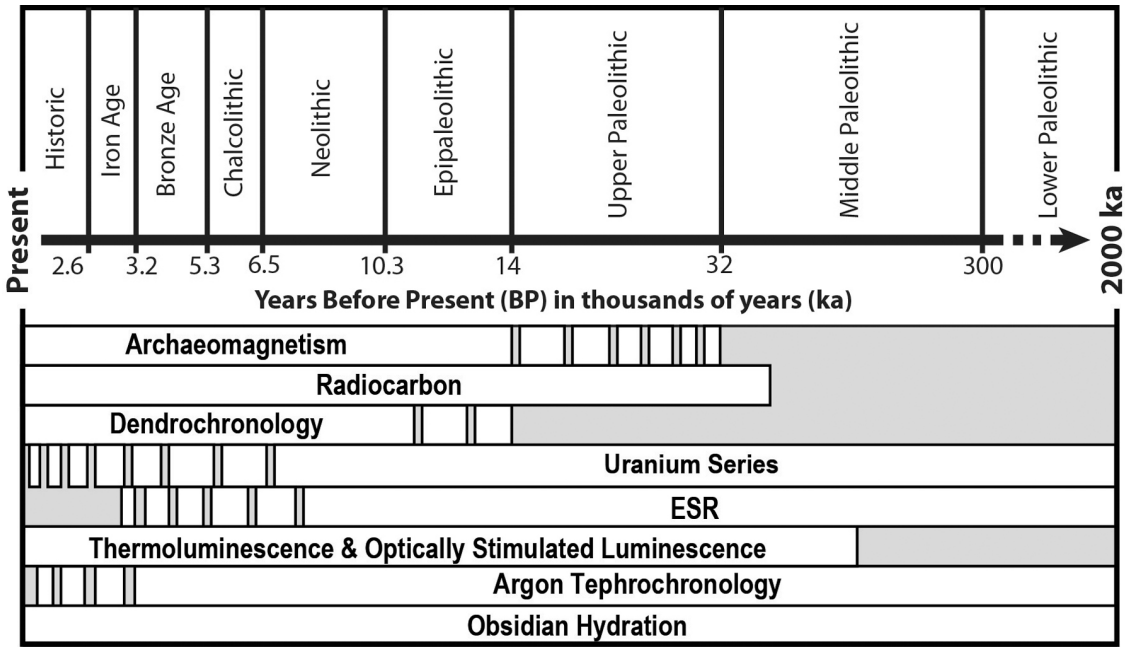

Figure 3-1 Applicable Dating Methods by Time Period

Table 3-1 Target Materials for Applicable Dating Methods

Dating Method	Wood,Seeds, &Organics	Bone/Antler/teeth	Shell & Corals	Speleothems	Pottery/Baked Clay & Sediments	Metal Slag	Burnt Flint/Stone	Unburnt Sediment	Obsidian	Volcanic Deposits
Archaeomagnetism				x	x	x	x	x		x
Radiocarbon	x	x	x	x	x	x		x		
U-Series		x	x	x				x		x
Dendrochronology	x									
ESR		x	x	x	x		x			x
TL/OSL				x	x	x	x	x		x
Argon Tephrochronology										x
Obsidian Hydration									x	

(modified from Rapp and Hill, 2006)

Archaeomagnetic dating, a subfield of paleomagnetism is unique in that it falls between the standard definitions of relative and absolute dating. While the geomagnetic field record stored in archaeomagnetic materials is highly quantifiable data, the

calibration of that data to calendar years for prehistoric periods is currently based on a combination of relatively and absolutely dated associated materials, often radiocarbon dating for the latter. Following is summary of the absolute dating techniques primarily utilized today in Holocene archaeology, with an emphasis on radiocarbon dating.

3.3.1 Radiocarbon Dating

Most archaeologists today utilize radiocarbon dating as their primary absolute dating technique. Radiocarbon dating is based on the radioactive decay of the carbon-14 isotope and has become the standard for accurately and objectively dating organic archaeological materials less than 50 ka old. The majority of the Earth's naturally occurring carbon consists of two stable non-radioactive isotopes: carbon-12 (^{12}C) at ~99% and carbon-13 (^{13}C) at ~1%. A third isotope, Carbon-14 (^{14}C), is found in trace amounts. Most ^{14}C (99%) is produced in the troposphere and stratosphere through the bombardment of nitrogen atoms by neutrons that are produced when cosmic rays interact with gases in the upper atmosphere. The ^{14}C isotope quickly reacts with oxygen to form carbon-14 monoxide, which slowly oxidizes to form $^{14}CO_2$ or radioactive carbon dioxide. This $^{14}CO_2$ distributes throughout the Earth's atmosphere on timescales of weeks and is eventually transferred to the terrestrial biosphere and hydrosphere carbon reservoirs of the planet [*Anderson et al.*, 1947; *Libby et al.*, 1949; *Nydal*, 1968; *Damon et al.*, 1978].

All isotopes of carbon in CO_2 are taken up by terrestrial plants through the process of photosynthesis or dissolved in the ocean, where they are subsequently

transferred through the food chain to other organisms or stored in carbonate sediments. Plants and animals convert this CO_2 to organic compounds necessary for growth and survival through the process of carbon fixation. Organisms continually exchange CO_2 with the atmosphere while living, and thus, maintain a measureable ratio of radioactive ^{14}C atoms to stable ^{12}C atoms in their system. The amount of ^{14}C in an organism is, on average, in equilibrium or proportional to atmospheric ^{14}C. When an organism dies and is no longer taking in new carbon (time zero) the ratio of the radioactive ^{14}C to the stable ^{12}C in the organism begins to decrease at a known exponential rate. This rate for ^{14}C, known as a half-life, is 5730±40 years [*Arnold and Libby*, 1949; *Engelkemeir et al.*, 1949; *Libby*, 1952; *Stuiver and Polach*, 1977]. A comparison of the remaining ^{14}C in an organic sample with the expected equilibrium ratio of the living organism that sample represents is then used along with a series of calibrations to determine the age (since death) of that organism [*Taylor*, 2001; *Dunai*, 2010].

The decay of ^{14}C is measured in two ways: (1) by counting the intensity of the beta (β) radiation emitted during decay using a proportional gas counter or liquid scintillation detector, or (2) by directly measuring the ions of remaining ^{14}C to ^{12}C in the sample using an accelerator mass spectrometer (AMS) [*Taylor*, 2001; *van der Plicht and Bruins*, 2001]. The β-radiation method requires several grams of sample and several days to weeks to process, whereas the newer more sensitive AMS method allows for faster measurements and smaller sample sizes (less than 1 mg). This advantage of AMS has expanded the applicability of radiocarbon analysis to problematic samples or priceless museum artifacts previously untested due to the older

requirement for large samples in [*Taylor*, 2001; *van der Plicht and Bruins*, 2001; *Rapp and Hill*, 2006].

Conventional radiocarbon age estimates are reported at one and two standard deviations (σ) in calendar years BP, with present or time zero corresponding to 1950 CE. This date was adopted by the U.S. National Institute of Standards and Technology (NIST) to account for the rapid changes in global radiocarbon levels resulting from human activities. Rapid industrialization since the 1800s and burning of carbon reservoirs in the form of fossil fuels like coal has decreased the natural concentration of atmospheric ^{14}C, while an artificial and rapid increase in ^{14}C resulted during the 1950s and 1960s due to nuclear bomb testing [*Damon et al.*, 1978; *Hua et al.*, 2013]. To account for these changes, the theoretical standard for natural ^{14}C is now based on a wood sample grown in 1950. Parameters for reporting radiocarbon include: (1) the use of the NIST oxalic acid standard or equivalent during testing, (2) the use of the original (and incorrect) half-life determination for ^{14}C of 5568± 30 years, (3) an isotopic fractionation normalization of ^{14}C to a common $^{13}C/^{12}C$ ($\delta^{13}C$) value of -25 per mil, and (4) the assumption that all reservoir ratios of $^{14}C/^{12}C$ have remained constant in the past (pre-1950) [*Stuiver and Polach*, 1977; *Taylor*, 2001].

Despite this latter assumption, natural ^{14}C activity has not remained constant through time but varies both temporally and spatially in the different carbon reservoirs as a result of sunspot activity, cosmic ray intensity, the Earth's magnetic field, and even past human induced alterations to the carbon cycle. A low magnetic field intensity, for

example, allows more cosmic rays to interact with the Earth's atmosphere resulting in increased ^{14}C production [*Elsasser et al.*, 1956; *Stuiver*, 1961; *Kigoshi and Hasegawa*, 1966]. The field's modulating affect on ^{14}C production rates cause variations, called de Vries effects and plateaus, to the radiocarbon curve, which would otherwise display a simple linear relationship between measured radiocarbon age and calendar age (see Figure 2-2). These fluctuations, which have frequencies of decades to centuries, are due to variations in sunspot activity, cosmic ray intensity and the strength of the Earth's magnetic field [*de Vries*, 1958; *Stuiver*, 1961; *Damon and Long*, 1962; *Suess*, 1965]. De Vries effects result in age distributions with two or more calendar age intersects on the curve for one radiocarbon age determination. Plateaus on the other hand, are periods in the calibration curve where no ^{14}C variation occurs for several decades, such as those spanning some of the disputed periods (1000-700 BCE) of the Iron Age II in the Levant region. These plateaus are the result of abrupt decreases in ^{14}C production in the atmosphere [*Kitagawa and van der Plicht*, 1998b], the result of increased magnetic field strength, and can result in an indeterminate span of potential calendar dates.

To account for these variations, radiocarbon dates are calibrated against another dating technique in order to accurately convert radiocarbon years (BP) to calendar years (AD/CE or BC/BCE) and a 'reservoir correction' age provided if applicable [*Stuiver and Suess*, 1966; *Stuiver and Polach*, 1977; *Damon et al.*, 1978]. Initially, textually derived dates from Egyptian chronologies believed to be definitive were used for calibration [*Arnold and Libby*, 1949], however, a nearly 300 year discrepancy in traditional chronologies between the two dating methods highlighted the problem of

circular referencing and relative dating. This problem discouraged many Near Eastern archaeologists from accepting radiocarbon analysis. By 1985, more precise calibration curves based on dendrochronology (annual tree-ring counts) became the standard [*Damon and Peristykh*, 2000; *van der Plicht and Bruins*, 2001]. While widely accepted as the most accurate calibration for radiocarbon dates and well suited to Holocene archaeological chronologies, dendrochronology (discussed below) is limited in its precision to materials less than 12,000 years BP and to the availability of suitable trees in a particular region.

Marine-sourced calibrations, such as paired ^{14}C and Uranium series dating of coral samples, has now extended accuracy of the radiocarbon curve from 12,000 to 50,000 years. Standard radiocarbon dating reference curves, such as the International Calibration Curve (IntCal13) [*Reimer et al.*, 2013a], are now calibrated with a combination of dendrochronology, foraminifera in varved and non-varved marine sediments, and uranium-series dating of coral and speleothems [*Hughen et al.*, 2004; *Reimer et al.*, 2004, 2009, 2013a; *Fairbanks et al.*, 2005; *Bronk Ramsey*, 2009]. Varves, the annual or seasonal deposition of fine laminations of sediments composed of calcite, diatoms, aragonite, and organic material, offer an absolute chronology representing actual calendar years, similar to dendrochronology. In some instances, lake varves have also been used to calibrate radiocarbon measurements [*Kitagawa and van der Plicht*, 1998a] and as evidence for solar-geomagnetic events affecting fluctuations in ^{14}C [*Anderson et al.*, 1993].

As can be discerned from the above information, calibration data is highly variable, with some exact/annual ages, ranges, and inferred ages based on *a priori* knowledge. Therefore, the construction of the radiocarbon dating curve, which represents a dynamic sequence of data, must incorporate a number of statistical corrections, such as Gaussian and Bayesian probability analyses [*Steier et al.*, 2001; *Buck and Blackwell*, 2004; *Blackwell et al.*, 2006; *Heaton et al.*, 2009; *Reimer et al.*, 2013b]. Modern ^{14}C analysis can result in age determinations with uncertainty less than 100 years for Holocene materials and less than 30 years for Iron Age materials. Dating uncertainty increases the older the material, reaching ~250 years for materials 40 to 50 ka in age [*Reimer et al.*, 2013a].

3.3.1.1 Considerations and Limitations to Radiocarbon Dating

A number of anthropological and natural influences on the carbon system must be taken into consideration before accurate radiocarbon measurements can be obtained or reported. Proper radiocarbon sample selection must consider the source of the archaeological features, micro context, or matrix containing the carbon sample, local environmental conditions affecting soil/sediment deposition and development, location near water sources, and potential artifact transport mechanisms [*Boaretto*, 2009]. The first and most obvious source of radiocarbon dating error is micro-contamination of samples before and during collection. The physical handling and preservation of the specimen can transfer modern carbon to the sample, such as tobacco, dirt, skin, packing materials, and glues for preserving bones, resulting in erroneous dates. Natural contamination can occur through plant root penetration of samples and incorporation of

fossil organics from bioturbation or ancient and modern human disturbances. Chemical weathering processes, such as the dissolution and precipitation of carbonates via meteoric water [*van der Plicht and Bruins*, 2001; *Boggs Jr.*, 2006], may also contaminate samples, especially at archaeological sites located in humid and hot environments, which have poor ^{14}C preservation [*Liritzis et al.*, 2013]. Additionally, the convenience of using smaller samples in AMS testing has resulted in the tendency to collect isolated specks of carbon material for radiocarbon analysis, which are more likely to have resulted from bioturbation or other contamination. It has been suggested that standardized sample amounts typical for traditional ^{14}C testing may result in more reliable AMS radiocarbon dates [*van der Plicht and Bruins*, 2001].

Second, the suitability of the sample itself must be considered. The best samples include short-lived grains, seeds, olive pits, and wood for examples, representing a 'single year' of time. Archaeologists frequently attempt to use ancient wood from buildings in order to date time of occupation; however, large beams are often reused in later construction, thus giving a radiocarbon age older than the construction of the building as revealed by dendrochronological calibration (see below) [*van der Plicht and Bruins*, 2001]. If available, collagen from unburnt or charred (heated to 200-300°C) human and animal bones can be use for radiocarbon dating; however, for human bone in particular, possible sources of dietary proteins must be considered as diets rich in marine or freshwater fish and shellfish will produce a reservoir effect (see below) [*Lanting et al.*, 2001].

As mentioned previously, the ratio of atmospheric ^{14}C to ^{12}C and ^{13}C, is also affected by burning of fossil fuels, the detonation of nuclear devices (collectively termed Suess Effects), and by natural isotope fractionation, all of which must be carefully corrected for [*Suess*, 1955, 1965, 1971; *Stuiver and Suess*, 1966; *Damon et al.*, 1978; *Reimer et al.*, 2008]. Isotope fractionation is the separation of the different isotopes of carbon during physical and chemical processes, such as photosynthesis, resulting in the enrichment of one isotope relative to another. For examples, the stable isotopes ^{12}C and ^{13}C are used by different plant species at different rates, and shell carbonates have a relatively high level of ^{13}C in comparison to bone or antler. Variability in carbon uptake can result in apparent radiocarbon ages that are older than actual if not corrected for through normalization [see *Stenström et al.*, 2011].

Finally, carbon reservoir effects must be taken into consideration particularly when comparing terrestrial carbon samples to those derived from the ocean, such as samples from shell middens, a common archaeological feature at coastal sites. Therefore, different radiocarbon curves have been developed for dating terrestrially derived samples and marine samples [*Reimer et al.*, 2009, 2013a] and appropriate reservoir correction factors are applied. However, these larger reservoir correction factors may not take into account smaller 'micro-reservoir' effects to archaeological sites that have been saturated by groundwater, are located in caves, or are adjacent to small bodies of water. Some sites may be even affected by a "hard water effect" [e.g. *Spennemann and Head*, 1998; *Rapp and Hill*, 2006], the contribution of depleted ^{14}C via rainwater dissolution of limestone. The hard water effect causes the contamination

of more recent carbon-rich materials in the soil or sediment with geologically 'old' carbon, resulting in a measured ^{14}C age much older than the samples actual age. For example, comparison of Polynesian pottery seriation dates with radiocarbon dates derived from shell middens on the island of Tongatapu [*Spennemann and Head*, 1998] resulted in a larger dating discrepancy than could be accounted for just by applying the ocean reservoir effect correction factor. This dating discrepancy was due to a lagoon-specific reservoir effect. Water moving through groundwater reservoirs discharged into the lagoon at a faster rate and a higher concentration than surface runoff. The mixing of depleted ^{14}C groundwater with seawater amplified the 'old' carbon effect in bivalve species living in the lagoon, which take up this depleted carbon during shell formation. When radiocarbon tested, these bivalves result in a ^{14}C age nearly two times greater than open sea bivalves of the same age [*Spennemann and Head*, 1998].

The results of radiocarbon analysis of a sample are typically presented in the form of graph depicting the relevant portion of the radiocarbon curve showing the likely associated calendar dates for the measured radiocarbon. Results are also given to one (68% probability) and two (95% probability) standard deviations. In the case of bimodal distribution of potential ^{14}C dates, the archaeologist may use Gaussian and Bayesian statistical analysis to determine the most probable dates based on stratigraphic and relative dating assumptions for a particular site [*Bronk Ramsey*, 2009; *Lee et al.*, 2013; *Niu et al.*, 2013; *Lanos and Philippe*, 2015]. In some instances comparisons between internal and external pottery chronologies, such as Cypriot wares are used [e.g. *Toffolo et al.*, 2014; *Fantalkin et al.*, 2015; *Finkelstein and Piasetzky*, 2015]. Bias and

inconsistencies associated with chronologies built using these inter-site comparisons has been a primary factor in the three competing Levantine chronology paradigms.

3.3.2 Dendrochronological Dating

Dendrochronology or 'tree-ring' dating is based on the age of trees evidenced as concentric 'rings' of annual growth with distinctive cellular banding and is the primary calibration of radiocarbon curves for the past 12,000 years. Every species' growth pattern is different based on genetics and environmental conditions, but generally, trees will add a distinguishable ring of growth every year, making them one of the most absolute chronometers, having annual or sub-annual resolution. Small cores (~ 0.5 cm diameter wide and 20 cm long) are taken from living trees, snags (standing dead trees), fossils, and/or trees used as building materials and successively lined up matching distinctive patterns of ring growth to build a chronology back through time (Figure 3-1). For example, growth during periods of drought or stress are typically displayed as very narrow rings in comparison to average annual growth, and patterns of narrow rings within a population are used as distinctive signatures for cross-dating. These patterns are also excellent indicators of precipitation or climate variability. Patterns of missing rings, disease, fire, and insect damage can also offer distinct signatures [*Baillie*, 1995; *Kuniholm*, 2001].

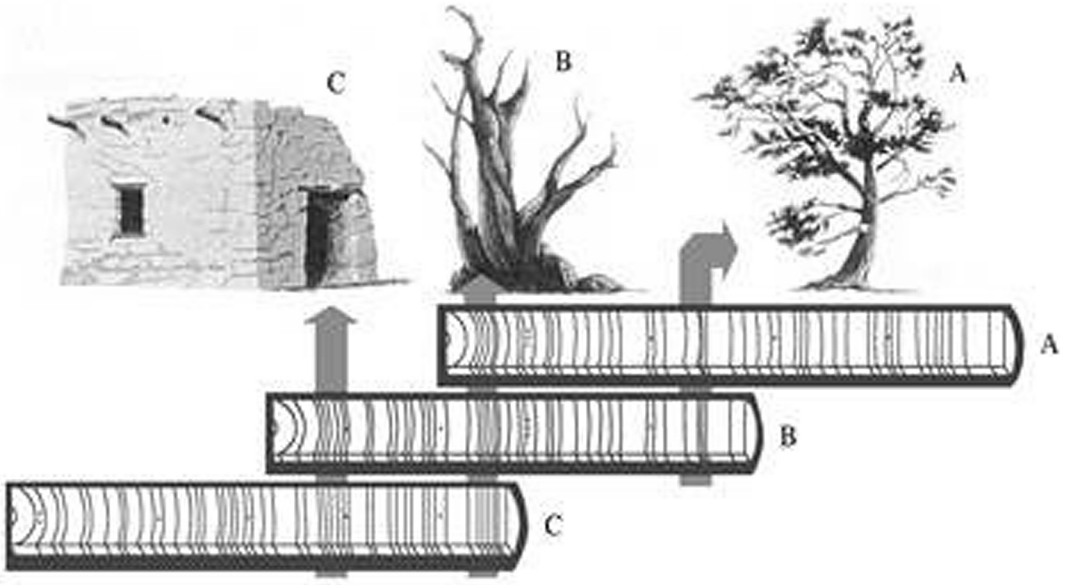

Figure 3-2 Dendrochronological Cross-Dating
A tree core from a species of known age (A) is compared to a core from a dead tree of the same species in the same region (B) and an archaeological beam from a structure (C). Distinguishable patterns of annual growth rings are matched (grey arrows) to build an age chronology back through time. *Photo courtesy of the Laboratory of Tree-Ring Research, University of Arizona.*

Trees of a specific species growing in similar environmental conditions will have similar growth patterns; therefore, core samples from several specimens can be 'cross-dated' by matching these signatures, creating a chronology that spans a period longer than the age of a single specimen. While many tree species can live several hundreds of years, deadwood, tree stumps, fossilized wood, wood submerged in bogs and rivers, and archaeological wood are also key to building chronologies. Large trees used as beams, poles or planks in construction, and fragments of burnt wood that can be identified with a particular species and location can extend cross-dating where living, dead, or fossilized wood is no longer available. Currently, over 180 species of trees

have been utilized for dendrochronology, with some interspecies cross-dating also achievable [*Kuniholm*, 2001].

The annual resolution of dendrochronology provides one of the primary calibration methods for radiocarbon dating curves for the Holocene as individual rings with known ages can be sampled for ^{14}C. Radiocarbon dating of decade-long sections of wood can also be applied to periods of de Vries effects to refine radiocarbon ages, known as 'wiggle-matching' [*Kuniholm*, 2001; *Manning et al.*, 2001, 2003; *Griggs and Manning*, 2009]. In North American, tree ring chronologies for fir (*Abies*) and pine (*Pinus*) have been constructed dating back to 8400 BCE [*Kuniholm*, 2001]. For Europe, oak (*Quercus*) and *Pinus* species in Germany have provided dates back to over 10,400 BCE [*Baillie*, 1995; *Friedrich et al.*, 2004]. The Aegean Dendrochronology Project has collected suitable tree rings from un-charred archaeological timbers from Gordion and other sites in Anatolia and the Mediterranean region to produce an accurate curve for the Mediterranean Bronze and Iron Ages [*Manning et al.*, 2001, 2003].

In addition to its obvious utilization in calibration of radiocarbon dates, dendrochronology can be used to directly date archaeological structures, ships, artwork, or other objects made of wood, to source timber used in these constructions (implying ancient trade routes), and to infer climate and landscape changes, aiding in environmental reconstructions which affect human migration and settlement patterns [*Baillie*, 1995; *Kuniholm*, 2001; *Pearson et al.*, 2012]. For example, periods of rapid construction and those with no apparent new construction have been identified with

dendrochronology, such as the building hiatus during the Black Death in Europe [*Baillie*, 1995]. Growth anomalies in the Aegean dendrochronological record were used to identify the impact of the Theran eruption through the increase in sulfur, calcium, rare earth elements, and spikes of zinc and hafnium in rings post-dating the eruption [*Pearson et al.*, 2009]. Similar anomalies in Ireland, Germany, England, China, and the US tree rings were correlated with Greenland ice-core records to identify several possible volcanic eruptions preceding environmental changes that were subsequently followed by major famines and societal collapse in several regions [*Baillie*, 1995].

3.3.2.1 Considerations and Limitations in Dendrochronological Dating

The primary considerations in dendrochronological dating are: 1) the accurate identification of the tree species being dated, 2) whether or not it is indigenous to the region, particularly for the time period in question, 3) the availability of suitable trees for dating, and 4) the problem of 'old wood' or the 'art-historical problem'. For example, dendrochronological dating of British medieval oak panels used for paintings were assumed to be made with British oak, but later discovered to be imported, a reminder that long distance trade has been occurring since the Bronze Age in Europe and the Near East. This study also highlights the need to recognize the re-use of wood in construction and other artifacts. The use of signed dates on artwork or engraved construction dates on buildings and boats does not imply that the wood used was freshly cut. Reuse of old timbers in buildings could result in an incorrect age assignment [*Baillie*, 1995]. Therefore, when directly applied to archaeological timbers, dendrochronology often only provides the last possible construction or use date.

In addition, certain species are not suitable for dendrochronology depending on their growth pattern or life span. Short-lived species (lifespans less than 100 years) are particularly problematic because they may not record periods of environmental change or disturbances that are on cycles longer than a decade; therefore, specific markers for cross-dating are not present. Dendrochronology as a direct dating method becomes difficult in regions or time periods where deforestation has cleared away the majority of forest, destructive fires have removed all suitable dating evidence, and large timbers are continually reused for many generations due to lack of building materials. For example, the Near East and Aegean, often contain only limited small samples for dating back to the Bronze Age or prior (often charred wood from construction timbers) [*Griggs and Manning*, 2009]. This lack of regionally specific dendrochronological data means that the radiocarbon dating curves are primarily calibrated with European and North American tree species, resulting in a radiocarbon curve biased to the Northern Hemisphere.

3.3.3 Uranium Series Dating

Due to the reliability of radiocarbon dating, uranium-series dating is rarely applied to materials less than 50 ka. Instead, it is the primarily dating tool used to date early hominid materials from the Pleistocene, usually from Paleolithic cave sites and rock shelters [e.g. *Falguères et al.*, 2010, 2013; *Mercier et al.*, 2013]. However, in the case of some Holocene sites with no radiocarbon materials, U-series can still be a viable option for absolute dating, especially if archaeological materials are associated with

speleothems, shells, bone, or other calcite-rich deposits.

Uranium (U) series dating is based on the radioactive decay of long-lived, naturally occurring isotopes of the element uranium (^{235}U and ^{238}U). These "parent" isotopes decay through a series of short-lived radiogenic "daughter" isotopes to a stable form of lead (Pb), which can take billions of years. Uranium-Pb dating is primarily used for dating geological deposits millions of years old. U-series dating utilizes the decay rate of daughter isotopes and the re-establishment of parent/daughter equilibrium through time, and can be used on younger materials. The primary U-series method applicable to archaeological materials is the decay of the more abundant ^{238}U isotope, first to the daughter ^{234}U, then to daughter isotope ^{230}Th, and then to radium (^{226}Ra). The thorium and radium daughter isotopes have a half-lives of 75,400 years and 1600 years, respectively, suitable for dating Quaternary archaeological deposits [*Schwarcz*, 1980, 1997; *Taylor and Aitken*, 1997; *Adriaens et al.*, 1999; *Latham*, 2001; *Grün*, 2006]. At present, there has been limited application of radium dating to archaeology (mainly metals and lead paint in art) as it is usually used for river sediments, soils, and environmental applications [e.g. *Keisch*, 1968; *Hanslík et al.*, 2005; *Ioannis*, 2006; *Lauer and Vengosh*, 2016].

A marine mollusk, for example, takes up naturally occurring uranium through the water as it is growing and incorporates it into its calcium carbonate-rich shell. A living mollusk has virtually no thorium in its shell because thorium is insoluble. Therefore, the activity ratio of ^{230}Th/^{238}U is at zero at the time of formation. As ^{238}U

starts to decay the ^{230}Th daughter isotopes start to grow. In an ideal system, the activity/ratio of the isotopes remains in equilibrium, i.e. the number of atoms lost by a parent isotope in a given time period is the same as the atoms gained by the daughter isotope. However, different geochemical behaviors of uranium and its daughter isotopes, such as water solubility, whether the system is open (e.g. exposed to external sources of uranium in groundwater) or closed, and mechanisms of uptake and loss, such as leaching or diffusion, cause disequilibrium in the system. U-series ages are calculated from the activity ratio of Th/U and a mathematical function that takes into account disequilibrium [*Grün*, 2006].

Archaeological materials rich in calcium carbonate and phosphate, and hydroxyapatite, such as marine shells from middens, egg shells (ostrich and emu), animal and human bones and teeth, are typically used for U-series dating [e.g. *Rae and Ivanovich*, 1986; *Bischoff et al.*, 1988; *McDermott et al.*, 1993; *Grün and Taylor*, 1996; *Eggins et al.*, 2003, 2005, *Grün et al.*, 2005, 2010, 2014]. Associated geological materials such as stalagmites, stalactites, flowstone, travertine, and other calcite cave deposits (collectively termed "speleothems") are also suitable materials as they can trap uranium during their precipitation [e.g. *Schwarcz et al.*, 1979; *Schwarcz*, 1980; *Richards and Dorale*, 2003; *Ortega et al.*, 2005; *Drysdale et al.*, 2012; *Falguères et al.*, 2013; *García-Diez et al.*, 2013; *Lascu et al.*, 2016]. For example, flowstones are frequently association with archaeological deposits found in caves and may "sandwich" or cover an existing archaeological deposit such as a hearth. Coral, which accumulates uranium as it grows, is also used in U-series dating, particularly as a calibration for ^{14}C

dating. Two of the most significant contributions of U/Th dating to archaeology have been the resetting of ^{14}C calibration of the last glacial maximum from 18 ka to 20 ka by U-series dating of ocean corals, modifying the chronology for the Upper Paleolithic transition and extending the applicability of radiocarbon dating curve back to 50 ka [*Edwards et al.*, 1986, 1987; *Reimer et al.*, 2013a].

In the lab, samples are dissolved in acid and the thorium and uranium chemically separated through ion-exchange chromatography. A 'spike' (isotopically enriched standard) is added and the purified sample is analyzed with alpha (α) particle spectrometry, thermal ionization mass spectrometry (TIMS), or more recently, sector field inductively coupled plasma mass spectrometry (ICP-MS), and then the isotopic ratios determined. Like radiocarbon dating, mass spectrometry techniques have the advantage of decreasing counting times, increasing the precision of age determinations to within 1%, and they require only milligram size samples, allowing for the testing of smaller materials. Gamma spectrometry has also been used with limited success to analyze bulk samples without chemical separation, applicable to rare samples that cannot be destroyed, such as hominid skeletal remains [*Schwarcz*, 1997; *Latham*, 2001].

3.3.3.1 Considerations and Limitations in U-series Dating

The primary concern in U-series dating is the problem of open-system uranium mobilization, the loss or gain of uranium during burial and deposition subsequently resetting the radiometric clock. An 'ideal' U-series dating scenario assumes that the system has remained closed to contamination or alteration such as heating, interaction

with aqueous solutions, and chemical weathering, which may reset the clock to a later date than the stratigraphic layer represents. Examples of contamination which can alter time-zero Th/U ratios include: colloidal detritus containing ^{230}Th deposited in calcite precipitates, additional ^{238}U parent isotope uptake in sediments that are frequently saturated, or naturally occurring ^{232}Th added from wind-blown dust or floods. Speleothems, for example, can accumulate wind and water borne contaminants if located near cave entrances, therefore, interiorly located samples are more ideal. Migration of detritus rich in uranium or thorium might also wash down the sides of the stalagmites; therefore, sampling location must be taken into consideration [*Schwarcz*, 1997; *Schwarcz and Rink*, 2001]. In marine samples, secondary mineralization, indicating deposition of additional uranium, can often be verified through thin-section and microscopy to check for limestone clasts in the samples), which act as contaminants interfering with the primary carbonate being dated [e.g. *Pike and Pettitt*, 2003; *Grün et al.*, 2010].

Uranium uptake history has a particularly strong effect on archaeological bone and teeth. Hollow cavities in bones, for example, can fill with calcite at any time during or after deposition, affecting age interpretation. U-series ages of teeth are often cross-dated with electron spin resonance (ESR) (see below), which measures the accumulated radiation dose from burial, allowing for a dose average comparison to estimate age. However, the issues of leaching and uptake in human teeth and bones constrain its use to dating materials approximately100 ka or greater, as the error rates can be ±10 ka [see *Ludwig*, 2003 for error estimation]. At present, the best application of U-series dating

to Holocene archaeological materials is its potential to date annually deposited layers on fast-growing cave deposits associated with human occupations, such as speleothems and soda straws [*St Pierre et al.*, 2009, 2012]. A number of studies are now using U-series dating in conjunction with ESR, radiocarbon, and thermoluminescence narrow dating ranges in these environments [e.g. *St Pierre et al.*, 2012; *Taçon et al.*, 2012; *García-Diez et al.*, 2013]. For example, the combined use of ESR with U-series, typically applied to account for both early and linear uranium uptake, may result in age precisions close to 10% [*Grün*, 2001; *Latham*, 2001; *Mercier et al.*, 2013]. Despite these advances, current U-series dating studies still focus on materials older than the Holocene, indicating that more U-series studies, particularly ^{226}radium isotope dating, are necessary to date recent archaeological materials in situations where radiocarbon does not work.

3.3.4 Trapped Charge Dating (ESR/TL/OSL)

Trapped charge dating (TCD) methods are based on the time-dependent accumulation of trapped electrons in the crystal lattice of certain minerals, which act as radiation dosimeters [*Grün*, 2001, 2006]. When the mineral is first formed (i.e. igneous rocks cooled from high temperatures), all electrons are in their lowest energy, neutral ground state or valence bands. Prolonged exposure to naturally occurring radioactive isotopes of uranium, thorium, and potassium or electromagnetic radiation, such as light, can displace electrons, transferring them to a higher energy state (conduction band) and create vacancies or positively charged 'holes' in valence band. Most of these displaced

electrons quickly return to fill these holes through diffusion; however, if the crystal lattice contains defects, the electrons (and holes) will get trapped between valence states producing paramagnetic centers. The holes can then be filled with other elements (impurities). The more trapped electrons present in these paramagnetic centers, the older the age of the sample. In some materials, like tooth enamel, ionizing radiation can also split molecules producing free radicals that behave like paramagnetic centers (for example $CO_3^- \rightarrow CO_2^- + O$). In TCD methods, either the number of trapped electrons in a sample are directly measured to determine age, or the light emitted (luminescence) upon their release from these traps, through optical or thermal stimulation, is measured and compared to a laboratory induced luminescence value [*Aitken*, 1985, 1998, *Grün*, 2001, 2006; *Schwarcz and Rink*, 2001; *Liritzis et al.*, 2013; *Athanassas and Wagner*, 2016].

3.3.4.1 Electron Spin Resonance Dating

Electron Spin Resonance (ESR) spectrometry measures the amount of absorbed microwave energy with a known frequency needed to flip the magnetic moments of paramagnetic defect centers in the crystal. The ESR spectra generated is proportional to the total number of centers present. If a known or constant rate of past radiation can be determined, the ESR signal will be proportional to time of last zeroing or electron ground state and thus the formation or burial age of the sample [*Grün*, 2001; *Schwarcz and Rink*, 2001]. ESR dating in combination with U-series is typically applied to fossil bone, teeth and shell from archaeological sites and is frequently used to date Paleolithic

artifacts, but can be applicable to materials down to several thousand years old [e.g. *Grün et al.*, 2005; *Grün*, 2006].

To determine an ESR date the initial paleodose or dose equivalent (D_e) at time zero must be determined. First, the current natural ESR intensity or total accumulated dose (AD) in a sample is measured. This value is function of the total number of traps, time, and the strength of radioactivity or dose rate (D_R) applied, which is based on the concentration of radioactive elements (U, Th, and K) in the sample and surrounding material. Once the natural intensity is determined, the sample is progressively irradiated in the laboratory with known dose rates of β and/or γ rays from one or more radioactive elements, producing more paramagnetic centers and increasing the ESR signal up to a saturation dose. A plot of ESR intensity (Y-axis) and laboratory dose rate (X-axis) produces a dose response curve. Using an exponential function, this curve is used to extrapolate back to time zero (intercept with the X-axis) and find D_e. If the known dose rate is constant, the ratio of D_e to D_R is the age of the sample.

3.3.4.2 Thermoluminescence and OSL Dating

Thermoluminescence (TL) dating utilizes the light emitted by the trapped charges and impurities filling vacancies in the crystal when they are reset to their valence state through heating (to ~ 400˚C). The emitted photons are converted to electric pulses in a photomultiplier and plotted against the temperature to create a glow curve [*Grün*, 2001] for determining D_e. The color of the light is characteristic of the impurity and the intensity is proportional to age of the sample. TL dating is typically

used on thermally altered archaeological samples such as ceramics, kilns, burnt rocks, lithics, soils and sediments, that contain quartz and feldspar grains [*Troja et al.*, 1996; *Rapp and Hill*, 2006; *Liritzis*, 2010] and can be used on materials between hundreds of years to several hundred ka old.

Optically Stimulated Luminescence (OSL) dating involves subjecting the sample to ultraviolet (UV) or visible light in a specific frequency range (such as red for feldspars and green for quartz), which activates light sensitive electron traps causing the electrons to move to luminescence centers and emit light, similar to TL dating. The emitted light is plotted against time since the light was switched on, called the shine-down curve [*Aitken*, 1998; *Grün*, 2001] and dates a sample's last exposure to sunlight. OSL dating is typically applied to quickly deposited aeolian, fluvial, lake, and other sediment deposits associated with archaeological strata [e.g. *Huntley et al.*, 1985; *Aitken*, 1998; *Rittenour*, 2008; *von Suchodoletz et al.*, 2008; *Lahaye et al.*, 2013; *Liritzis et al.*, 2013] but has also been applied to megalithic structures in the Mediterranean [*Liritzis et al.*, 2013] and Europe such as the White Horse chalk structure in Uffington Downs, UK, setting its construction back to the Bronze Age [*Aitken*, 1998]. OSL dating has also been successfully used on ceramics and lithics in situations where pre-depositional components affect TL dating. A variant of OSL dating is infrared stimulated luminescence (IRSL), which is often used with feldspars, one of the most common minerals in soils and sediments. Unlike other TCD methods, IRSL measures the IR signal around the luminescent traps during laboratory ionization and not the eviction of trapped electrons [*Liritzis et al.*, 2013]. IRSL has been successfully used to

date Neolithic, loessic and colluvial sediments related to soil erosion caused by human activity [*Lang and Wagner*, 1996].

3.3.4.3 Considerations and Limitations in TCD Dating

For ESR dating, one of the primary considerations is the continual uptake of uranium in teeth and bones during burial, complicating dose rate determinations [*Grün*, 2001]. The same geological and hydrological processes, such as leaching and open-system effects, that impact U-series dating can affect uranium and thorium content in samples used in TCD, therefore site conditions and proper radioactive dose rate calibrations must be considered.

For TL dating, it is important to heat samples to a minimum 400˚C or higher to remove electrons trapped in 'deep' traps, those that are more stable against heat exposure. For example, TL dating of ceramics must consider the original firing conditions. If a piece of pottery was not originally fired to high enough temperature to reset the "luminescent clock' of previously exposed minerals, the sample may contain grains with deeply trapped electrons accumulated at some previous time period [*Aitken*, 1985]. Some electrons may also be trapped in 'shallow' traps that can be released at low temperatures or simply by exposure to sunlight.

Exposure to sunlight is also the primary concern in OSL dating. Sunlight exposure, even for a few moments, during sampling can release trapped electrons and effectively reset the OSL clock to time zero. Therefore, samples must be taken from features unexposed to sunlight since their original deposition. OSL sampling usually

occurs at night with a long cylinder that can be pushed into the sediment to extract a core of material [*Aitken*, 1998]. Solar bleaching of stone in archaeological structures used in OSL dating must also be considered as each rock type has a different UV penetration level. In addition, the level of varnish or surface debris that has accumulated since the construction as well as processes of erosion must be considered.

Finally, there is the issue of anomalous fading, caused by athermal loss of luminescence signals, which results from quantum-mechanical tunneling affecting the transition of electrons between traps and luminescence centers. This fading affects feldspars in particular, resulting in age underestimations [*Liritzis et al.*, 2013]. Thus, while not as optically luminescent as feldspar, quartz is usually used for dating materials younger than 100 ka. However, the heterogeneous nature of quartz results in variable UV emissions, some too low for luminescence [*Liritzis et al.*, 2013]. Currently ESR, TL and OSL dating are accurate down to ±10% of the known age for materials 20 ka and older and around ±20% for Holocene materials [*Aitken*, 1998; *Liritzis and Laskaris*, 2011].

3.3.5 Argon Tephrochronology

Similar in process to U-series dating, Argon tephrochronology ($^{40}Ar/^{39}Ar$) dating is applied to geologically 'young' deposits (Precambrian to late Quaternary), particularly fine grained lavas and obsidians [*Walter*, 1997], and is frequently used in Pleistocene Paleolithic deposits to date early hominid remains and artifacts. The method has been extensively used on Olduvai Gorge sequences in East Africa to

investigate human evolution. While argon dating works best if applied to strata older than 100 ka, it has been successfully used to date volcanic deposits into the Holocene, allowing for a limited but applicable archaeological dating tool. For example, argon dating of pumice clasts from the eruption of Mt Vesuvius has extended the limits of the technique as young as 2000 years BP. Forty-six $^{40}Ar/^{39}Ar$ measurements of Vesuvius lavas were obtained that corresponded to an age of 1925 ± 94 years BP, closely corresponding to the 79 CE eruption [*Renne et al.*, 1997]. The results were revisited in 2007 using updated methodology, yielded a weighted mean age of 1921±66 years BP, corresponding exactly to 79 CE [*Lanphere et al.*, 2007]. The primary limitation of argon dating is re-heating of the material, and like U-series, its application is limited to dating associated geological deposits.

3.3.6 Obsidian Hydration

Obsidian, a volcanic glass formed from silica-rich lava flows, is a common material found in archaeological deposits throughout the world because of its use in making sharp cutting blades. When a piece of obsidian acquires a fresh surface through natural fracturing during transport or through flaking during stone tool manufacture, it can develop a hydration "rind" as water diffuses into microscopic cracks in the fresh surface [*Ambrose*, 2001; *Rogers*, 2010]. The thickness of this hydrated surface (X) is measured through optical microscopy, ion beam reactions, and Fourier transform interference analysis and calibrated with associated radiocarbon dating or other dating technique to determine an age of manufacture [*Ambrose*, 2001; *Liritzis and Laskaris*,

2011]. Hydration dating of obsidian has been extensively used in the Americas to date settlements, often in conjunction with ceramic-seriation and ^{14}C dating to clarify chronologies [*Hammond*, 1989; *Ambrose*, 2001], in East Africa to date Middle Stone Age to Neolithic lithic deposits [*Michels et al.*, 1983], and in Greece to date 4th millennium BCE obsidian blades in conjunction with luminescence dating of masonry [*Liritzis*, 2010].

The rate of hydration is a function of the environment or microclimate of the site where formation occurred, such as temperature and relative humidity, burial depth, and the chemical composition of the obsidian itself [*Ambrose*, 2001; *Liritzis and Laskaris*, 2011]. In ideal situations, hydration rates and ages can be determined if the depositional conditions are constant; however, even brief environmental changes, such as extreme heating in a forest fire or excess water saturation during a prolonged flood, can alter the rate of hydration. For example, the extreme temperature dependency of hydration reactions results in a ± 10% rate difference per ± 1°C change [*Ambrose*, 2001]. Human activity such as destruction of occupations and ritual burning of artifacts can also alter the rate of hydration. Spalling, additional flaking through transport of the artifact, and weathering processes will reset the hydration clock. These factors typical result in dating error rates of approximately 20-30%, on the decadal scale for specimens 100 to 1000 years old, and several hundred years for specimens 10 ka old or more [*Ambrose*, 2001; *Rogers*, 2010]. The more recent application of secondary ion mass spectrometry (SIMS) profiling, which models sigmoidal curves of hydrogen (H) concentration as a function of hydration depth, has increased precision but can be as

cost prohibitive as ^{14}C dating [*Liritzis and Laskaris*, 2011]. The high error rate due to the effects of thermal history, chemical processes, and weathering, typically limits hydration dating to use as a complementary dating technique.

3.4 Archaeomagnetic Dating

As introduced in Chapter 2, the Earth's magnetic field is dynamic, both temporally and spatially, from small daily fluctuations to complete polarity shifts that occur at intervals of millions of years or more. Under the right circumstances, these secular variations in the magnetic field can be recorded in materials that contain magnetic minerals. Details of how the ancient field record (magnetic remanence) is measured in archaeomagnetic materials is covered in Chapter 4, but a brief summary will be presented here.

The primary type of magnetization in the archaeological materials used in this research is one acquired through heating, called a thermal remanent magnetization (TRM). For example, during manufacture, pottery is heated in a kiln to high temperatures, usually over 800˚C. This thermal energy resets the original magnetization of the iron-oxide grains within the clay matrix. As the pottery is cooled, the magnetization of those grains can realign parallel with the Earth's magnetic field, recording its direction and strength. When the pottery reaches a specific temperature, called the blocking temperature, the magnetization of the grains locks in place. This recording or remanent magnetization can be measured in the laboratory using a superconducting quantum interference device or (SQUID) magnetometer. These

measurements can be plotted to create secular variation curves of field variability through time. The ancient field strength (archaeointensity) is the primary field parameter used for constructing dating curves.

To determine the archaeointensity of an object, the natural remanent magnetization (NRM) or total sum of all magnetic remanence acquired and stored in the object must first be measured. Then the sample is reheated in the lab in incremental steps up to approximately 700˚C (above the blocking temperature of most grains) to slowly remove that original NRM. During the procedure, each temperature step is repeated, once in a known laboratory field (imparting a new laboratory magnetization (M_{lab}) of known strength and direction) and once in a zero field. The remaining NRM and the M_{lab} are measured after each step. By the final temperature step, the original NRM has been completely removed and a new laboratory magnetization with a known field strength and direction has been imparted to the sample. Magnetizations imparted to minerals by natural processes are often linearly related to the applied magnetic field when that field is weak (like the Earth's); therefore, the ancient field can be determined using the following relationship where $Field_{anc}$ is the ancient field intensity, $Field_{lab}$ is the known lab field intensity, M_{lab} is the imparted laboratory magnetization, and NRM is the original natural remanent magnetization of the sample:

$$Field_{anc} = \frac{NRM}{M_{lab}} Field_{lab}$$

A series of calibrated ancient field measurements for a region are combined to create a

graph of field variability (y-axis) to calendar date (x-axis). This reference curve can then be used similar to a radiocarbon dating curve to ascribe dates to materials of unknown age if they contain suitable magnetic grains for archaeomagnetic dating.

Pioneering TRM research and the first experimental protocols were developed by Koenigsberger [*Koenigsberger*, 1932], later expanded and refined by the Thelliers who established the field of archaeomagnetism and sampling and measurement techniques designed to improve the accuracy of measuring TRM. They also introduced the double heating technique of thermal demagnetization utilized in this research (Chapter 4) and published the very first secular variation curves [*Thellier and Thellier*, 1959].

Since the 1980s, most archaeomagnetic studies have focused on producing archaeomagnetic dating curves for two regions: Western Europe and the Near East [*Le Goff et al.*, 2002; *Genevey and Gallet*, 2003; *Gallet and Le Goff*, 2006; *De Marco et al.*, 2008; *Gallet et al.*, 2008, 2014, 2015, *Genevey et al.*, 2013, 2016, 2009, *Ben-Yosef et al.*, 2012, 2017; *Ertepinar et al.*, 2012; *Hervé et al.*, 2013; *Pavón-Carrasco et al.*, 2014; *Stillinger et al.*, 2015; *Gómez-Paccard et al.*, 2016; *Shaar et al.*, 2016]. This research identified a period of unusually high magnetic field strength during the 1st millennium BCE, which naturally coincided with a period of reduced atmospheric carbon 14 (^{14}C) production causing a significant plateau on the radiocarbon dating curve. Because of this, recent archaeomagnetic research has focused on constructing secular variation curves down to the decadal scale in order to refine the radiocarbon dating curve.

3.4.1 Considerations and Limitations in Archaeomagnetic Dating

The primary consideration in archaeomagnetic dating is whether or not the assumptions governing the standard archaeointensity equation above are met. The above archaeointensity equation, for example, assumes that: 1) the original NRM was linearly acquired (a function of grain shape, size, concentration, and field strength among other factors), 2) the ability of the sample to acquire a remanence since its initial acquisition has not been altered through weathering, crystallization of new minerals, chemical alteration of the magnetic grains, or laboratory induced changes, 3) the original NRM is not carried entirely by multidomain or large grains that are poor recorders of remanence (see Section 4.2.3), 4) the specimen does not exhibit anisotropic remanence acquisition (section 4.2.5), 5) the mechanisms involved in the original acquisition are not difficult to reproduce in the lab, and finally, 6) the NRM is not comprised of multiple components of remanence [*Tauxe*, 2016].

This final condition is often a problem with archaeological deposits. Magnetic materials can acquire a secondary or partial remanence, one that follows and partially obscures the primary remanence acquisition under investigation. Secondary remanence in archaeological deposits typically occurs due to lightning strikes or other instantaneous magnetizations, called isothermal remanence (IRM) or chemical alteration (CRM), which can occur, for example, if hematite precipitates from iron-rich sediments where artifacts are deposited. Prolonged exposure to weak fields, called viscous remanence (VRM), can also occur [*Dunlop and Özdemir*, 1997]. Secondary

remanence is frequently found in pottery due to processes such as successive reheating, as might be found in cooking vessels, or by weathering, such as might occur during saturation of the pottery with water after burial. Large destructive fires can also partially or completely reset the magnetization initially acquired during pottery manufacture. Fortunately, artifacts found in association with undisturbed destruction debris can be used to date the event itself. An additional concern is objects that are used long after their manufacture date, such as ritual objects, large storage vessels or archaeological features constructed with old building materials (similar to dendrochronology dating of old wood).

For kiln fired ceramics used in archaeomagnetic dating, the cooling rate effect is also accounted for, which can result in a 5 to 20% overestimate of intensity in thermal remanent magnetization experiments [*Halgedahl et al.*, 1980; *Walton*, 1980; *Genevey and Gallet*, 2002]. Traditional kiln firing techniques involve slow cooling of the pottery within the kiln for 24 hours or more, while lab cooling rates are typically less than one hour. The slower the cooling rate, the more time for magnetic grains to align with the Earth's field, resulting in a higher magnetization. Additionally, the depth of heat conduction must be considered when sampling from kilns or ovens in the field. Surfaces in direct contact with the fire have been shown to be unsuitable for archaeomagnetic sampling, therefore, samples should be approximately 60-80 mm thick [*Spassov and Hus*, 2006]. Another important correction is for the anisotropic nature of the material. Anisotropy is the preference of magnetic grains to align their magnetization in a particular orientation based on the crystalline structure of the grain.

Some ceramics can be highly anisotropic due to the nature of their fabrication. For example, the magnetic grains within the clay in wheel-thrown pottery can be pressed together along tightly bound parallel planes. Bricks, which are formed through tamping into molds, do not show this preferential alignment [*Kovacheva et al.*, 2000]. Both of these effects are addressed in archaeointensity experiments and may be corrected in final calculations.

Finally, it is important to reiterate that the current resolution of archaeomagnetic dating is subject to the availability of high quality data for a particular region and the definitive dating of artifacts used as curve calibration points. Direct measurement of the magnetic field exists only back to 1600 CE. Secular variation prior to 1600 is age-calibrated with historical documentation, pottery seriation, and radiocarbon dating primarily from northern hemisphere archaeological materials. These calibration methods can introduce potential bias and/or error in curve construction. For example, many current secular variation models (see Section 5.2.7) are strongly biased to the northern hemisphere, and may not capture unusual field features such as the current South Atlantic dipole low near Brazil [*Pinto Jr et al.*, 1992; *Tarduno et al.*, 2015; *Constable et al.*, 2016; *Pavón-Carrasco and De Santis*, 2016].

4 Magnetic Theory

4.1 Geomagnetism

The field of archaeomagnetism combines the methodological principles of rock and paleomagnetism in order to understand the Earth's magnetic field variability (geomagnetism). Following is a brief review of the magnetic theories relevant to this research with an emphasis on geomagnetism. For a more comprehensive examination of rock and paleomagnetism, the fundamentals are extensively covered in books by [*Butler*, 1992; *Dunlop and Özdemir*, 1997, 2007; *Tauxe*, 2016]. Geomagnetism is the study of the morphology, origin, and variation of the Earth's magnetic field. The structure of our surface magnetic field is similar to that which would be generated by a giant dipole magnet if it were situated in the Earth's core and oriented along the spin axis. However, unlike a simple permanently magnetized solid body, the Earth's field is actually generated by fluid dynamics and electromagnetic induction within the electrically-conductive liquid iron-nickel outer core, and therefore, acts as a self-exciting geodynamo. The latent heat released by solidification of the inner core drives convection currents in the liquid outer core, and the rotation of the Earth coordinates these currents via the Coriolis Affect. The interaction of flowing conductive liquid with an ambient magnetic field creates circulating electrical currents that can amplify or sustain the magnetic field. The field then propagates through the mantle and crust and surrounds the planet with an invisible shield of dense magnetic flux (B) that protects our

atmosphere from solar and cosmic radiation (Figure 4-1) [*Butler*, 1992].

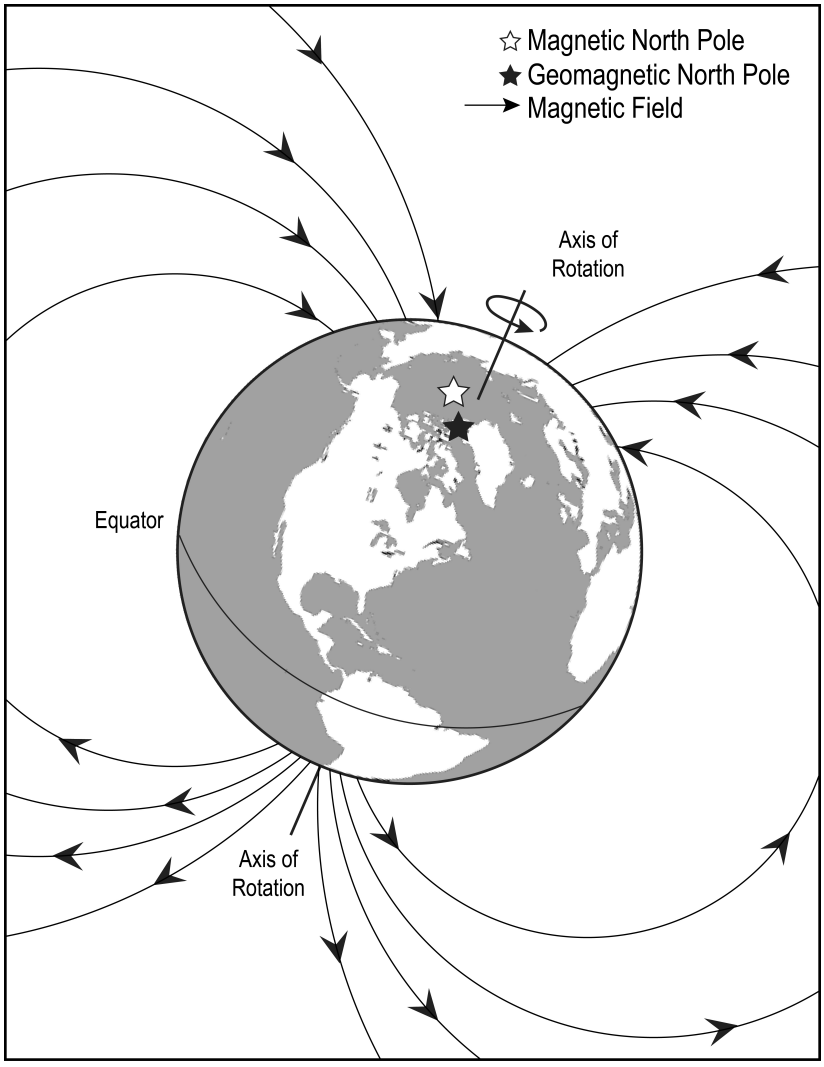

Figure 4-1 Earth's Magnetic Field

4.1.1 Components of the Field

The total field measured at a specific point on the surface of the Earth is described by a vector (**H**) composed of horizontal (H_H) and vertical (H_V) components,

which are related to the angles of declination and inclination, respectively (Figure 4-2). Declination (**D**) is the horizontal angle in degrees from 0˚ to 360˚ between the H_H (which points towards magnetic north) and geographic north, with positive declination being measured east. Westward declinations would have negative values. Inclination (**I**) is the vertical dip of the field in degrees from the horizontal and ranges from -90˚ (south pole) to +90˚ (north pole), the equator = 0˚, and downward inclination dips into the Earth are considered positive. The length of **H** represents the magnitude or intensity of the field and is measured in units of amps per meter (A/m). In archaeomagnetism, **H** at a specific point on the Earth's surface is usually expressed in terms of the equivalent **B** field or flux density, where:

$$\mathbf{B} = \mu_0 \mathbf{H} \tag{4-1}$$

μ_0 = the permeability of free space, and B has units of Tesla (T). In three-dimensional Cartesian coordinates, H_H is defined by north (X) and east (Y) components where:

$$\mathbf{H_X} = \mathbf{H} \cos \mathbf{I} \cos \mathbf{D} \tag{4-2}$$

$$\mathbf{H_Y} = \mathbf{H} \cos \mathbf{I} \sin \mathbf{D} \tag{4-3}$$

In the case of the location depicted in Figure 4-2, H_Y is to the west and thus D is negative. H_V is perpendicular to X and Y in the Z direction:

$$\mathbf{H_Z} = \mathbf{H} \sin \mathbf{I} \tag{4-4}$$

The magnitude of H can be then calculated as:

$$\mathbf{H} = \sqrt{\mathbf{H_X^2} + \mathbf{H_Y^2} + \mathbf{H_Z^2}} \tag{4-5}$$

These three field components can be directly measured at a location with a portable

fluxgate magnetometer aligned with the geographic reference frame. The remanent or ancient recording of the Earth's field stored in rocks, soils, sediments, and archaeological materials can be indirectly measured in discrete samples using a super conducting rock magnetometer in the laboratory. From these three components, the ancient **D** and **I** can then be determined as:

$$\mathbf{D} = \tan^{-1}\frac{\mathbf{H_Y}}{\mathbf{H_X}} \tag{4-6}$$

$$\mathbf{I} = \sin^{-1}\frac{\mathbf{H_Z}}{\mathbf{H}} \tag{4-7}$$

If the Earth's field were perfectly aligned with its rotational axis, declination would be zero (**D**=0) at all sites and **I** could also be calculated using the geographic latitude (λ):

$$\tan \mathbf{I} = \frac{\mathbf{H_V}}{\mathbf{H_H}} = \left(\frac{2\sin\boldsymbol{\lambda}}{\cos\boldsymbol{\lambda}}\right) = 2\tan\boldsymbol{\lambda} \tag{4-8}$$

This geocentric axial dipole (GAD) assumption is central to the study of paleomagnetism and archaeomagnetism as it represents the time-averaged field behavior over millions of years. Magnetic intensity or strength of the field also varies over the surface of the planet similar to inclination, with higher field intensity at the poles and lower intensity at the equator. Archaeointensity values are often expressed in terms of the equivalent geocentric or virtual axial dipole moment (VADM) that would produce an observed intensity ($\boldsymbol{B_{anc}}$) at a given site colatitude ($\boldsymbol{\theta_s}$):

$$\boldsymbol{VADM} = \frac{4\pi r^3}{\mu_0} B_{anc}(1 + 3cos^2\theta_s)^{-\frac{1}{2}} \tag{4-9}$$

Where r = radius of earth, and $\boldsymbol{\theta_s}$ is measured from the North Pole (0˚) to the South Pole

(180˚), such that $\theta_s = 90 - \lambda$.

The actual field, particularly on shorter time scales, is not as simple. The current polarity of the field is such that the field is oriented out of the Southern Hemisphere and into the Northern Hemisphere, with the dipole aligned approximately 10˚ west from the Earth's rotational axis (geographic north and south) and intersecting the surface of the Earth at the geomagnetic north and south poles (Figure 4-1). Additionally, the locations of the magnetic poles (points where the measured magnetic field is perfectly vertical or **I**= ±90˚) and the geomagnetic poles do not generally coincide. This is due to dynamic core processes and structures, crustal features, and non-dipolar magnetic contributions to the field. The result is a temporally and spatially-varying field, which manifests as north and south magnetic poles that wander and various field anomalies that can change on daily, millennial, and even million year time scales. Fortunately, these secular variations, which are often regionally specific, enable the quantification of the Earth's field variability through time and, subsequently, the ability to use those variations for archaeological dating.

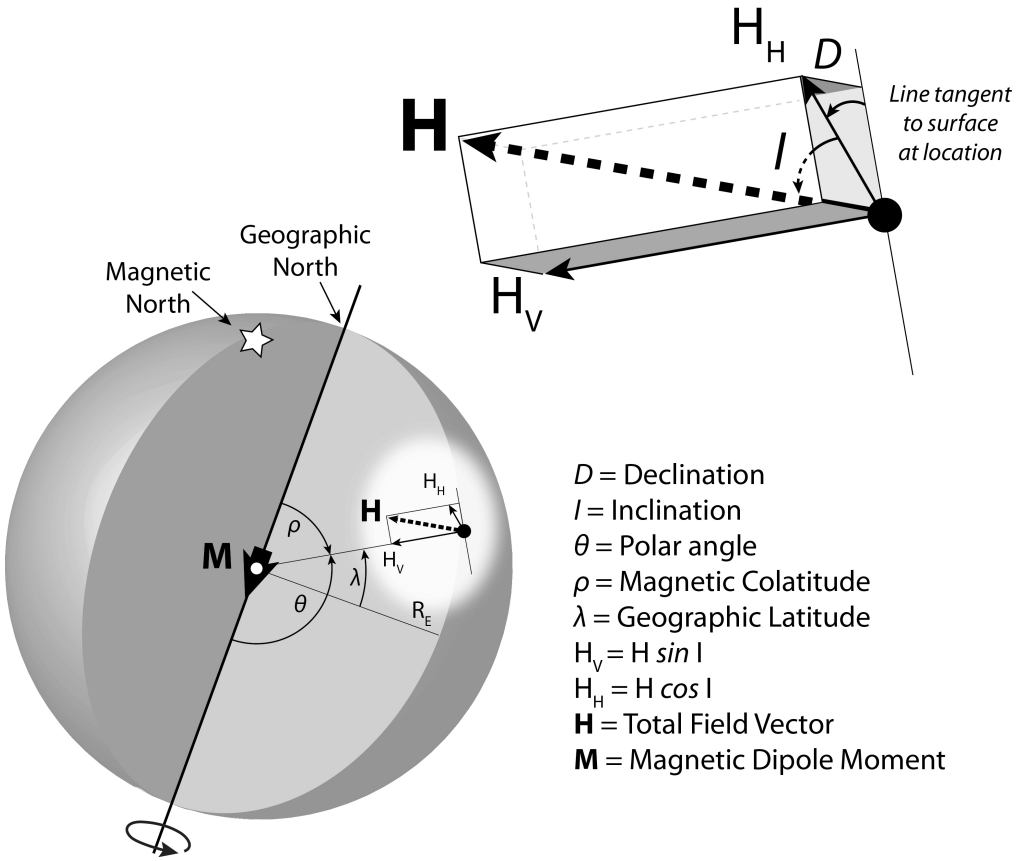

Figure 4-2 Vector Components of the Earth's Field

4.1.2 Modeling the Field

To capture the dipolar and non-dipolar magnetic features, spherical harmonics theory is used to create reference models of the average planetary field. The current (2015) International Geomagnetic Reference Field (IGRF) model for example (Figure 4-3), is computed using satellite and ground observations and calculates the Earth's main field as generated by the core, excluding any crustal or external contributions [*Thébault et al.*, 2015]. The current field varies in intensity from approximately 30 μT

(30000 nT) at the equator to 60 μT at the poles. Fortunately, the total of all non-dipolar contributions is significantly smaller than the total dipole field contribution, resulting in a global average field (45 μT) that is still generally dipolar in nature. For the purposes of determining the ancient field vectors stored in geological or archaeological materials, the GAD model is used as a reference frame and results are typically transformed into virtual geomagnetic pole position (VGP) for declination and inclination data, and virtual axial dipole moment (VADM) for intensity data. VADM is a measure of the equivalent GAD field that would have produced an observed intensity at a specific location. These data are then incorporated into spherical harmonics computations to create the IGRF and other models of secular variation back through time. For the purposes of archaeomagnetic dating or understanding certain regionally specific field anomalies, field models are often generated and based on data representing the field within a specific distance of the area of interest. In this research, model data is centralized around Jerusalem, Israel and extends out approximately 2000 km.

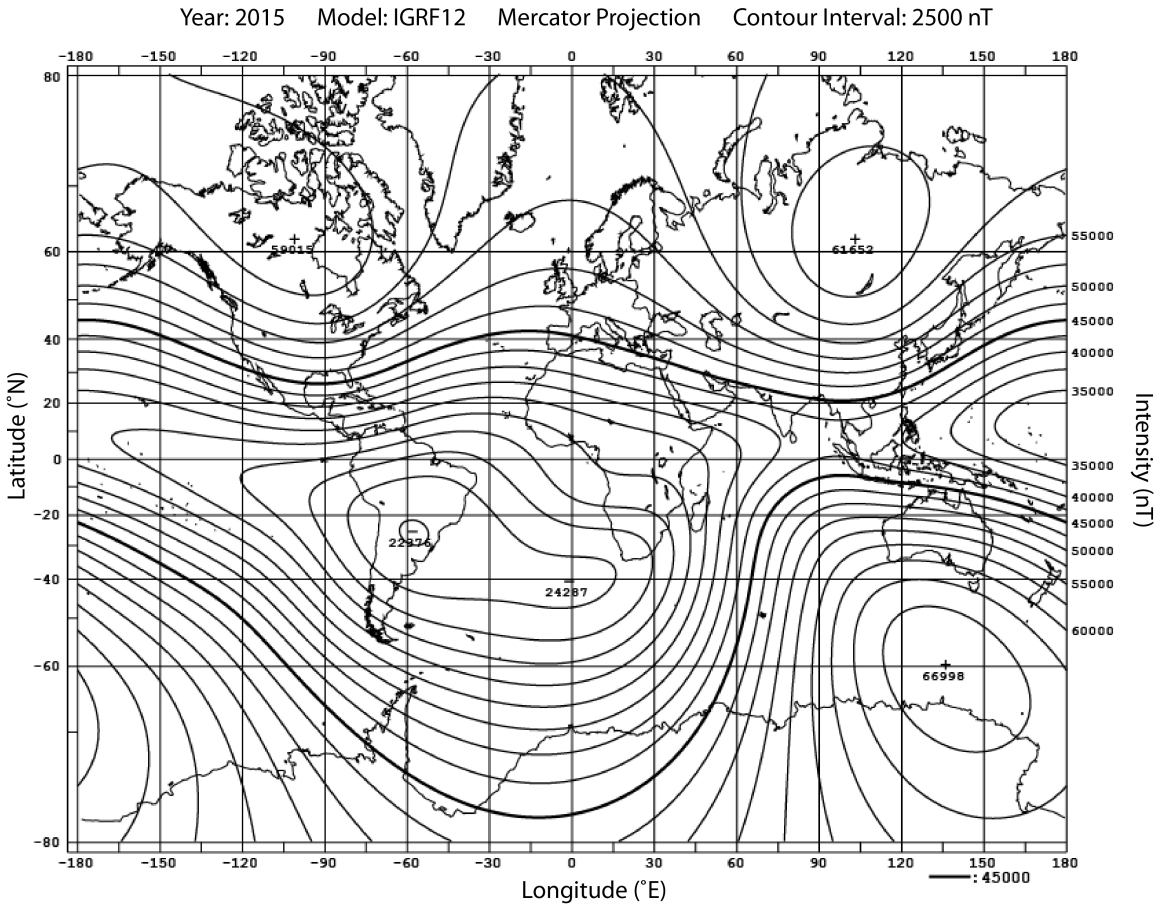

Figure 4-3 Global Average Field Intensity as of 2015
(Reproduced from *Thébault et al.*, 2015)

Several time-varying models based on measurements from previous studies and relevant to the Holocene geomagnetic field are used as comparisons to the new regional model generated in this research. These models are available through the GEOMAGIA50v3 website [*Brown et al.*, 2015b, 2015a]. The ARCH10K.1 field model [*Constable et al.*, 2016] is constructed using all currently available (through 2015) archaeomagnetic and lava flow data spanning the last 10 ka. This model has uneven

data coverage for periods older than 3ka B.P. Another 10 ka model, CALS10k.2 includes sedimentary records to increase temporal and spatial resolution [*Constable et al.*, 2016]. However, both of these models tend to minimize short-term field variability that may be present in a specific region. An additional model, HFM.0L1[*Panovska et al.*, 2015], was developed to capture southern hemisphere variability. This 10 ka model incorporates the same data as CALS10k.2, but incorporates calibrations for relative paleointensities from sediments and iterative outlier rejection. It has a higher temporal but lower spatial resolution than CALS10k.2. The PFM9k.1a model [*Nilsson et al.*, 2014] is also similar to the CALS10k model but incorporates new data treatments and sedimentary data. This final model more closely captures regional variability but continues to smooth out high-frequency perturbations. This smoothing feature of all the global average models underscores the importance of regionally specific field models for use as archaeomagnetic dating curves. For more on spherical harmonics and field modeling see [*Kono and Roberts*, 2002; *Korte et al.*, 2005, 2009, 2011; *Finlay et al.*, 2010; *Korte and Constable*, 2011; *Nilsson et al.*, 2014; *Brown et al.*, 2015a, 2015b; *Panovska et al.*, 2015; *Thébault et al.*, 2015; *Constable et al.*, 2016].

4.2 Rock Magnetism

Rock magnetism is the geophysical study of natural magnetic materials (mineralogy, grain size distribution, particle shapes of magnetic mineral assemblages, and associated magnetic properties such as remanence and susceptibility). Rock magnetic characterization techniques identify the specific carrier of magnetic

remanence and the suitability of a material to record and store the Earth's ancient field. Archaeological materials like pottery and bricks are made of clay-rich sediments formed from the erosion of igneous and sedimentary rocks, and contain iron-rich magnetic minerals, such as magnetite and hematite down to the nanometer size. These two minerals are often the primary carriers of magnetic remanence in materials used for archaeomagnetic studies because they have the ability to become permanently magnetized when exposed to a strong external magnetic field at ambient temperatures, or when cooling from elevated temperatures in the presence of a weak field.

4.2.1 Magnetism of Solids

Magnetization of any material begins at the atomic level and is produced through electron-spin interaction of adjacent atoms. All magnetic moments are equated as dipoles as no magnetic monopoles exist in nature. A magnetic moment is a property that describes the level of magnetization of a body, is material dependent, and defined in terms of the torque or force that a body experiences in an applied external magnetic field. On the atomic scale, magnetic moments are associated with the spin of an electron and its orbital motion around a nucleus. Atoms or cations have net magnetic moments if the electron-spin moments are not mutually cancelling (i.e. if there are unpaired spins). As the electrons orbit around the nucleus (which has a dipole moment of its own) they effectively act like a current loop in a wire, producing what is called the orbital magnetic moment. Individual electrons can also interact within an atom and between adjacent atoms causing changes in the magnetic moment. The net magnetic

dipole moment per unit volume averaged over a region of many atoms comprising a molecular unit is the magnetization (M) of that molecule, quantified as a vector with a magnitude and direction [*Stacey and Banerjee*, 1974; *Dunlop and Özdemir*, 1997; *Tauxe*, 2016].

The magnetization (M) of a solid is a combination of induced (by an externally applied field) and remanent (recorded or fixed internal) components. Induced magnetization (M_i) is the temporary acquisition of magnetization resulting from an applied magnetic field (H) and a material's bulk magnetic susceptibility (χ), a measure of the ability or extent to which a substance becomes magnetized under H:

$$\mathbf{M_i} = \boldsymbol{\chi}\mathbf{H} \tag{4-10}$$

Susceptibility is a function of the physical properties of the material as well as the applied field strength and orientation, frequency, and temperature. If these properties result in no preferential magnetic direction, the material is considered isotropic, χ is a simple scalar quantity, and M_i and H are parallel. However, most magnetic materials are anisotropic and M_i will have a directional component that is not parallel to H. In either case, when the applied field is removed, M_i will return to zero.

Magnetization in solids comes in three basic forms: diamagnetic, paramagnetic, and ferromagnetic. Diamagnetic materials, like quartz, do not have atoms with net magnetic moments and have a small negative χ that is not temperature dependent; therefore, they are inherently non-magnetic and will only acquire a small magnetization opposite (antiparallel) to an externally applied field. Diamagnetism is a property of all

matter but has a negligible effect in materials that contain strong atomic magnetic moments.

Paramagnetic solids in iron-bearing clays, have individual atoms that contain weak net magnetic moments, but they are randomly oriented when H=0 and do not interact, thus, these solids have no net permanent magnetism. Paramagnetic solids can acquire a M_i in an applied field but it is often very weak due to the randomizing effect of thermal energy. Many types of clay used for ceramics manufacture are hydrous sheet silicates (phyllosilicates) with a large proportion of iron ions, which contribute a paramagnetic component to their net magnetization.

4.2.2 Ferromagnetism

Ferromagnetic solids, like iron oxides, contain atoms with magnetic spin moments that strongly interact and mutually align to produce a spontaneous or permanent magnetization in the material even in the absence of an externally applied field. This exchange coupling produces magnetic ordering with adjacent atomic moments in either parallel or antiparallel directions (Figure 4-4). Permanent or remanent magnetization (M_R) in ferromagnetic materials is dependent on the size, shape, and crystallographic structure of the individual magnetic minerals, as well as the overall shape anisotropy of the material fabric (Section 4.2.5). If a strong enough field is applied to ferromagnetic solids they will reach a characteristic saturation magnetization (M_S), which does not continue to increase as the applied field increases. When the field is removed, ferromagnetic materials can then display a permanent M_R.

These characteristic magnetic properties can be identified through hysteresis experiments (Section 4.2.4) [*Butler*, 1992; *Tauxe*, 2016].

The stability of M in ferromagnetic solids is temperature dependent and above a specific temperature unique to each mineral, the Curie Temperature (T_C), the material becomes paramagnetic due to thermal energy excitation of the atomic magnetic moments. The T_C of a material is a diagnostic signature of the magnetic carriers of remanence and a fundamental property of the thermal remanent magnetization (TRM) acquisition of heat-treated archaeological materials (Section 4.2.7). The ability to become permanently magnetized after cooling from high temperatures is what makes ferromagnetic minerals the ideal recorders of the Earth's ancient field strength and direction.

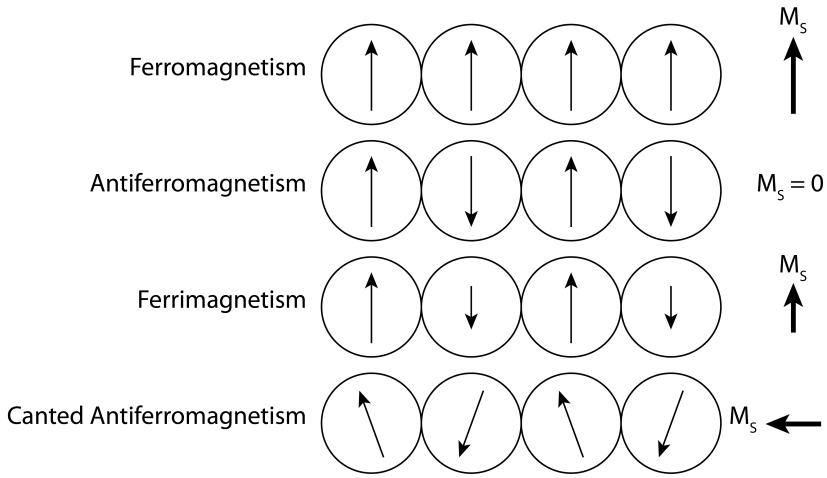

Figure 4-4 Atomic Exchange Interactions

The alignment of neighboring atomic moments of magnetic minerals come in four specific forms or states of ordering: ferromagnetic, antiferromagnetic, ferrimagnetic, and spin-canted antiferromagnetic (Figure 4-4). In ferromagnetic minerals the electron spins of neighboring atoms are coupled parallel to each other, producing a maximal net magnetic moment. Ferromagnetic minerals include pure iron (Fe) and iron-nickel alloys (Fe_xNi_x), which are rare in nature and mainly found in meteorites [*Dunlop and Özdemir*, 2007].

Table 4-1 Rock Magnetic Properties

Mineral	Magnetic Ordering	T_C (°C)	M_S (Am^2/kg) Room Temperature	Max (Cubic) SD Size (μm)
Magnetite (Fe_3O_4)	Ferrimagnetic	580	90-92	0.1
Hematite (Fe_2O_3)	Canted Antiferromagnetic	675	0.4	15
Titanomagnetite TM60 ($Ti_{0.6}Fe_{2.4}O_4$)	Ferromagnetic	150-200	24	0.3
Titanomagnetite TM20 ($Ti_{0.2}Fe_{2.8}O_4$)	Ferromagnetic	450	68	0.1
Ilmenite ($FeTiO_3$)	Antiferromagnetic	-230	0	NA
Maghemite (γFe_2O_3)	Ferrimagnetic	590 to 675	70-80	0.06

T_C = Curie temperature; M_S = saturation magnetization; SD = single domain

The two most common terrestrial magnetic minerals relevant to this research are magnetite (Fe_3O_4), which is ferrimagnetic, and hematite (Fe_2O_3), which has two states depending on temperature, antiferromagnetic and canted-antiferromagnetic. When

archaeological clays dehydrate they can form magnetite (in reducing environments) and hematite (in oxidizing conditions). Magnetite has two different crystalline lattice sites (tetrahedral and octahedral) containing two different types of iron cation, Fe^{2+} and Fe^{3+}. The number of each cation type on the two different lattice sites results in antiparallel spins that are not equal; therefore, their individual moments do not completely cancel and can produce a net magnetization approximately 1/3 that of ferromagnetic iron.

In antiferromagnetic hematite ($Fe^{3+}{}_2O_3$), the spin moments of the atoms align antiparallel, resulting in a zero net magnetization that behaves like a paramagnet. This magnetic state of hematite is usually only stable at temperatures below 258 Kelvin (K) or -15˚ Celsius (C). At room temperature (300 K), hematite can act as a weak permanent magnet because the spins are slightly angled or canted away from antiparallel. This weakly magnetic phase of hematite has an intensity approximately 0.5% that of magnetite [*Dunlop and Özdemir*, 2007].

Magnetite, hematite, and maghemite (γFe_2O_3), can incorporate trace metals, like aluminum (Al), Magnesium (Mg), or chromium (Cr), and form distinct magnetic phases such as titanomagnetite ($Ti_xFe_{3-x}O_4$). These incorporated metals affect the overall exchange interactions and thus, the T_C, M_S, and M_R of the magnetic minerals in the bulk material. For example titanomagnetite can be found in clays made from weathered basalts. As the titanium content increases, the T_C and M_S begin to drop. Table 4-1 outlines the characteristic rock magnetic properties of some of the common magnetic minerals found in archaeological clays.

4.2.3 Magnetic Domain State

Magnetic domains are uniformly magnetized regions within an individual ferromagnetic grain (hereafter ferromagnetic includes all ferromagnetic states) that form in order to minimize the surface pole charge (magnetostatic energy). There are four broad categories of domain structure, which are grain size dependent: superparamagnetic (SPM), single domain (SD), pseudo-single domain (PSD), and multi-domain (MD) (Figure 3.5) [*Stacey*, 1963; *Dunlop et al.*, 1974; *Stacey and Banerjee*, 1974; *Butler and Banerjee*, 1975; *Banerjee*, 1977; *Moskowitz and Banerjee*, 1979].

Larger grains of magnetite (> 10 μm) tend to have MD structure or several regions of magnetization separated by microscopic (<100 nm wide) barriers or walls within which the magnetization direction rotates progressively between those of the adjacent domains. The individually magnetized domain regions in an MD grain are saturated but tend to align antiparallel to adjacent domains, thus cancelling each other out and effectively reducing the net magnetization of the whole grain. MD grains are considered magnetically soft in that their interior domain walls can be easily moved in low magnetic fields, changing the number and size of domains and the overall remanent magnetization of the grain. This makes MD grains poor recorders of the Earth's magnetic field [*Butler*, 1992; *Dunlop and Özdemir*, 1997].

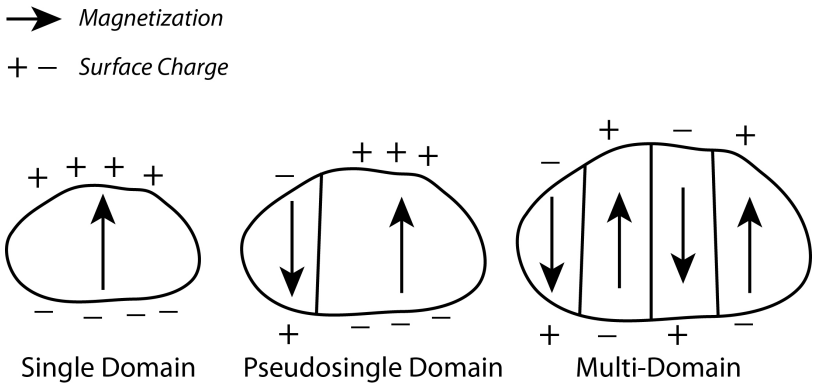

Figure 4-5 Magnetic Domains

As grain size decreases, the number of domains also decreases and the magnetostatic energy increases. SD grains have only one domain, with M uniformly in one direction; therefore, the grain has a strong net magnetization. SD grains are considered magnetically hard in that it takes a great deal of energy to rotate or change their magnetization. This resistance is referred to as anisotropy (Section 4.2.5) and leads to a preferred magnetic direction within SD (and MD) grains. This makes SD grains highly efficient at carrying a remanent magnetization. As grain shape changes, such as elongation of magnetite, the maximum SD size can also increase. The critical (maximum) size limits at room temperature for equidimensional SD grains is given in Table 4-1. The behaviors of SD grains under applied fields and temperatures are the basis for the laws governing TRM experiments (Section 4.2.7.1), which are necessary for calculating the ancient magnetic field strength recorded in archaeological materials [*Butler and Banerjee*, 1975; *Dunlop and Özdemir*, 2007]. While SD grains are optimal, most magnetic grains in both paleomagnetic and archaeological materials fall

somewhere between the SD and MD size range. These PSD grains often exhibit SD-like properties and carry a significant magnetic remanence, which can make them suitable for archaeomagnetic experiments. PSD size ranges for magnetite and titanomagnetite is usually between 1-10 μm [*Moskowitz and Banerjee*, 1979; *Butler*, 1992; *Pokhil and Moskowitz*, 1997].

As grain size continues to decrease below a stable SD threshold, they become so small that they can be thermally excited even at room temperature and their magnetic moments will fluctuate on timescales of nanoseconds to minutes. These superparamagnetic (SPM) grains are analogous to a paramagnetic state and are highly susceptible to field changes and room temperature thermal energy, thus, they do not hold a remanence. Rock magnetic susceptibility experiments under different field frequencies are often used to determine the SPM contribution to the total induced remanent magnetization in a bulk material [e.g. *Maher*, 1988].

4.2.4 Magnetic Susceptibility and Hysteresis

Magnetic susceptibility (χ) is a unit-less value and is a measure of the magnetic response of a material to an externally applied field. If the applied field is small, the resulting induced magnetization in the material will disappear immediately after the external field is removed and the sample will remain both physically and magnetically unaltered. The χ of a specimen is frequently interpreted as a proxy for the concentration of magnetic minerals present. Susceptibility measurements can be normalized by mass (reported as m^3kg^{-1}) in order to make a more meaningful comparison between samples

of different sizes. By measuring χ as a function of temperature it is also possible to quickly determine a specimen's Curie temperature.

Prior to any thermal experiments, it is typical to determine the internal magnetic homogeneity of ceramic samples by measuring χ at room temperature, usually in a field of < 500 A/m and a frequency of tens of thousands of Hz (experiments in this research used an applied field of 300 A/m and 920 Hz). In order to test for the presence of SPM grains in the bulk sample, they are further subjected to paired measurements at both a low frequency (e.g. 465 Hz), which affects all grains, and a high frequency (e.g. 4650 Hz). Like blocking temperatures, grains have a size-dependent property known as blocking frequency (f_b). Nanoparticles behave as stable SD grains (low susceptibility) above f_b and as SPM grains (high susceptibility) below f_b. This frequency dependency of susceptibility (χ_{fd}) test can then be used to determine the percentage of superparamagnetic grains in the sample using the following equation:

$$\boldsymbol{\chi fd} = \mathbf{100\ x} \left(\frac{\boldsymbol{\chi low} - \boldsymbol{\chi high}}{\boldsymbol{\chi low}} \right) \tag{4-11}$$

Hysteresis is the magnetic reaction of a material under a cycling, applied magnetic field in the laboratory. This reaction is graphically represented by a hysteresis loop, which provides both quantitative and qualitative interpretation of several mineralogical characteristics including the concentration of ferromagnetic minerals in a material, average domain state behavior, relative stability of magnetic grains, anisotropic effects, and the paramagnetic or diamagnetic contributions.

Figure 4-6 depicts a generalized hysteresis loop for a hypothetical ferromagnetic

material and the relevant magnetic parameters that it captures. The X-axis represent an external magnetic field (H) applied in a specific direction to a specimen and the Y-axis represents the bulk magnetization (M) or magnetic response to that field. As the applied field increases (to the right or H+), the magnetic moments of the grains in the specimen align parallel to the field. At the point that all moments align the specimen reaches saturation magnetization (M_S) in the applied field. When the applied field is removed, the moments of the grains either flip back to their previous direction or into an angle of minimum energy. The resulting zero-field saturation remanent magnetization (M_R) represents the maximum remanence for the material. The field is then increasingly applied in the opposite direction (H-), progressively flipping the magnetization until a reverse M_S is reached. The field is reversed again, completing the loop. The bulk coercivity (H_C) is the average field strength required to reduce the induced magnetization to zero (when M=0 about half of the grains have flipped and half are statistically aligned with the previous saturation field, thus summing to zero). Specimens can also be subjected to a successively increasing, small, reverse fields to create a backfield remanence curve, which is used to determine the distribution of reverse fields required to flip the remanence of different sized grains in a sample (i.e. identify presence of SD and MD grains). First the sample is saturated to produce an initial M_R. Small negative H fields are then applied, each followed by measurement of the remaining M_R in zero field. The applied backfield H for which the all the M_R is reduced to zero is called the coercivity of remanence (H_{CR}).

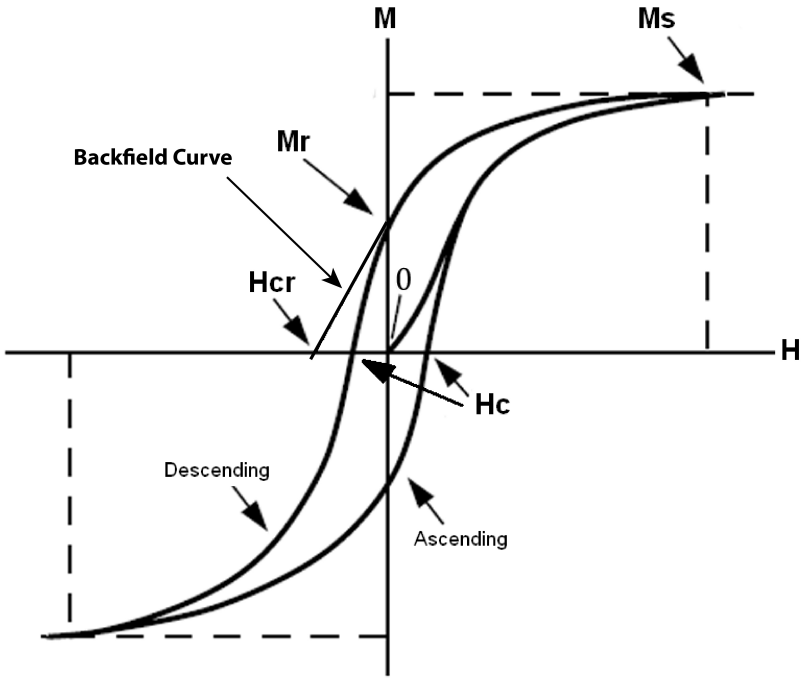

Figure 4-6 Generalized Hysteresis Loop
(Adapted from Butler, 1992)

These quantitative hysteresis measurements are used in a number of calculations to characterize the magnetic mineral assemblage of a material. Additionally, the overall shape of the hysteresis loop can be used to make inferences of the dominant magnetic minerals present, domain size, and shape anisotropy. For example, H_C is a measure of the average stability of the magnetization of the ferromagnetic minerals in the sample. The higher the H_C value, the harder the mineralogy (e.g., higher hematite/magnetite ratio) or higher the concentration of stable SD grains present. Therefore, wider loops indicate a larger proportion of hard minerals or SD grains, while narrower loops occur in specimens containing PSD and MD grains, soft minerals, or a fraction of SPM grains.

Additionally, the smaller the ratio of H_{CR} to H_C, the more likely the sample is dominated by SD remanent carrying grains [*Butler*, 1992].

4.2.5 Anisotropy of Magnetic Remanence

Individual magnetic grains and bulk materials are seldom isotropic in their magnetic and physical properties. All ferromagnetic minerals minimize energy by aligning their atomic magnetizations along easy crystalline axes within the crystal lattice (magnetocrystalline anisotropy), and/or aligning their magnetization along the easy or long axes of the individual magnetic grain (shape anisotropy). These preferential forms of magnetic alignment produce magnetic barriers to rotation of the net magnetic moment towards the direction of the applied field and draw the moment back into alignment with the easy or long axis of the individual grain, thus causing a directionally biased recording of remanence in each individual grain. Without these anisotropic energy barriers, magnetic remanence would not exist. If the easy axes of a large number of grains in a sample are randomly oriented, then the bulk sample is isotropic and records the field without bias; however, the preferred orientation of the remanence carrying grains still results in an overall anisotropic recording. [*Stacey*, 1960; *Fuller*, 1963; *Uyeda et al.*, 1963; *Stacey and Banerjee*, 1974; *Coe*, 1979; *Rogers et al.*, 1979; *Jackson*, 1991; *Selkin et al.*, 2000].

In addition to individual grain anisotropy, certain formation or manufacturing processes can preferentially align magnetic grains in the bulk material or rock. For example, the clay platelets in wheel-thrown pottery are smoothed and pressed together

along tightly bound parallel planes creating a material characterized by a biased magnetic orientation resulting in an anisotropy of magnetic remanence (AMR) [*Chauvin et al.*, 2000; *Rice*, 2005]. To a lesser degree, molded bricks, formed by pounding or extrusion, can also develop a fabric parallel to the horizontal surface similar to the compaction of sediments [*Kovacheva et al.*, 2000; *Tema*, 2009]. These types of petrofabric shape anisotropies can strongly affect the accuracy of the M_R acquired, particularly in thermally acquired remanence [*Coe*, 1979; *Tema*, 2009]. The result is a final M direction that is not perfectly oriented parallel to the ambient field but is instead biased towards the plane of the fabric and the preferred orientation of the long or easy axis of the magnetic grains (Figure 4-7).

When determining the ancient magnetic field intensity recorded by anisotropic materials, AMR is typically quantified and corrected for by calculating the anisotropy of anhysteretic remanent magnetization (AARM). An anhysteretic remanence (ARM) is a laboratory remanence acquired when the material is subjected to an applied magnetic field in the form of a decreasing alternating field (AF) that is larger than the H_C of the material determined from hysteresis, and a simultaneous unidirectional direct current (DC) field that is significantly smaller than Hc, usually comparable to typical geomagnetic fields (e.g. 50 microtesla) [*Dunlop and Özdemir*, 1997; *Moskowitz*, 2007]. This procedure is repeated at least six times in different directions to determine a second-rank tensor. If the material is isotropic, it will record a M_R parallel and proportional to the DC field intensity. Anisotropic materials will record a slight statistical bias to the DC field direction and intensity. Because ARM reasonably

approximates the anisotropic recording properties identified through TRM experiments, it is used as a substitute for TRM determination in delicate materials and as a simplified correction procedure for determining the anisotropy of the materials with biased fabric. This correction assumes that the shape and orientation of the AMR is unaffected by temperature [*Rimbert*, 1959; *McCabe et al.*, 1985; *Jackson et al.*, 1988; *Jackson*, 1991; *Selkin et al.*, 2000].

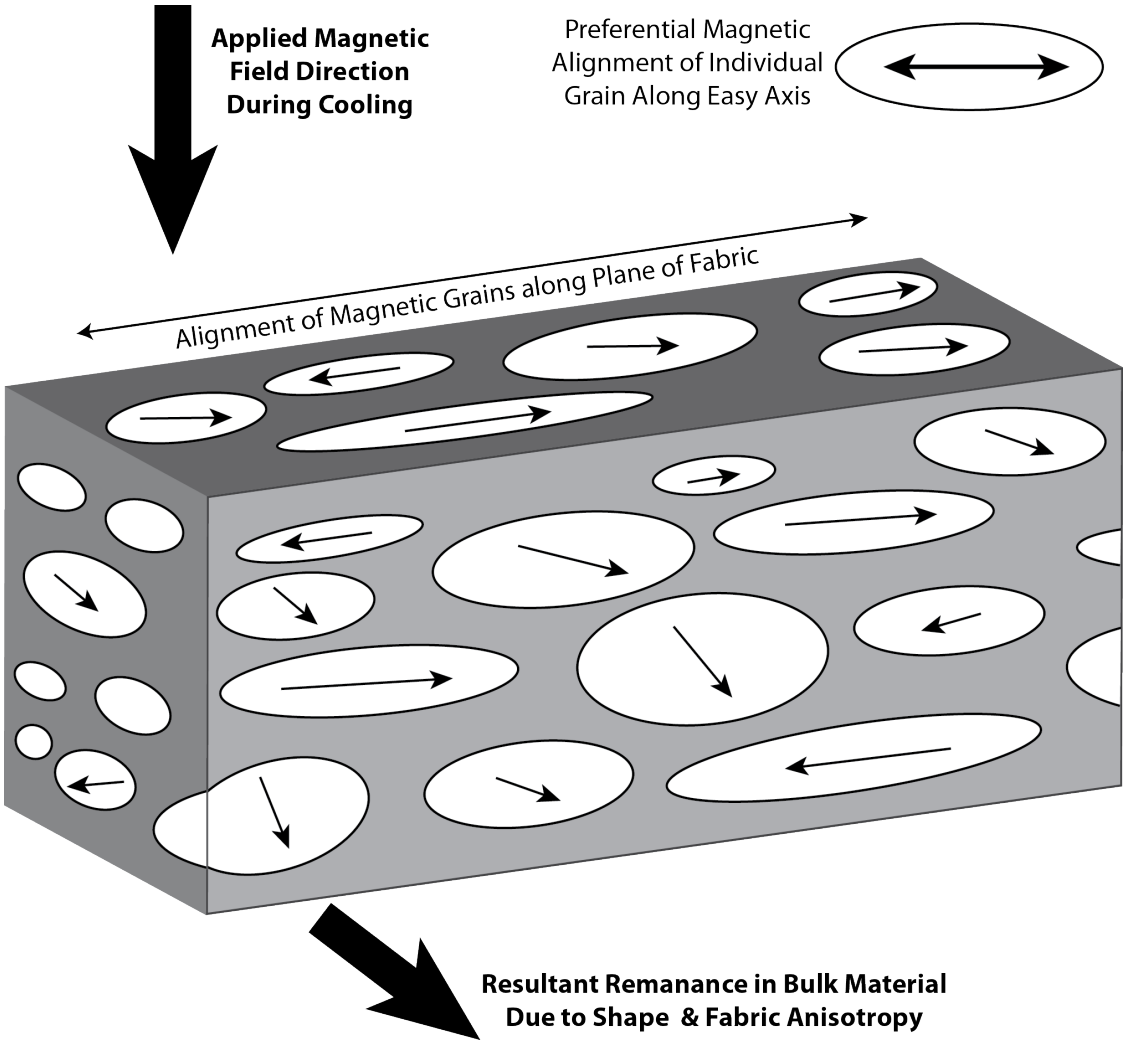

Figure 4-7 Shape and Fabrication Anisotropy

The shape of the grains pull the magnetic moment away from the applied field direction towards their easy axes. This in combination with the fabric alignment produces a final remanence that is not in-line with the applied magnetic field. *(Modified from Tema 2009 Figure 1)*.

4.2.6 Remanent Magnetization

As mentioned above, remanent magnetization (M_R) is a permanent recording in magnetic grains of an applied magnetic field after that field is removed and is a function of the atomic properties, size, and shape of the grain. M_R is also dependent on the formation conditions under which remanence acquisition occurs. The natural remanent magnetization (NRM) of a material is the sum of all the magnetizations acquired through various natural processes. The strongest NRMs are the result of exposure to strong fields, (e.g. lightning strikes). The next most intense NRM's result from exposure to typical geomagnetic fields during cooling from very high temperatures (greater than the T_C of the magnetic constituents), called thermal remanent magnetization (TRM), which typically occurs during igneous rock formation, such as the cooling and solidification of magmas. The primary form of NRM in high-fired ceramic materials is also a TRM. In some cases, archaeological materials undergo heating at temperatures below the T_C of their magnetic minerals. This results in the acquisition of a partial thermal remanent magnetization (pTRM), a type of secondary magnetization often found in pottery due to processes such as successive reheating. Cooking vessels commonly display several pTRM signatures and are, therefore, less than ideal for archaeomagnetic experiments.

NRMs can also occur through chemical alteration of magnetic minerals, such as oxidation, precipitation of new magnetic minerals, and diagenesis, resulting in materials recording a chemical remanence (CRM). CRMs are often common in chemically active

soils or wet depositional environments and can become a problem in hematite rich sediments when trying to identify primary NRM [*Dunlop and Özdemir*, 2007; *Tauxe*, 2016]. Prolonged exposure to weak fields can cause sediments and rocks to obtain a secondary magnetization called viscous remanence (VRM) or re-recording of the magnetic field through time. VRMs are usually minor and accounted for in archaeointensity experiments as they are easily removed at low temperatures and fields. Soils and other materials can also be exposed to high magnetic field during lightning strikes, which can align or realign their magnetization to record an isothermal remanent magnetization (IRM). Finally, bulk sediments can acquire a depositional remanence (DRM), which results when magnetic grains in sediments preferentially align with the Earth's field as they settle towards a depositional surface, such as a lakebed. When the sediment becomes consolidated the remanent magnetization is locked in place. This form of NRM is usually very weak and can only be used to determine a paleomagnetic direction and relative paleointensity.

Most sediments, rocks and even archaeological materials contain one or more of these different components of remanence. If enough magnetic minerals are present in an object and those minerals have recorded a magnetization through one or more of these processes, the NRM will be measureable in the laboratory using a Superconducting Rock Magnetometer (SRM). Typical NRM's for small (1.0 cm^3) fired pottery samples from the Levant, for example, are on the order of 1.0 x 10^{-3} Am^2kg^{-1}. The relatively strong magnetic remanence of fired ceramics makes them an ideal material for both paleomagnetic and archaeomagnetic research and indispensable for

developing geomagnetic field models of the Holocene.

4.2.7 Thermal Remanent Magnetization (TRM)

The remanence-carrying component targeted by a specific demagnetizing technique is termed the characteristic remanent magnetization (ChRM). The materials use in this research acquired their NRM through heating to high temperatures, a thermal remanent magnetization (TRM). As pottery is fired, the magnetic grains in the clay matrix become thermally unstable and the moments begin to randomize. Above the T_C of those grains the moments become paramagnetic due to thermal energy excitation.

As the pottery begins to cool, the magnetization begins to stabilize and the individual moments within the grains are drawn to the ambient magnetic field (or other externally applied field if in a laboratory situation). As the material continues to cool, the magnetic grains reach a temperature ($<T_C$) where their moments become blocked from further rotation, the blocking temperature (T_B). At this temperature, barriers to magnetic rotation form, the moment becomes fixed, and the material essentially records the applied field direction and intensity at that moment in time. This process of TRM acquisition by ancient fired ceramics can occur if kilns or firing techniques reach a temperature over 700˚C. Fortunately, high-fired manufacturing technology was well developed in the Near East by the Bronze Age (3300-1200 BCE) [*Rice*, 2005]. The T_C for pure magnetite and hematite are 580˚C and 680˚C, respectively, distinctive temperatures that allow for laboratory identification of magnetic mineralogy in a material.

4.2.7.1 Néel Theory and the Thellier Laws

In the late 1930s, Émile Thellier formulated the fundamental ideas of partial TRM (pTRM) and T_B and their relationship to TRM. With his wife Odette, they later developed the Thellier-Thellier method of paleointensity determination, the standard paleointensity technique still used today [*Thellier and Thellier*, 1959; *Dunlop*, 2011]. Not long after, Louis Néel developed the theory relating T_B for SD grains of magnetite to properties such as particle volume, anisotropy and magnetization intensity [*Néel*, 1949, 1955]. Together, the concepts developed by these researchers are fundamental to understanding the behavior of remanence-carrying non-interacting SD grains when determining ancient paleo and archaeointensity.

The NRM of a material is in a state of non-equilibrium (with respect to the present ambient field) that eventually decays or "relaxes" over time. Magnetic relaxation (τ) is not only a function of time but also the energy barriers to magnetic rotation and thermal energy. For example, larger SD grains with strong shape anisotropy can maintain a NRM for billions of years if not reheated, while smaller SPM grains may relax in seconds at room temperature. Strong externally applied fields or high temperatures break down these energy barriers to allow the preferential magnetic direction to rotate and randomize. Rock magnetic experiments by Néel identified the fundamental properties of magnetic relaxation and provided the theoretical model by which ferromagnetic non-interacting SD grains acquire and maintain a stable TRM. Magnetic relaxation time is exponential and is given by:

$$\boldsymbol{\tau = \frac{1}{f_0} \exp\left(\frac{\mu_0 V M_S H_k}{2kT}\right)} \tag{4-12}$$

where f_0= frequency factor (~10^9 Hz), μ_0=permeability of free space constant, V=volume of the magnetic grain, M_S=saturation magnetization, H_k=microscopic coercive force of the grain, and kT=thermal energy (k=Boltzmann constant, T=absolute temperature). From this equation, it can be seen that magnetic blocking is highly dependent on the grain volume and coercivity. Additionally, τ is strongly temperature dependent and Néel Theory is used to determine the transition point at which remanent magnetization is blocked or unblocked, a property essential to the behavior of TRM in SD grains. For example, given an elongated SD magnetite grain of approximately 0.1μm by 0.02μm, relaxation time can be less than a microsecond at 575˚C but a million years at 520˚C (Figure 4-8).

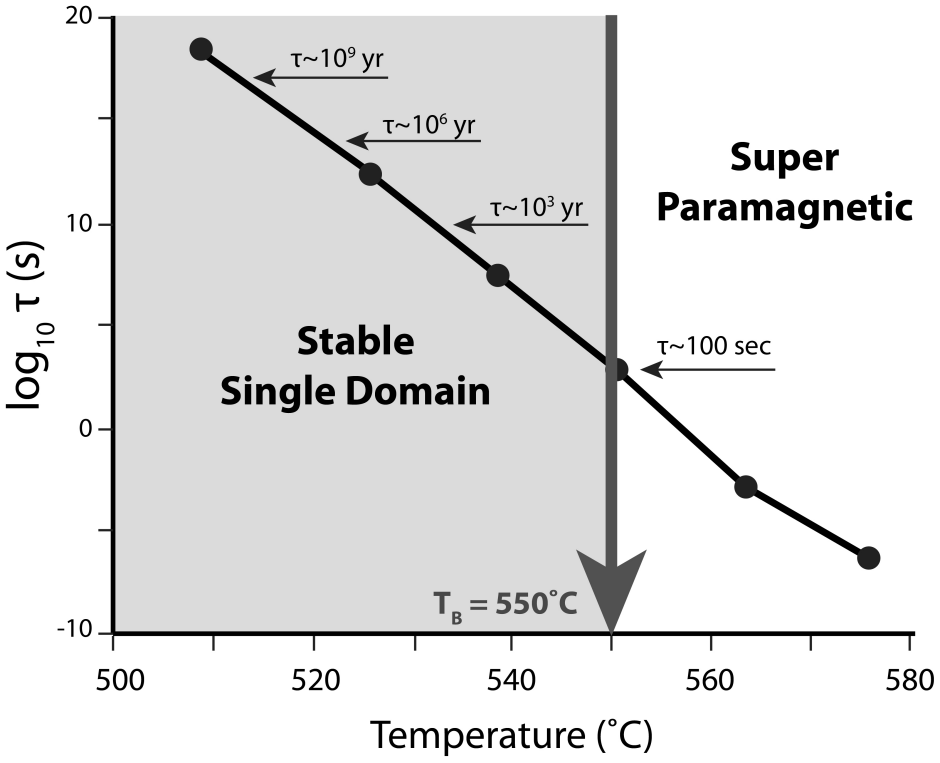

Figure 4-8 Relaxation Time for SD Elongate Magnetite

Semi-log plot of relaxation time (τ) for elongated particle of SD magnetite as a function of temperature. Blocking Temperature (T_B) at approximately 550˚C. At $T<T_B$ grains are stable (shaded region) and maintain a remanence. *(Figure adapted from Butler, 1992).*

The blocking temperatures identified by Néel Theory are key to the behavior of SD grains during TRM experiments and the basis of the ***Thellier Laws***:

1) ***The Law of Reciprocity*** states that the blocking and unblocking temperature for SD grains are the same (an assumption that fails for MD grains).
2) ***The Law of Independence*** states that mutually exclusive T_B's (and thus laboratory imparted pTRMs) are non-overlapping and independent.
3) ***The Law of Additivity*** states that individual pTRMs are dependent on the magnetic field present as they cool through their respective T_B and not affected by lower temperature intervals. Because pTRMs are a vector quantity, they may be added to produce a total TRM.

Because a material is made of different magnetic minerals and gran sizes, the total TRM is acquired over a distribution of T_C and T_B temperatures. For ideal, non-interacting SD grains, the total TRM in a sample can be calculated as sum of all the individual pTRMs blocked at any particular temperature interval (*i*):

$$\boldsymbol{TRM} = \sum_{\boldsymbol{i}}^{\boldsymbol{n}} \boldsymbol{pTRM}\ (\boldsymbol{T_{Bi}}) \tag{4-13}$$

During TRM Thellier-Thellier experimental procedures, the NRM of the sample is slowly removed through successive heating steps in a field free environment (zero field). The NRM remaining is measured after each heating cycle. Each temperature step is then repeated a second time but with a known laboratory field (or in-field step) (H_{lab}), slowly giving the material a new pTRM or lab Magnetization (M_{lab}). Eventually, the material is heated to approximately 700˚C, removing all the original NRM. Upon

cooling in the final in-field step, the material gains a final new laboratory remanence (M_{lab}) in the known field.

If the Thellier Laws hold and the remanent magnetizations held by the rocks or archaeological materials are acquire by similar mechanisms (in nature and the lab), then the ancient field strength and/or direction (M_{anc}) can be calculated as:

$$\boldsymbol{M_{NRM} = \alpha_{anc} H_{anc}} \tag{4-14}$$

where α is a proportionality constant based on remanence acquisition and a factor of grain size, shape, and concentration, and H equals the applied field. If α is assumed to be the same for both the ancient and laboratory conditions, M_{NRM} can be measured, and the laboratory conditions are known, then:

$$\boldsymbol{M_{lab} = \alpha_{lab} H_{lab}} \tag{4-15}$$

The ancient field (H_{anc}) can then be determined by setting these two equations equal to each other:

$$\boldsymbol{H_{anc} = \left(\frac{M_{NRM}}{M_{lab}}\right) H_{lab}} \tag{4-16}$$

This equation is the slope of a line on an Arai plot of NRM removed (y-axis) to pTRM gained (x-axis) (Figure 4-9).

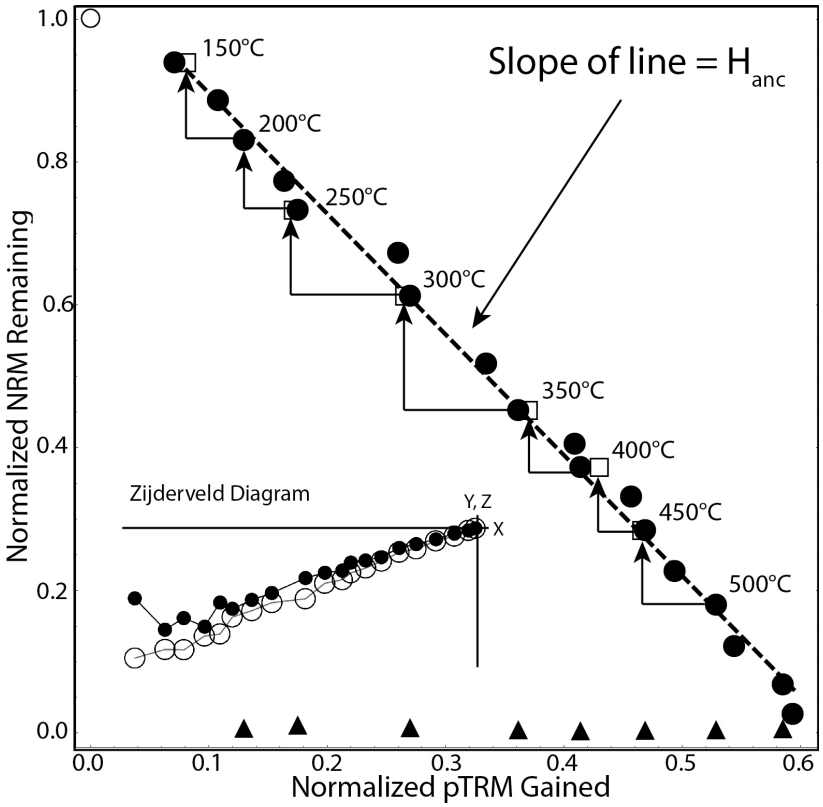

Figure 4-9 Sample Arai Plot

Arai plot of NRM removed (y-axis) to pTRM gained (x-axis). Solid circles are paired in-field/zero-field temperature steps, open squares are repeated thermal (pTRM) checks for non-linear behavior (with backwards stepping arrows to show when check is run), and solid triangles are checks for multi-domain behavior. If multidomain contributions are high, the Arai plot will sag. The inset Zijderveld diagram displays the decay of the vertical and horizontal components of magnetization under an AF. The relatively straight decay indicates only one component of remanence is carried by the sample.

5 Materials and Methods

5.1 Overview

Materials for this study were collected in conjunction with the Tel El Hesi Regional Project's excavation at Khirbet Summeily during the summers of 2011, 2012, and 2014. Six nearby archaeological sites in the Negev Shephelah region (low hill country) were also sampled: Tel 'Eton, Tel Gezer, Tell Halif, Tel Burna, Tel Lachish, and Jaffa (Joppa) (Figure 5-1). These sites were chosen as sources of archaeomagnetic calibration samples as they contained significant destruction deposits that bound the estimated ages of the phases of Khirbet Summeily. Archaeomagnetic samples included high-fired pottery, fired mudbrick from destruction layers, and tabun fragments from occupational strata dating from the late Bronze Age (~1400 BCE), through the Iron Age, and into the Persian Empire Period (6th Century BCE). Tables 5-1 and 5-2 outline the materials and ages for the calibration sites and the samples from Khirbet Summeily, respectively. In total, over 150 unique artifact samples were collected. Representative sample photos can be found in Appendix A, Figure A-1.

During the course of sample processing two of the calibration sites were removed from the study. The materials from Jaffa were collected from a 13th century BCE conflagration that destroyed an Egyptian palace complex. Unfortunately, they were highly friable and had disintegrated in shipping; therefore, they were left out of

this study. Materials from Lachish were unprocessed at the time of this paper.

Figure 5-1 Location of Archaeological Sites Sampled

The materials from Tel 'Eton were collected from a massive destruction layer in the Area A courtyard of a large governor's residency. Pottery samples were archaeologically dated (by pottery seriation and inter-site comparison) to either the 701 BCE Assyrian campaign of Sennacherib or the slightly older Assyrian campaign (734 BCE) of Tiglath-Pileser III [*Katz and Faust*, 2012; *Faust*, 2017; *Faust and Sapir*, 2018] and bounded by radiocarbon dates collected from the floor surface. The tabun fragments from Tel Halif are similarly dated to either the 701 or 734 BCE destructions

[*Borowski*, 2017] but the radiocarbon dates for the strata for inconclusive, therefore materials were dated by seriation and associated artifacts. Egyptian campaigns and massive conflagrations are frequent during the Levantine Iron Age and the relatively contemporary nature of these two campaigns has drawn criticism on the preferred assignment of many late 8th Century BCE destructions to the Sennacherib campaign [*Baillie*, 1991; *Blakely and Hardin*, 2002; *Finkelstein and Na'aman*, 2004]. Unfortunately, archaeomagnetic analysis of 701 BCE destructions has yet to be performed. Until further data can clarify this issue, materials from these two calibration sites are ascribed an age of 717 BCE, halfway between 701 and 734.

Materials from Tel Gezer provided radiocarbon dated and detailed stratigraphic calibrations for three destruction events: the 1208 BCE Egyptian campaign of Merneptah (19th Dynasty), the 925 BCE Egyptian campaign of Shoshenq I (22nd Dynasty), and the 833 BCE Hazael of Damascus campaign that destroyed Tel es-Safi (ancient Gath) [*Ortiz and Wolff*, 2017]. Tel Burna materials are from the early 13th Century BCE open-air courtyard of Area B1. Similar to the courtyard of 'Eton, these areas would have been used for food processing and feasting activities and usually contained tabuns for baking bread. The TabunB01 was unusually large and made from a broken Cypriot pithoi vessel. While no radiocarbon dates are currently available for Area B1, imports of Cypriot wares ended by the 12th and other diagnostic archaeological materials limit the age of the samples to the 13th Century BCE [*Sharp C.*, 2017; *McKinny et al.*, 2018; *Shai and McKinny*, 2018].

Table 5-1 Samples from Calibration Sites

Sample ID	Material	Date	Calibration Method	Stratum/ Locus	Notes
Tel Burna					
BUR01	TabunB01	1300-1200 BCE	AS	Area B1	*in situ* Cypriot pithoi used in tabun construction
BUR03	TabunB01				
BUR04	TabunB02				Locally made clay tabun fragments
Tel Gezer					
GZ03	TabunGZ01	833 BCE	RC	Stratum 7/ Rm 1	*in situ,* domestic bldg
GZ06	TabunGZ01				
GZ07	TabunGZ01				
GZ04	Pottery				Inside tabun
GZ05	Pottery				
GZ08	Pottery	925 BCE	RC	Stratum 8/ Rm 6	Under collapsed wall, courtyard of administrative bldg
GZ10	Pottery				
GZ13	Pottery	1208 BCE	RC	Stratum 12/ Rm A	Late Bronze Age Patrician bldg
GZ14	Pottery				
GZ15	Pottery				
GZ16	Pottery				
GZ17	Pottery				
GZ18	Pottery				
GZ19	Pottery				
GZ20	Pottery				
Tel Halif					
LH02	TabunH01	734-701 BCE	AS	Stratum, VIB/ Locus I2/3	Clay, collapsed tabun
LH03	TabunH02			Stratum VIB/ Locus E7	
LH04	TabunH02				
LH05	TabunH03			Stratum VIB/ Locus A8	
LH06	TabunH03				
Tel 'Eton					
ET01	Pottery	734-701 BCE	AS	Area A Courtyard	*in situ* complete vessels
ET03	Pottery				
ET04	Pottery				
ET05	Pottery				
ET06	Pottery				
ET08	Pottery				
ET10	Pottery				

AS = Archaeological and stratigraphically defined age, primarily based on pottery seriation
RC = Radiocarbon defined age

Table 5-2 Samples from Khirbet Summeily

Sample ID	Material	Estimated Age (BCE)	Phase	Unit/Locus	Setting Notes
KS1414	Pottery	825-775	Phase 2	I63.006	Interior possibly burnished, found in ash layer
KS1419	Pottery	825-775	Phase 2	I33.012	Found in Hearth
KS1604	Pottery	825-775	Phase 2	I33.013	Hearth
KS1606	Pottery	825-775	Phase 2	I33.013	Hearth
KS1760	Pottery	825-775	Phase 2	I43.005	Found near TabunKS01
KS2357A	Pottery	825-775	Phase 2	I43.018	Foundation trench - could predate phase 2 to the construction of wall
KS2357B	Pottery	825-775	Phase 2	I43.018	Foundation trench - could predate phase 2 to the construction of wall
KS2378	Pottery	825-775	Phase 2	I43.018	Large cooking pot with dense shell temper, Foundation trench - could predate phase 2 to the construction of wall
KSMDS01	Pottery	825-775	Phase 2	I33.013	Found in Hearth, charred
KSMDS02	Pottery	825-775	Phase 2	I33.013	Found in Hearth, charred
KSMDS03	Pottery	825-775	Phase 2	I33.013	Found in Hearth, charred
KSMDS04	Pottery	825-775	Phase 2	I33.013	Found in Hearth, charred
KSMDS05	Pottery	825-775	Phase 2	I33.013	Found in Hearth, charred
KSMDS06	Pottery	825-775	Phase 2	I33.013	Found in Hearth, charred
KSMDS07	Pottery	825-775	Phase 2	I33.013	Found in Hearth
KSMDS08	Pottery	825-775	Phase 2	I33.013	Found in Hearth
KSMDS09	Pottery	825-775	Phase 2	I33.013	Found in Hearth
KSMDS10	Pottery	825-775	Phase 2	I33.013	Found in Hearth
KS1411	TabunKS01	825-775	Phase 2	I43.005	*in situ* Tabun, from interior 2 cm portion of wall
KS1412	TabunKS01	825-775	Phase 2	I43.005	*in situ* Tabun, most interior smoothed surface, approx. 0.5 cm thick
KS1413	TabunKS01	825-775	Phase 2	I43.005	*in situ* Tabun, from interior 2 cm portion of wall
KS1420	Pottery	950-910	Phase 3	I55.013	Silt above top plaster floor layer
KS2362	Pottery	950-910	Phase 3	I44.031	Hematite burnished crator with dark burnished interior, no older than 970 BCE, found near pot stand on Cult Room floor

KS710	Pottery	950-910	Phase 3	I44	Cult Room offering stand/chalice
KSG24	Pottery	950-910	Phase 3	I54.028	Complete bowl, Cult Room, near wall and possible oil spill
KS1417	TabunKS02	950-910	Phase 3	I73.010	*in situ* Tabun, from interior 2 cm portion of wall
KS1418	TabunKS02	950-910	Phase 3	I73.010	*in situ* Tabun, from interior 2 cm portion of wall
KS1474	TabunKS02	950-910	Phase 3	I73.012	Interior collapse contents of tabun
KS1607	TabunKS02	950-910	Phase 3	I73.010	*in situ* Tabun, from interior 2 cm portion of wall
KS1608	TabunKS02	950-910	Phase 3	I73.010	*in situ* Tabun, from interior 2 cm portion of wall
KS1609	TabunKS02	950-910	Phase 3	I73.010	*in situ* Tabun, from interior 2 cm portion of wall
KS1840	TabunKS02	950-910	Phase 3	I73.012	Interior collapse contents of tabun
KS1859	TabunKS02	950-910	Phase 3	I73.009	Interior collapse contents of tabun
KS2348A	Pottery	1000-950	Phase 4	I44.036	Found in silt above top plaster floor layer
KS2348B	Pottery	1000-950	Phase 4	I44.036	Likely cooking vessel, found in silt above top plaster floor layer
KS2348C	Pottery	1000-950	Phase 4	I44.036	Highly porous, charred, found in silt above top plaster floor layer
KS2348D	Pottery	1000-950	Phase 4	I44.036	Cooking vessel, found in silt above top plaster floor layer
KS2348E	Pottery	1000-950	Phase 4	I44.036	Silt above top plaster floor layer
KS2348F	Pottery	1000-950	Phase 4	I44.036	residue/materials coating on interior, found in silt above top plaster floor layer
KS2202	TabunKS03	1000-950	Phase 4	I73.018	Found under floor associated with phase 3 tabun, possible rebuild in same area
KS2368	Pottery	1025-970	Phase 5	I65.019	Red-slipped, unburnished
KS2369	Pottery	1025-970	Phase 5	I65.019	Red-slipped, unburnished
KS2370	Pottery	1025-970	Phase 5	I65.019	Red-slipped, unburnished, possible cooking vessel, residue on interior surface
KS2371	Pottery	1025-970	Phase 5	I65.019	Red-slipped, unburnished
KS2372	Pottery	1025-970	Phase 5	I65.019	Red-slipped, unburnished
KS2373	TabunKS04	1025-970	Phase 5	I65.019	Fragments

[1] *Archaeological age estimates based on pottery seriation, stratigraphy, material association, and revised traditional chronology paradigm*

The bulk of this research was conducted using locally produced pottery found displaced from its original firing context. Pottery tends to yield a strong thermal ChRM, ideally suited for determining the intensity of the ancient field strength. Several *in-situ* bread ovens (tabuns) constructed from local clay sediments were also tested to determine ancient magnetic declination and inclination (not presented in this study). Tabuns were often constructed into a beehive shape (Figure 5-2) for baking bread, similar to the small household tandoor ovens still used in India today. Kilns and ovens have increasingly been used in archaeomagnetic research to determine ancient field direction [*Schnepp*, 2003; *Gómez-Paccard et al.*, 2006; *Catanzariti et al.*, 2008; *Schnepp et al.*, 2009; *Hervé et al.*, 2011; *Spatharas et al.*, 2011; *Osete et al.*, 2016]; however, special handling techniques are necessary as some of these materials can be brittle and disintegrate during Thellier-Thellier experiments. In addition, depending on the area sampled, they may have been insufficiently heated (i.e. exterior of oven) or display multiple low-firing episodes. All but one of the tabuns (Burna) used in this research were approximately 2-3 cm thick, constructed with local clays, and either intact, or collapsed. TabunB01 at Burna was an unique, unusually large tabun constructed using an old broken pithoi vessel as the primary oven chamber. The vessel was approximately 3-5 cm thick. It was sampled to verify if it would have been heated hot enough to reset the original magnetization of the pithoi and could be utilized as suitable archaeomagnetic material. For all of the tabuns, the first centimeter of the interior oven wall (presumed to be the area heated to the highest temperature) was used for archaeomagnetic measurements.

After initial cleaning and visual inspection of the samples to determine their suitability for archaeomagnetic experiment (e.g. completely oxidized core), a total of 76 samples (221 specimens) representing 11 unique tabuns and 52 pottery samples were found suitable. Emphasis was placed on running several sample sets of the tabuns in order to determine their viability as archaeomagnetic recorders; therefore some tabuns had more than 3 replicate specimens. Specimens were measured using a suite of rock magnetic characterization techniques and standard paleomagnetic/archaeomagnetic methods at the University of Minnesota's Institute for Rock Magnetism. The detailed methodology outlined was designed to not only increase the reliability of archaeomagnetic dating but also advance our understanding of the magnetic mineralogy of anthropogenic materials and how they record the Earth's field. The paleomagnetic methods for determining the ancient field intensity outlined in Section 5.2 were developed during archaeomagnetic dating of materials from Tell Mozan, Syria [*Stillinger et al.*, 2015]. Minor changes to those methods, particularly selection criteria, have been applied to this research and are outlined in section 5.3.

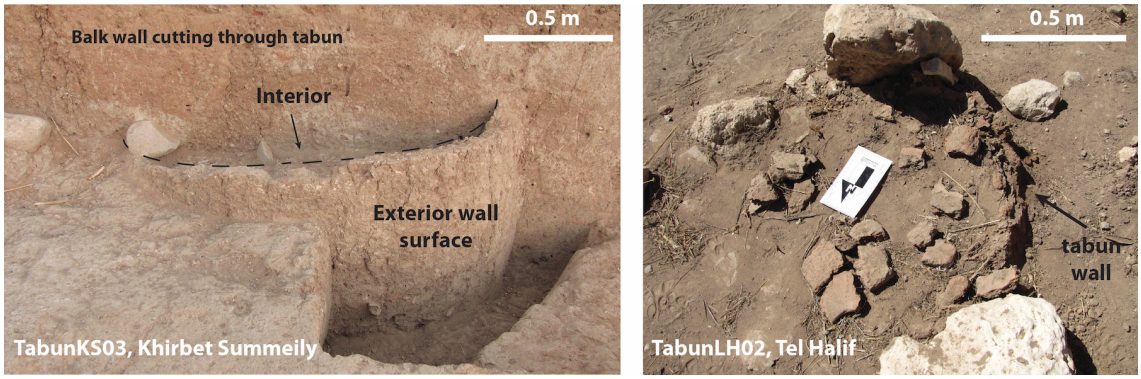

Figure 5-2 *in situ* Tabuns or bread ovens from Summeily and Tel Halif
TabunKS02 was found with its exterior walls intact. TabunLH02 was collapsed with only a portion of the exterior wall still standing. Rocks were typically used around the exterior as support and insulation.

5.2 Archaeointensity Methods

The contents of this section were originally published in the *Journal of Archaeological Science*, reproduced here with permission from the authors. Stillinger, M.D., Feinberg, J.M., Frahm, E. 2015. Refining the Archaeomagnetic Dating Curve for the Near East: New Intensity Data from Bronze Age Ceramics at Tell Mozan, Syria, *Journal of Archaeological Science*, Vol. 53, pp. 345-355. Note: Some of the images and tables from the original article are included in Appendix B.

Synopsis

Uncertainty in radiocarbon dates for the Near East, caused by a bimodal distribution of ages due to the natural fluctuations of ^{14}C in the atmosphere, has demonstrated the need for an alternative absolute dating technique to aid in the construction of site chronologies. Here we present a new archaeointensity reference curve model for the first three millennia BCE for the Levant (Syria, Israel, Jordan) for use in archaeomagnetic dating and contribute twelve new intensity results to an increasingly dense geomagnetic field record for the period between 2400 and 1200 BCE in the Near East. Archaeomagnetic analysis was conducted on ceramic samples (i.e. pottery sherds) from seven sequential and well-constrained occupational layers at the site of Tell Mozan (Bronze Age Urkesh) in northeastern Syria, resulting in a 90% success rate by specimen (n=42) for archaeointensity determination and an 86% correspondence between the model and the archaeologically derived dates within one standard deviation (1σ). Age standard deviations as low as ±24 years were obtained after integration with stratigraphic constraints. We also outline the techniques and sampling procedures of archaeomagnetic dating in a manner suitable for the non-paleomagnetist while detailing methodology for archaeomagnetic researchers.

5.2.1 Introduction

Chronological resolution is a fundamental issue in any archaeological investigation and has often focused on relative dating techniques, such as ceramic seriation or textual evidence. These methods rely heavily on interpretations of cultural change and technological dispersion. The introduction of radiocarbon dating more than six decades ago provided archaeologists with an absolute dating technique removing much of the subjective nature of relative dating and resulting in the aptly named Radiocarbon Revolution, which undermined certain theories of cultural diffusion and civilization [*Libby et al.*, 1949; *Renfrew*, 1979]. While radiocarbon dating is now widely accepted and utilized in archaeology, the natural fluctuations in the production rate of ^{14}C in the atmosphere results in "wiggles" and plateaus in the global reference curve, which occur on timescales of one decade up to a few centuries [*de Vries*, 1958; *Suess*, 1965; *Damon et al.*, 1978]. This can result in complicated, even multi-modal, distributions of ages. These problems are especially apparent during the first millennium BCE and have resulted in continued chronology debates in Near Eastern archaeology, where tightly constrained site chronologies are necessary for interpreting site associations with biblical events and locations (e.g., Finkelstein and Piasetzky, 2011).

Archaeomagnetic dating provides both a complementary absolute dating technique that can refine broad chronologies and an alternative in situations where materials suited to radiocarbon analysis are not abundant. As a subfield of

paleomagnetism, archaeomagnetism investigates the record of geomagnetic field direction and/or intensity stored within archaeological materials such as fired mudbrick, ceramics, stone, and metal slags. Early archaeomagnetic research was partially responsible for the development of standard paleomagnetic techniques used today due to the ability of heat-treated archaeological materials containing common iron oxide minerals, such as magnetite and hematite, to carry a strong fixed remanence [*Sternberg*, 1990, 2001]. Archaeomagnetism enables the study of small secular variations in the Earth's magnetic field on scales from decades to millennia. These changes can be plotted through time to create regional reference curves suitable for dating archaeological materials carrying a stable magnetic remanence [*Sternberg and McGuire*, 1990].

Here we discuss the fundamental methods, sampling procedures, and applications of archaeomagnetism in the context of magnetic remanence held by pottery at the site of Tell Mozan in northeastern Syria. Detailed discussions of geomagnetism and paleomagnetic techniques are found in Butler (1992), Hulot et al. (2010), and Tauxe (2014), and their application to archaeomagnetism in Eighmy and Sternberg (1990). Interested readers are forwarded to Courtillot and Le Mouël (2007) regarding the development of these fields. Recent archaeointensity data for the Near East, derived from separate studies, have been sufficiently consistent to yield a relatively robust reference curve of field intensity for the last five millennia. Our principal focus here is to demonstrate that the archaeologically defined chronology at Tell Mozan is consistent with that curve. Following our detailed measurement and analysis protocols, all of our

well-constrained archaeological dates corresponded to the regional reference curve within a 2σ confidence interval. We also discuss the importance of analyzing and reporting each sample's archaeointensity results separately, rather than averaging results across a stratigraphic phase. This more nuanced approach may allow researchers to identify and resolve inconsistencies that are due to poor temporal constraints or artifact-feature association.

5.2.2 Archaeological Overview of Tell Mozan

Tell Mozan has been identified as the ancient city of Urkesh, a political and religious center of the Hurrian culture during at least the third and second millennia BCE [*Buccellati*, 2005; *Buccellati and Kelly-Buccellati*, 2005]. The 130-ha site (37˚03'24"N, 40˚59'45"E, elev. 463 m) is located in the Syrian piedmont region, the interface between the Taurus Mountains in southern Anatolia and the Mesopotamian lowlands, along the northern edge of the Fertile Crescent (Fig. B-1, Appendix B).

Historically, Urkesh was considered a small vassal of the Akkadian empire (circa 2300-2200 BCE); however, the city's strategic geographic location might have enabled its residents to exert trade control over copper and other goods entering from the north as well as the local agricultural economy [*Buccellati*, 2005; *Buccellati and Kelly-Buccellati*, 2005]. The prominence of Urkesh is evidenced by monumental architecture, specifically an Early Dynastic temple complex (circa 2800-2300 BCE) and a royal palace structure constructed during the Early Bronze Age (EBA) III (2269-2240 BCE), as well as cuneiform tablets, seals, and textual inscriptions belonging to the royal

household with uniquely Hurrian nomenclature [*Buccellati*, 2005]. Seals belonging to Tar'am-Agade, daughter of the Akkadian king Naram-Sin, suggest that she may have been a queen or Akkadian administrator at Urkesh (Buccellati, 2005). The origins of obsidian artifacts at this time suggest that the city was especially cosmopolitan, having connections throughout Central and Eastern Anatolia [*Frahm and Feinberg*, 2013a, 2013b; *Frahm*, 2014].

The chronology of Tell Mozan represents more than 20 years of excavations, which have identified five millennia of occupation (Frahm, 2010:171, and citations within). The period considered in this study is represented by five site-specific phases beginning with an EBA III pre-palace construction in Phase 1 (2334-2270 BCE) and ending with scattered occupations during Phase 6 (1600-1200 BCE) corresponding to the Middle Bronze Age (MBA) IIC to Late Bronze Age (LBA)/Mitanni period (Table B-1, Appendix B). Phases 3 and 4 at the site are further constrained into two distinct time periods each, resulting in a total of seven sequential strata from which archaeomagnetic samples were taken. Phase 2 (2269-2240 BCE) pottery fragments were unavailable at the time of this study.

5.2.3 Materials & Sampling Procedures

All samples used in this research were pottery fragments. The remanent magnetization held in pottery is typically thermal in origin (thermoremanent magnetization, TRM). The best ceramic materials for archaeomagnetic experiments are those that have been fully fired to high temperatures (over 650˚C), presumably above

the unblocking temperatures of their magnetic constituents, which is the temperature at which magnetization becomes randomized. While it may be possible to extract meaningful archaeomagnetic information from ceramics fired at lower temperatures, in this study only fragments that lacked a gray carbon-rich core and appeared fully oxidized, as evidenced by a clear orange, red, or buff coloration, were accepted. While color alone is not a conclusive test of oxidation, it is a helpful first order selection criterion for ensuring that the original pottery had been heated to a high enough temperature necessary to fully combust all carbonaceous materials in the clay (at least 500˚C). Fragments containing large pore spaces and/or lithic temper inclusions were also rejected to avoid crumbling during heating and to minimize the effects of large magnetic grains, respectively. Samples were further chosen based on their size suitability for four replicate 2 x 2 cm specimens. These strict selection criteria resulted in a total of 14 suitable samples (56 specimens) from an original sample size of 97 pottery fragments. See Figure B-2, Appendix B for photographs of representative fragments. As the target magnetic material is the ceramic body, specimens were cleaned of all debris and surface treatments (i.e., paint and slip), which might alter magnetic measurements and, thus, the resulting dates.

5.2.4 Rock Magnetic Analysis

All pottery fragments (hereafter referred to as samples) underwent a series of standard rock magnetic measurements to determine their suitability for high-temperature experiments, including magnetic susceptibility, hysteresis, and room

temperature remanence measurements. The initial natural remanent magnetization (NRM), the sum of all naturally occurring remanence carried by the pottery, as well as all subsequent demagnetizations and partial thermal remanent magnetizations (pTRMs), were measured using either a 2G Enterprises 755 Long Core Magnetometer (referred to hereafter as 2G LC) or a 2G Enterprises 765 Superconducting Rock Magnetometer (SRM). NRM measurement indicated that all specimens carried a strong initial magnetic remanence and subsequent rock magnetic analyses indicated that all samples were resistant to mineral alteration and suitable for thermal experiments necessary for final ancient intensity determination. Rock magnetic experiment results described below are presented in Table B-3, Appendix B.

5.2.4.1 Susceptibility

Low-field magnetic susceptibility (χ) was measured on all four replicate specimens at room temperature to verify the internal homogeneity of each 2 x 2 cm specimen. One specimen from each sample (Specimen Set #1) was tested for the presence of superparamagnetic (SP) grains, nanometer-scale magnetic grains which do not hold a remanence and can spontaneously change their magnetization with small changes in applied field and/or temperature. Susceptibility experiments on all specimens indicated a high degree of internal homogeneity of the pottery samples and, with the exception of one sample, less than 10% SP contribution to magnetization. Susceptibility experiments were conducted on a Kappabridge KLY-2 Magnetic Susceptibility Meter in a field of 300 A/m and a frequency of 920 Hz with a sensitivity of $4x10^{-8}$ SI. SP measurements were conducted on a Magnon Variable Frequency

Susceptibility Meter in a field of 300 A/m at a low frequency (χ_{465}) of 465 Hz and a high frequency (χ_{4650}) of 4650 Hz. The frequency dependency of susceptibility (χ_{fd}), which corresponds to the percentage of susceptibility held by SP grains, was calculated as:

$$\chi_{fd} = 100\% \left(\frac{\chi_{465} - \chi_{4650}}{\chi_{465}}\right) \quad (5\text{-}1)$$

5.2.4.2 Magnetic Hysteresis

Room temperature hysteresis loops, which depict the induced magnetization of a substance in response to an applied magnetic field of varying strength, were generated for Specimen Set #1. How easily magnetic grains respond to an external field (by changing the direction of their magnetization parallel to that field) indicates the stability of the magnetic grains and their ability to carry a remanence. These loops can also be used to interpret mineralogical characteristics of the material, including the concentration of ferromagnetic material and average magnetic domain state behavior. Magnetic domains are regions of uniform magnetization within a magnetic particle or grain and are related to their size and shape. Ideally, for paleointensity experiments specimens would contain small elongated magnetic grains, approximately 30 to 100 nm for pure magnetite, for example [*Dunlop and Özdemir*, 2007], and display non-interacting single domain (SD) behavior where all the magnetization in a grain lies in one direction. SD grains carry a strong stable remanence and are ideally suited to archaeomagnetic experiments; however, perfect SD grains are rare in nature and

remanence is ultimately affected by grain size, shape, and magnetic interactions [*Day et al.*, 1977; *Butler*, 1992; *Dunlop and Özdemir*, 1997; *Muxworthy*, 2003]. Instead, most materials used for paleointensity experiments display a range of magnetic domain states, from very small SP grains (<30 nm) to large multidomain (MD) grains (>10-20 μm).

Day plots [*Day et al.*, 1977] are often used to display the general domain state in specimens based on hysteresis measurements (Figure 5-3). While the Day plot parameters are based on specific grain sizes and compositions, the plot can still be used as a first order determination of specimen suitability for paleointensity measurements. Hysteresis measurements indicated that all Tell Mozan specimens generally fell in the pseudo-single domain (PSD) range (~100 nm to 10-20 μm for pure magnetite), which appears typical of materials made of levigated or refined clays used in ceramics. PSD grains display SD-like qualities under archaeomagnetic experiments, but may also contain a proportion of larger MD grains, which do not carry a stable remanence. Hysteresis loops were measured on a Princeton Applied Research Vibrating Sample Magnetometer (VSM) from 0 to 1 tesla (T) with a nominal sensitivity of 2×10^{-8} Am^2.

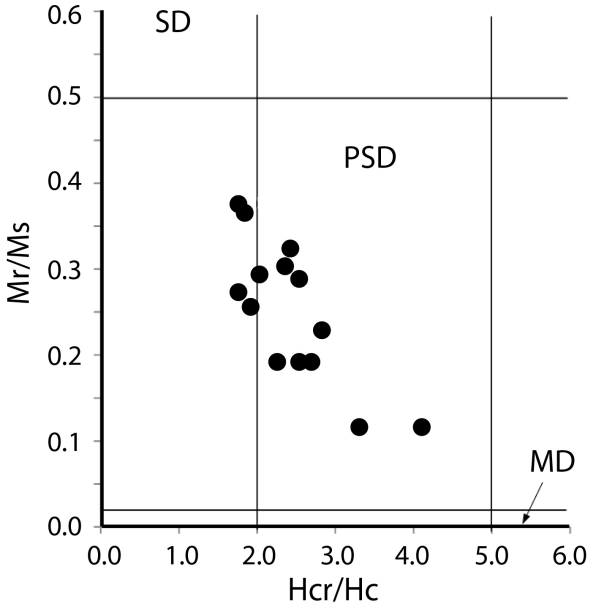

Figure 5-3 Day Plot of Tell Mozan Samples

Magnetic domain state or grain size distribution of Tell Mozan samples. SD is single domain, PSD is pseudosingle domain, and MD is multidomain.

5.2.4.3 Alternating Field (AF) Demagnetization

While archaeointensity methods work best on samples that carry a single magnetic remanence, most geologic and archaeologic materials are capable of recording more than one component of magnetization. This frequently occurs in cooking vessels that are reheated to a lower temperature than the initial kiln firing. The result is multiple components of remanence in different directions and/or intensities that affect the total NRM. These secondary components are usually minor and their effects can often be eliminated from final intensity calculations. To ascertain which samples, if any, contained more than one component of magnetization, the NRMs of specimen Set #1 were demagnetized (prior to hysteresis measurements) in a stepwise alternating

field (AF) from 2.5 to 170 mT using the 2G LC. Analysis of vector endpoint diagrams, which display the directional decay of remanence during demagnetization (see insets of Figure 5-4 for examples), indicated that all Tell Mozan samples contained only weak secondary components that were removed quickly at low fields. The demagnetization spectra generated for each sample were also used to calculate their median destructive field (MDF), which is the field strength required to demagnetize half of the NRM. An elevated MDF value indicates that the sample's magnetic mineral assemblage contains a higher fraction of SD or PSD grains.

5.2.5 Archaeointensity Methods

5.2.5.1 Thermal Analysis

Because all pottery samples were magnetically unoriented (not found in their original firing position), only the strength or intensity of the ancient field could be determined. All archaeointensity experiments were conducted at the Institute for Rock Magnetism at the University of Minnesota in a shielded room with a background field less than 200 nT. Archaeointensity data were obtained using the IZZI protocol of Tauxe and Staudigel (2004), a modification of the Thellier-style double heating method [*Thellier and Thellier*, 1959]. This method involves repeated heating and cooling of a specimen over successive temperature intervals, where each temperature step (T_i) demagnetizes a portion of the NRM held by grains whose blocking temperatures are $<T_i$ and replaces it with a laboratory or partial thermal remanent magnetization (pTRM) created with a user-specified field strength. The ancient magnetic field intensity can be

determined in materials that contain SD-like magnetic grains using the following relationship (simplified based on Thellier laws of SD behavior):

$$\boldsymbol{B_{anc} = \left(\frac{M_{NRM}}{M_{lab}}\right) B_{lab}} \tag{5-2}$$

where B_{anc} is the unknown ancient field intensity (B), B_{lab} is the laboratory-applied field, M_{lab} is the laboratory-acquired magnetization, and M_{NRM} is the original NRM of the specimen.

Three unaltered specimens from each sample were heated in air using an ASC Model TD-48SC Thermal Demagnetizer Furnace from 150˚C to a maximum of 650˚C and then fan-cooled to room temperature. In-field steps were performed at 30μT. Remanent magnetization was measured after each heating step with the 2G LC. Ideally, heating steps should be chosen such that the percentage of pTRM gained is the same as the NRM lost after each temperature interval (distributed across a minimum of 5 temperature intervals). Temperature intervals that are too large may remove the majority of remanence so quickly that paleointensity estimates are inaccurate. Conversely, temperature intervals that are too narrow can be too time-consuming. In this study, three specimens from each sample were heated in 25˚C intervals beginning at 150˚C and continuing to 650˚C, or until <5% of the NRM remained. Each heating cycle was applied such that specimens were first warmed to 20˚C below T_i, held at this temperature for 10 minutes, then slowly heated to T_i where they were held for 15 minutes before being fan-cooled to room temperature. This cautious approach to

heating allowed us to avoid extreme heat differentials with the samples that may have caused them to fracture and avoid overshooting the temperature set points.

To identify mineralogical changes and the effects of multidomain grains during the procedure, pTRM checks [*Coe et al.*, 1978] and pTRM tail checks [*Riisager and Riisager*, 2001], respectively, were performed every other step starting from the third temperature interval. These checks involve reheating the specimen to a previous lower temperature interval to see if the pTRM gained at that blocking temperature is repeatable.

5.2.5.2 Correction for Magnetic Anisotropy

The direction of magnetization in archaeological ceramics can be highly anisotropic depending on the method of fabrication. Wheel-thrown pottery is particularly susceptible to such effects, as the preferential alignment of clay platelets and the shape of magnetic grains can alter the acquisition of magnetization during stepped heating procedures [*Rogers et al.*, 1979; *Aitken et al.*, 1981]. To quantify and correct for this effect, the anisotropy of anhysteretic remanent magnetization (AARM) was calculated as a second rank tensor for each specimen in Set #1 and then used to correct the paleointensity data accordingly. AARM is qualitatively similar to a TRM in that it is a magnetization acquired in response to a stable applied field in an environment with progressively decreasing amounts of randomizing energy. However, the energy in an ARM arises from rapidly fluctuating magnetic fields rather than thermal energy, thus, AARMs do not generate the same thermochemical alteration in a

sample that is often associated with a TRM. Prior to AARM experiments, specimens were completely demagnetized at room temperature along their X, Y, and Z-axes using the 1.1 T AF demagnetization function on the VSM. Samples were further AF demagnetized along all axes in a 200 mT field with a 0.01 mT decay rate using a Precision Instruments D-2000 DTECH AF Demagnetizer (DTECH). Each specimen's demagnetized state was measured using the SRM. The specimens were then given an ARM using a 30 μT DC biasing field and a 150 mT AF demagnetization field with a 0.01 mT per half-cycle decay rate on the DTECH. ARM intensities and directions were measured on the SRM and the procedure was repeated along all six coordinate axes (±x, ±y, ±z).

5.2.5.3 Cooling Rate Correction

The difference between laboratory cooling and natural kiln cooling rates can also alter the magnitude of a TRM, with slower cooling rates resulting in a higher TRM when more SD sized grains are present [*Dodson and McClelland-Brown*, 1980; *Halgedahl et al.*, 1980; *Yu*, 2011; *Biggin et al.*, 2013]. To correct for this cooling rate effect, one previously heated specimen from each sample was heated to 600˚C and cooled to room temperature three times: first at a "fast" laboratory cooling rate of ~60 minutes (T1), then at a slower cooling rate of 24 hours (T2) at ~25˚C per hour, to approximate kiln cooling, and then again at the fast rate (T3). The addition of a second fast cooling cycle allows for the identification of any mineralogical changes that might be occurring during successive heating. The ratio of the average of the fast cooling rates and the slow cooling is the cooling rate correction (F_c) calculated as:

$$F_c = \frac{\left(\frac{T1 + T3}{2}\right)}{T2} \quad (5\text{-}3)$$

The initial thermal demagnetization of the samples revealed that most of the remanence was carried by magnetite and titanomagnetite, or their partially oxidized equivalents (Curie temperature ≤580˚C). Therefore, by cooling the specimens from 600˚C we can determine the cooling rate effects on the minerals holding the primary remanence. The difference in TRM intensity between the two fast cooling rate steps was less than 5% for all samples with the exception of one (sample TM51 at 6.4%). The majority of samples also displayed little difference (less than 9%) between slow and fast cooling rates, with the exception of sample TM40 (12%), an indication that PSD grains carry the majority of remanence in most specimens [*Yu*, 2011]. Final F_c values can be found in Table B-5, Appendix B, and the correction was used in final intensity determinations.

5.2.6 Final Selection Criteria

As outlined in section 5.2.5.1, the final ancient field intensity recorded by a specimen can be determined from the product of the laboratory field and the ratio between the natural (NRM) and laboratory remanence (pTRM). This ratio is the absolute value of the slope of a normalized Arai plot [*Nagata et al.*, 1963], which shows a specimen's remaining NRM on the y-axis versus the pTRM gained on the x-axis as the sample is heated in successive steps in a known laboratory field (Figure 5-4). The

choice of which temperature steps to include in the ancient intensity calculation can be subjective, and requires the consideration of secondary remanence and multidomain contributions. To make such analyses more objective, the best-fit line of the data (bounded by a series of temperature intervals) is typically subjected to a number of selection criteria to ensure that only the highest quality intensity data are accepted (see Paterson et al., (2014) for a summary of current paleointensity statistics). Intensity results generated for each specimen in this study were subjected to the following five acceptance criteria:

1) A Deviation Angle (DANG) of <5˚ (the angle between the best-fit line of the directional data used in the slope calculation and the best-fit line from the origin through the center of mass of the directional data as represented in the vector endpoint diagram) [*Tauxe and Staudigel*, 2004].
2) A maximum angular deviation (MAD) of <10˚ (representing the variance of the points within a particular temperature interval used to define the direction) [*Kirschvink*, 1980].
3) An f_{VDS} value of >0.8 (fraction of the total NRM used to calculate the slope of the line normalized by the vector difference sum ($_{VDS}$) of the zero field demagnetization data) [*Gee et al.*, 1993]. The VDS of the magnitudes between successive demagnetization steps more closely estimates the actual total NRM by aligning all remanence components in the same direction. A smaller f_{VDS} value indicates multiple components of remanence.
4) A mean difference ratio (Mean DRAT) value of <10% (the average

difference between the pTRM and pTRM checks normalized by the best-fit line [*Selkin and Tauxe*, 2000], which is an indication of alteration during heating.

5) A mean multidomain (Mean MD) value of <5% (here calculated as the average of the absolute difference between pTRM and pTRM tail checks normalized by the best-fit line of the zero-step NRM data) indicating the percent contribution from multidomain grains.

If a specimen failed two or more criteria it was immediately rejected. If a specimen failed only one of the selection criteria, the result of that criterion was scrutinized and compared to the strength of the other criteria before determining if the specimen should be rejected. For example, specimen TM09C (see Figure 5-4) failed the Mean DRAT test by only 8%; however, the Arai plot displayed a prominent dip or concave appearance, indicating MD behavior or significant overlapping remanence contributions. Therefore, this specimen was rejected. A minimum of two specimens (out of three) per sample needed to pass all five of the above criteria for the sample to be accepted. Archaeointensity determinations and paleointensity statistics generated for each specimen are listed in Table B-5, Appendix B. Criteria results are listed in Table B-4.

5.2.7 Archaeointensity Results for Tell Mozan

Of the 42 specimens used in archaeointensity experiments, 38 passed the acceptance criteria for a 90% success rate in final intensity determination. Specimens

TM64C and TMm04C failed more than one criteria and were immediately rejected. Specimen TM09C failed only one criterion (Mean DRATS) but also displayed a concave Arai plot (Figure 5-4) indicating possible MD contribution to magnetization and a disproportionate gain in pTRM to NRM lost, suggesting that the total NRM may not have been the result of the original firing. This specimen was rejected. Specimen TMmds01D failed the Mean MD criterion, which was significantly larger than all other specimens. Given that only 11 of the temperature steps were used for the best-fit line, it was determined the results for this specimen were poor and it was also rejected. Specimen MD35C failed the Mean DRAT criterion by only 4%; however, results for the remaining criteria were strong enough that we felt this specimen should be accepted in final intensity calculations. Therefore, the final intensities for samples TM09, TM64, TMM01, and TMm04 were calculated on the average of only two specimens each.

Average intensity results for each sample, corrected for anisotropy and cooling rate, are presented in Table B-2, Appendix B, along with their corresponding archaeological phase dates and the virtual axial dipole moment (VADM), which is the estimate of the strength of the magnetic dipole aligned with the rotational axis that would generate the ancient intensity observed at specific location. Final intensity results and error rates are based on a weighted average of the specimens for each sample. Individual results from each sample were kept separate to recognize variability or concurrence of intensity within each phase and to identify unusual intensity values that might be the result of artifact contamination between phases.

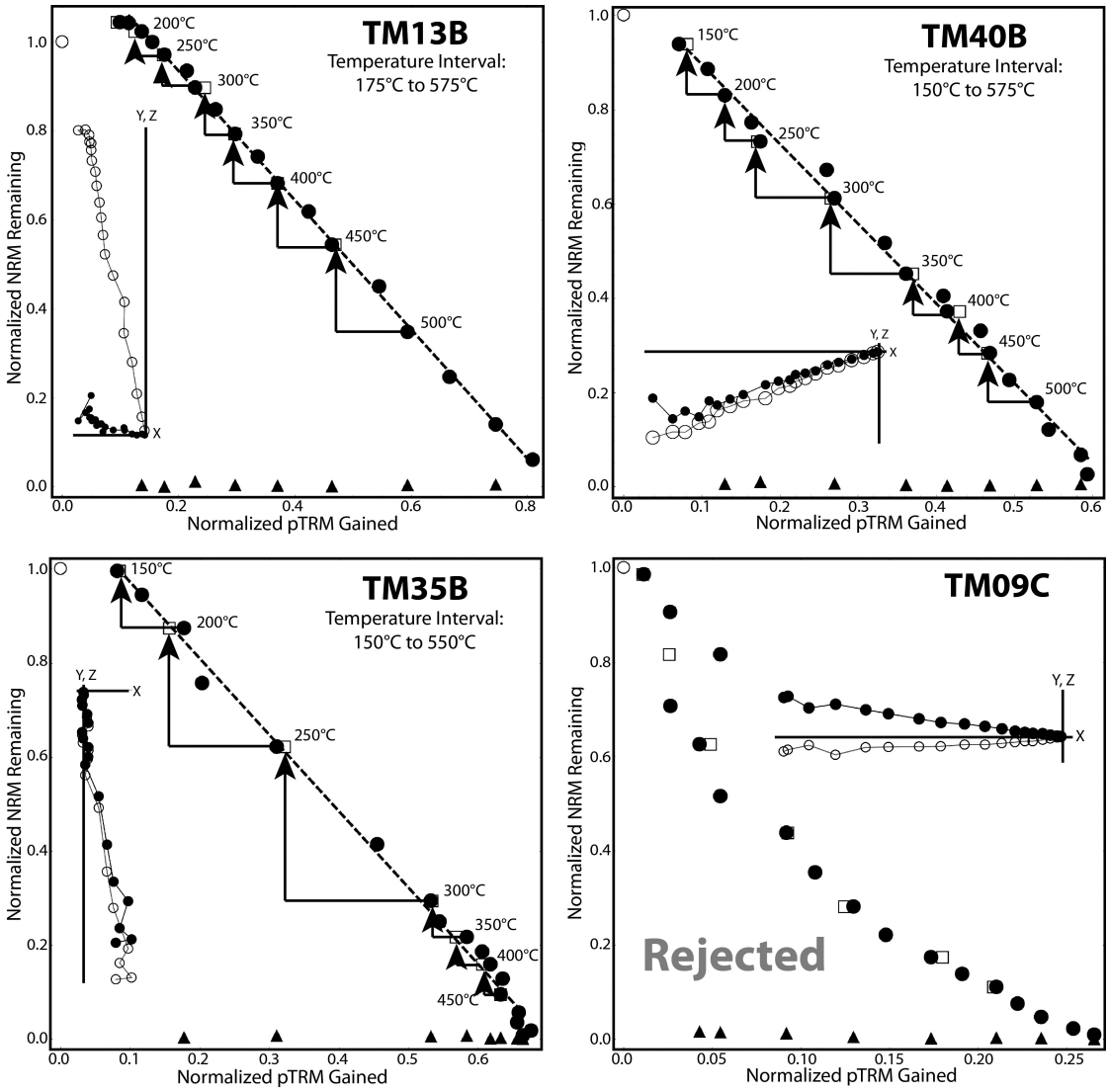

Figure 5-4 Representative Arai Plots for Tell Mozan

Representative Arai plots and vector endpoint diagrams (inset) for Tell Mozan samples. Closed circles (open squares) on Arai plot are in-field steps (pTRM checks). Closed triangles are pTRM-Tail or multidomain (MD) checks. Dashed line represents the temperature interval used in slope calculation to estimate the paleointensity. Inset vector endpoint plots are based on specimen coordinates and show convergence to the origin and one major component of remanence for all specimens.

Results from this study are juxtaposed with existing regional archaeointensity data for Syria, Israel, Jordan, Egypt, and Turkey in Figure 5-5 [*Aitken et al.*, 1984; *Walton*, 1986, 1990; *Hussain*, 1987; *Odah et al.*, 1995; *Odah*, 1999; *Genevey and Gallet*, 2003; *Gallet and Le Goff*, 2006; *Gallet et al.*, 2006, 2008, 2014, *Ben-Yosef et*

al., 2008, 2009; *Gallet and Al-Maqdissi*, 2010; *Shaar et al.*, 2011; *Ertepinar et al.*, 2012]. Regional data were compiled from the GEOMAGIA50 online database [*Donadini et al.*, 2006; *Korhonen et al.*, 2008] or the individual study if not available online. Regional data chosen for the base curve were constrained to those archaeomagnetic studies that employed the IZZI protocol or other double heating methods, which applied pTRM checks. To include only the highest quality data for the base curve, the regional data were further reduced to include only those studies applying some form of anisotropy correction, with two exceptions: 1) intensity data from metal slags, where no correction was necessary [*Ben-Yosef et al.*, 2008, 2009; *Shaar et al.*, 2011], and 2) recent high-quality results from studies where anisotropy was considered negligible due to selective alignment of the samples during measurements [*Gallet et al.*, 2008, 2014; *Gallet and Al-Maqdissi*, 2010; *Ertepinar et al.*, 2012].

In Figure 5-5, regional data points (gray open circles) represent average archaeointensity vs. archaeological date. These dates are derived from relative dating techniques such as pottery seriation, stratigraphy, and/or textual evidence. Black open squares represent average archaeointensity results where archaeomagnetic samples were calibrated using radiocarbon-dated strata [*Walton*, 1986; *Ben-Yosef et al.*, 2008, 2009; *Shaar et al.*, 2011]. The purple dashed line is the CALS7K.2 global paleomagnetic field model generated using archaeomagnetic full vector and lake sediment data for the past seven millennia [*Korte et al.*, 2005]. This model was chosen for comparison as it most closely captures the low-frequency paleointensity trends for the time period in question. The CALS10k.1b model [*Korte et al.*, 2011] covering the past 10 ka has

superseded this model; however, it is controlled by sediment data and tends to strongly smooth the curve when compared to such a narrow time interval, therefore it was not included here. It should be noted that the CALS7K.2 model also underestimates the dipole moment, particularly for the period around 1000 BCE.

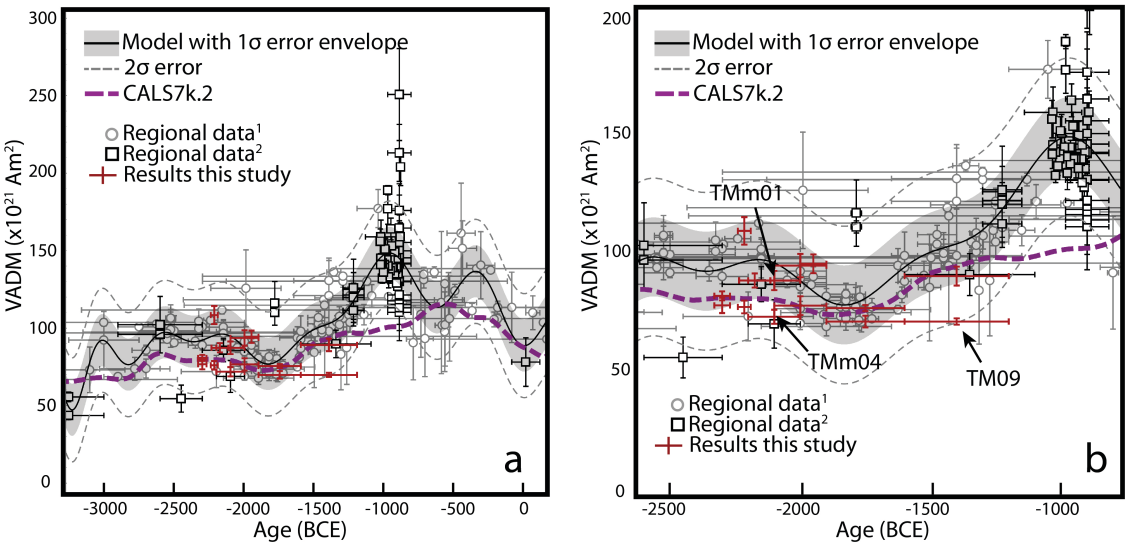

Figure 5-5 Regional Curve of Field Intensity for the Near East

Regional curve (a) of field intensity for the Near East for the Bronze and Iron Ages as modeled in this study. Regional data[1] are those intensities calibrated with traditional archaeological dating techniques, regional data[2] are those intensities calibrated with radiocarbon dating (see article text). (b) Close-up of Mozan intensity results.

Figure 5-5 also illustrates a new regional curve model based on a 25th order polynomial fit of the high-quality regional data. A 25th order polynomial was selected because it produced the lowest residual standard deviation without introducing spurious features in the reference curve that were unsupported by data. In essence, it captures the major intensity trends while eliminating the contributions from outlying data points.

The strengths of the ceramic seriation ages for Tell Mozan were confirmed if the intensity results correlated with the model within one standard deviation (σ) (represented by the shaded region about the line). Figure 5-5b focuses in on the region of the curve representing the Tell Mozan results. From this figure, it can be seen that all samples fell within 2σ of the model (dashed line), with the majority of intensities from Phases 1 through 5 (2334-1600 BCE) falling within 1σ.

Sample TM09, from Phase 6 (1600-1200 BCE), yielded a paleointensity estimate with very low uncertainty but fell well outside the 1σ confidence interval. Three interpretations of this result may apply. First, the actual age of this sample may be closer to its oldest possible archaeological age (1600 BCE as defined by the phase) in order to correspond with a period of intensity minimum that occurred around 1800 BCE. Second, this sample may record an extension of the regional intensity minimum into the first part of the 15th century BCE for the northeastern portion of Syria. Third, this sample may be simple contamination from Phase 5. We favor this final scenario as the most likely explanation as there was no documented feature association for the samples from Phase 6, the style of pottery is similar to those found in Phase 5 deposits, and the paleointensity estimate for TM09 is identical to that of TM14 and nearly identical to TM13, both from Phase 5. Sample TMm04 also falls just outside the 1σ error envelope. Upon reexamination of the feature association, it was determined that this sample was from a pit-like feature that cut down through 4b to 3a strata but contained primarily materials from Phase 3b/4a. Therefore, this sample could quite easily be a slightly younger contamination from Phase 4a/4b or incorrect phase

association in the database. Based on these assessments, both of these samples were ultimately rejected as representative intensities for their time period.

5.2.8 Discussion

From Figure 5-5, it is clear that our results display somewhat lower archaeointensity measurement uncertainties than previous studies, due in part to detailed methodology and strict selection criteria. Additionally, we have plotted each sample (from independent vessels) separately. Some of the regional results are from studies that have averaged multiple samples within a phase, which can result in high intensity uncertainties. Because the magnetic field is dynamic and fluctuates yearly, variability in intensity across broadly defined phases would be expected. Reporting only the mean of archaeointensities for a phase may not capture the mode in the data and result in a curve with larger standard deviations. Individual sample results from Mozan were plotted separately on the model to recognize this variability and highlight the differences that can occur in even relatively short phases. This also allows for the scrutiny of possible discrepancies in artifact association at the site level. For example, if only the average of the Phase 3b/4a (2192-2004 BCE) samples were considered, the resulting intensity would more closely match the curve. By keeping the results separate in our initial analysis of the results, we can see that sample TMm04 may be slightly younger than TMm01, and is most likely the result of an artifact from Phase 4b being displaced from its original depositional context.

The results of samples TMm04 and TM09 highlight the importance of assessing

the strength of the original archaeological interpretation of the artifacts or features themselves. For example, by plotting intensity results for each sample separately, we were able to identify samples that appear to be in disagreement with their defined chronology. In one instance, this likely reflects contamination of strata from the re-use of previous occupational materials in later construction, a typical practice at ancient tells in the Near East. However, this object may also represent an item that was used long after the original firing, such as an heirloom object or long-lived storage vessel passed down through the generations. The careful analysis of individual sample results highlights the importance of increasing sample size per phase. Ultimately, the combination of relative and absolute dating techniques, detailed site records, and strict sample selection is necessary for the construction of an accurate site chronology.

The regional trend calculated in Figure 5-5 also assumes that the previously published data are relatively accurate; however, the dates used to fix the regional intensity values are themselves based primarily on relative archaeological chronologies. Only four of the archaeomagnetic studies represented in Figure 5-5 utilized radiocarbon dating along with stratigraphic seriation to date their samples [*Walton*, 1986; *Ben-Yosef et al.*, 2008, 2009; *Shaar et al.*, 2011], which in some cases results in narrower chronological association when compared to the other regional data. If only radiocarbon dated studies were considered, they would not supply enough data to create a meaningful intensity curve. If radiocarbon or other absolute dating is not available or utilized in cross calibration, then the archaeologically defined dates will be based solely on relative dating techniques, such as pottery seriation, which is common in Near East

archaeology. In many cases, phases or site dates are broadly defined, resulting in equally broad archaeomagnetic results. For example, Phase 6 at Tell Mozan contained 400 years of deposits representing occupations that have not yet been as thoroughly evaluated as the first five phases. As many of the regional intensity studies used in the base model are a decade old or more, a reassessment of their associated chronologies and an update of the online paleointensity databases with more recent results may be in order.

Finally, it should be noted that the standard deviation around the curve in our model is constant. As can be seen, certain periods are better represented by archaeointensity data than others. An alternative approach would be to apply a moving window average to capture the variability in the data set [*Sternberg and McGuire*, 1990; *Kovacheva and Toshkov*, 1994]. Here we apply a 300-year moving window average in 20-year increments to the regional data (Figure 5-6b) to compare against our polynomial model (Figure 5-6a) and expand the models out to 800 CE. Both intensity models (bold lines) are similar and capture the intensity maxima at ~900 and ~450 BCE and the relative plateau between ~2600 and 2200 BCE. The moving window model does appear to minimize the standard deviation in periods with more data; however, it also displays slightly more noise, particularly around 2800 BCE and 50 BCE where there is a lack of data. Figure 5-6c displays the calculated difference between the two curves. Here we see very minor variance between the models' VADM values, with only $\pm$ 1 x10^{21} Am^2 for dates between ~3000 and 50 BCE, indicating both models generate a similar average intensity curve. A comparison of the difference between the

standard deviations in the models (Figure 5-6d) highlights where there is a great deal of archaeomagnetic data available (area above the horizontal line) and where more data are needed (area below the line). Important to note is the area between ~1000 and 800 BCE in Figure 5-6d (shaded) where there appears to be plenty of data, but the broad variability in that data results in a larger standard deviation for the moving window model. These data are represented by extremely narrow chronological associations and two short-lived spikes in intensity. A 300-year moving window average is not appropriate to capture such short-period geomagnetic behavior. From these two model comparisons, we can see that more data are needed for the first millennium BCE but that both model curves are relatively similar.

An alternative approach is to apply a cubic spline model to the regional data; however, this type of model suffers from the same problems as the moving window model in that they both have time-dependent errors, which are more difficult to broadly disseminate. The polynomial model provides a single continuous function that sufficiently captures the same geomagnetic behavior as the standard moving window model and eliminates the effects of uncertain data points, providing a smoother curve more suitable for archaeomagnetic dating. We argue that the polynomial-based reference curve is more useful and accessible to the archaeological community because the model and its associated error can be readily reproduced by other researchers for comparison (see Appendix B Figure B-3 for polynomial coefficients).

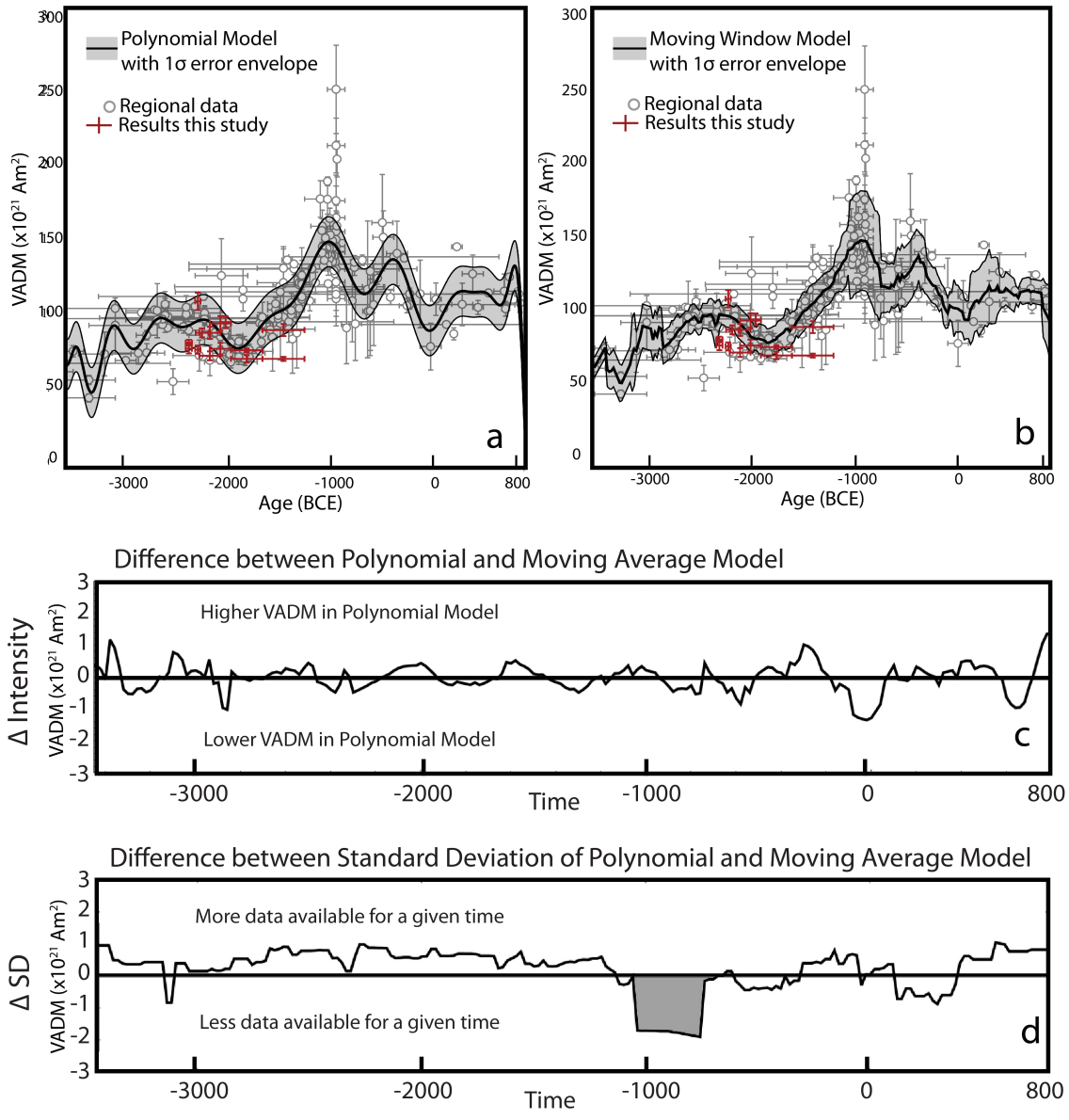

Figure 5-6 Comparison of Polynomial Models

Comparison of polynomial model (a) generated from this research and a 300-year moving window average model (b). Difference between the two models (Polynomial minus Moving Average) (c) and difference between their standard deviations (d). The gray shaded region in (d) represents a region where data are abundant but have such narrow chronologies that they are not captured by the moving window model (see text).

5.2.9 Conclusion

Archaeomagnetic measurements were conducted on fourteen pottery samples from seven well-defined and constrained strata dated between 2334 and 1200 BCE at Tell Mozan, Syria. Our results are plotted against prior archaeointensity data for the Near East obtained from recently published studies using similar paleointensity measurement and correction techniques. Initial sample selection and intensity measurements underwent strict acceptance criteria before estimating final archaeointensity, which resulted in a 90% success rate using the detailed paleointensity techniques outlined. We also introduce a new archaeointensity model for the region derived from a 25^{th} order polynomial fit of the regional data and spanning the first three millennia BCE. This model reduces the standard deviation of the residuals about the best-fit line of the data, minimizes the effects of outlying data points, and provides a smooth reference curve suitable for dating artifacts of unknown age. We obtain an 86% concurrence between the archaeologically defined ages and the new model within 1σ.

The results of our study highlight three important considerations for future archaeomagnetic research. First, consistent measurement techniques and strict acceptance criteria result in lower error rates for archaeomagnetic measurements. Second, the application of rigorous sampling criteria can significantly reduce a large sample population, requiring that more samples from each site phase be taken; however, the relatively high NRM held by most of the pottery samples in this study indicates that specimens smaller than 8 cm^3 could be utilized, which would allow researchers to

increase their overall sample populations. Finally, we propose that future archaeointensity results are always uploaded to the regional GEOMAGIA50 database by individual sample (or by individual heated object) for each time period they represent, instead of the reporting only an average of multiple samples from a specific phase. This would allow for a more detailed interpretation of the data, such as identifying modes in intensity distributions. This study adds to the literature confirming the applicability of archaeomagnetism as an independent and complementary tool in constructing archaeological chronologies, provides a new regional reference curve model for archaeomagnetic dating, and contributes twelve new results to the increasingly dense paleointensity data for Syria and the greater Near Eastern region during the Bronze Age.

5.3 Adjustments to Previous Methods

5.3.1 Thellier Method

The general Thellier double heating procedures outlined above were used in this research with the following minor adjustments:

1) Pottery samples were cut into smaller specimen sizes (1cm x 1cm) due to their strong NRM.
2) Because tabuns tend to crumble during heating experiments, specimens were placed in quartz glass tubes, the ends packed with quartz wool, and then fixed with potassium silicate.

3) To ensure the most accurate intensity determination, a laboratory field of 50 μT was chosen for the Thellier-Thellier and cooling rate experiments to more closely match the estimated Iron Age field strength (although some samples were initially run at 30 μT prior to this change). See discussion, Chapter 7.

4) Archaeointensity determination and statistical analysis was performed using the PmagPY *Thellier GUI* open-source software program accessible through the earthref.org website [*Shaar and Tauxe*, 2013].

5) New selection criteria designed to account for multidomain effects on Arai plots (outlined below) were used, thus, the pTRM tail-checks were eliminated during Thellier heating procedures.

6) Cooling rate experiment temperatures were ran at two different temperatures, 550˚C and 625˚C for comparison and evolution check was set to 10% (see Section 6.1.2 for details).

5.3.2 Criteria Changes

The archaeointensity selection criteria for this research follow those suggested by [*Shaar et al.*, 2016] and further outlined in [*Paterson et al.*, 2014]. Data for all specimens were analyzed using the PmagPY *Thellier GUI* program, an open source paleointensity processing program available through earthref.org website [*Shaar and Tauxe*, 2013; *Tauxe et al.*, 2016]. This program allows for manual or auto-interpretation of paleo and archaeointensity data given a user defined set of selection

pass/fail criteria. All archaeointensity results for this research were determined using the auto-interpretation function of the program. The five selection criteria outlined in section 5.2.6 were adjusted to the following:

1) The minimum number of in-field/zero field combination data point steps and minimum number of pTRM checks from the Arai plot used to determine the best-fit line for archaeointensity determination were set to 4 and 2, respectively.

2) The DANG and MAD angles were set to < 10%.

3) A fraction of remanence parameter (FRAC) with a threshold value of 0.70 was used in place of the f_{vds} parameter (with the exception of one sample, see results section), which tends to amplify the VDS of a zigzagged Zijderveld plot and underestimate the quality of the Arai plot [*Shaar and Tauxe*, 2013]. FRAC is the VDS of the selected component on the Arai plot divided by the total VDS:

$$\boldsymbol{FRAC} = \frac{\sum_{i=start}^{i=end-1} |\boldsymbol{NRM}_{i+1} - \boldsymbol{NRM}_i|}{\sum_{i=0}^{i=n_0-1} |\boldsymbol{NRM}_{i+1} - \boldsymbol{NRM}_i| + |\boldsymbol{NRM}_{n_0}|} \quad (5\text{-}4)$$

where start and end are the first and last points of the chosen segment, NRM_i is the NRM vector at step i, and n_0 is the total number of data points in the Arai plot.

4) To minimize the number of statistics and account for alteration and multidomain contributions, a scatter statistic (SCAT) based on the threshold value of β (0.1) was used (see Shaar and Tauxe (2013) for

illustrated description of how this criteria is calculated and applied). The SCAT criteria, which yields either a PASS or FAIL, replaces the DRAT and MD check criteria.

A minimum of two specimens per sample needed to pass all above criteria for the sample archaeointensity to be determined. Similar to the previous Syrian study, all sample intensities were determined by taking the weighted average of the representative specimens.

6 Results

6.1 Overview

In total, 220 specimens were measured for archaeointensity (two to three replicate specimens per sample). Of these, 92 exhibited one primary component of remanence and passed all the selection criteria as outlined in section 5.3, a success rate of 43%. None of the Phase 4 samples from Khirbet Summeily passed the FRAC criteria. As this phase is critical to understanding the chronology at Summeily, the FRAC criteria was slightly altered by lowering from 70% to 60% for this sample only. This allowed for an additional two specimens from sample KS2348A to pass and provide at least one archaeointensity result for the phase. Specimen archaeointensity results (after AARM and CRC) were average as outlined in section 5.2.7.

Final archaeointensity determination at the sample level was further limited to those samples that had two or more replicate specimens pass criteria. As the viability of tabuns as archaeointensity recorders was of particular importance in this research, several samples from various locations on each tabun were sampled, resulting in an average of seven specimens per tabun. The final data reduction resulted in intensity results for 28 unique archaeological samples: 19 pottery sherds and 9 different tabuns. Table 6-1 displays the AARM and cooling rate corrected ancient field intensity (βa) in μT and Virtual Axial Dipole Moment (VADM) in ZAm^2 of these 28 artifacts by

location and absolute/relatively ascribed archaeological age (or phase).

Following is a brief summary of IZZI TRM results, comparison of cooling rate correction protocols, and final archaeointensity results for all sites. Rock magnetic characterization data for Khirbet Summeily can be found in Tables A-1 of Appendix A. Recently published archaeointensity results from the contemporary sites of Tel Megiddo and Hazor are used as primary comparisons and are highlighted in Figures 6.3 and 6.4 as filled grey circles [*Shaar et al.*, 2016]. Both sites were well dated both stratigraphically and with radiocarbon analysis. Archaeointensity results for these sites were obtained using similar protocols and criteria as those in this research.

6.1.1 IZZI TRM Results

Two different IZZI protocols were used during this research, one with a temperature interval of 25˚C from 150˚C to 600˚C and one where intervals were reduced to 15˚C from 450˚C to 575˚C. The first protocol was implemented to avoid deterioration of the tabun samples, as many were crumbly. Fortunately, by fixing tabun specimens in plaster or quartz glass tubes, most could be heated to 575˚C. Overall, the latter IZZI protocol, which focused on measuring remanence at higher blocking temperatures, produced the better intensity results. Arai plots for representative tabun and pottery samples are displayed in Figures 6-1 and 6-2, respectively.

Pottery samples that passed archaeointensity selection criteria (see section 5.2.6) primarily contained one component of remanence; however, several specimens that passed criteria (e.g. KS2369C, Fig. 6-2) did display minor directional variance at low

temperature intervals. Similar results were found with the tabun samples. These minor components of remanence were likely overprinting from low temperature reheating in their associated conflagration. Several tabun specimens also displayed a loss in pTRM at 575˚C, indicating the likely oxidation of magnetite to hematite. Since tabuns are usually used for baking bread, they typically would not be heated to temperatures above 500˚C.

An example of a pottery sample that failed archaeointensity experiments (KS2362B) is also included in Figure 6-2. This specimen contained two components of remanence with half of the total NRM held at high temperatures (>475˚C). Most of the specimens from Khirbet Summeily displayed a change in remanence direction around 350 to 450˚C, indicating the conflagration did not burn hot enough in certain portions of the structure to reset all of the original magnetization. For example, the fire in the Summeily Cult Room (Phase 3), which was of particular interest to the archaeological researchers, appears quite variable, with pottery specimens located near oil vessels (e.g. KSG24) being completely re-fired to high temperatures, while those located in the center of the room (e.g. KS710) displaying two remanence directions and a partial reheating to 350˚C. A similar problem occurred with pottery samples from Tel 'Eton, where most specimens displayed multiple components of remanence typical of low temperature reheating.

All of the tabun specimens from the Tel Burna displayed minor directional variation at low temperatures including the Cypriot pithoi vessel fragment from

TabunB01. Surprisingly, the pithoi also displayed a decrease in pTRM acquisition around 575˚C. It is possible that the vessel was never fully fired during its manufacture. The locally made clay fragments from TabunB02 did not display this alteration. The Tel Halif tabun specimens displayed similar alteration at 575˚C.

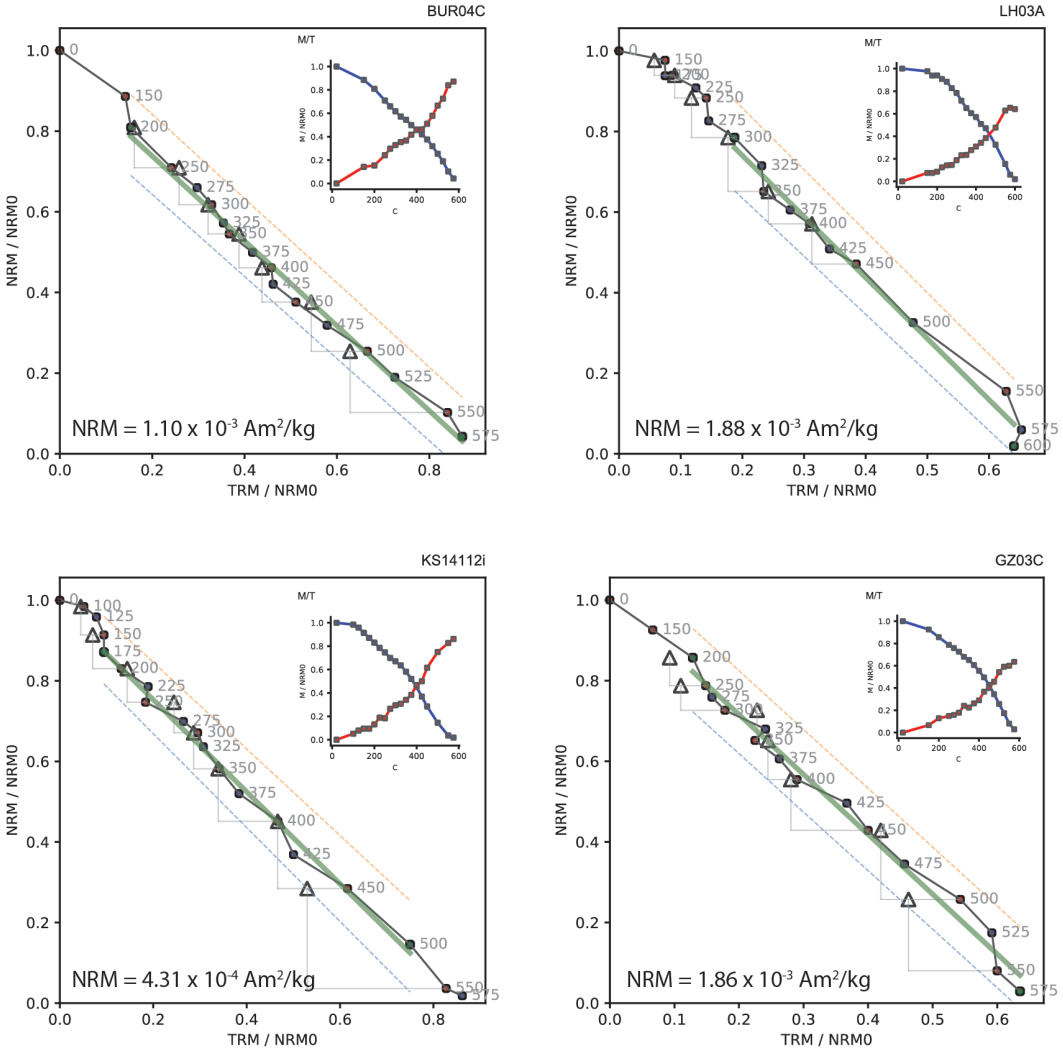

Figure 6-1 Representative Arai Plots for Tabun Specimens

Red circles, blue circles, and triangles in the Arai plot are "ZI" steps, "IZ" steps and pTRM checks, respectively. Light grey lines connecting to the pTRM checks indicate the temperature interval where the check was completed (i.e. step 400 was repeated at 450). The green line indicates the least squares line (slope) of the selected temperature interval used for intensity determination. The dashed orange and blue lines bounding the temperature interval are the graphical representation of the SCAT statistical parameter. If all temperature steps and pTRM checks fall with this area, the sample passes. Inset is the normalized moment to temperature plot showing the decrease in NRM (blue) and the increase in pTRM gained (red) for each temperature step.

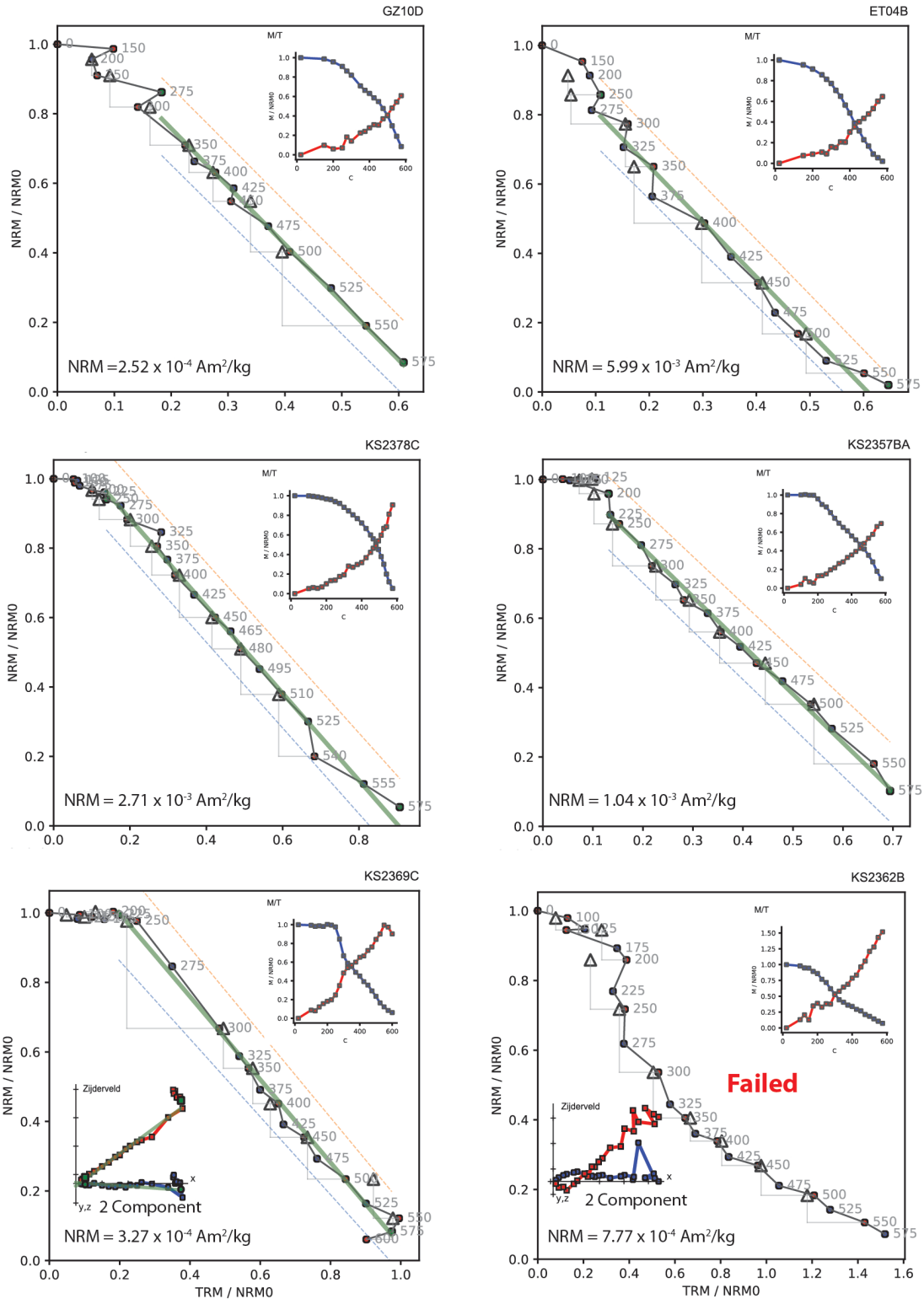

Figure 6-2 Representative Arai Plots for Pottery Specimens

See Figure 6-1 for description of Arai plot. Inset Zijderveld plots (KS2369C and KS2362B) are the x-y (blue) and x-z (red) projections of the NRMs in specimen coordinates.

6.1.2 Cooling Rate Correction Results

Two different protocols were used in this research to determine the ideal temperature for performing the cooling rate correction (CRC) experiment (see section 5.2.5.3 for cooling rate correction protocol and justification). Other researchers have performed the correction experiment at temperatures ranging from 450˚C to 700˚C, with no clarification as to the reasoning behind the temperature chosen. For example, a CR temperature of 600˚C was chosen for the Tell Mozan samples used to develop the procedures used here [*Stillinger et al.*, 2015]. Two specimens from 24 of the 28 samples that passed selection criteria underwent different temperature protocols to determine the best CRC experimental temperature and whether previously unheated specimens produced better results: one specimen (previously unheated) was heated to 550˚C and the second specimen (previously used in the IZZI TRM experiment) was heated to 625˚C. One or two additional previously heated specimens from some samples were also heated to 550˚C to compare the difference at that specific temperature. In total, 35 specimens were heated to 550˚C and 29 specimens to 625˚C. A single specimen was heated to 600˚C using the Mozan protocol. The percent evolution or change in TRM is used as a test to determine if alteration occurs during the multiple heating cycles during the CRC experiment. The % evolution is determined from the difference in TRM of the two fast heating steps:

$$\%\boldsymbol{Evol} = \left|\frac{\boldsymbol{TRM_{T1} - TRM_{T3}}}{\boldsymbol{TRM_{T1}}}\right| \quad (6\text{-}1)$$

In general, those specimens with an evolution of less than 5% are considered suitable and can be used for the CRC [*Genevey and Gallet*, 2002]. In this research any evolution less than 10% was considered successful and the corresponding correction value was applied to the AARM archaeointensity result.

Without regard to whether the specimens were previously heated or not, those heated to 550˚C displayed slightly lower cooling rate evolutions than those at 625˚C. Of the 35 specimens heated to 550˚C, only 17.1% failed the evolution test (> 10% evolution) versus 27.6% at 625˚C. However, when comparing specimens that had never been previously heated (CRC @ 550˚C) to those that had previously undergone multiple heating cycles during IZZI experiments (CRC @ 625˚C), the failure rate was the same (25%) and the previously heated specimens had far better low (<5%) evolutions (41.7% vs. 29.2%). For the few samples that had both unheated and previously heated specimens used in the 550˚C CRC experiment, there appeared to be no significant difference in evolution. In addition, the final CRC correction factors (Equation 5-3) calculated for all specimens with low (<5%) and slightly higher (5 to 10%) evolutions were similar for each sample, with less than 10% difference between specimens. All samples in this research had at least one specimen with an evolution less than 10%. Twenty-three samples had specimens with evolutions less than 5%. The final CRC factors were generally between 0.93 and 0.83, with an average of 0.88 or 12% correction (decrease) in final intensity applied to the AARM corrected archaeointensity results. The one exception was sample KS2369, which required a correction of 23%. Overall, these correction factors were slightly higher than for the

ceramics from Tell Mozan.

From these results, it appears that using previously heated specimens for the CRC experiment and heating them to between 550˚C and 600˚C will provide a suitable correction factor at a temperature range that captures the majority of the remanence used in archaeointensity determinations. Final CRC factors can be found in Appendix A, Table A-2.

6.2 Archaeointensity Results

Final archaeointensity determinations for each sample by location are reported in Table 6-1. Results and statistics at the specimen level can be found in Appendix A, Table A-2. Final archaeointensity (expressed as VADM) are plotted against data from nine previous studies in Figures 6-3 and 6-4 [*Genevey and Gallet*, 2003; *Gallet and Le Goff*, 2006; *Ben-Yosef et al.*, 2008, 2009; *Gallet and Al-Maqdissi*, 2010; *Shaar et al.*, 2011, 2015, 2016; *Ertepinar et al.*, 2012] with results from Megiddo and Hazor highlighted in gray filled circles. An additional four studies [*Gallet et al.*, 2006, 2008, 2014; *Stillinger et al.*, 2015] spanning the first three millennia BCE were used to construct a new NEAC model of secular variation for the Levantine Iron Age (~1300 to 600 BCE) based on a 300-year moving window average model shifted in 20-year increments. All thirteen studies contained high quality archaeointensity results for the region with similar protocols, criteria, and corrections as those used here. Regional data were compiled from the GEOMAGIA50 and Earthref.org websites.

Table 6-1 Archaeointensity Results

Location	Age (BCE) or Phase	Sample	Material	n	βa (μT) Corr	βa error	VADM (ZAm^2)	VADM Error
Tel 'Eton	734-701	ET04	Pottery	2	80.7	6.0	155.4	11.6
		ET05	Pottery	2	92.6	10.6	178.3	20.5
Tel Halif	734-701	LH06	TabunH03	2	61.3	4.0	118.1	7.6
		Multiple	TabunH02	6	66.3	4.2	127.8	8.1
Tel Gezer	833	GZ04	Pottery	3	56.0	2.1	107.2	4.1
		GZ05	Pottery	2	74.6	4.1	142.9	7.8
		Multiple	TabunGZ01	5	65.3	3.7	125.1	7.1
	925	GZ10	Pottery	2	78.9	5.1	151.0	9.8
	1208	GZ14	Pottery	3	40.7	1.9	77.9	3.6
		GZ15	Pottery	3	65.0	3.3	124.6	6.3
		GZ17	Pottery	2	47.7	2.4	91.3	4.6
		GZ20	Pottery	2	46.7	1.9	89.4	3.6
Tel Burna	1250 ±50	Multiple	TabunB01	6	43.2	1.4	83.0	2.7
		BUR04	TabunB02	3	46.1	1.9	88.5	3.7
Khirbet Summeily	2	KS1419	Pottery	2	59.1	6.3	113.5	12.1
		KS2357A	Pottery	3	66.5	4.4	127.8	8.5
		KS2357B	Pottery	3	61.1	1.6	117.5	3.0
		KS2378	Pottery	2	59.0	2.0	113.3	3.9
		KSMDS01	Pottery	3	60.5	2.8	116.2	5.4
		KSMDS04	Pottery	2	53.5	1.8	102.8	3.5
		Multiple	TabunKS01	2	45.6	1.4	87.7	2.6
	3	KSG24	Pottery	3	50.5	3.1	97.1	6.0
		Multiple	TabunKS02	6	45.1	2.7	86.6	5.3
	4	KS2348A	Pottery	2	26.5	0.8	50.9	1.5
	5	KS2369C	Pottery	3	47.2	1.8	90.7	3.5
		KS2371	Pottery	2	76.8	5.7	147.6	1.1
		KS2372	Pottery	3	72.8	3.6	140.0	7.0
		KS2373	TabunKS04	3	58.3	2.7	112.0	5.2

n = number of specimens passing archaeointensity criteria used for final intensity determination. Ba = AARM and cooling rate corrected (Corr) archaeointensity in μT. VADM = Virtual Axial Dipole Moment expressed in $Am^2 \times 10^{21}$.

6.2.1 Archaeointensity Results for Calibration Sites

The most recent archaeological time period for the calibration sites is the late 8th century, BCE, represented by Tel 'Eton and Tel Halif materials. Only two pottery

samples from Tel ‘Eton passed selection criteria. Both exhibited very high ancient field intensities (βa), consistent with the second spike in intensity for the late 8th century (734 BCE) as identified at Megiddo and Hazor [*Shaar et al.*, 2016] (See Figure 6-3). Sample ET05 had an archaeointensity value of 92.6 μT after all corrections (VADM of 178.3 ZAm^2), one of the highest recorded intensities for the 8th century BCE (without the cooling rate correction the sample’s intensity was 102.9 μT (VADM of 198 ZAm^2). The tabuns from Tel Halif exhibit somewhat lower intensities but still similar to those recorded at Megiddo and Hazor for this period. If the radiocarbon and archaeointensity interpretations of Megiddo and Hazor are correct, the conflagration at ‘Eton is likely the result of the 734 campaign of Tiglath Pileser III and not the 701 Sennecharib destruction as previously surmised. The results for Tel Halif could be interpreted as either 734 or 701 BCE. Results from these two sites are plotted in Figure 6-3 as 717 ± 17 BCE until further archaeological analysis can be performed on materials from the Sennecharib 701 BCE destruction, which are lacking in the region.

Tel Gezer provided the broadest chronological coverage, with materials from the late 13th through the late 9th century BCE. Stratum 7 samples (~ 833 BCE) display slightly lower intensities than Halif and Eton, similar to Hazor stratum VII and as predicted by the ARCH2k.1e global model. These results are a further indicator that there was a likely dip in field strength between the two Iron Age spikes. Gezer Stratum 8 (925 BCE) displayed a high intensity consistent with the intensity identified by other sites in the region. Pottery from the late 13th Century BCE at Gezer displayed a range of intensities, one consistent with other intensities in the region, and some slightly

lower, more consistent with the early 13th Century BCE (~1300 BCE). The tabuns at Burna from the same period display similar low intensity results, but are likely from the early 13th Century as the import of Cypriot wares ended in the early 12th Century [*Shai et al.*, 2015; *Shai and McKinny*, 2018]. Again, the lack of well-calibrated intensity data for the period between 1300 and 1050 BCE limits comparison with other results in the region.

The sample results within each stratum age for the calibration sites are relatively consistent with minor exceptions. The intensity for Tel Gezer's Stratum 7 (833 BCE) samples varied by as much as 15% from an average of 65.3 μT. As both pottery samples were found inside the tabun, these results highlight the variability in field intensity obtained from different materials that can occur in a single stratum. The relatively low intensity results for GZ14 and GZ20 compared to other pottery samples from Gezer Stratum 12 (1208 BCE) could also indicate that they are slightly older contamination artifacts, materials reincorporated into the floor structure.

6.2.2 Archaeointensity Results for Khirbet Summeily

The majority of Khirbet Summeily samples that passed archaeointensity criteria were from Phases 2 and 5. Phases 3 and 4 had only three passing samples. The final results from Summeily were analyzed using the *Chronomodel* software program [*Lanos and Lanos*, 2016], which applies Markov Chain Monte Carlo algorithms for sampling probability distribution of the data and presents results using Bayesian statistical inference. The *Chronomodel* age constraints ('bounds' in Table 6-2) were set to

slightly larger than the maximum and minimum ages defined by the archaeological research team (Table 5-2) to ensure that the age determinations were not overly biased by the relative chronology. The mean age and standard deviation of the four Summeily phases as identified by the *Chronomodel* software program (with a 95% Confidence Interval) are listed in Table 6-2.

Phases 2, 3, and 5 date within the expected archaeological relative ages using *Chronomodel*. The larger sample population sizes for Phases 2 and 5 provide results that are more sound. The Phase 3 destruction dates to approximately 935 ± 20 BCE, within the period of the Sheshonq 925 BCE campaign, as hypothesized. Phase 4 dates slightly older than estimated, closer to the age of Phase 5. It is important to note; however, that the limited number of samples for both of these phases (and the unusually low intensity value for Phase 4) may have biased the *Chronomodel* results. The rather low intensity value for Phase 3 is especially evident when comparing with Gezer Stratum 8, which definitively dates to 925 BCE. The results are markedly different (see Figure 6-4). However, previous intensity estimates by Shaar et al. (2011) and Ben-Yosef et al. (2009) also identified a number of lows in field intensity at Timna and Ken between 925 and 910 BCE. These results were slightly modified in a later publication [*Shaar et al.*, 2016]. Some of the Phase 2 samples at Summeily also display a low intensity similar to Phase 3.

Again, the general spread in the data from other sites for the 10th Century BCE is quite extensive and it is possible that the geomagnetic field experienced a number of

rapid intensity fluctuations with a reverse spike, or several intensity lows, between the two major intensity highs. For example, the other samples from Phase 4, which didn't pass all of the selection criteria due to slight data scatter, also displayed this unusual low intensity, and the ARCH3k.1e global model (purple line Figures 6-3 and 6-4), while outdated, does predict a significant drop in field intensity during the early 10th century.

Table 6-2 Chronology Results for Khirbet Summeily

Chronomodel Bounds[1]	***Estimated Relative Age***[2]	**Sample**	**βa (μT) Corr**	**βa Error**	**VADM (ZAm^2)**	**VADM Error**	**Phase Age (BCE)**[3]
Phase 2 (900-750 BCE)	*825-775 BCE*	TabunKS01	45.6	1.4	87.7	2.6	**825 ± 44**
		KS1419	59.1	6.3	113.5	12.1	
		KS2357A	66.5	4.4	127.8	8.5	
		KS2357B	61.1	1.6	117.5	3.0	
		KS2378	59.0	2.0	113.3	3.9	
		KSMDS01	60.5	2.8	116.2	5.4	
		KSMDS04	53.5	1.8	102.8	3.5	
Phase 3 (970-900 BCE)	*950-910 BCE*	TabunKS02	45.1	2.7	86.6	5.3	**935 ± 20**
		KSG24	50.5	3.1	97.1	6.0	
Phase 4 (1100-925 BCE)	*1000-950 BCE*	KS2348A	26.5	0.8	50.9	1.5	**1013± 51**
Phase 5 (1100-970 BCE)	*1025-970 BCE*	KS2369C	47.2	1.8	90.7	3.5	**1036 ± 38**
		KS2371	76.8	5.7	147.6	1.1	
		KS2372	72.8	3.6	140.0	7.0	
		KS2373/ TabunKS04	58.3	2.7	112.0	5.2	

[1] *Phase age limits/bounds used in estimating final dates with Chronomodel program*

[2] *Estimated relative age from archaeological analysis*

[3] *Posterior distribution phase date and standard deviation as determine from Chronomodel Bayesian analysis*

Finally, the results for Summeily Tabuns KS01 and KS02, both of which appear to have been completely reheated to a temperature above 575˚C, are very similar, with KS01 being significantly lower than the other samples from Phase 2. This may indicate that the tabuns are from the same period and that the stratigraphy at the site was incorrectly interpreted. Alternatively, since all of the tabuns at Summeily display slightly lower intensity results than the associated pottery from the same phase, this may indicate that the tabuns are not perfect recorders of intensity. The only other site where both tabun and pottery samples were taken from the same strata was Tel Gezer. In that instance, the tabun intensity value was midway between two pottery intensities found within the tabun.

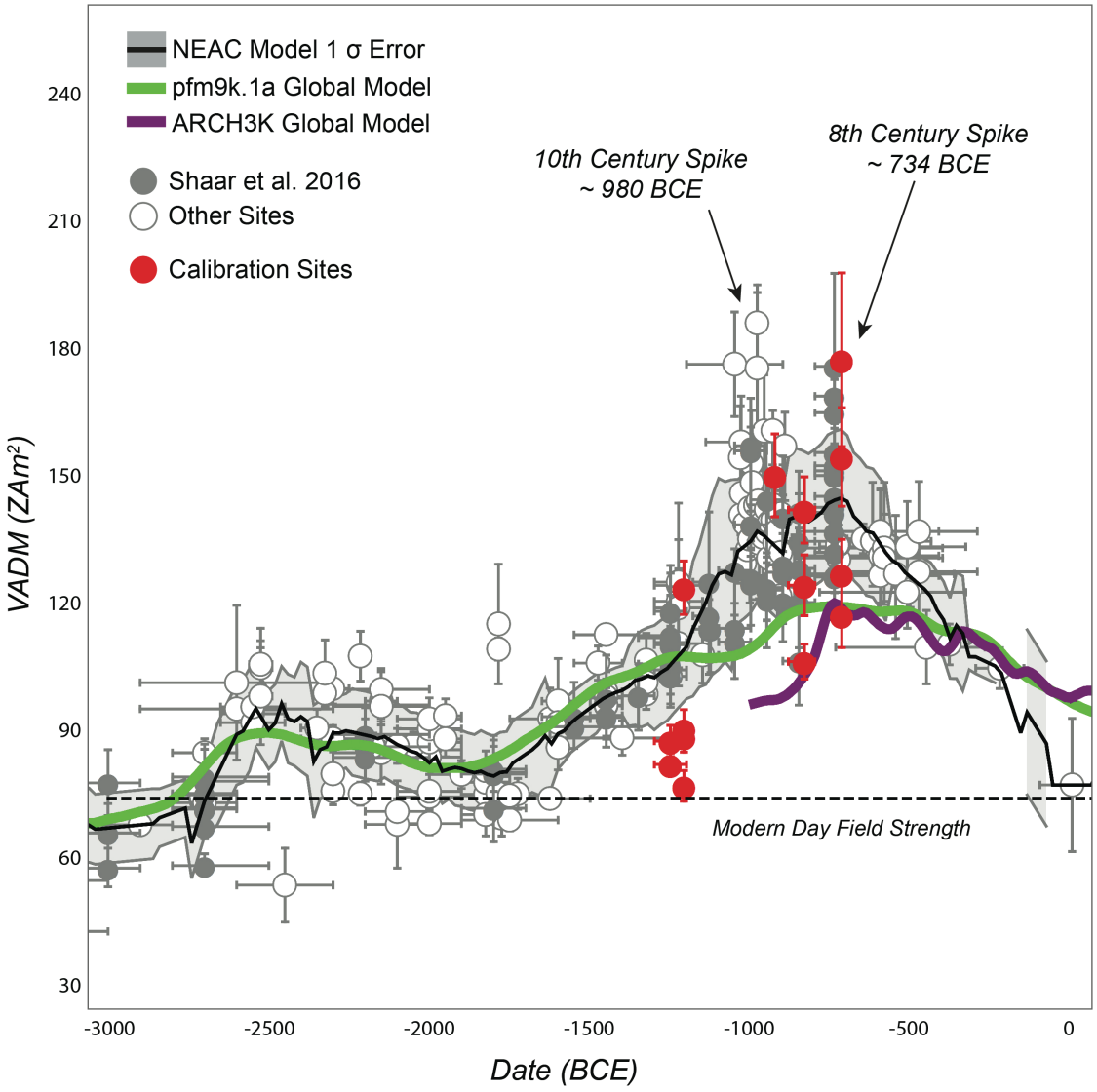

Figure 6-3 Near East Archaeomagnetic Curve (NEAC)

NEAC model based on 300-year moving average window shifted every 20 years. Calibration sites from this study in red. Grey points most recent data for Levant. See text for further descriptions.

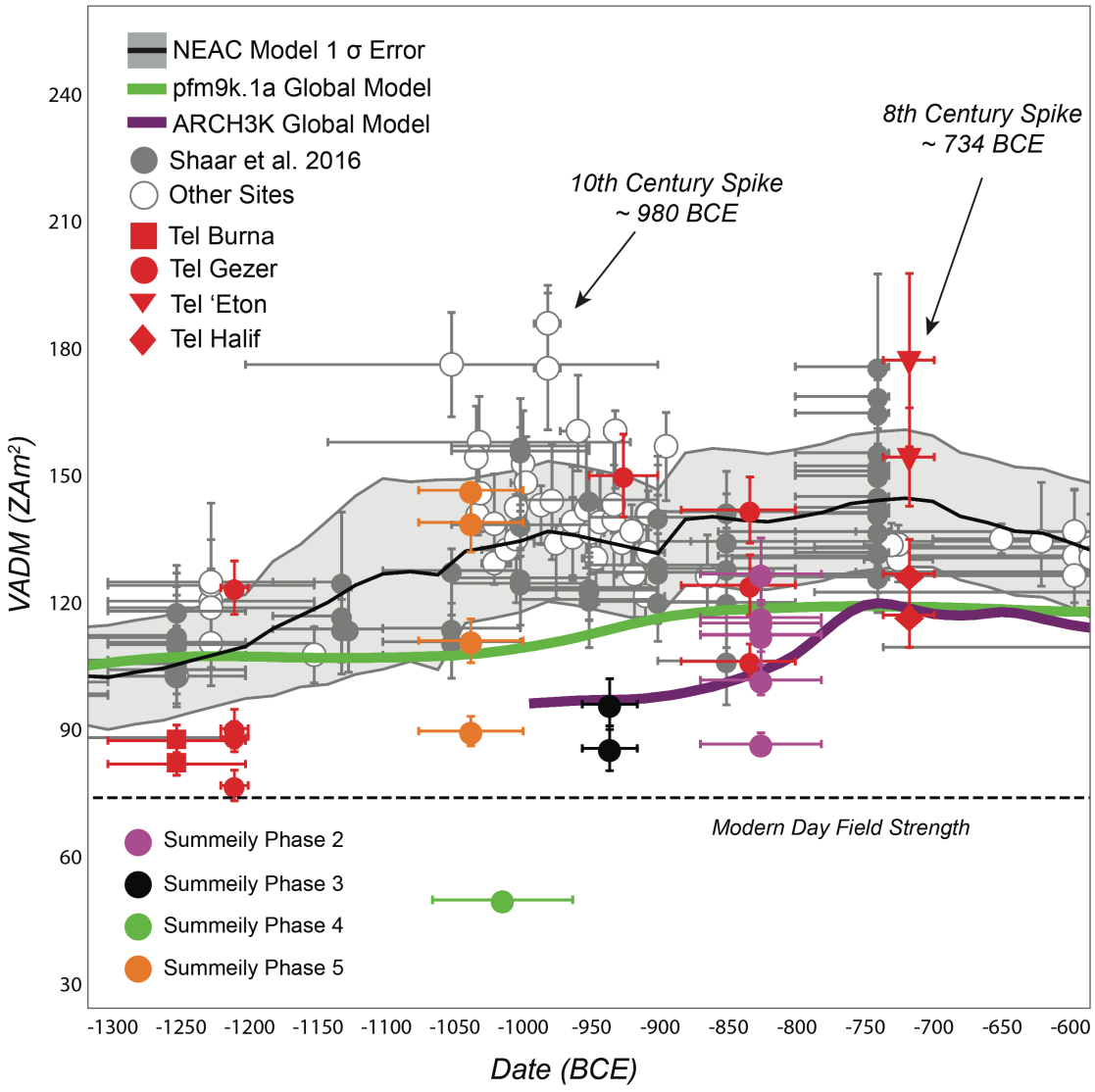

Figure 6-4 NEAC Zoomed to Levantine Iron Age

Calibration site data plotted by location (See Table 6-1 for dates). Khirbet Summeily phase data plotted as defined by *Chronomodel* program (Table 6-2).

7 Discussion

Until recently, study of the Earth's magnetic field variability had focused on large-scale changes, such as reversals, suitable for interpreting plate tectonics. Any unusual rapid fluctuations recorded in the rock record were believed to be merely statistical noise. During the last 8000 years, variability in the field's overall strength has been relatively minor (±20% of average), leading researchers to conclude that the high spikes in magnetic field strength identified in the Near East were more statistical noise. It is now clear that rapid, high frequency, and high amplitude fluctuations do occur.

The rate of change of the Near East spikes are on the order of four to five μT per year; nearly fifty times faster than the modern day rate of change and eight times faster than the regional estimated rate [Livermore et al., 2014]. New spikes have now been identified in China and North America [*Cai et al.*, 2014; *Bourne et al.*, 2016], confirming their occurrence. However, it is still unclear if these spikes are simply coincident unrelated field features, the products of a related columnar convention structure within the fluid outer core, [Shaar et al., 2015], or the result of a westward migrating magnetic flux patch [*Dumberry and Finlay*, 2007; *Amit et al.*, 2011; *Cai et al.*, 2014; *de Groot et al.*, 2015].

While current geomagnetic field models for investigating these questions (e.g.

pfm9k.1a) are incredibly useful (and improving), they remain limited in terms of capturing short-term variability for two reasons: 1) they are constructed using primarily northern hemisphere European data, and 2) they are excessively smoothed from the use of geological data with coarsely defined ages. Archaeomagnetic dating is ideally suited to address these issues as it can potentially provide data down to the decadal scale.

This research utilized archaeomagnetic dating to accomplish two primary objectives. First, it shows that small household bread ovens (tabuns) can accurately record the Earth's magnetic field, thus, providing a new source of intensity data to refine our understanding of field variability. The success rate of the tabuns was unexpectedly high given their friable texture. It can now be confirmed that tabuns make excellent archaeointensity recorders provided that the walls have been thoroughly heated to high temperatures and materials are properly fixed in appropriate containers for IZZI experiments.

The second objective was to demonstrate the application of archaeomagnetic dating to addressing the Iron Age chronology paradigm by ascribing ages to four occupational phases at the Iron Age site of Khirbet Summeily, Israel. Archaeomagnetic materials collected from four nearby, contemporary, and well-dated sites were utilized as calibrations along with archaeointensity results from other studies to construct a new archaeomagnetic dating curve for the region, the NEAC or Near East Archaeomagnetic Curve. The model of this curve was combined with Bayesian statistical analysis to firmly date Phases 5 and 2 at Summeily to approximately 1036 BCE and 825 BCE

respectively. Phase 4 results were unusually low and will require additional samples to confirm if an archaeointensity low exists somewhere between 1036 and 935 BCE. Phase 3 results indicate that the destruction at Summeily was likely the result of the 925 BCE campaign of Sheshonq I (22nd Dynasty); however, the results were markedly different than the 925 BCE results obtained for the Tel Gezer calibration site. More sampling from Summeily, Gezer, and other sites with 925 BCE destruction deposits will be needed to confirm the results.

In the process of answering these two research questions, one additional and significant outcomes were achieved; the confirmation of a secondary Iron Age intensity spike occurring around 734 BCE, obtained from the calibration site of Tel 'Eton, now the highest intensity measured for the region. Additionally, the difference between intensities for Tel 'Eton and Tel Halif may indicate their destructions are also differently attributed, with the Halif destruction potentially dating to 701 BCE, or vise versa.

Interpretation of the results from this study highlight two important issues that still need to be addressed. At the regional scale, new intensity results from confirmed 701 BCE destruction deposits are required to compare and distinguish between the two Assyrian destructions. Analysis of the samples collected from Lachish Level III (701 BCE) will aid in accomplishing this goal. Additionally, materials from distinct stratigraphic deposits at a single site for the period between 980 and 900 BCE are still needed to determine if there exists a corresponding drop in intensity between the two

spikes as indicated by the Phase 3 results at Summeily. Given the low intensity error rates obtained from the Khirbet Summeily samples used in this research and the range of results from previous studies [i.e. *Ben-Yosef et al.*, 2009; *Shaar et al.*, 2011], it is reasonable to presume that unusual lows or reverse spikes in intensity could also occur. It may be that the Phase 3 results at Summeily identify one potential reverse spike. A possible means of analyzing this is to combine results from paleomagnetic studies of the Dead Sea lake core sediments, which would provide annual resolution, similar to dendrochronology.

Second, this research shows that materials from conflagration deposits are problematic archaeomagnetic recorders, primarily because destruction fire temperatures may not be high enough to completely reset the original magnetization recorded by the artifacts. The success rate of the conflagration materials in this study was unusually low when compared to traditional (single firing) materials from other sites [e.g. *Stillinger et al.*, 2015]. However, it is necessary to attempt measurement on these types of materials for the Levant since the Iron Age dating paradigms encompass a period of extreme political unrest and the numerous conflagrations at key archaeological sites are often used as stratigraphic markers and the basis of phase determinations. The high number of pottery samples displaying two components of remanence, which failed acceptance criteria in this research, may still have the potential to provide future remanence data. For example, if it can be shown that two different heating episodes at two temperatures (an Arai plot with two distinct but accurate slopes) can be separated out, these samples may provide both original and secondary firing dates, potentially

dating conflagrations.

Finally, while numerous recent studies have focused on solving the Iron Age chronology paradigms, providing much needed data, the currently published regional intensities are still presented as individual sample results for a single archaeological stratum (e.g. the 734 BCE results from Hazor and Megiddo, Figure 6-4). This results in an archaeomagnetic dating curve with an over-abundance of data for certain time periods causing continued confusion and ambiguity.

In an attempt to determine if any specific patterns in the Earth's secular variation can be seen for the period between 1300 BCE and 600 BCE, a simple averaging of all available intensities by reported year was performed here, and a 200-year moving window average model applied, shifted every 20 years. This "average intensity" model (yellow line, Figure 7-1) appears to more closely match the NEAC curve than either of the global models. It also confirms that the average results for Tel 'Eton (734 BCE) are far higher than the average results for Tel Megiddo and Tel Hazor. Additionally, it reduces the overall magnitude of the 980 BCE spike and identifies a potential (third) spike around 1050 BCE. If we zoom in further, to the period represented by Khirbet Summeily (Figure 7-2), we can see that the intensity of the Levantine field appears to fluctuate or oscillate up and down between 1050 and 875 BCE. Again, given this behavior, there is potential for two or more reverse spikes.

In conclusion, archaeomagnetic dating holds the power to identify short-term geomagnetic field variability and is now a viable complementary and alternative dating

technique, which can aid in constructing archaeological chronologies, provide new secular variability data for recent time periods, and contribute to our understanding and modeling of long term geomagnetic field behaviors.

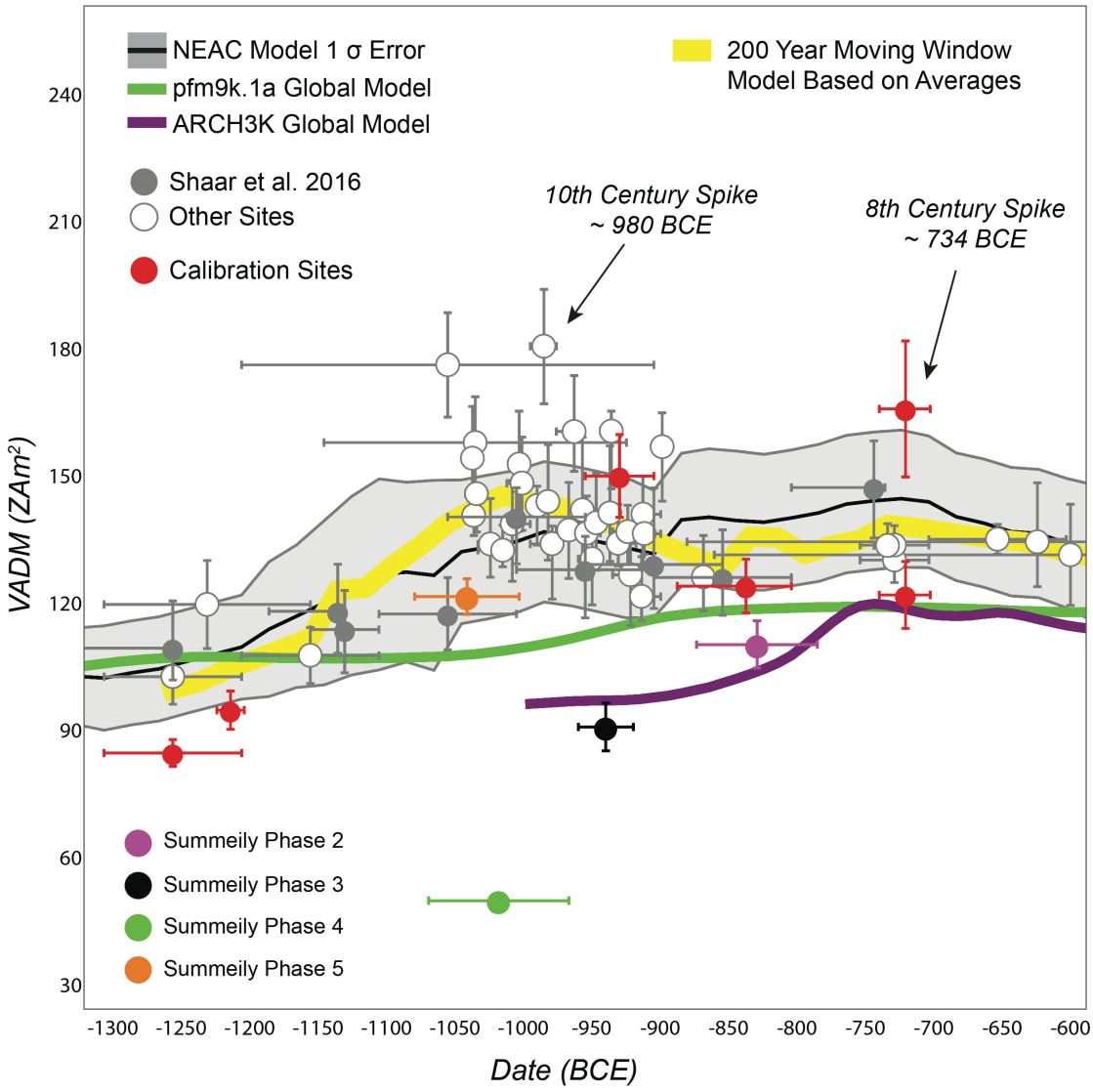

Figure 7-1 Average Archaeomagnetic Intensity for the Levant
Simple averaging of data used to construct NEAC model (Figure 6-3). See text for details.

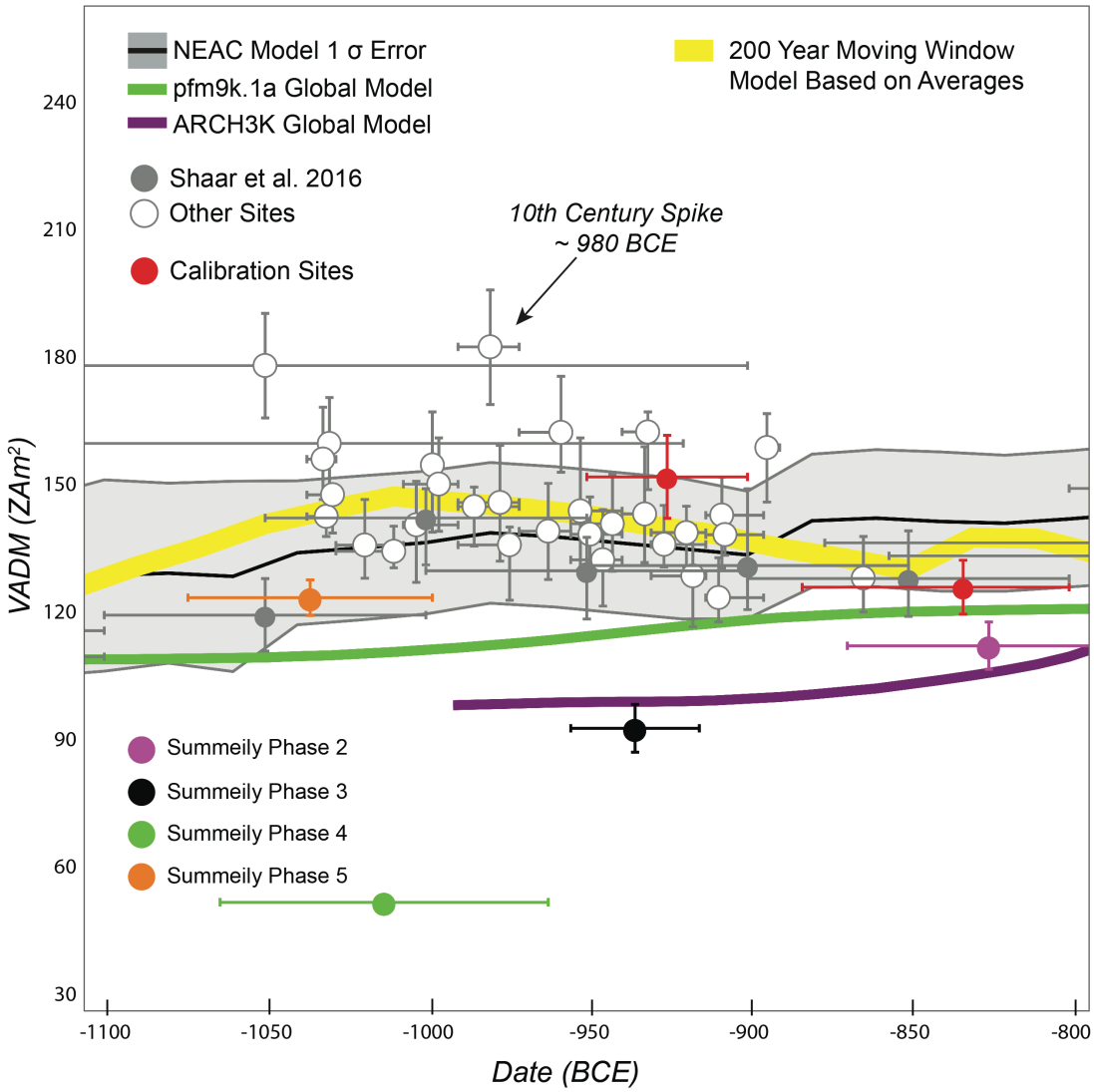

Figure 7-2 NEAC Average Intensity for Iron Age II Period in the Levant

Bibliography

Adriaens, A., K. A. Yener, and F. Adams (1999), An Analytical Study Using Electron and Ion Microscopy of Thin-walled Crucibles from Göltepe, Turkey, *Journal of Archaeological Science*, *26*(8), 1069–1073, doi:DOI: 10.1006/jasc.1999.0411.

Aitken, M. J. (1985), *Thermoluminescence Dating*, Academic Press Inc. (London) Ltd., London.

Aitken, M. J. (1998), *An Introduction to Optical Dating: the Dating of Quaternary Sediments by the Use of Photon-stimulated Luminescence*, Oxford University Press, New York.

Aitken, M. J., P. A. Alcock, G. D. Bussell, and C. J. Shaw (1981), Archaeomagnetic determination of the past geomagnetic intensity using ancient ceramics: allowance for anisotropy, *Archaeometry*, *23*(1), 53–64, doi:10.1111/j.1475-4754.1981.tb00954.x.

Aitken, M. J., A. L. Allsop, G. D. Bussell, and M. B. Winter (1984), Geomagnetic intensity in Egypt and western Asia during the second millennium BC, *Nature*, *310*, 305–306.

Ambrose, W. R. (2001), Obsidian Hydration Dating, in *Handbook of Archaeological Sciences*, edited by D. R. Brothwell and A. M. Pollard, pp. 81–92, John Wiley & Sons, Ltd., Chichester.

Amit, H., M. Korte, J. Aubert, C. Constable, and G. Hulot (2011), The time-dependence of intense archeomagnetic flux patches, *Journal of Geophysical Research: Solid Earth*, *116*(12), 1–13, doi:10.1029/2011JB008538.

Anderson, E. C., W. F. Libby, W. S, A. F. Reid, A. D. Kirshenbaum, and A. V Grosse (1947), Radiocarbon from Cosmic Radiation, *Science*, *105*(2735), 576–577.

Anderson, R. Y., J. P. Bradbury, W. E. Dean, and M. Stuiver (1993), Chronology of Elk Lake Sediments: Coring, Sampling, and Time-Series Construction, in *Elk Lake, Minnesota: Evidence for Rapid Climate Change in the North-Central United States*, edited by J. P. Bradbury and W. E. Dean, pp. 37–44, Geological Society of America, Inc., Boulder.

Arnold, J. R., and W. F. Libby (1949), Age determinations by radiocarbon content; checks with samples of known age., *Science (New York, N.Y.)*, *110*(2869), 678–80.

Athanassas, C. D., and G. A. Wagner (2016), Geochronology Beyond Radiocarbon: Optically Stimulated Luminescence Dating of Palaeoenvironments and Archaeological Sites, *Elements*, *12*(1), 27–32, doi:10.2113/gselements.12.1.27.

Baillie, M. G. L. (1991), Suck-in and Smear: Two Related Chronological Problems for the 90s, *Journal of Theoretical Archaeology*, *2*, 12–16.

Baillie, M. G. L. (1995), *A Slice Through Time: Dendrochronology and precision dating*, B.T. Batsford Ltd, London.

Banerjee, S. K. (1977), On the Origin of Stable Remanence in Pseudo-Single Domain Grains, in *Origin of Thermoremanent Magnetization*, edited by D. J. Dunlop, pp. 87–97, Springer, Dordrecht.

Ben-Yosef, E., H. Ron, L. Tauxe, A. Agnon, A. Genevey, T. E. Levy, U. Avner, and M. Najjar (2008), Application of copper slag in geomagnetic archaeointensity research, *Journal of Geophysical Research*, *113*(B08101), doi:https://doi.org/10.1029/2007JB005235.

Ben-Yosef, E., L. Tauxe, T. E. Levy, R. Shaar, H. Ron, and M. Najjar (2009), Geomagnetic intensity spike recorded in high resolution slag deposit in Southern Jordan, *Earth and Planetary Science Letters*, *287*(3/4), 529–539, doi:https://doi.org/10.1016/j.epsl.2009.09.001.

Ben-Yosef, E., R. Shaar, L. Tauxe, and R. Hagai (2012), A New Chronological Framework for Iron Age Copper Production at Timna (Israel), *Bulletin of the American Schools of Oriental Research*, *367*, 31–71.

Ben-Yosef, E., M. Millman, R. Shaar, L. Tauxe, and O. Lipschits (2017), Six centuries of geomagnetic intensity variations recorded by royal Judean stamped jar handles, *Proceedings of the National Academy of Sciences*, *114*(9), doi:https://doi.org/10.1073/pnas.1615797114.

Biggin, A. J., S. Badejo, E. Hodgson, A. R. Muxworthy, J. Shaw, and M. J. Dekkers (2013), The effect of cooling rate on the intensity of thermoremanent magnetization (TRM) acquired by assemblages of pseudo-single domain, multidomain and interacting single-domain grains, *Geophysical Journal International*, *193*(3), 1239–1249, doi:10.1093/gji/ggt078.

Bischoff, J. L., R. J. Rosenbauer, A. Tavoso, and H. de Lumley (1988), A test of uranium-series dating of fossil tooth enamel: results from Tournal Cave, France, *Applied Geochemistry*, *3*(2), 145–151, doi:10.1016/0883-2927(88)90002-9.

Blackwell, P., C. Buck, and P. Reimer (2006), Important features of the new radiocarbon calibration curves, *Quaternary Science Reviews*, *25*(5–6), 408–413, doi:10.1016/j.quascirev.2005.12.001.

Blakely, J. A. (2002), Reconciling two maps: archaeological evidence for the Kingdoms of David and Solomon, *Bulletin of the American Schools of Oriental Research*, *327*, 49–54.

Blakely, J. A., and Hardin (2002), Southwestern Judah in the Late Eighth Century BCE, *Bulletin of the American Schools of Oriental Research*, *326*, 11–64, doi:10.2307/147843.

Blakely, J. A., J. W. Hardin, and D. M. Master (2014), The Identification of the Southwest Border of Judah and the 10th Century Debate, in *Material Culture Matters: Essays on the Archaeology of the Southern Levant in Honor of Seymour Gitin*, edited by J. R. Spencer, R. A. Mullins, and A. J. Brody, pp. 33–52, Eisenbrauns, Indiana.

Boaretto, E. (2008), Determining the chronology of an archaeological site using radiocarbon: Minimizing uncertainty, *Israel Journal of Earth Sciences*, *56*, 207–216.

Boaretto, E. (2009), Dating materials in good archaeological contexts: The next challenge for radiocarbon analysis, *Radiocarbon*, *51*(1), 275–281, doi:10.1017/S0033822200033804.
Boaretto, E., A. J. T. Jull, A. Gilboa, and I. Sharon (2005), Dating the Iron Age I/II Transition in Israel: First Intercomparison Results, *Radiocarbon*, *47*(1), 39–55.
Boggs Jr., S. (2006), *Principles of Sedimentology and Stratigraphy*, 4th ed., Pearson Prentice Hall, New Jersey.
Borowski, O. (2017), Tell Halif in the Late Bronze and Iron Age, in *The Shephelah during the Iron Age: Recent Archaeological Studies*.
Bourne, M., J. M. Feinberg, T. W. Stafford Jr., M. R. Waters, E. Lundelius Jr., and S. L. Forman (2016), High-intensity geomagnetic field "spike" observed at ca. 3000 cal BP in Texas, USA, *Earth and Planetary Science Letters*, *442*, 80–92.
Bronk Ramsey, C. (1995), Radiocarbon Calibration and Analysis of Stratigraphy: The OxCal Program, *Radiocarbon*, *37*(2), 425–430.
Bronk Ramsey, C. (2009), Bayesian Analysis of Radiocarbon Dates, *Radiocarbon*, *51*(1), 337–360, doi:10.2458/azu_js_rc.v51i1.3494.
Brown, M. C., F. Donadini, M. Korte, A. Nilsson, K. Korhonen, A. Lodge, S. N. Lengyel, and C. G. Constable (2015a), GEOMAGIA50.v3: 1. general structure and modifications to the archeological and volcanic database, *Earth, Planets and Space*, *67*, 83, doi:10.1186/s40623-015-0232-0.
Brown, M. C., F. Donadini, A. Nilsson, S. Panovska, U. Frank, K. Korhonen, M. Schuberth, M. Korte, and C. G. Constable (2015b), GEOMAGIA50.v3: 2. A new paleomagnetic database for lake and marine sediments, *Earth, Planets and Space*, *67*(1), 70, doi:10.1186/s40623-015-0233-z.
Bruins, H. J., J. Van Der Plicht, A. Mazar, C. B. Ramsey, and S. W. Manning (2005), The Groningen Radiocarbon Series from Tel Rehov: OxCal Bayesian computations for the Iron IB-IIA Boundary and Iron IIA destruction events, in *The Bible and Radiocarbon Dating: Archaeology, Text, and Science*, edited by T. E. Levy and T. Higham, pp. 271–293, Equinox Publishing Ltd., London.
Buccellati, G. (2005), Tell Mozan Urkesh: special topics, Available from: http://www.urkesh.org/attach/English A4 O908 special topics.pdf
Buccellati, G., and M. Kelly-Buccellati (2005), Urkesh as a Hurrian religious center, *Studi Micenei ed Egeo-Anatolici*, *47*, 27–59.
Buck, C. E., and P. G. Blackwell (2004), Formal statistical models for estimating radiocarbon calibration curves., *Radiocarbon*, *46*(3), 1093–1102, doi:10.2458/azu_js_rc.v.4170.
Buck, C. E., J. B. Kenworthy, C. D. Litton, and A. F. M. Smith (1991), Combining Archaeological and Radiocarbon information: A Bayesian Approach to Calibration, *Antiquity*, *65*(249), 808–821.
Butler, R. F. (1992), *Paleomagnetism: Magnetic Domains to Geologic Terranes*, Blackwell Scientific Publishing, Boston.
Butler, R. F., and S. K. Banerjee (1975), Theoretical Single-Domain Grain Size Range in Magnetite and Titanomagnetite, *Journal of Geophysical Research*, *80*(29), 4049–4058.

Cai, S., L. Tauxe, C. Deng, Y. Pan, G. Jin, J. Zheng, F. Xie, H. Qin, and R. Zhu (2014), Geomagnetic intensity variations for the past 8 kyr: New archaeointensity results from Eastern China, *Earth and Planetary Science Letters*, *392*, 217–229, doi:10.1016/j.epsl.2014.02.030.

Catanzariti, G., G. McIntosh, M. Gómez-Paccard, V. C. Ruiz-Martínez, M. L. Osete, and A. Chauvin (2008), Quality control of archaeomagnetic determination using a modern kiln with a complex NRM, *Physics and Chemistry of the Earth, Parts A/B/C*, *33*(6–7), 427–437, doi:10.1016/j.pce.2008.02.028.

Chauvin, A., Y. Garcia, P. Lanos, and F. Laubenheimer (2000), Paleointensity of the geomagnetic field recovered on archaeomagnetic sites from France, *Physics of the Earth and Planetary Interiors*, *120*, 111–136.

Coe, R. S. (1979), The effect of shape anisotropy on TRM direction, *Geophysical J. Royal Astronomical Soc.*, *56*, 369–383.

Coe, R. S., S. Grommé, and E. A. Mankinen (1978), Geomagnetic paleointensities from radiocarbon-dated lava flows on Hawaii and the question of the Pacific nondipole low, *Journal of Geophysical Research*, *83*(B4), 1740–1756.

Constable, C., M. Korte, and S. Panovska (2016), Persistent high paleosecular variation activity in southern hemisphere for at least 10 000 years, *Earth and Planetary Science Letters*, *453*, 78–86, doi:10.1016/j.epsl.2016.08.015.

Courtillot, V., and J.L. Le Mouël (2007), The study of Earth's magnetism (1269-1950): a foundation by Peregrinus and subsequent development of geomagnetism and paleomagnetism, *Reviews of Geophysics*, *45*(RG3008), doi:10.1029/2006RG000198.1.

Damon, P. E., and A. Long (1962), Arizona Radiocarbon Dates III, *Radiocarbon*, *4*, 239–249.

Damon, P. E., and A. N. Peristykh (2000), Radiocarbon Calibration and Application to Geophysics, Solar Physics, and Astrophysics, *Radiocarbon*, *42*(1), 137–150.

Damon, P. E., J. C. Lerman, and A. Long (1978), Temporal fluctuations of atmospheric 14C: causal factors and implications, *Annual Review of Earth and Planetary Sciences*, *6*(1), 457–494, doi:10.1146/annurev.ea.06.050178.002325.

Day, R., M. Fuller, and V. A. Schmidt (1977), Hysteresis properties of titanomagnetites: grain-size and compositional dependence, *Physics of the Earth and Planetary Interiors*, *13*, 260–267.

Dodson, M. H., and E. McClelland-Brown (1980), Magnetic blocking temperatures of single-domain grains during slow cooling, *Journal of Geophysical Research*, *85*(B5), 2625–2637.

Donadini, F., K. Korhonen, P. Riisager, and L. J. Pesonen (2006), Database for Holocene Geomagnetic Intensity Information, *Eos*, *87*(14), doi:10.1029/2003JB002672.Gallet.

Drysdale, R. N., C. Spötl, J. C. Hellstrom, and D. A. Richards (2012), New advances in the dating of speleothems - An introduction, *Quaternary Geochronology*, *14*, 1–4, doi:10.1016/j.quageo.2012.11.008.

Dumberry, M., and C. C. Finlay (2007), Eastward and westward drift of the Earth's magnetic field for the last three millennia, *Earth and Planetary Science Letters*, *254*(1–2), 146–157, doi:10.1016/j.epsl.2006.11.026.

Dunai, T. J. (2010), *Cosmogenic Nuclides: Principles, Concepts and Applications in the Earth Sciences*, Cambridge University Press, Cambridge.
Dunlop, D. J. (2011), Physical basis of the Thellier–Thellier and related paleointensity methods, *Physics of the Earth and Planetary Interiors*, *187*(3–4), 118–138, doi:10.1016/j.pepi.2011.03.006.
Dunlop, D. J., and Ö. Özdemir (1997), *Rock Magnetism: Fundamentals and Frontiers*, Cambridge University Press, Cambridge.
Dunlop, D. J., and Ö. Özdemir (2007), Magnetizations in rocks and minerals, in *Geomagnetism, Treatise on geophysics, 5*, edited by G. Schubert, pp. 277–336, Elsevier, Amsterdam, The Netherlands.
Dunlop, D. J., F. D. Stacey, and D. E. W. Gillingham (1974), The origin of thermoremanent magnetization: Contribution of pseudo-single-domain magnetic moments, *Earth and Planetary Science Letters*, *21*(3), 288–294, doi:10.1016/0012-821X(74)90163-0.
Edwards, R. L., J. H. Chen, and G. L. Wasserburg (1986), 238U- 234U- 230Th- 232Th systematics and the precise measurement of time over the past 500, 000 years, *Earth and Planetary Science Letters*, *81*, 175–192.
Edwards, R. L., J. H. Chen, T.-L. Ku, and G. J. Wasserburg (1987), Precise Timing of the Last Interglacial Period from Mass Spectrometric Determination of Thorium-230 in Corals, *Science*, *236*(4808), 1547–1553, doi:10.1126/science.236.4808.1547.
Eggins, S., R. Grün, A. W. G. Pike, M. Shelley, and L. Taylor (2003), 238U,232Th profiling and U-series isotope analysis of fossil teeth by laser ablation-ICPMS, *Quaternary Science Reviews*, *22*(10–13), 1373–1382, doi:10.1016/S0277-3791(03)00064-7.
Eggins, S. M. et al. (2005), In situ U-series dating by laser-ablation multi-collector ICPMS: New prospects for Quaternary geochronology, *Quaternary Science Reviews*, *24*(23–24), 2523–2538, doi:10.1016/j.quascirev.2005.07.006.
Eighmy, J. L., and R. S. Sternberg (Eds.) (1990), *Archaeomagnetic Dating*, University of Arizona Press, Tucson.
Elsasser, W., E. P. Ney, and J. R. Winckler (1956), Cosmic-Ray Intensity and Geomagnetism, *Nature*, *178*, 1226–1227.
Engelkemeir, A. G., W. H. Hamill, M. G. Inghram, and W. F. Libby (1949), The Half-Life of Radiocarbon (C14), *Physical Review*, *75*(12), 1825–1833.
Ertepinar, P., C. G. Langereis, A. J. Biggin, M. Frangipane, T. Matney, T. Ökse, and A. Engin (2012), Archaeomagnetic study of five mounds from Upper Mesopotamia between 2500 and 700 BCE: further evidence for an extremely strong geomagnetic field ca. 3000 years ago, *Earth and Planetary Science Letters*, *357–358*, 84–98, doi:https://doi.org/10.1016/j. epsl.2012.08.039.
Fairbanks, R. G., R. a. Mortlock, T.-C. Chiu, L. Cao, A. Kaplan, T. P. Guilderson, T. W. Fairbanks, A. L. Bloom, P. M. Grootes, and M.-J. Nadeau (2005), Radiocarbon calibration curve spanning 0 to 50,000 years BP based on paired 230Th/234U/238U and 14C dates on pristine corals, *Quaternary Science Reviews*, *24*(16–17), 1781–1796, doi:10.1016/j.quascirev.2005.04.007.

Falguères, C., J.-J. Bahain, M. Duval, Q. Shao, F. Han, M. Lebon, N. Mercier, A. Perez-Gonzalez, J.-M. Dolo, and T. Garcia (2010), A 300–600ka ESR/U-series chronology of Acheulian sites in Western Europe, *Quaternary International*, *223–224*, 293–298, doi:10.1016/j.quaint.2009.10.008.

Falguères, C. et al. (2013), Combined ESR/U-series chronology of Acheulian hominid-bearing layers at Trinchera Galería site, Atapuerca, Spain., *Journal of human evolution*, *2013*, 1–17, doi:10.1016/j.jhevol.2013.05.005.

Fantalkin, A., I. Finkelstein, and E. Piasetzky (2011), Iron Age Mediterranean Chronology: A Rejoinder, *Radiocarbon*, *53*(1), 179–198.

Fantalkin, A., I. Finkelstein, and E. Piasetzky (2015), Late Helladic to Middle Geometric Aegean and Contemporary Cypriot Chronologies: A Radiocarbon View from the Levant, *Bulletin of the American Schools of Oriental Research*, *373*(373), 25–48, doi:10.5615/bullamerschoorie.373.0025.

Faust, A. (2017), Tel 'Eton Excavations and the History of the Shephelah during the Iron Age, in *Le-ma'an Ziony : Essays in Honor of Ziony Zevit*, edited by F. E. Greenspahn and G. A. Rendsburg, Wipf and Stock, Eugene, Oregon.

Faust, A., and Y. Sapir (2018), The "Governor's Residency" at Tel 'Eton, the United Monarchy, and the impact of the old-house effect on large-scale archaeological reconstructions, *Radiocarbon*, (May), 1–20, doi:10.1017/RDC.2018.10.

Finkelstein, I. (1996), The Archaeology of the United Monarchy: an Alternative View, *Levant*, *28*, 177–187.

Finkelstein, I. (2002), Chronology Rejoinders, *Palestine Exploration Quarterly*, *134*(2), 118–129.

Finkelstein, I. (2010), A Great United Monarchy? Archaeological and Historical Perspectives, in *One God - One Cult - One Nation: Archaeological and Biblical Perspectives*, edited by R. G. Kratz, H. Spieckermann, B. Corzilius, and T. Pilger, pp. 3–28, De Gruyter, Berlin/New York.

Finkelstein, I., and N. Na'aman (2004), The Judahite Shephelah in the Late 8th and Early 7th Centuries BCE, *Journal of the Institute of Archaeology of Tel Aviv University*, *31*(1), 60–79.

Finkelstein, I., and E. Piasetzky (2010a), Radiocarbon dating the Iron Age in the Levant: a Bayesian model for six ceramic phases and six transitions, *Antiquity*, *84*, 374–385.

Finkelstein, I., and E. Piasetzky (2010b), The Iron I/IIA Transition in the Levant: A Reply to Mazar and Bronk Ramsey and a New Perspective, *Radiocarbon*, *52*(4), 1667–1680.

Finkelstein, I., and E. Piasetzky (2011), The Iron Age chronology debate: is the gap narrowing?, *Near Eastern Archaeology*, *74*(1), 50–54.

Finkelstein, I., and E. Piasetzky (2015), Radiocarbon dating Khirbet Qeiyafa and the Iron I-IIA phases inthe Shephelah: methodological comments and a Bayesian model, *Radiocarbon*, *57*(5), 891–907, doi:10.2458/azu.

Finlay, C. C. et al. (2010), International Geomagnetic Reference Field: The eleventh generation, *Geophysical Journal International*, *183*(3), 1216–1230, doi:10.1111/j.1365-246X.2010.04804.x.

Folgheraiter, G. (1899), Sur les variations séculaires de l'inclinaison magnétique dans l'antiquité, *Journal de Physique Theor. Appl.*, *8*(1), 660–667, doi:10.1051/jphystap:018990080066001.

Frahm, E. (2014), Buying local or ancient outsourcing? Locating production of prismatic obsidian blades in Bronze-Age Northern Mesopotamia, *Journal of Archaeological Science*, *41*, 605–621, doi:10.1016/j.jas.2013.10.007.

Frahm, E., and J. M. Feinberg (2013a), Empires and resources: Central Anatolian obsidian at Urkesh (Tell Mozan, Syria) during the Akkadian period, *Journal of Archaeological Science*, *40*(2), 1122–1135, doi:10.1016/j.jas.2012.07.019.

Frahm, E., and J. M. Feinberg (2013b), Environment and collapse: Eastern Anatolian obsidians at Urkesh (Tell Mozan, Syria) and the third-millennium Mesopotamian urban crisis, *Journal of Archaeological Science*, *40*(4), 1866–1878, doi:10.1016/j.jas.2012.11.026.

Frahm, E. E. (2010), The Bronze-Age obsidian industry at Tell Mozan (Ancient Urkesh), Syria, University of Minnesota.

Friedrich, M., S. Remmele, B. Kromer, J. Hofmann, M. Spurk, K. F. Kaiser, C. Orcel, and M. Küppers (2004), The 12,460-Year Hohenheim Oak and Pine Tree-Ring Chronology from Central Europe: A Unique Annual Record for Radiocarbon Calibration and Paleoenvironment Reconstructions, *Radiocarbon*, *46*(3), 1111–1122.

Fuller, M. D. (1963), Magnetic Anisotropy and Paleomagnetism, *Journal of Geophysical Research*, *68*(I), 293–309.

Gallet, Y., and M. Al-Maqdissi (2010), Archéomagnétisme à Mishirfeh-Qatna: Nouvelles données sur l'évolution de l'intensité du champ magnétique terrestre au Moyen-Orient durant les derniers millénaires, *Akkadica*, *131*, 29–46.

Gallet, Y., and M. Le Goff (2006), High-temperature archeointensity measurements from Mesopotamia, *Earth and Planetary Science Letters*, *241*(1–2), 159–173, doi:10.1016/j.epsl.2005.09.058.

Gallet, Y., A. Genevey, M. Legoff, F. Fluteau, and S. Alieshraghi (2006), Possible impact of the Earth's magnetic field on the history of ancient civilizations, *Earth and Planetary Science Letters*, *246*(1–2), 17–26, doi:10.1016/j.epsl.2006.04.001.

Gallet, Y., M. Le Goff, A. Genevey, J. Margueron, and P. Matthiae (2008), Geomagnetic field intensity behavior in the Middle East between ~3000 BC and ~1500 BC, *Geophysical Research Letters*, *35*(2), L02307, doi:10.1029/2007GL031991.

Gallet, Y., M. D'Andrea, A. Genevey, F. Pinnock, M. Le Goff, and P. Matthiae (2014), Archaeomagnetism at Ebla (Tell Mardikh, Syria). New data on geomagnetic field intensity variations in the Near East during the Bronze Age, *Journal of Archaeological Science*, *42*, 295–304, doi:http://dx.doi.org/10.1016/j.jas.2013.11.007.

Gallet, Y., M. Molist Montaña, A. Genevey, X. Clop García, E. Thébault, A. Gómez Bach, M. Le Goff, B. Robert, and I. Nachasova (2015), New Late Neolithic (c. 7000-5000 BC) archeointensity data from Syria. Reconstructing 9000years of archeomagnetic field intensity variations in the Middle East, *Physics of the Earth and Planetary Interiors*, *238*, 89–103,

doi:http://dx.doi.org/10.1016/j.pepi.2014.11.003.
García-Diez, M., D. L. Hoffmann, J. Zilhão, C. D. Las Heras, J. a. Lasheras, R. Montes, and A. W. G. Pike (2013), Uranium series dating reveals a long sequence of rock art at Altamira cave (Santillana del Mar, Cantabria), *Journal of Archaeological Science*, 1–9, doi:10.1016/j.jas.2013.05.011.
Garfinkel, Y., K. Streit, S. Ganor, and P. J. Reimer (2015), King David's City at Khirbet Qeiyafa: Results of the Second Radiocarbon Dating Project, *Radiocarbon*, *57*(5), 881–890, doi:10.2458/azu.
Gee, J., H. Staudigel, L. Tauxe, T. Pick, and Y. Gallet (1993), Magnetization of the La Palma Seamount Series : implications for seamount paleopoles, *Journal of Geophysical Research*, *98*(B7), 11,743-11,767.
Genevey, A., and Y. Gallet (2002), Intensity of the geomagnetic field in western Europe over the past 2000 years: New data from ancient French pottery, *Journal of Geophysical Research*, *107*(B11), doi:10.1029/2001JB000701.
Genevey, A., and Y. Gallet (2003), Eight thousand years of geomagnetic field intensity variations in the eastern Mediterranean, *Journal of Geophysical Research*, *108*(B5), 2228, doi:10.1029/2001JB001612.
Genevey, A., Y. Gallet, J. Rosen, and M. Le Goff (2009), Evidence for rapid geomagnetic field intensity variations in Western Europe over the past 800 years from new French archeointensity data, *Earth and Planetary Science Letters*, *284*(1–2), 132–143, doi:10.1016/j.epsl.2009.04.024.
Genevey, A., Y. Gallet, E. Thébault, S. Jesset, and M. Le Goff (2013), Geomagnetic field intensity variations in Western Europe over the past 1100 years, *Geochemistry, Geophysics, Geosystems*, *14*(8), 2858–2872, doi:10.1002/ggge.20165.
Genevey, A., Y. Gallet, S. Jesset, E. Thébault, J. Bouillon, A. Lefèvre, and M. Le Goff (2016), New archeointensity data from French Early Medieval pottery production (6th–10th century AD). Tracing 1500years of geomagnetic field intensity variations in Western Europe, *Physics of the Earth and Planetary Interiors*, *257*, 205–219, doi:10.1016/j.pepi.2016.06.001.
Gilboa, A., I. Sharon, and E. Boaretto (2013), Radiocarbon Dating of the Iron Age Levels, in *Megiddo V: The 2004-2008 Seasons*, edited by I. Finkelstein, D. Ussishkin, and E. H. Cline, pp. 1117–1127, Institute of Archaeology of Tel Aviv University, Tel Aviv.
Le Goff, M., Y. Gallet, A. Genevey, and N. Warmé (2002), On archeomagnetic secular variation curves and archeomagnetic dating, *Physics of the Earth and Planetary Interiors*, *134*(3–4), 203–211, doi:10.1016/S0031-9201(02)00161-9.
Gómez-Paccard, M., A. Chauvin, P. Lanos, J. Thiriot, and P. Jiménez-Castillo (2006), Archeomagnetic study of seven contemporaneous kilns from Murcia (Spain), *Physics of the Earth and Planetary Interiors*, *157*(1–2), 16–32, doi:10.1016/j.pepi.2006.03.001.
Gómez-Paccard, M., M. L. Osete, A. Chauvin, F. J. Pavón-Carrasco, M. Pérez-Asensio, P. Jiménez, and P. Lanos (2016), New constraints on the most significant paleointensity change in Western Europe over the last two millennia. A non-dipolar origin?, *Earth and Planetary Science Letters*, *454*, 55–64,

doi:10.1016/j.epsl.2016.08.024.
Griggs, C. B., and S. W. Manning (2009), A Reappraisal of the Dendrochronolgy and Dating of Tille Höyük (1993), *Radiocarbon*, *51*(2), 711–720.
de Groot, L. V., A. Béguin, M. E. Kosters, E. M. van Rijsingen, E. L. M. Struijk, A. J. Biggin, E. a. Hurst, C. G. Langereis, and M. J. Dekkers (2015), High paleointensities for the Canary Islands constrain the Levant geomagnetic high, *Earth and Planetary Science Letters*, *419*, 154–167, doi:10.1016/j.epsl.2015.03.020.
Grün, R. (2001), Trapped Charge Dating (ESR, TL, OSL), in *Handbook of Archaeological Sciences*, edited by D. R. Brothwell and A. M. Pollard, pp. 47–62, John Wiley & Sons, Ltd., Chichester.
Grün, R. (2006), Direct Dating of Human Fossils, *Yearbook of Physical Anthropology*, *49*, 2–48.
Grün, R., and L. Taylor (1996), Uranium and thorium in constituents of fossil teeth, *Ancient TL*, *14*(1), 21–24.
Grün, R., C. Stringer, F. McDermott, R. Nathan, N. Porat, S. Robertson, L. Taylor, G. Mortimer, S. Eggins, and M. McCulloch (2005), U-series and ESR analyses of bones and teeth relating to the human burials from Skhul, *Journal of Human Evolution*, *49*(3), 316–334, doi:10.1016/j.jhevol.2005.04.006.
Grün, R., M. Aubert, J. Hellstrom, and M. Duval (2010), The challenge of direct dating old human fossils, *Quaternary International*, *223–224*, 87–93, doi:10.1016/j.quaint.2009.10.005.
Grün, R., S. Eggins, L. Kinsley, H. Moseley, and M. Sambridge (2014), Laser ablation U-series analysis of fossil bones and teeth, *Palaeogeography, Palaeoclimatology, Palaeoecology*, *416*, 150–167, doi:10.1016/j.palaeo.2014.07.023.
Halgedahl, S. L., R. Day, and M. Fuller (1980), The effect of cooling rate on the intensity of weak-field TRM in single domain magnetite, *Journal of Geophysical Research*, *85*(B7), 3690–3698.
Hammond, N. (1989), Hydration Dating of Tecep Phase Occupation at Nohmul, Belize, *American Antiquity*, *54*(3), 513–521.
Hanslík, E. et al. (2005), Radium isotopes in river sediments of Czech Republic, *Limnologica*, *35*(3), 177–184, doi:10.1016/j.limno.2005.05.004.
Hardin, J. W., C. A. Rollston, and J. A. Blakely (2012), Biblical Geography in Southwestern Judah, *Near Eastern Archaeology*, *75*(1), 20–35.
Hardin, J. W., C. A. Rollston, and J. A. Blakely (2014), Iron Age Bullae from Officialdom's Periphery: Khirbet Summeily in Broader Context, *Near Eastern Archaeology*, *77*(4), 299–301.
Heaton, T. J., P. G. Blackwell, and C. E. Buck (2009), A Bayesian Approach to the Estimation of Radiocarbon Calibration Curves: the Intcal09 Methodology, *Radiocarbon*, *51*(4), 1151–1164.
Hervé, G., E. Schnepp, A. Chauvin, P. Lanos, and N. Nowaczyk (2011), Archaeomagnetic results on three Early Iron Age salt-kilns from Moyenvic (France), *Geophysical Journal International*, *185*(1), 144–156, doi:10.1111/j.1365-246X.2011.04933.x.

Hervé, G., A. Chauvin, and P. Lanos (2013), Geomagnetic field variations in Western Europe from 1500BC to 200AD. Part II: New intensity secular variation curve, *Physics of the Earth and Planetary Interiors*, *218*, 51–65, doi:10.1016/j.pepi.2013.02.003.

Hua, Q., M. Barbetti, and A. Z. Rakowski (2013), Atmospheric Radiocarbon for the Period 1950-2010, *Radiocarbon*, *55*(2), 1–14.

Hughen, K. A. et al. (2004), Marine04 Marine Radiocarbon Age Calibration, 0-26 CAL KYR BP, *Radiocarbon*, *46*(3), 1059–1086.

Hulot, G., C. C. Finlay, C. G. Constable, N. Olsen, and M. Mandea (2010), The magnetic field of planet Earth, *Space Science Reviews*, *152*(1–4), 159–222, doi:10.1007/s11214-010-9644-0.

Huntley, D. J., D. I. Godfrey-Smith, and M. L. W. Thewalt (1985), Optical dating of sediments, *Nature*, *313*(10), 105–107, doi:10.1038/314141a0.

Hussain, A. G. (1987), The secular variation of the geomagnetic field in Egypt in the last 5000 years, *Pure and Applied Geophysics*, *125*(1), 67–90.

Ioannis, L. (2006), The dating of ancient metals: review and a possible application of the 226Ra/230Th method (a tutorial), *Mediterranean Archaeology and Archaeometry*, *6*(2), 77–91.

Jackson, M. (1991), Anisotropy of magnetic remanence: A brief review of mineralogical sources, physical origins, and geological applications, and comparison with susceptibility anisotropy, *Pure and Applied Geophysics PAGEOPH*, *136*(1), 1–28, doi:10.1007/BF00878885.

Jackson, M., W. Gruber, J. Marvin, and S. K. Banerjee (1988), Partial Anhysteretic Remanence and its Anisotropy: Applications and Grainsize-Dependence, *Geophysical Research Letters*, *15*(5), 440–443.

Katz, H., and A. Faust (2012), The Assyrian Destruction Layer at Tel 'Eton, *Israel Exploration Journal*, *62*(1), 22–53.

Keisch, B. (1968), Dating Works of Art through Their Natural Radioactivity: Improvements and Applications, *American Association for the Advancement of Science*, *160*(3826), 413–415.

Kigoshi, K., and H. Hasegawa (1966), Secular variation of atmospheric radiocarbon concentration and its dependence on geomagnetism, *Journal of Geophysical Research*, *71*(4), 1065–1071, doi:10.1029/JZ071i004p01065.

Kirschvink, J. L. (1980), The least-squares line and plane and the analysis of palaeomagnetic data, *Geophysical Journal International*, *62*(3), 699–718, doi:10.1111/j.1365-246X.1980.tb02601.x.

Kitagawa, H., and J. van der Plicht (1998a), A 40,000-Year Varve Chronology from Lake Suigetsu, Japan: Extension of the 14C Calibration Curve, *Radiocarbon*, *40*(1), 505–515.

Kitagawa, H., and J. van der Plicht (1998b), Atmospheric Radiocarbon Calibration to 45,000 yr B .P.: Late Glacial Fluctuations and Cosmogenic Isotope Production, *Science*, *279*, 1187–1190, doi:10.1126/science.279.5354.1187.

Koenigsberger, J. G. (1932), Spontane Magnetisierung und Thermoremanenz in ferromagnetischen Einkristallen, *Phys. Zeits*, *33*, 763–767.

Kono, M., and P. H. Roberts (2002), Recent geodynamo simulations and observations of the geomagnetic field, *Reviews of Geophysics*, *40*(4), 1013, doi:10.1029/2000RG000102.

Korhonen, K., F. Donadini, P. Riisager, and L. J. Pesonen (2008), GEOMAGIA50: an archaeointensity database with PHP and MySQL, *Geochemistry, Geophysics, Geosystems*, *9*, doi:10.1029/2007GC001.893.

Korte, M., and C. Constable (2011), Improving geomagnetic field reconstructions for 0-3ka, *Physics of the Earth and Planetary Interiors*, *188*(3–4), 247–259, doi:10.1016/j.pepi.2011.06.017.

Korte, M., A. Genevey, C. G. Constable, U. Frank, and E. Schnepp (2005), Continuous geomagnetic field models for the past 7 millennia: 1. A new global data compilation, *Geochemistry, Geophysics, Geosystems*, *6*(2), doi:10.1029/2004GC000800.

Korte, M., F. Donadini, and C. G. Constable (2009), Geomagnetic field for 0-3 ka: 2. A new series of time-varying global models, *Geochemistry Geophysics Geosystems*, *10*(6), Q06008, doi:10.1029/2008gc002297.

Korte, M., C. Constable, F. Donadini, and R. Holme (2011), Reconstructing the Holocene geomagnetic field, *Earth and Planetary Science Letters*, *312*(3–4), 497–505, doi:10.1016/j.epsl.2011.10.031.

Kovacheva, M., and A. Toshkov (1994), Geomagnetic field variations as determined from Bulgarian archaeomagnetic data part I: the last 2000 years AD, *Surveys in Geophysics*, *15*, 673–701.

Kovacheva, M., V. Spatharas, and I. Liritzis (2000), New Archaeointensity Results from Greek Materials, *Archaeometry*, *2*, 415–429.

Kovacheva, M., M. Kostadinova-Avramova, N. Jordanova, P. Lanos, and Y. Boyadzhiev (2014), Extended and revised archaeomagnetic database and secular variation curves from Bulgaria for the last eight millennia, *Physics of the Earth and Planetary Interiors*, *236*, 79–94, doi:10.1016/j.pepi.2014.07.002.

Kuniholm, P. I. (2001), Dendrochronology and Other Applications of Tree-ring Studies in Archaeology, in *Handbook of Archaeological Sciences*, edited by D. R. Brothwell and A. M. Pollard, pp. 35–46, John Wiley & Sons, Ltd., Chichester.

Lahaye, C. et al. (2013), Human occupation in South America by 20,000 BC: the Toca da Tira Peia site, Piauí, Brazil, *Journal of Archaeological Science*, *40*(6), 2840–2847, doi:10.1016/j.jas.2013.02.019.

Lang, A., and G. A. Wagner (1996), Infrared Stimulated Luminescence Dating of Archaeosediments, *Archaeometry*, *38*(1), 129–141.

Lanos, P., and A. Philippe (2015), Hierarchical Bayesian modeling for combining Dates in archaeological context, *HAL archives-ouvertes.fr*. Available from: https://hal.archives-ouvertes.fr/hal-o1162404v2

Lanos, P. A., and P. H. Lanos (2016), Chronomodel: Chronological Modelling of Archaeological Data Using Bayesian Statistics,

Lanphere, M., D. Champion, L. Melluso, V. Morra, A. Perrotta, C. Scarpati, D. Tedesco, and A. Calvert (2007), 40Ar/39Ar ages of the AD 79 eruption of Vesuvius, Italy, *Bulletin of Volcanology*, *69*(3), 259–263, doi:10.1007/s00445-006-0071-8.

Lanting, J. N., A. T. Aerts-Bijma, and J. van der Plicht (2001), Dating Of Cremated Bones, *Radiocarbon*, *43*(2A), 249–254, doi:10.2458/azu_js_rc.v.3946.
Lascu, I., J. M. Feinberg, J. A. Dorale, H. Cheng, and R. L. Edwards (2016), Age of the Laschamp excursion determined by U-Th dating of a speleothem geomagnetic record from North America, *Geology*, *44*(2), 139–142, doi:10.1130/G37490.1.
Latham, A. G. (2001), Uranium-Series Dating, in *Handbook of Archaeological Sciences*, edited by D. R. Brothwell and A. M. Pollard, pp. 63–72, John Wiley & Sons, Ltd., West Sussex.
Lauer, N., and A. Vengosh (2016), Age Dating Oil and Gas Wastewater Spills Using Radium Isotopes and Their Decay Products in Impacted Soil and Sediment, *Environmental Science & Technology Letters*, *3*(5), 205–209.
Lee, S., C. Bronk Ramsey, and A. Mazar (2013), Iron Age Chronology in Israel: Results from Modeling with a Trapezoidal Bayesian Framework, *Radiocarbon*, *55*(2–3), 731–740, doi:10.2458/azu_js_rc.55.16213.
Libby, W. F. (1952), *Radiocarbon Dating*, University of Chicago Press, Chicago.
Libby, W. F., E. C. Anderson, and J. R. Arnold (1949), Age determination by radiocarbon content: world-wide assay of natural radiocarbon., *Science (New York, N.Y.)*, *109*(2827), 227–228, doi:10.1126/science.109.2827.227.
Liritzis, I. (2010), Strofilas (Andros Island, Greece): new evidence for the cycladic final neolithic period through novel dating methods using luminescence and obsidian hydration, *Journal of Archaeological Science*, *37*(6), 1367–1377, doi:10.1016/j.jas.2009.12.041.
Liritzis, I., and N. Laskaris (2011), Fifty years of obsidian hydration dating in archaeology, *Journal of Non-Crystalline Solids*, *357*(10), 2011–2023, doi:10.1016/j.jnoncrysol.2011.02.048.
Liritzis, I., A. K. Singhvi, J. K. Feathers, G. A. Wagner, A. Kadereit, N. Zacharias, and S.-H. Li (2013), *Luminescence Dating in Archaeology, Anthropology, and Geoarchaeology: An Overview*, Springer, New York.
Livermore, P. W., A. Fournier, and Y. Gallet (2014), Core-flow constraints on extreme archeomagnetic intensity changes, *Earth and Planetary Science Letters*, *387*, 145–156, doi:10.1016/j.epsl.2013.11.020.
Ludwig, K. R. (2003), Mathematical–Statistical Treatment of Data and Errors for 230Th/U Geochronology, *Reviews in Mineralogy and Geochemistry*, *52*, 631–656, doi:10.2113/0520631.
Maher, B. A. (1988), Magnetic properties of some synthetic sub-micron magnetites, *Geophysical Journal*, *94*(1), 83–96, doi:10.1111/j.1365-246X.1988.tb03429.x.
Manning, S. W., B. Kromer, P. I. Kuniholm, and M. W. Newton (2001), Anatolian tree rings and a new chronology for the east Mediterranean Bronze-Iron Ages., *Science (New York, N.Y.)*, *294*(5551), 2532–5, doi:10.1126/science.1066112.
Manning, S. W., B. Kromer, P. I. Kuniholm, and M. W. Newton (2003), Confirmation of near-absolute dating of east Mediterranean Bronze-Iron Dendrochronology, *Antiquity*, *77*(295).

De Marco, E., V. Spatharas, M. Gómez-Paccard, A. Chauvin, and D. Kondopoulou (2008), New archaeointensity results from archaeological sites and variation of the geomagnetic field intensity for the last 7 millennia in Greece, *Physics and Chemistry of the Earth, Parts A/B/C*, *33*(6–7), 578–595, doi:10.1016/j.pce.2008.02.025.

Mazar, A. (1997), Iron Age Chronology: A Reply to I. Finkelstein, *Levant*, *29*, 157–167.

Mazar, A. (2005), The Debate over the Chronology of the Iron Age in the Southern Levant, in *The Bible and Radiocarbon Dating: Archaeology, Text, and Science*, edited by T. E. Levy and T. Higham, pp. 13–28, Equinox Publishing, London.

Mazar, A. (2010), Archaeology and Biblical Narrative: The Case of the United Monarchy, in *One God - One Cult - One Nation: Archaeological and Biblical Perspectives*, edited by R. Kratz, H. Spieckermann, B. Corzilius, and T. Pilger, pp. 29–58, De Gruyter, Berlin/New York.

Mazar, A. (2011), Chronology Debate: Is the Gap Narrowing? Another Viewpoint, *Near Eastern Archaeology*, *74*(2), 105–111.

Mazar, A., and C. Bronk Ramsey (2008), 14C Dates and the Iron Age Chronology of Israel: A Response, *Radiocarbon*, *50*(2), 159–180.

Mazar, A., and C. Bronk Ramsey (2010), A response to Finkelstein and Piasetzky's criticism and "new perspective," *Radiocarbon*, *52*(4), 1681–1688.

McCabe, C., M. Jackson, and B. B. Ellwood (1985), Magnetic anisotropy in the Trenton Limestone: Results of a new technique, anisotropy of anhysteretic susceptibility, *Geophysical Research Letters*, *12*(6), 333–336, doi:10.1029/GL012i006p00333.

McDermott, F., R. Grün, C. B. Stringer, and C. J. Hawkesworth (1993), Mass-spectrometric U-series dates for Israeli Neanderthal/ early modern human sites, *Nature*, *363*(6426), 252–255.

McKinny, C., B. Yang, D. Cassuto, and I. Shai (2018), Illuminating a Canaanite and Judahite Town: The Archaeological Background of Tel Burna, in *The Old Testament in Theology and Teaching: Essays in Honor of Kay Fountain*, edited by T. Chai and D. Johnson, Wipf and Stock, Eugene, Oregon.

Mercier, N., H. Valladas, C. Falguères, Q. Shao, A. Gopher, R. Barkai, J.-J. Bahain, L. Vialettes, J.-L. Joron, and J.-L. Reyss (2013), New datings of Amudian layers at Qesem Cave (Israel): results of TL applied to burnt flints and ESR/U-series to teeth, *Journal of Archaeological Science*, *40*(7), 3011–3020, doi:10.1016/j.jas.2013.03.002.

Michels, J. W., I. S. T. Tong, and C. M. Nelson (1983), Obsidian Dating and East African Archeology, *Science*, *219*(4583), 361–366.

Moskowitz, B. M. (2007), Magnetization, Anhysteretic Remanent, in *Encyclopedia of Geomagnetism and Paleomagnetism*, pp. 572–580, Springer-Verlag Netherlands, Netherlands.

Moskowitz, B. M., and S. K. Banerjee (1979), Grain Size Limits for Pseudosingle Domain Behavior in Magnetite: Implications for Paleomagnetism, *IEEE Transactions on Magnetics*, *15*(5), 1241–1246, doi:10.1109/TMAG.1979.1060319.

Muxworthy, A. (2003), Effect of magnetostatic interactions on the hysteresis parameters of single-domain and pseudo-single-domain grains, *Journal of Geophysical Research*, *108*(B11), 2517, doi:10.1029/2003JB002588.

Nagata, T., Y. Arai, and K. Momose (1963), Secular variation of the geomagnetic total force during the last 5000 years, *Journal of Geophysical Research*, *68*(18), 5277, doi:10.1029/JZ068i018p05277.

Néel, L. (1949), Théorie du trainage magnétique des ferro magnétiques en grains fins avec applications aux terres cuites, *Annales de Géophysique*, *5*, 99–137.

Néel, L. (1955), Some theoretical aspects of rock-magnetism, *Advances in Physics*, *4*(14), 191–243.

Nilsson, A., R. Holme, M. Korte, N. Suttie, and M. Hill (2014), Reconstructing Holocene geomagnetic field variation: new methods, models and implications, *Geophysical Journal International*, *198*(1), 229–248, doi:10.1093/gji/ggu120.

Niu, M., T. J. Heaton, P. G. Blackwell, and C. E. Buck (2013), The Bayesian approach to radiocarbon calibration curve estimation: the IntCal13, Marine13, and SHCal13 methodologies, *Radiocarbon*, *55*(4), 1905–1922, doi:10.2458/azu_js_rc.55.17222.

Nydal, R. (1968), Further investigation on the transfer of radiocarbon in nature, *Journal of Geophysical Research*, *73*(12), 3617–3635.

Odah, H. (1999), Improvement of the secular variation curve of the geomagnetic field in Egypt during the last 6000 years, *Earth Planets Space*, *51*, 1325–1329.

Odah, H., F. Heider, A. G. Hussain, V. Hoffmann, H. Soffel, and M. ElGamili (1995), Paleointensity of the geomagnetic field in Egypt from 4000 BC to 150 AD using the Thellier method, *Journal of Geomagnetism and Geoelectricity*, *47*, 41–58.

Ortega, R., R. Maire, G. Devès, and Y. Quinif (2005), High-resolution mapping of uranium and other trace elements in recrystallized aragonite-calcite speleothems from caves in the Pyrenees (France): Implication for U-series dating, *Earth and Planetary Science Letters*, *237*(3–4), 911–923, doi:10.1016/j.epsl.2005.06.045.

Ortiz, S. M., and S. R. Wolff (2017), Tel Gezer Excavations 2006-2015: The Transformation of a Border City, in *The Shephelah during the Iron Age: Recent Archaeological Studies*, edited by O. Lipschits and A. M. Maeir, pp. 61–102, Eisenbrauns, Winona Lake, Indiana.

Osete, M. L., A. Chauvin, G. Catanzariti, A. Jimeno, S. A. Campuzano, J. P. Benito-Batanero, C. Tabernero-Galán, and P. Roperch (2016), New archaeomagnetic data recovered from the study of celtiberic remains from central Spain (Numantia and Ciadueña, 3rd-1st centuries BC). Implications on the fidelity of the Iberian paleointensity database, *Physics of the Earth and Planetary Interiors*, *260*, 74–86, doi:10.1016/j.pepi.2016.09.006.

Panovska, S., M. Korte, C. C. Finlay, and C. G. Constable (2015), Limitations in paleomagnetic data and modelling techniques and their impact on Holocene geomagnetic field models, *Geophysical Journal International*, *202*(1), 402–418, doi:10.1093/gji/ggv137.

Paterson, G. A., L. Tauxe, A. J. Biggin, R. Shaar, and L. C. Jonestrask (2014), On improving the selection of Thellier-type paleointensity data, *Geochemistry, Geophysics, Geosystems*, *15*, 1180–1192, doi:10.1002/2013GC005135.Received.

Pavón-Carrasco, F. J., and A. De Santis (2016), The South Atlantic Anomaly: The Key for a Possible Geomagnetic Reversal, *Frontiers in Earth Science*, *4*(April), 40, doi:10.3389/feart.2016.00040.

Pavón-Carrasco, F. J., M. Gómez-Paccard, G. Hervé, M. L. Osete, and A. Chauvin (2014), Intensity of the geomagnetic field in Europe for the last 3 ka: Influence of data quality on geomagnetic field modeling, *Geochemistry, Geophysics, Geosystems*, *15*, 2515–2530, doi:10.1002/2014GC005311.Received.

Pearson, C. L., D. S. Dale, P. W. Brewer, P. I. Kuniholm, J. Lipton, and S. W. Manning (2009), Dendrochemical analysis of a tree-ring growth anomaly associated with the Late Bronze Age eruption of Thera, *Journal of Archaeological Science*, *36*(6), 1206–1214, doi:10.1016/j.jas.2009.01.009.

Pearson, C. L., C. B. Griggs, P. I. Kuniholm, P. W. Brewer, T. Ważny, and L. Canady (2012), Dendroarchaeology of the mid-first millennium AD in Constantinople, *Journal of Archaeological Science*, *39*(11), 3402–3414, doi:10.1016/j.jas.2012.05.024.

Pike, a W. G., and P. B. Pettitt (2003), U-series Dating and Human Evolution, *Reviews in Mineralogy and Geochemistry*, *52*(15), 607–630, doi:10.2113/0520607.

Pinto Jr, O., W. D. Gonzalez, I. R. C. A. Pinto, A. L. C. Gonzalez, and O. Mendes Jr (1992), The South Atlantic Magnetic Anomaly : three decades of research, *Journal of Atmospheric and Terrestrial Physics*, *54*(9), 1129–1134.

van der Plicht, J., and H. J. Bruins (2001), Radiocarbon Dating in Near-Eastern Contexts: Confusion and Quality Control, *Radiocarbon*, *43*(3), 1155–1166.

van der Plicht, J., H. J. Bruins, and A. J. Nijboer (2009), The Iron Age Around the Mediterranean: A high chronology perspective from the Groningen radiocarbon database, *Radiocarbon*, *51*(1), 213–242.

Pokhil, T. G., and B. M. Moskowitz (1997), Magnetic domains and domain walls in pseudo-single-domain magnetite studied with magnetic force microscopy, *Journal of Geophysical Research*, *102*(B10), 22681–22694, doi:10.1029/97JB01856.

Rae, A. M., and M. Ivanovich (1986), Successful application of uranium series dating of fossil bone, *Applied Geochemistry*, *1*(3), 419–426, doi:10.1016/0883-2927(86)90026-0.

Rapp, G., and C. L. Hill (2006), *Geoarchaeology: The Earth-Science Approach to Archaeological Interpretation*, 2nd ed., Yale University Press, New Haven and London.

Reimer, P. J. et al. (2004), Intcal04 Terrestrial Radiocarbon Age Calibration, 0-26 Cal KYR BP, *Radiocarbon*, *46*(3), 1029–1058.

Reimer, P. J., T. A. Brown, and R. W. Reimer (2008), Discussion: Reporting and Calibration of Post-Bomb 14C Data, *Radiocarbon*, *46*(3), 1299–1304, doi:10.2458/azu_js_rc.v.4183.

Reimer, P. J. et al. (2009), Intcal09 and Marine09 Radiocarbon Age Calibration Curves, 0-50,000 Years Cal BP, *Radiocarbon*, *51*(4), 1111–1150.

Reimer, P. J., E. Bard, A. Bayliss, J. W. Beck, P. G. Blackwell, and C. B. Ramsey (2013a), IntCal13 and Marine13 Radiocarbon Age Calibration Curves 0–50,000 Years cal BP, *Radiocarbon*, *55*(4), 1869–1887, doi:10.2458/azu_js_rc.55.16947.

Reimer, P. J. et al. (2013b), Selection and Treatment of Data for Radiocarbon Calibration: An Update to the International Calibration (IntCal) Criteria, *Radiocarbon*, *55*(4), 1923–1945, doi:10.2458/azu_js_rc.55.16955.
Renfrew, C. (1979), *Before Civilization: The Radiocarbon Revolution and Prehistoric Europe*, Cambridge University Press, Cambridge.
Renne, P. R., W. D. Sharp, A. L. Deino, G. Orsi, and L. Civetta (1997), 40Ar/39Ar Dating into the Historical Realm: Calibration Against Pliny the Younger, *Science*, *277*, 1279–1280, doi:10.1126/science.277.5330.1279.
Rice, P. M. (2005), *Pottery Analysis: A Sourcebook*, University of Chicago Press, Chicago.
Richards, D. A., and J. A. Dorale (2003), Uranium-series Chronology and Environmental Applications of Speleothems, *Reviews in Mineralogy and Geochemistry*, *52*(1), 4086–460, doi:10.2113/0520407.
Riisager, P., and J. Riisager (2001), Detecting multidomain magnetic grains in Thellier palaeointensity experiments, *Physics of the Earth and Planetary Interiors*, *125*(1–4), 111–117, doi:10.1016/S0031-9201(01)00236-9.
Rimbert, F. (1959), Contribution à l'étude de l'action des champs alternatifs sur les aimantations remanentes de roches. Applications geophysiques, *Revue de l'Institut français du Pétrole et Annales des combustibles liquides*, *14*(17–54).
Rittenour, T. M. (2008), Luminescence dating of fluvial deposits: applications to geomorphic, palaeoseismic and archaeological research, *Boreas*, *37*(4), 613–635, doi:10.1111/j.1502-3885.2008.00056.x.
Rogers, A. K. (2010), Accuracy of obsidian hydration dating based on obsidian–radiocarbon association and optical microscopy, *Journal of Archaeological Science*, *37*(12), 3239–3246, doi:10.1016/j.jas.2010.07.023.
Rogers, J., J. M. W. Fox, and M. J. Aitken (1979), Magnetic anisotropy in ancient pottery, *Nature*, *277*(22), 644–646.
Schnepp, E. (2003), Paleomagnetic directions and thermoluminescence dating from a bread oven-floor sequence in Lübeck (Germany): A record of 450 years of geomagnetic secular variation, *Journal of Geophysical Research*, *108*(B2), 2078, doi:10.1029/2002JB001975.
Schnepp, E., P. Lanos, and A. Chauvin (2009), Geomagnetic paleointensity between 1300 and 1750 A.D. derived from a bread oven floor sequence in Lübeck, Germany, *Geochemistry, Geophysics, Geosystems*, *10*(8), n/a-n/a, doi:10.1029/2009GC002470.
Schwarcz, H. P. (1980), Absolute age determination of archaeological sites by uranium-series dating of travertines, *Archaeometry*, *22*, 3–24.
Schwarcz, H. P. (1997), Uranium Series Dating, in *Chronometric Dating in Archaeology*, edited by R. E. Taylor and M. J. Aitken, pp. 159–182, Plenum Press, New York.
Schwarcz, H. P., and W. J. Rink (2001), Dating methods for sediments of caves and rockshelters with examples from the Mediterranean Region, *Geoarchaeology*, *16*(4), 355–371, doi:10.1002/gea.1008.

Schwarcz, H. P., B. Blackwell, P. Goldberg, and A. E. Marks (1979), Uranium series dating of travertine from archaeological sites, Nahal Zin, Israel [10], *Nature*, *277*(5697), 558–560, doi:10.1038/277558a0.

Selkin, P. A., and L. Tauxe (2000), Long-term variations in palaeointensity, *Philosophical Transactions of the Royal Society A: Mathematical, Physical and Engineering Sciences*, *358*, 1065–1088, doi:10.1098/rsta.2000.0574.

Selkin, P. A., J. S. Gee, L. Tauxe, W. P. Meurer, and A. J. Newell (2000), The effect of remanence anisotropy on paleointensity estimates: a case study from the Archean Stillwater Complex, *Earth and Planetary Science Letters*, *183*, 403–416.

Shaar, R., and L. Tauxe (2013), Thellier GUI: An integrated tool for analyzing paleointensity data from Thellier-type experiments, *Geochemistry, Geophysics, Geosystems*, *14*(3), 677–692, doi:10.1002/ggge.20062.

Shaar, R., E. Ben-Yosef, H. Ron, L. Tauxe, A. Agnon, and R. Kessel (2011), Geomagnetic field intensity: How high can it get? How fast can it change? Constraints from Iron Age copper slag, *Earth and Planetary Science Letters*, *301*(1–2), 297–306, doi:10.1016/j.epsl.2010.11.013.

Shaar, R., L. Tauxe, E. Ben-yosef, V. Kassianidou, B. Lorentzen, J. M. Feinberg, and T. E. Levy (2015), Decadal-scale variations in geomagnetic field intensity from ancient Cypriot slag mounds, *Geochemistry, Geophysics, Geosystems*, *16*(1), 195–214, doi:10.1002/2014GC005455.

Shaar, R., L. Tauxe, H. Ron, A. Agnon, Y. Ebert, S. Zuckerman, and I. Finkelstein (2016), Large geomagnetic field anomalies revearled in Bronze to Iron Age archeomagnetic data from Tel Megiddo and Tel Hazor, Israel, *Earth and Planetary Science Letters*, *442*, 173–185, doi:http://dx.doi.org/10.1016/j.epsl.2016.02.038.

Shai, I., and C. McKinny (2018), Canaanite Religion at Tel Burna in the 13th Century BCE, *Ancient Near East Today*, *VI*(3), 1–11.

Shai, I., C. McKinny, and J. Uziel (2015), Late Bronze Age Cultic Activity in Ancient Canaan: A View from Tal Burna, *BASOR*, *374*, 115–133, doi:10.5615/bullamerschoorie.374.0115.

Sharon, I., A. Gilboa, T. A. J. Jull, and E. Boaretto (2007), Report on the First Stage of the Iron Age Dating Project in Israel: Supporting the Low Chronology, *Radiocarbon*, *49*(1), 1–46.

Sharp C., S. I. O. A. Š. L. Mck. C. C. D. (2017), The Agricultural Landscape of Tel Burna : Ecology and Economy of a Bronze Age / Iron Age Settlement in the Southern Levant, *Journal of Landscape Ecology*, *10*(3), 165–188.

Spassov, S., and J. Hus (2006), Estimating baking temperatures in a Roman pottery kiln by rock magnetic properties: implications of thermochemical alteration on archaeointensity determinations, *Geophysical Journal International*, *167*(2), 592–604, doi:10.1111/j.1365-246X.2006.03114.x.

Spatharas, V., D. Kondopoulou, E. Aidona, and K. G. Efthimiadis (2011), New magnetic mineralogy and archaeointensity results from Greek kilns and baked clays, *Stud. Geophys. Geod.*, *55*, 131–157.

Spennemann, D. H. R., and M. J. Head (1998), Tongan Pottery Chronology, 14C Dates and the Hardwater Effect, *Quaternary Geochronology*, *17*, 1047–1056.

St Pierre, E., J. xin Zhao, and E. Reed (2009), Expanding the utility of Uranium-series dating of speleothems for archaeological and palaeontological applications, *Journal of Archaeological Science*, *36*(7), 1416–1423, doi:10.1016/j.jas.2009.02.004.

St Pierre, E., J. Zhao, Y. Feng, and E. Reed (2012), U-series dating of soda straw stalactites from excavated deposits: method development and application to Blanche Cave, Naracoorte, South Australia, *Journal of Archaeological Science*, *39*(4), 922–930, doi:10.1016/j.jas.2011.10.027.

Stacey, F. D. (1960), Magnetic anisotropy of igneous rocks, *Journal of Geophysical Research*, *65*(8), 2429–2442, doi:10.1029/JZ065i008p02429.

Stacey, F. D. (1963), The physical theory of rock magnetism, *Advances in Physics*, *12*(45), 45–133.

Stacey, F. D., and S. K. Banerjee (1974), *The Physical Principals of Rock Magnetism*, Elsevier, New York.

Steier, P., W. Rom, and S. Puchegger (2001), New methods and critical aspects in Bayesian mathematics for 14C calibration, *Radiocarbon*, *43*(2), 373–380.

Stenström, K. E., G. Skog, E. Georgiadou, J. Genberg, and A. Johansson (2011), *A guide to radiocarbon units and calculations*, Lund.

Sternberg, R. S. (1990), The geophysical basis of archaeomagnetic dating, in *Archaeomagnetic Dating*, edited by J. L. Eighmy and R. S. Sternberg, pp. 6–32, University of Arizona Press, Tucson.

Sternberg, R. S. (2001), Magnetic properties and archaeomagnetism, in *Handbook of Archaeological Sciences*, edited by D. R. Brothwell and A. M. Pollard, pp. 73–79, John Wiley & Sons, Ltd., Chichester.

Sternberg, R. S., and R. H. McGuire (1990), Techniques for constructing secular variation curves and for interpreting archaeomagnetic dates, in *Archaeomagnetic Dating*, edited by J. L. Eighmy and R. S. Sternberg, pp. 109–134, University of Arizona Press, Tucson.

Stillinger, M. D., J. M. Feinberg, and E. Frahm (2015), Refining the archaeomagnetic dating curve for the Near East: New intensity data from Bronze Age ceramics at Tell Mozan, Syria, *Journal of Archaeological Science*, *53*, 345–355, doi:10.1016/j.jas.2014.10.025.

Stillinger, M. D., J. W. Hardin, J. M. Feinberg, and J. A. Blakely (2016), Archaeomagnetism as a Complementary Dating Technique to Address the Iron Age Chronology Debate in the Levant, *Near Eastern Archaeology*, *79*(2), 90–106, doi:10.5615/neareastarch.79.2.0090.

Stuiver, M. (1961), Variations in Radiocarbon Concentration and Sunspot Activity, *Journal of Geophysical Research*, *66*(1), 273–276.

Stuiver, M., and H. A. Polach (1977), Discussion: Reporting of 14C Data, *Radiocarbon*, *19*(3), 355–363, doi:10.2458/azu_js_rc.v.493.

Stuiver, M., and H. E. Suess (1966), On the Relationship Between Radiocarbon Dates and True Sample Ages, *Radiocarbon*, *8*, 534–540.

von Suchodoletz, H., M. Fuchs, and L. Zöller (2008), Dating Saharan dust deposits on Lanzarote (Canary Islands) by luminescence dating techniques and their implication for palaeoclimate reconstruction of NW Africa, *Geochemistry, Geophysics, Geosystems*, *9*(2), n/a, doi:10.1029/2007GC001658.

Suess, H. E. (1955), Radiocarbon Concentration in Modern Wood, *Science*, *122*(3166), 415–417.

Suess, H. E. (1965), Secular variations of the cosmic-ray-produced carbon 14 in the atmosphere and their interpretations, *Journal of Geophysical Research*, *70*(23), 5937–5952.

Suess, H. E. (1971), Climate Changes and the Atmospheric Radiocarbon Level, *Palaeogeography, Palaeoclimatology, Palaeoecology*, *10*, 199–202.

Taçon, P. S. C., M. Aubert, L. Gang, Y. Decong, L. Hong, S. K. May, S. Fallon, J. Xueping, D. Curnoe, and A. I. R. Herries (2012), Uranium-series age estimates for rock art in southwest China, *Journal of Archaeological Science*, *39*(2), 492–499, doi:10.1016/j.jas.2011.10.004.

Tarduno, J. A., M. K. Watkeys, T. N. Huffman, R. D. Cottrell, E. G. Blackman, A. Wendt, C. A. Scribner, and C. L. Wagner (2015), Antiquity of the South Atlantic Anomaly and evidence for top-down control on the geodynamo, *Nature Communications*, *6*, 1–6, doi:10.1038/ncomms8865.

Tauxe, L. (2016), *Essentials of Paleomagnetism: 4th Web Edition*, 4th ed., University of California Press.

Tauxe, L., and H. Staudigel (2004), Strength of the geomagnetic field in the Cretaceous Normal Superchron: new data from submarine basaltic glass of the Troodos Ophiolite, *Geochemistry Geophysics Geosystems*, *5*(2), doi:10.1029/2003GC000635.

Tauxe, L., R. Shaar, L. Jonestrask, N. L. Swanson-Hysell, R. Minnett, A. A. P. Koppers, C. G. Constable, N. Jarboe, K. Gaastra, and L. Fairchild (2016), PmagPy: Software package for paleomagnetic data analysis and a bridge to the Magnetics Information Consortium (MagIC) Database, *Geochemistry, Geophysics, Geosystems*, *17*, doi:10.1002/2016GC006307.

Taylor, R. E. (2001), Radiocarbon Dating, in *Handbook of Archaeological Sciences*, edited by D. R. Brothwell and A. M. Pollard, pp. 23–34, John Wiley & Sons, Ltd., West Sussex.

Taylor, R. E., and M. J. Aitken (Eds.) (1997), *Chronometric Dating in Archaeology*, Plenum Press, New York.

Taylor, R. E., C. V. Haynes Jr., D. L. Kirner, and J. R. Southon (1999), Radiocarbon Analysis of Modern Organics at Monte Verde, Chile: No evidence for a local reservoir effect, *American Antiquity*, *64*(3), 455–460.

Tema, E. (2009), Estimate of the magnetic anisotropy effect on the archaeomagnetic inclination of ancient bricks, *Physics of the Earth and Planetary Interiors*, *176*(3–4), 213–223, doi:10.1016/j.pepi.2009.05.007.

Thébault, E. et al. (2015), International Geomagnetic Reference Field: the 12th generation, *Earth, Planets and Space*, *67*(1), 79, doi:10.1186/s40623-015-0228-9.

Thellier, E., and O. Thellier (1959), Sur l'intensité du champ magnétique terrestre dans le passé historique et géologique, *Annales de Geophysique*, *15*, 285–378.

Toffolo, M., E. Arie, M. A. S. Martin, E. Boaretto, and I. Finkelstein (2014), Absolute Chronology of Megiddo, Israel, in the Late Bronze and Iron Ages: High-Resolution Radiocarbon Dating, *Radiocarbon*, *56*(1), 221–244, doi:10.2458/56.16899.

Troja, S. O., A. Cro, and A. M. Gueli (1996), Characterization and Thermoluminescence Dating of Prehistoric Pottery Sherds from Milena, *Archaeometry*, *38*(1), 113–128.

Ussishkin, D. (2015), Gath, Lachish and Jerusalem in the 9th Cent . B . C . E . – an Archaeological Reassessment *, in *Zeitschrift des Deutschen Palästina-Vereins*, edited by J. Kamlah, A. Lichtenberger, and M. Witte.

Uyeda, S., M. D. Fuller, J. C. Belshé, and R. W. Girdler (1963), Anisotropy of magnetic susceptibility of rocks and minerals, *Journal of Geophysical Research*, *68*(1), 279–291, doi:10.1029/JZ068i001p00279.

de Vries, H. (1958), Variation in concentration of radiocarbon with time and location on Earth, in *Koninklijke Nederlandse Akademie van Wetenschappen, B61*, pp. 94–102.

Walter, R. C. (1997), Potassium-Argon/Argon-Argon Dating Methods, in *Chronometric Dating in Archaeology*, edited by R. E. Taylor and M. J. Aitken, pp. 97–126, Plenum Press, New York.

Walton, D. (1980), Time-temperature relations in the magnetization of assemblies of single domain grains, *Nature*, *286*(17), 245–247.

Walton, D. (1986), Alteration and its effects on the reproducibility of archaeomagnitudes from Tel El-Amarna, *Journal of Geomag. Geoelectr.*, *38*, 1349–1352.

Walton, D. (1990), The intensity of the geomagnetic field in the eastern Mediterranean between 1600 BC and AD 400, *Journal of Geomag. Geoelectr.*, *42*, 929–936.

Waters, M. R., and T. W. Stafford (2013), The First Americans : A Review of the Evidence for the Late-Pleistocene Peopling of the Americas, *Paleoamerican Odyssey*, 543–562.

Yu, Y. (2011), Importance of cooling rate dependence of thermoremanence in paleointensity determination, *Journal of Geophysical Research*, *116*(B9), B09101, doi:10.1029/2011JB008388.

Appendix A

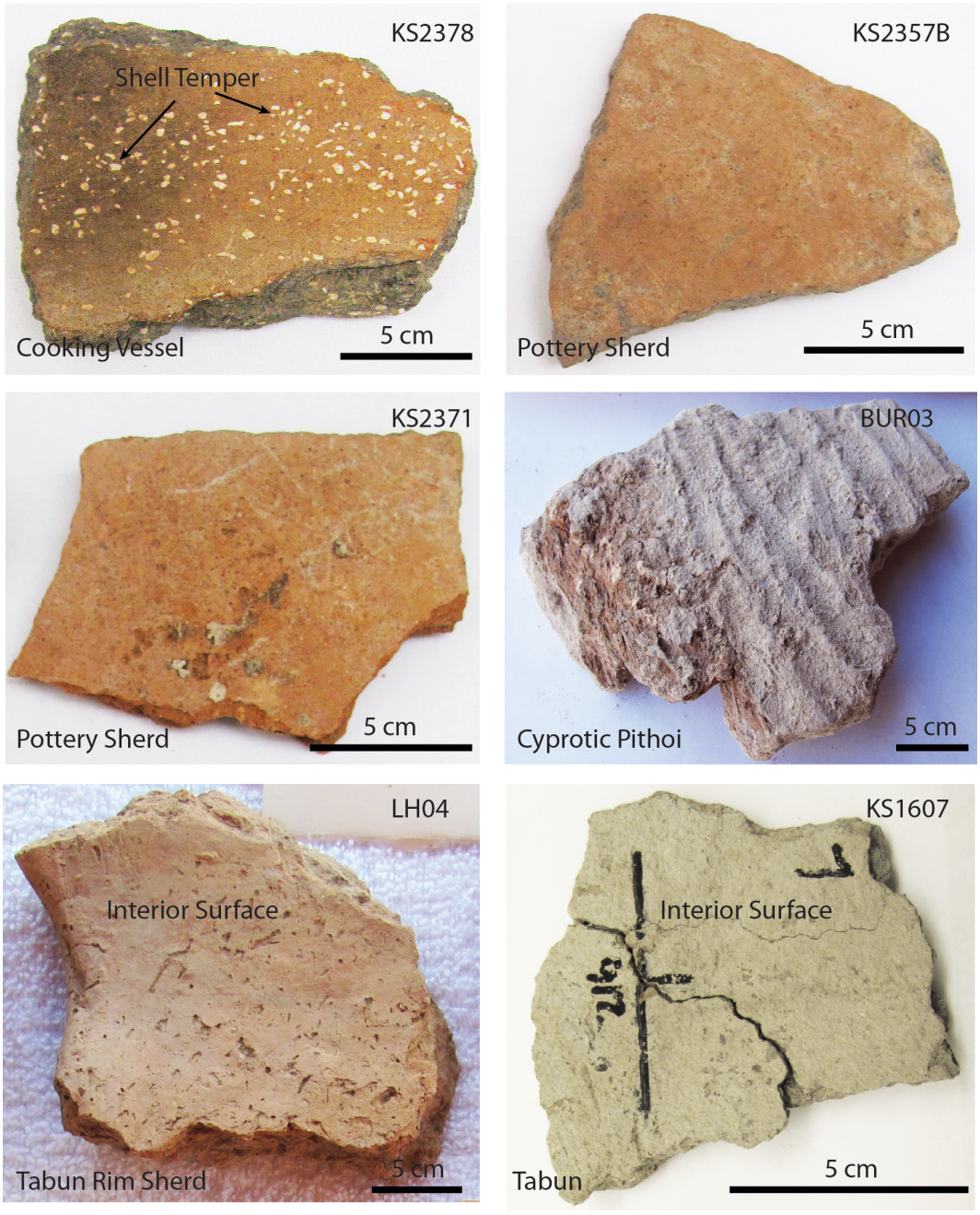

Figure A - 1 Representative Samples

Table A - 1 Rock Magnetic Properties of Khirbet Summeily Samples

Sample	Material	Avg NRM	Bulk Susceptibility (χ)[1]	Low Field FD[2] χ	High Field FD[3] χ	Avg FD χ	MDF
KS1411	TabunKS01	3.03E-04	8.00E-04	5.63E-07	5.32E-07	5.5	16.4
KS1412	TabunKS01	8.85E-04	2.48E-03	1.61E-06	1.52E-06	5.5	—
KS1413	TabunKS01	2.65E-04	6.68E-04	2.89E-07	4.56E-07	-329.5	19.3
KS1418	TabunKS02	4.06E-04	1.59E-03	9.44E-07	8.94E-07	5.3	24.6
KS1474	TabunKS02	6.54E-04	1.16E-06	1.18E-06	1.12E-06	5.4	—
KS1607	TabunKS02	3.87E-04	1.65E-03	1.13E-06	1.07E-06	5.3	—
KS1608	TabunKS02	3.03E-04	1.58E-03	—	—	—	20.1
KS1609	TabunKS02	3.70E-04	1.78E-03	9.95E-07	9.45E-07	5.0	24.3
KS1419	Pottery	9.53E-04	2.16E-06	—	—	—	—
KS2348A	Pottery	2.79E-03	—	5.57E-06	5.21E-06	6.5	26.0
KS2357A	Pottery	5.20E-04	8.25E-07	7.91E-07	7.27E-07	8.1	31.8
KS2357B	Pottery	1.05E-03	1.14E-06	1.10E-06	1.02E-06	7.1	34.3
KS2369	Pottery	3.80E-04	6.49E-07	6.62E-07	6.03E-07	9.0	54.2
KS2371	Pottery	9.27E-04	1.13E-06	1.10E-06	1.01E-06	8.1	24.9
KS2372	Pottery	6.72E-04	1.02E-06	1.00E-06	9.17E-07	8.3	28.0
KS2373	TabunKS04	6.31E-04	—	—	—	—	15.3
KS2378	Pottery	2.75E-03	3.88E-06	3.78E-06	3.53E-06	6.6	45.2
KS710	Pottery	5.37E-04	1.36E-06	1.38E-06	1.27E-06	8.1	48.0
KSG24	Pottery	2.10E-03	4.15E-06	4.13E-06	3.79E-06	8.4	23.0
KSMDS01	Pottery	3.01E-03	—	3.10E-06	2.85E-06	8.1	26.6
KSMDS04	Pottery	1.41E-03	—	2.32E-06	2.15E-06	7.3	28.8

NRM = Natural Remanent Magnetization, FD = frequency dependence of susceptibility (χ), MDF = mean destructive field, the field value when 50% of the remanence is removed during AF demagnetization experiment.

[1] Bulk Susceptibility at 920 Hz and 300 A/m

[2] Low field FD measured at 465 Hz; [3] High field FD measured at 4650 Hz

Table A - 2 Archaeointensity and Criteria Results by Specimen

Specimen	Material	Temp Min (°C)	Temp Max (°C)	Br (µT)	AARM Corr Ba (µT)	CRC	Ba (µT) all Corr	Error (Ba)	σ	n	pTRM Cks	IZZI Field (µT)	β	FRAC	SCAT	DANG	MAD	g
Tel Burna																		
Bur01A	TabunB01	250	600	45.3	44.8	0.88	**39.4**	1.58	0.04	13	6	50	0.05	0.72	TRUE	6.7	9.0	0.89
Bur01B	TabunB01	225	575	47.3	46.4	0.88	**40.8**	1.22	0.03	13	6	50	0.03	0.74	TRUE	1.5	7.4	0.90
Bur01C	TabunB01	225	600	50.5	49.7	0.88	**43.7**	2.19	0.05	14	6	50	0.05	0.72	TRUE	3.4	8.6	0.89
Bur03A	TabunB01	250	600	51.9	52.4	0.88	**46.1**	0.92	0.02	13	6	50	0.02	0.75	TRUE	1.7	7.6	0.87
Bur03B	TabunB01	225	600	53.2	52	0.88	**45.8**	1.37	0.03	14	6	50	0.03	0.78	TRUE	1.1	8.4	0.88
Bur03C	TabunB01	250	600	52.5	51.3	0.88	**45.1**	1.35	0.03	13	6	50	0.03	0.73	TRUE	0.9	6.8	0.87
BUR04A	TabunB02	150	575	56.2	56	*0.90*	**50.4**	3.53	0.07	16	7	50	0.06	0.89	TRUE	4.7	10.0	0.92
BUR04B	TabunB02	275	575	45.9	45	*0.90*	**40.5**	1.62	0.04	13	7	50	0.05	0.7	TRUE	0.5	5.2	0.91
BUR04C	TabunB02	200	575	52.6	54.8	*0.90*	**49.3**	1.48	0.03	15	7	50	0.03	0.72	TRUE	5.6	9.5	0.91
Tel Eton																		
ET04B	Pottery	250	575	79.8	86.2	0.93	**80.2**	5.61	0.07	14	7	50	0.05	0.75	TRUE	1.1	3.9	0.91
ET04C	Pottery	250	575	81.6	87.5	0.93	**81.4**	6.51	0.08	14	7	50	0.05	0.74	TRUE	1.4	6.3	0.91
ET05B	Pottery	300	575	101	105.3	0.90	**94.8**	11.37	0.12	12	7	50	0.06	0.71	TRUE	6.5	6.4	0.87
ET05C	Pottery	275	575	96.8	100.8	0.90	**90.7**	9.98	0.11	13	7	50	0.06	0.83	TRUE	6.9	6.9	0.86

Tel Gezer

GZ03A	TabunGZ01	200	575	72.2	75.2	0.85	**63.9**	3.20	0.05	15	7	50	0.03	0.73	TRUE	4.7	9.8	0.91
GZ03B	TabunGZ01	250	575	77.2	82.1	0.85	**69.8**	4.19	0.06	14	7	50	0.04	0.78	TRUE	2.3	9.8	0.90
GZ03C	TabunGZ01	200	575	74.3	78.5	0.85	**66.7**	3.34	0.05	15	7	50	0.03	0.71	TRUE	2.0	8.1	0.91
GZ06B	TabunGZ01	200	575	76.7	81.2	0.85	**69.0**	4.14	0.06	15	7	50	0.04	0.88	TRUE	1.0	9.7	0.91
GZ07C	TabunGZ01	0	525	79.2	67.8	0.85	**57.6**	4.03	0.07	14	6	50	0.04	0.88	TRUE	2.3	8.8	0.88
GZ04B	Pottery	275	575	69.2	73.2	*0.87*	**63.7**	1.91	0.03	12	7	50	0.02	0.75	TRUE	1.5	5.6	0.90
GZ04C	Pottery	275	575	44.4	45.8	*0.87*	**39.8**	1.99	0.05	12	7	50	0.05	0.75	TRUE	1.7	5.1	0.89
GZ04E	Pottery	250	575	72.6	76.8	*0.87*	**66.8**	2.67	0.04	13	7	50	0.03	0.78	TRUE	3.1	7.4	0.88
GZ05B	Pottery	250	575	80.5	81.7	*0.85*	**69.4**	3.47	0.05	13	7	50	0.03	0.7	TRUE	0.4	4.8	0.91
GZ05D	Pottery	250	575	90.6	96.4	*0.85*	**81.9**	4.92	0.06	13	7	50	0.03	0.75	TRUE	0.7	4.8	0.90
GZ10C	Pottery	275	575	80.7	88.9	0.87	**77.3**	5.41	0.07	11	7	50	0.04	0.73	TRUE	2.3	7.6	0.87
GZ10D	Pottery	275	575	83.3	92.2	0.87	**80.2**	4.81	0.06	12	7	50	0.04	0.7	TRUE	1.4	5.9	0.88
GZ14A	Pottery	275	575	46.2	45.5	0.91	**41.4**	1.66	0.04	12	7	50	0.05	0.7	TRUE	1.5	4.6	0.89
GZ14B	Pottery	200	575	47.3	46.9	0.91	**42.7**	2.13	0.05	14	7	50	0.05	0.74	TRUE	0.9	4.5	0.90
GZ14C	Pottery	300	575	42.3	41.8	0.91	**38.0**	1.90	0.05	11	7	50	0.06	0.7	TRUE	1.4	3.4	0.89
GZ15A	Pottery	350	575	60.5	62.6	0.92	**57.6**	2.30	0.04	10	7	50	0.03	0.71	TRUE	3.6	4.7	0.87
GZ15B	Pottery	350	575	71.2	76.6	0.92	**70.5**	3.52	0.05	10	7	50	0.03	0.71	TRUE	2.4	5.8	0.87
GZ15E	Pottery	275	575	73.9	80.2	0.92	**73.8**	5.16	0.07	12	7	50	0.05	0.73	TRUE	4.1	8.6	0.89
GZ17C	Pottery	275	575	37.2	48.6	0.92	**44.7**	2.24	0.05	12	7	50	0.07	0.7	TRUE	1.1	6.8	0.88

GZ17D	Pottery	300	575	52.9	55.5	0.92	**51.1**	2.55	0.05	11	7	50	0.05	0.73	TRUE	2.7	6.8	0.88
GZ20B	Pottery	250	575	53.7	54.5	0.86	**46.9**	1.87	0.04	13	7	50	0.04	0.73	TRUE	3.6	9.4	0.89
GZ20C	Pottery	275	575	53.4	54.1	0.86	**46.5**	1.86	0.04	12	7	50	0.03	0.71	TRUE	2.1	5.4	0.89
Tel Halif																		
LH03A	TabunH02	300	600	75.7	75.4	0.91	**68.6**	4.12	0.06	11	6	50	0.04	0.74	TRUE	0.3	5.4	0.85
LH03B	TabunH02	250	600	81.1	80.4	0.91	**73.2**	4.39	0.06	13	6	50	0.04	0.71	TRUE	0.9	4.5	0.88
LH03C	TabunH02	225	600	68.1	67.5	0.91	**61.4**	3.69	0.06	14	6	50	0.04	0.7	TRUE	0.8	3.2	0.86
LH04A	TabunH02	275	600	83.1	75.7	0.91	**68.9**	6.20	0.09	12	6	50	0.06	0.73	TRUE	1.6	7.0	0.84
LH04B	TabunH02	225	600	82.6	75.4	0.91	**68.6**	4.12	0.06	14	6	50	0.04	0.76	TRUE	1.8	5.8	0.88
LH04C	TabunH02	200	600	72.4	66	0.91	**60.1**	3.60	0.06	15	6	50	0.04	0.83	TRUE	1.6	9.8	0.87
LH06A	TabunH03	250	575	63.5	65.3	0.92	**60.1**	4.21	0.07	12	6	50	0.06	0.74	TRUE	1.1	7.4	0.85
LH06B	TabunH03	200	575	65.8	67.8	0.92	**62.4**	3.74	0.06	14	6	50	0.05	0.71	TRUE	1.6	7.4	0.86
Khirbet Summeily																		
KS14112i	TabunKS01	175	500	57.1	52.7	0.83	**43.7**	1.31	0.03	13	7	50	0.03	0.7	TRUE	0.3	6.5	0.89
KS14132	TabunKS01	225	575	59.3	57.4	0.83	**47.6**	1.43	0.03	13	8	50	0.02	0.71	TRUE	1.5	3.6	0.88
KS14183	TabunKS02	150	575	45.8	46.9	0.86	**40.3**	2.42	0.06	16	8	50	0.06	0.76	TRUE	0.9	7.1	0.90
KS1474B	TabunKS02	225	575	52.1	54	0.86	**46.4**	2.32	0.05	13	5	50	0.05	0.75	TRUE	5.2	9.5	0.88
KS1474C	TabunKS02	225	575	61.3	64.3	0.86	**55.3**	2.76	0.05	13	5	50	0.04	0.74	TRUE	1.5	8.5	0.87
KS16071	TabunKS02	175	575	42.2	41.2	0.86	**35.4**	1.77	0.05	15	8	50	0.06	0.71	TRUE	1.8	7.1	0.88
KS16073	TabunKS02	0	450	65.6	64.2	0.86	**55.2**	3.31	0.06	16	7	50	0.04	0.73	TRUE	6.6	7.6	0.92
KS16074	TabunKS02	125	500	58.7	56.9	0.86	**48.9**	3.91	0.08	15	7	50	0.07	0.71	TRUE	2.4	9.9	0.90

KS16091	TabunKS02	175	550	49.4	47.4	0.86	**40.8**	2.85	0.07	14	8	50	0.07	0.73	TRUE	2.4	8.3	0.87
KS16093	TabunKS02	100	500	57.6	55.3	0.86	**47.6**	4.28	0.09	16	7	50	0.07	0.72	TRUE	2.9	9.2	0.89
KS2373A	TabunKS04	250	575	60.8	63	0.88	**55.4**	2.77	0.05	12	6	50	0.04	0.76	TRUE	1.1	2.6	0.87
KS2373B	TabunKS04	275	575	65.5	66.9	0.88	**58.9**	2.94	0.05	11	6	50	0.04	0.71	TRUE	1.3	3.2	0.87
KS2373C	TabunKS04	250	575	61.2	68.5	0.88	**60.3**	2.41	0.04	12	6	50	0.03	0.75	TRUE	2.2	6.8	0.89
KS1419A	Pottery	250	550	63.8	68.3	0.85	**58.1**	5.22	0.09	13	7	30	0.04	0.73	TRUE	3.9	6.8	0.90
KS1419C	Pottery	275	600	63	71.3	0.85	**60.6**	7.88	0.13	14	9	30	0.06	0.73	TRUE	2.6	8.0	0.89
KS2348AA[1]	Pottery	275	600	27.4	27.9	0.91	**25.4**	0.76	0.03	14	10	50	0.05	***0.62***	TRUE	6.4	8.3	0.90
KS2348AC[1]	Pottery	275	600	26.8	30.4	0.91	**27.7**	0.83	0.03	14	9	50	0.06	***0.61***	TRUE	6.6	8.9	0.90
KS2357AA	Pottery	250	600	75.7	85	0.84	**71.4**	5.00	0.07	15	10	50	0.05	0.72	TRUE	1.0	4.9	0.90
KS2357AB	Pottery	250	600	69.1	76.8	0.84	**64.5**	3.87	0.06	15	10	50	0.04	0.7	TRUE	2.4	5.1	0.91
KS2357AC	Pottery	175	575	77.1	76.6	0.84	**64.3**	4.50	0.07	17	9	50	0.04	0.76	TRUE	2.2	8.6	0.91
KS2357BA	Pottery	200	575	70.1	73	0.86	**62.8**	1.88	0.03	16	9	50	0.02	0.72	TRUE	3.1	8.6	0.93
KS2357BB	Pottery	200	575	69.6	72.5	0.86	**62.4**	1.87	0.03	15	9	50	0.02	0.75	TRUE	0.3	6.1	0.92
KS2357BC	Pottery	200	575	68.6	69	0.86	**59.3**	1.19	0.02	16	9	50	0.02	0.7	TRUE	1.3	4.8	0.93
KS2369A	Pottery	200	575	53.8	61.6	*0.77*	**47.4**	1.90	0.04	16	9	50	0.04	0.75	TRUE	2.1	4.8	0.91
KS2369B	Pottery	225	575	51.7	61.6	*0.77*	**47.4**	2.37	0.05	15	9	50	0.04	0.72	TRUE	2.4	4.3	0.90
KS2369C	Pottery	225	575	59.7	60.9	*0.77*	**46.9**	1.41	0.03	15	9	50	0.03	0.76	TRUE	2.0	5.2	0.90
KS2371A	Pottery	250	600	101	95.2	0.89	**84.7**	6.78	0.08	15	10	50	0.04	0.71	TRUE	0.9	6.0	0.91

KS2371C	Pottery	200	575	82.6	79.7	0.89	**70.9**	4.97	0.07	16	9	50	0.04	0.71	TRUE	2.4	5.9	0.90
KS2372A	Pottery	275	590	70.7	84	*0.87*	**73.1**	3.65	0.05	17	8	50	0.03	0.71	TRUE	3.6	3.8	0.93
KS2372B	Pottery	250	590	68.8	83.4	*0.87*	**72.6**	3.63	0.05	18	8	50	0.03	0.76	TRUE	3.5	5.9	0.93
KS2372C	Pottery	200	575	71.3	39.4	*0.87*	**34.3**	1.71	0.05	19	8	50	0.03	0.74	TRUE	2.6	6.2	0.93
KS2378B	Pottery	275	575	57.2	62.7	0.90	**56.4**	2.26	0.04	16	8	50	0.03	0.71	TRUE	1.5	4.5	0.92
KS2378C	Pottery	250	575	62.8	67.8	0.90	**61.0**	1.83	0.03	17	8	50	0.03	0.72	TRUE	0.1	3.8	0.92
KSG24A	Pottery	175	550	47.3	52.9	0.88	**46.6**	3.26	0.07	16	7	30	0.04	0.72	TRUE	2.6	6.7	0.92
KSG24C	Pottery	200	600	53.2	59.6	0.88	**52.4**	3.67	0.07	17	9	30	0.04	0.73	TRUE	0.9	4.4	0.92
KSG24D	Pottery	200	600	52.5	59.4	0.88	**52.3**	2.61	0.05	16	8	30	0.03	0.73	TRUE	2.7	5.0	0.92
KSMDS01A	Pottery	200	575	75.3	72.5	0.88	**63.8**	3.19	0.05	19	8	50	0.03	0.7	TRUE	3.2	8.2	0.93
KSMDS01B	Pottery	200	575	68.7	65.5	0.88	**57.6**	2.31	0.04	19	8	50	0.03	0.71	TRUE	0.9	6.6	0.93
KSMDS01C	Pottery	200	575	72.4	69.3	0.88	**61.0**	3.05	0.05	19	8	50	0.04	0.71	TRUE	2.1	7.7	0.92
KSMDS04B	Pottery	225	575	57.5	60.3	0.89	**53.7**	2.15	0.04	18	8	50	0.04	0.71	TRUE	3.0	7.2	0.93
KSMDS04C	Pottery	225	575	52.9	59.9	0.89	**53.3**	1.60	0.03	18	8	50	0.03	0.73	TRUE	0.4	6.3	0.94
Tel Halif																		
LH03A	TabunH02	300	600	75.7	75.4	0.91	**68.6**	4.12	0.06	11	6	50	0.04	0.74	TRUE	0.3	5.4	0.85
LH03B	TabunH02	250	600	81.1	80.4	0.91	**73.2**	4.39	0.06	13	6	50	0.04	0.71	TRUE	0.9	4.5	0.88
LH03C	TabunH02	225	600	68.1	67.5	0.91	**61.4**	3.69	0.06	14	6	50	0.04	0.7	TRUE	0.8	3.2	0.86
LH04A	TabunH02	275	600	83.1	75.7	0.91	**68.9**	6.20	0.09	12	6	50	0.06	0.73	TRUE	1.6	7.0	0.84

LH04B	TabunH02	225	600	82.6	75.4	0.91	**68.6**	4.12	0.06	14	6	50	0.04	0.76	TRUE	1.8	5.8	0.88
LH04C	TabunH02	200	600	72.4	66	0.91	**60.1**	3.60	0.06	15	6	50	0.04	0.83	TRUE	1.6	9.8	0.87
LH06A	TabunH03	250	575	63.5	65.3	0.92	**60.1**	4.21	0.07	12	6	50	0.06	0.74	TRUE	1.1	7.4	0.85
LH06B	TabunH03	200	575	65.8	67.8	0.92	**62.4**	3.74	0.06	14	6	50	0.05	0.71	TRUE	1.6	7.4	0.86

Temp Min and Max are the temperature range of best fit line used to determine paleointensity, Br is the raw paleointensity, AARM Corr Ba is the anisotropy corrected paleointensity, CRC is the cooling rate correction, σ is sigma used to calculate error, n is number of in-field steps used in paleointensity determination. Data obtained using the PmagPy (Version 3.16) software set to Autointerpretation with selection criteria set to: a minimum of 4 data points (n) for paleointensity determination in the Arai plot and 2 pTRM checks, FRAC≥0.7, SCAT=True(Pass), Beta (β)=0.1, MAD and DANG ≤ 10°. [1]The FRAC criteria for the following two specimens was set to 0.6 to obtain a result as no other samples from this strata passed the criteria. See Chapter 5 Section 5.2 for further explaination of criteria definitions.

Appendix B

Following are additional figures and tables referred to in section 5.2, from Stillinger, et al., 2015. Refining the archaeomagnetic dating curve for the Near East: New intensity data from Bronze Age ceramics at Tell Mozan, Syria, *Journal of Archaeological Science*, Vol 53, pp. 345-355.

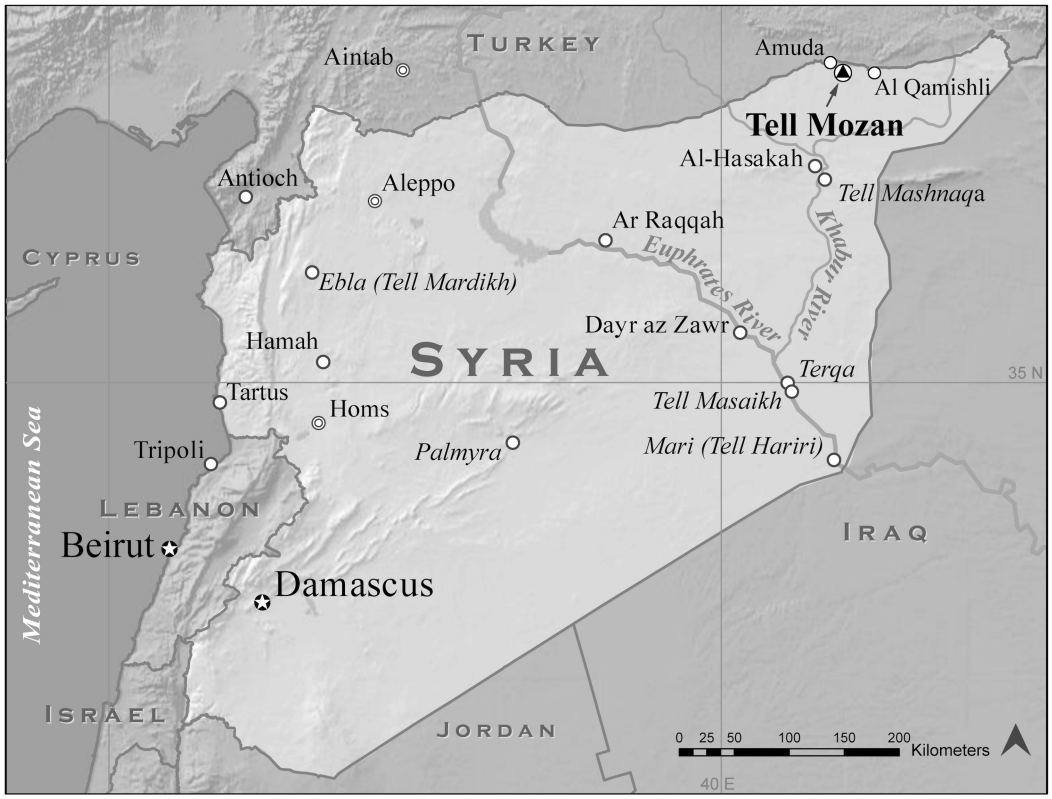

Figure B- 1 Location of Tell Mozan

Tell Mozan with respect to other prominent archaeological sites (in italics) and contemporary cities.

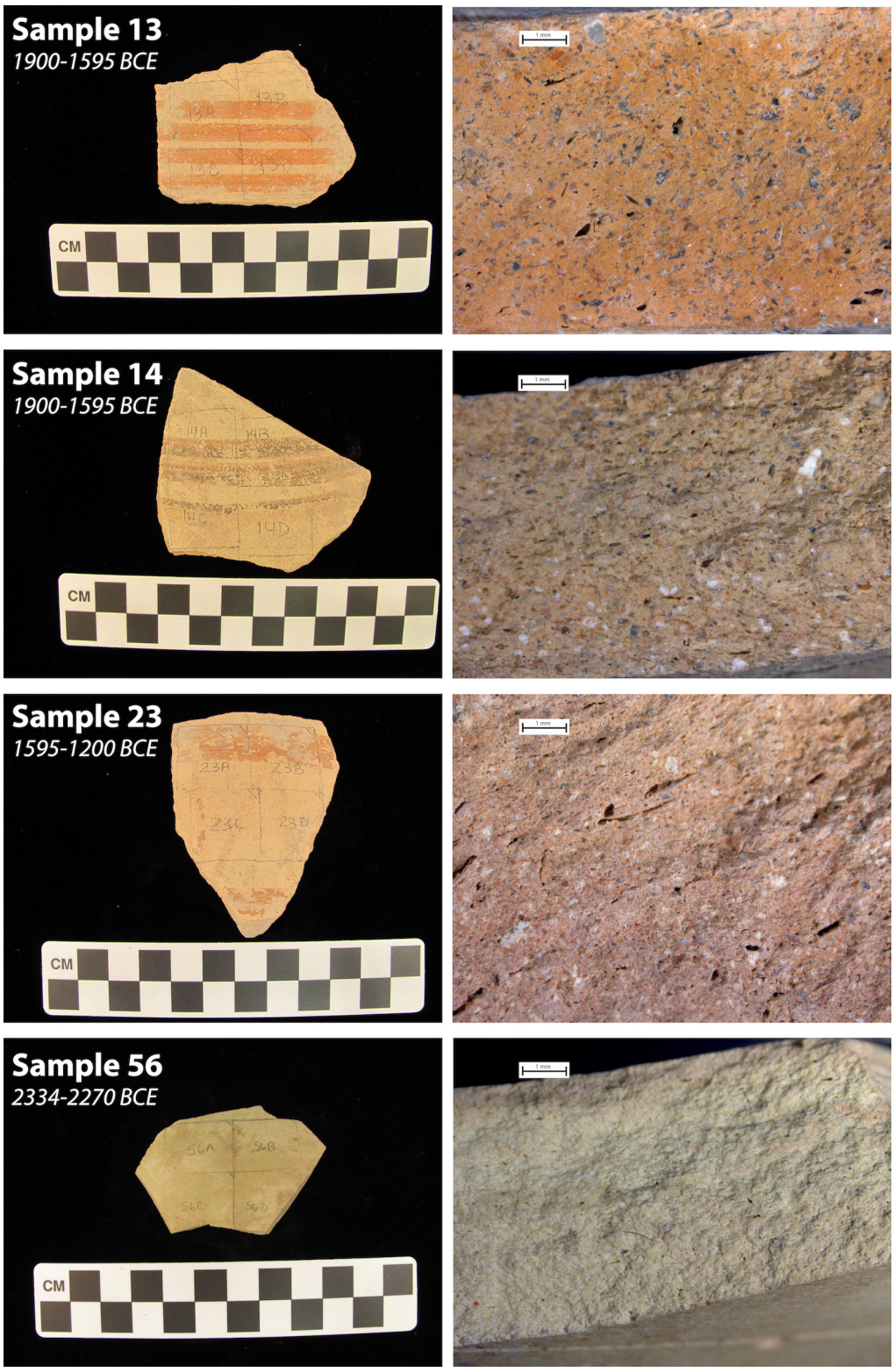

Figure B- 2 Representative Samples from Tell Mozan

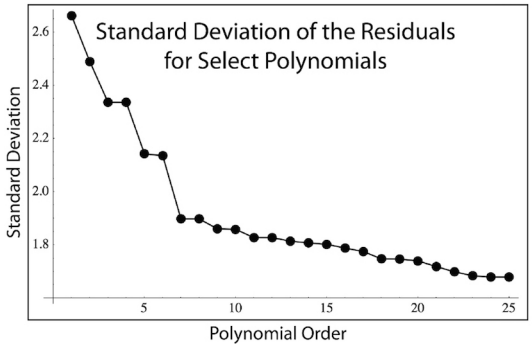

Linear model fit of the data to 25th order polynomial =
8.88972 + 0.0030953 x + 0.0000814326 x2 - 1.62243*10-7 x3
- 7.13646*10-10 x4 + 1.40044*10-12 x5 + 3.63513*10-15 x6
- 4.60042*10-18 x7 - 1.2095*10-20 x8 + 4.59519*10-24 x9 +
2.34357*10-26 x10 + 7.29769*10-30 x11 - 2.14858*10-32 x12
- 2.0279*10-35 x13 + 2.47986*10-39 x14 + 1.38538*10-41 x15
+ 8.14559*10-45 x16 - 5.2246*10-50 x17 - 2.73847*10-51 x18
- 1.88333*10-54 x19 - 7.17235*10-58 x20 - 1.77913*10-61 x21
- 2.95588*10-65 x22 - 3.19489*10-69 x23 - 2.04094*10-73 x24
- 5.86622*10-78 x25

Figure B- 3 Polynomial Model Calculation

Table B- 1 Chronology for Tell Mozan

Site Phase	Description	Mesopotamian	Standard Near Eastern Chronology	Syrian
6	scattered occupations	Middle Babylonian/Kassite/ Hittite (1595-1200 BCE)	MBA IIC through LBA	Mitanni
5	last settlements beginning with expansion over scattered occupations and ending in collapse	Old Babylonian-Khabur (1900-1595 BCE)	MBA IIA to C	OJ II to OJ III
4b	middle settlement north, scattered occupation south	Isin-Larsa (2000-1900 BCE)	MBA IIA	OJ I
4a	lower settlement north, scattered occupation south	Ur III (2112-2004 BCE)	MBA I	EJ V
3b	palace dependency, continued re-use	Post-imperial Akkadian (2192-2112 BCE)	EBA IV	EJ IV
3a	palace dependency, destruction and first re-use under Tar'am-Agade	Naram-Sin/Šar-kali-šarri (2240-2193 BCE)	EBA III to EBA IV	
2	Palace construction and occupation of Tupkish Palace	Man-ištu-šu/Naram-Sin (2269-2240 BCE)	EBA III	EJ III b
1	Pre-palace construction	Sargon/Rimuš (2334-2270 BCE)		
NA	Temple complex and external city walls constructed	Early Dynastic III (2500-2334 BCE)	EBA III	EJ III a

Adapted from Buccellati (2003)

Table B- 2 Archaeointensity Results for Tell Mozan

Sample ID	n	Site Phase	Near East Chronology	Phase Attributed Age (BCE)	Corrected Intensity (μT)	VADM (ZAm^2)
TM09	2	6	MBA IIC/LBA	1595-1200	38.9±0.8	69.8±1.4
TM23	3	6	MBA IIC/LBA	1595-1200	49.7±2.2	89.2±4.0
TM13	3	5	MBA II	1900-1595	42.1±0.7	75.6±1.3
TM14	3	5	MBA II	1900-1595	38.9±1.4	69.8±2.5
TM51	3	4b	MBA IIA	2000-1900	52.6±2.2	94.4±4.0
TM32	3	4a/4b	MBAI/MBA IIA	2112-1900	52.2±2.8	93.6±5.0
TM72	3	4a/4b	MBAI/MBA IIA	2112-1900	42.7±2.2	76.6±4.0
TMm01	2	3b/4a	EBA IV/MBA I	2192-2004	48.9±2.0	87.8±3.5
TMm04	2	3b/4a	EBA IV/MBA I	2192-2004	40.0±1.7	71.9±3.0
TM35	3	3a/3b	EBA III/EBA IV	2240-2112	48.6±1.7	87.3±3.0
TM64	2	3a	EBA III	2240-2193	60.4±3.3	108.4±5.9
TM65	3	3a	EBA III	2240-2193	42.4±1.5	76.0±2.7
TM40	3	1	EBA III	2334-2270	42.7±1.8	76.7±3.3
TM56	3	1	EBA III	2334-2270	44.9±1.1	80.7±1.9

VADM (ZAm^2) = Virtual axial dipole moment x 10^{21} Am^2, n = number of specimens per sample

Table B- 3 Rock Magnetic Results for Tell Mozan

Sample ID	Average χ ($m^3/kg \times 10^{-6}$)	χ_{lf} ($m^3/kg \times 10^{-6}$)	χ_{hf} ($m^3/kg \times 10^{-6}$)	χ_{fd} (%)	Ms ($Am^2/kg \times 10^{-2}$)	Mr ($Am^2/kg \times 10^{-2}$)	Hc (mT)	Hcr (mT)	NRM ($Am^2/kg \times 10^{-3}$)	MDF (mT)
TM09	3.50	2.92	2.80	3.93	15.60	5.69	17.6	32.3	3.05	27.6
TM13	4.31	4.15	3.74	9.98	13.80	2.66	8.3	21.1	1.37	9.4
TM14	3.99	4.05	3.71	8.39	14.80	4.51	12	28.5	1.36	25
TM23	4.86	4.96	4.50	9.13	15.70	3.01	7.4	16.5	2.42	14.6
TM32	5.47	5.75	5.19	9.81	25.90	7.48	11.6	29.5	3.05	15.4
TM35	3.65	3.70	3.55	4.02	43.30	11.20	6.6	12.9	2.65	11.2
TM40	0.23	0.21	0.21	1.63	1.39	0.32	7.8	22.1	0.13	15.6
TM51	1.95	2.16	1.90	11.97	3.83	0.44	3.7	15.2	0.20	18.5
TM56	0.42	0.41	0.40	2.3	1.42	0.53	16.1	28.7	0.39	11.2
TM64	5.65	5.54	5.22	5.81	16.70	4.55	6.6	11.8	13.70	10
TM65	4.11	4.13	3.86	6.54	11.00	3.25	7.9	16.1	3.01	14.8
TM72	6.45	6.79	6.13	9.68	21.80	2.51	4.4	14.4	0.92	7
TMm01	6.11	6.08	5.46	10.22	18.40	3.52	7.2	19.1	1.25	7.5
TMm04	2.48	2.42	2.25	6.8	8.26	2.68	13.6	33.2	1.19	25.1

Susceptibility (χ) is average for all three specimens in the sample, all remaining results based on measurements obtained from one of three specimen sets. χ_{lf} is low frequency susceptibility, χ_{hf} is high frequency susceptibility, χ_{fd} is frequency dependence of susceptibility, Ms is saturation magnetization, Mr is remanent magnetization, Hc is coercivity, Hcr is coercivity of remanence, NRM is natural remanent magnetization, and MDF is median destructive field.

Table B- 4 Selection Criteria for Tell Mozan Samples

Specimen	f_{VDS}	Mean DRAT %	Mean MD%	DANG	MAD	f_{VDS} test >.8	Mean DRAT <10%	Mean MD<5%	DANG <5	MAD<10
TM09A	0.96	5.0	0.6	0.2	1.9	PASS	PASS	PASS	PASS	PASS
TM09C	0.98	10.8	0.7	0.9	1.8	PASS	FAIL	PASS	PASS	PASS
TM09D	0.94	6.4	0.3	1	4.4	PASS	PASS	PASS	PASS	PASS
TM13A	0.93	8.6	0.4	0.2	3.3	PASS	PASS	PASS	PASS	PASS
TM13B	0.91	9.2	0.4	1	2.5	PASS	PASS	PASS	PASS	PASS
TM13C	0.94	9.2	0.4	0.4	4	PASS	PASS	PASS	PASS	PASS
TM14A	0.89	6.3	0.6	3.2	7.3	PASS	PASS	PASS	PASS	PASS
TM14B	0.89	5.1	0.6	0.6	3.6	PASS	PASS	PASS	PASS	PASS
TM14C	0.88	4.1	0.6	0.5	3.7	PASS	PASS	PASS	PASS	PASS
TM23A	0.84	4.8	0.8	0.2	1.7	PASS	PASS	PASS	PASS	PASS
TM23B	0.86	7.6	0.7	1	3.8	PASS	PASS	PASS	PASS	PASS

TM23D	0.88	5.4	0.8	0.7	3.9	PASS	PASS	PASS	PASS	PASS
TM32A	0.91	8.1	0.8	0.5	2.7	PASS	PASS	PASS	PASS	PASS
TM32B	0.92	5.6	0.7	1.2	4.5	PASS	PASS	PASS	PASS	PASS
TM32D	0.92	7.3	0.7	0.8	3.2	PASS	PASS	PASS	PASS	PASS
TM35A	0.93	4.3	0.4	0.6	4.4	PASS	PASS	PASS	PASS	PASS
TM35B	0.95	5.7	0.4	1.1	2.2	PASS	PASS	PASS	PASS	PASS
TM35C	0.92	10.4	0.5	0.2	1.9	PASS	FAIL	PASS	PASS	PASS
TM40A	0.95	4.9	0.6	1.8	4	PASS	PASS	PASS	PASS	PASS
TM40B	0.87	5.2	0.5	1.2	2.8	PASS	PASS	PASS	PASS	PASS
TM40D	0.90	6.9	0.8	2.5	5.1	PASS	PASS	PASS	PASS	PASS
TM51A	0.87	2.6	1.4	1.9	2.8	PASS	PASS	PASS	PASS	PASS
TM51B	0.87	0.5	1.1	0.3	3.8	PASS	PASS	PASS	PASS	PASS
TM51D	0.84	1.2	1.1	0.7	4.1	PASS	PASS	PASS	PASS	PASS
TM56A	0.96	4.2	0.8	0.2	3	PASS	PASS	PASS	PASS	PASS
TM56B	0.96	7.1	0.5	0.4	2.8	PASS	PASS	PASS	PASS	PASS
TM56D	0.94	3.5	0.5	0.6	2	PASS	PASS	PASS	PASS	PASS
TM58A	0.94	8.5	0.7	1.3	2.9	PASS	PASS	PASS	PASS	PASS
TM58B	0.92	7.3	0.7	1.5	4.1	PASS	PASS	PASS	PASS	PASS
TM58D	0.90	8.3	0.7	1.2	2.9	PASS	PASS	PASS	PASS	PASS
TM64B	0.90	7.4	0.4	0.4	2.8	PASS	PASS	PASS	PASS	PASS
TM64C	0.76	11.5	0.4	11.6	7.3	FAIL	FAIL	PASS	FAIL	PASS
TM64D	0.90	9.5	0.3	0.8	3.3	PASS	PASS	PASS	PASS	PASS
TM65A	0.90	8.4	0.6	0.4	2.2	PASS	PASS	PASS	PASS	PASS
TM65B	0.92	6.6	0.6	0.6	3	PASS	PASS	PASS	PASS	PASS
TM65C	0.93	4.0	0.5	0.4	2.9	PASS	PASS	PASS	PASS	PASS
TM72A	0.91	5.6	1.3	2.5	6.6	PASS	PASS	PASS	PASS	PASS
TM72B	0.90	3.2	1.0	1	3.3	PASS	PASS	PASS	PASS	PASS
TM72D	0.91	3.2	0.8	0.4	4.1	PASS	PASS	PASS	PASS	PASS
TMmds01A	0.89	5.4	0.9	1.7	8.5	PASS	PASS	PASS	PASS	PASS
TMmds01B	0.89	4.2	1.3	0.3	4.1	PASS	PASS	PASS	PASS	PASS
TMmds01D	0.86	1.9	5.2	0.3	7	PASS	PASS	FAIL	PASS	PASS
TMmds04A	0.94	8.6	0.4	1.7	7.1	PASS	PASS	PASS	PASS	PASS
TMmds04B	0.84	7.5	0.4	1.2	5.9	PASS	PASS	PASS	PASS	PASS
TMmds04C	0.80	12.1	0.4	6.6	5.4	FAIL	FAIL	PASS	FAIL	PASS

f_{VDS} =fraction of magnetization normalized by the vector difference sum (vds) of the NRM used to calculate the slope of the line that defines the intensity. The Mean Difference Ratio (Mean DRAT) indicates the average % difference between pTRMs and the pTRM checks incorporated by the best-fit straight line. Mean MD or multidomain contribution is the average % difference between pTRM and pTRM tail checks. The Deviation Angle (DANG) is the angle between the best-fit line of the data used in the slope calculation and the best-fit line from the origin through the center of mass of the data. The Maximum Angular Deviation (MAD) represents the variance of the points within a particular temperature interval used to define the direction.

Table B- 5 Archaeointensity Results and Criteria Statistics for Tell Mozan

Specimen	Tmin	Tmax	n	Raw Paleofield (μT)	ARM Corrected Paleofield (μT)	σ error	Fc	Negative slope (b)	β	q	f	g	sigma	f_{VDS}	Mean DRAT%	Mean MD%	MD Max%	DANG	MAD
TM09A	175	550	14	31.8	36.5	0.6	1.04	1.06	0.01	54.8	0.89	0.91	0.016	0.96	5.0	0.6	1.3	0.2	1.9
TM09C	150	550	17	112.0	127.2	39.4	1.04	3.73	0.08	12.5	1.12	0.92	0.310	0.98	10.8	0.7	1.6	0.9	1.8
TM09D	175	550	16	34.5	39.0	1.0	1.04	1.15	0.02	37.2	0.89	0.92	0.026	0.94	6.4	0.3	1.0	1.0	4.4
TM13A	100	600	18	42.4	44.1	0.9	0.94	1.41	0.01	53.4	0.89	0.89	0.021	0.93	8.6	0.4	1.4	0.2	3.3
TM13B	175	575	17	43.6	45.1	0.6	0.94	1.45	0.01	87.8	0.80	0.92	0.012	0.91	9.2	0.4	1.2	1.0	2.5
TM13C	175	600	18	44.0	45.7	0.9	0.94	1.47	0.02	52.4	0.85	0.93	0.022	0.94	9.2	0.4	1.0	0.4	4.0
TM14A	225	550	12	39.6	42.2	2.2	1.00	1.32	0.04	14.8	0.65	0.90	0.052	0.89	6.3	0.6	1.0	3.2	7.3
TM14B	225	575	15	37.1	39.4	1.4	1.00	1.24	0.03	22.8	0.70	0.92	0.035	0.89	5.1	0.7	1.3	0.6	3.6
TM14C	225	575	15	35.0	37.4	1.0	1.00	1.17	0.02	27.3	0.70	0.92	0.028	0.88	4.1	0.6	0.9	0.5	3.7
TM23A	100	550	17	44.5	49.5	1.9	1.01	1.48	0.03	33.0	0.90	0.93	0.038	0.84	4.8	0.8	1.2	0.2	1.7
TM23B	150	525	16	44.7	49.2	2.6	1.01	1.49	0.04	21.9	0.85	0.93	0.054	0.86	7.6	0.7	1.7	1.0	3.8
TM23D	150	550	17	44.2	48.8	2.3	1.01	1.47	0.03	25.2	0.87	0.93	0.047	0.88	5.4	0.8	1.3	0.7	3.9
TM32A	175	550	14	50.8	53.5	2.5	0.96	1.69	0.03	26.8	0.81	0.90	0.046	0.91	8.1	0.8	1.4	0.5	2.7
TM32B	150	575	18	56.2	59.0	6.6	0.96	1.87	0.06	13.7	0.87	0.94	0.112	0.92	5.6	0.7	1.3	1.2	4.5
TM32D	175	575	17	51.1	53.6	2.1	0.96	1.70	0.02	35.0	0.85	0.93	0.039	0.92	7.3	0.7	1.4	0.8	3.2
TM35A	175	550	16	49.7	49.5	2.3	0.98	1.66	0.03	24.9	0.80	0.88	0.047	0.93	4.3	0.4	1.6	0.6	4.4
TM35B	150	550	17	48.8	48.6	1.6	0.98	1.63	0.02	38.5	0.87	0.89	0.033	0.95	5.7	0.4	0.7	1.1	2.2
TM35C	175	500	13	49.0	50.4	1.5	0.98	1.63	0.02	40.3	0.82	0.87	0.029	0.92	10.4	0.5	1.6	0.2	1.9
TM40A	100	600	18	46.3	43.1	1.9	0.89	1.54	0.03	30.5	0.95	0.93	0.044	0.95	4.9	0.6	1.6	1.8	4.0
TM40B	150	575	18	50.7	47.3	1.6	0.89	1.69	0.02	40.6	0.86	0.94	0.033	0.87	5.2	0.5	1.0	1.2	2.8
TM40D	175	575	17	56.9	56.3	3.1	0.89	1.90	0.03	25.9	0.80	0.93	0.055	0.90	6.9	0.8	1.5	2.5	5.1
TM51A	100	600	18	51.4	54.1	2.3	0.96	1.71	0.02	28.5	0.75	0.94	0.042	0.87	2.6	1.4	2.5	1.9	2.8
TM51B	150	600	19	53.0	56.3	2.7	0.96	1.77	0.02	24.5	0.64	0.94	0.043	0.87	0.5	1.1	2.1	0.3	3.8
TM51D	175	600	18	50.9	53.8	2.4	0.96	1.70	0.02	22.3	0.58	0.94	0.041	0.84	1.2	1.1	2.6	0.7	4.1

TM56A	200	550	13	37.4	44.0	1.0	1.04	1.25	0.02	40.9	0.89	0.85	0.023	0.96	4.2	0.8	1.9	0.2	3.0
TM56B	250	550	13	37.9	47.9	1.0	1.04	1.26	0.02	43.0	0.83	0.88	0.021	0.96	7.1	0.5	1.0	0.4	2.8
TM56D	275	550	12	30.9	37.9	1.1	1.04	1.03	0.03	23.9	0.77	0.84	0.028	0.94	3.5	0.5	1.5	0.6	2.0
TM58A	125	600	17	46.7	55.9	1.7	0.89	1.56	0.02	40.7	0.88	0.92	0.031	0.94	8.5	0.7	1.4	1.3	2.9
TM58B	150	575	18	48.5	57.0	2.0	0.89	1.62	0.02	37.1	0.86	0.94	0.035	0.92	7.3	0.7	1.5	1.5	4.1
TM58D	175	575	17	47.2	53.8	1.5	0.89	1.57	0.02	40.7	0.79	0.93	0.029	0.90	8.3	0.7	1.3	1.2	2.9
TM64B	150	550	17	52.8	59.3	3.5	0.96	1.76	0.03	24.5	0.89	0.92	0.059	0.90	7.4	0.4	1.2	0.4	2.8
TM64C	225	450	10	69.0	64.6	10.2	0.96	2.30	0.07	7.9	0.62	0.87	0.158	0.76	11.5	0.4	1.1	11.6	7.3
TM64D	150	550	17	58.5	65.9	3.3	0.96	1.95	0.03	29.6	0.82	0.92	0.050	0.90	9.5	0.3	0.7	0.8	3.3
TM65A	150	450	13	38.9	44.2	1.0	0.95	1.30	0.02	40.8	0.83	0.89	0.024	0.90	8.4	0.6	1.4	0.4	2.2
TM65B	200	550	15	38.4	43.3	1.7	0.95	1.28	0.03	22.8	0.80	0.88	0.040	0.92	6.6	0.6	1.7	0.6	3.0
TM65C	200	550	15	42.3	47.4	2.8	0.95	1.41	0.04	15.2	0.74	0.87	0.060	0.93	4.0	0.5	1.8	0.4	2.9
TM72A	125	550	16	40.8	45.1	4.9	0.94	1.36	0.08	8.5	0.75	0.92	0.110	0.91	5.6	1.3	3.1	2.5	6.6
TM72B	175	550	16	39.2	43.5	1.8	0.94	1.31	0.03	20.2	0.70	0.92	0.041	0.90	3.2	1.0	2.0	1.0	3.3
TM72D	175	550	16	42.9	47.0	2.0	0.94	1.43	0.03	21.3	0.68	0.92	0.042	0.91	3.2	0.8	1.6	0.4	4.1
TMmds01A	225	600	13	47.2	54.2	2.2	0.96	1.57	0.03	20.1	0.57	0.90	0.040	0.89	5.4	0.9	1.4	1.7	8.5
TMmds01B	200	575	16	41.9	48.6	1.8	0.96	1.40	0.03	25.0	0.70	0.93	0.036	0.89	4.2	1.3	1.9	0.3	4.1
TMmds01D	350	600	11	44.9	49.6	4.3	0.96	1.50	0.06	6.8	0.44	0.89	0.086	0.86	1.9	5.2	24.0	0.3	7.0
TMmds04A	200	600	14	37.2	40.2	1.4	0.98	1.24	0.03	25.2	0.76	0.91	0.034	0.94	8.6	0.4	0.7	1.7	7.1
TMmds04B	225	600	16	38.8	42.0	2.5	0.98	1.29	0.04	17.4	0.77	0.93	0.053	0.84	7.5	0.4	1.1	1.2	5.9
TMmds04C	225	550	14	93.3	103.6	14.1	0.98	3.11	0.04	16.4	0.80	0.90	0.136	0.80	12.1	0.4	1.1	6.6	5.4

The Tmin and Tmax represent min and max temperatures of best-fit line used in intensity calculations. n = number of measurements within that temperature range. Fc = cooling rate correction. b = slope used in intensity calculation. Beta (β) = is the scatter parameter = sigma/slope. q or quality index = (b)(f)(gap)/sigma. f = remanence fraction of total NRM used from Arai plot. g = gap factor or spacing of the points along the slope (value of 1 is best). sigma = the standard error of the slope. fVDS =fraction of magnetization normalized by the vector difference sum (vds) of the NRM used to calculate the slope of the line that defines the intensity. The Mean Difference Ratio (Mean DRAT) = the average % difference between pTRMs and the pTRM checks incorporated by the best-fit straight line. Mean MD or multidomain contribution = the average % difference between pTRM and pTRM tail checks. MeanMDmax = the maximum % difference between pTRM and pTRM tail checks. The Deviation Angle (DANG) = the angle between the best-fit line of the data used in the slope calculation and the best-fit line from the origin through the center of mass of the data. The Maximum Angular Deviation (MAD) = the variance of the points within a particular temperature interval used to define the direction.